

# Nonequilibrium Quantum Dynamics in Driven Baths

## **Dissertation**

zur Erlangung des Doktorgrades  
an der Fakultät für Mathematik, Informatik und  
Naturwissenschaften

Fachbereich Physik  
der Universität Hamburg

vorgelegt von  
**Joscha Reichert**

Hamburg  
2020

urn:nbn:de:gbv:18-ediss-88367

Gutachter/innen der Dissertation:

Prof. Dr. Michael Thorwart  
Prof. Dr. Peter Nalbach

Zusammensetzung der Prüfungskommission:

Prof. Dr. Michael Thorwart  
Prof. Dr. Peter Nalbach  
Prof. Dr. Robin Santra  
Prof. Dr. Christian Bressler  
Prof. Dr. Daniela Pfannkuche

Vorsitzende/r der Prüfungskommission:

Prof. Dr. Daniela Pfannkuche

Datum der Disputation:

03.02.2020

Vorsitzender des Fach-Promotionsausschusses Physik:

Prof. Dr. Günter Hans Walter Sigl

Leiter des Fachbereichs Physik:

Prof. Dr. Wolfgang Hansen

Dekan der Fakultät MIN:

Prof. Dr. Heinrich Graener

## Abstract

This thesis is concerned with the dynamics in open quantum systems on the basis of so-called system-bath models. Therein, a physical problem is partitioned into a quantum system of interest and a (large) surrounding environment. The latter constitutes a (heat) bath. As a principle, however, the bath degrees of freedom are assumed to be in thermal equilibrium, even while the system can be perturbed by strong external driving forces. This thesis presents collected works concerned with extending the system-bath framework to the situation of driven bath modes.

We show that a dipole-type coupling of bath modes to a classical electric field leads to an effective force on the quantum system of interest. This force represents the effect of the nonequilibrium distribution of the bath and depends on its spectral characteristics. We analyze this force in detail and investigate its effect on suitable model systems. We find that the linear response for a polarizable molecule immersed in liquid water and a colloidal quantum-dot metal-nanoparticle setup is qualitatively altered and includes negative absorbance. Quantum dynamics are obtained for the driven spin-boson model by utilizing a Born-Markov quantum master equation approach and the non-interacting blip approximation. The resulting force is most relevant at low temperatures and small to intermediate system-bath coupling strength with strong external driving fields. We find evidence that excitation of the quantum system by way of this force is more effective when resonances are present in the environment.

As an example for a nonequilibrium environment, we also consider the optical response of liquid water to an intense terahertz pulse by analyzing the resulting Kerr effect. We employ a matrix method on the basis of an Euler-Langevin equation to characterize the rotational dynamics of a water molecule and compare the theoretical predictions with experimental data. We find some qualitative agreement and a strong influence of the permanent molecular dipole moment on the resulting signal. A preliminary analysis suggests that bath driving effects can secure better agreement with the experimental data.

Finally, we discuss the extension to parametrically driven bath modes and give an outlook to more applications where bath driving can be used as a modelling prescription. We hope that the research contained in this thesis paves the way for further research on the topic of driven quantum baths and is able to inform novel applications.

## Kurzfassung

Die vorliegende Dissertation behandelt die Dynamik in offenen Quantensystemen auf Basis sogenannter System-Bad-Modelle. Darin wird ein physikalisches Problem in ein zu untersuchendes Quantensystem und eine (große) Umgebung eingeteilt. Letzteres stellt ein (Wärme-) Bad dar. Im Allgemeinen wird das Bad als im thermischen Gleichgewicht angenommen, obwohl das System durch starke externe Treibkräfte beeinflusst werden kann. Diese Dissertation widmet sich daher der Verallgemeinerung von System-Bad-Modellen zu getriebenen Badmoden.

Wir zeigen, dass eine dipolartige Kopplung der Moden an ein klassisches elektrisches Feld zu einer effektiven Kraft auf das Quantensystem führt. Diese Kraft drückt die resultierende Nichtgleichgewichtsverteilung des Bades aus und hängt von dessen spektralen Eigenschaften ab. Wir betrachten diese Kraft im Detail und untersuchen deren Effekt auf verschiedene Modellsysteme. Konkret finden wir qualitative Änderungen und negative Absorption im linearen Antwortverhalten eines polarisierbaren Moleküls in Wasser, sowie dem eines kolloidalen Quantenpunktes in Kontakt mit einem metallischen Nanoteilchen. Weiterhin wird die Quantendynamik des getriebenen Spin-Boson-Modells mit Hilfe einer Born-Markov-Quantenmastergleichung und der “non-interacting-blip”-Näherung betrachtet. Es zeigt sich, dass die Kraft am wirkungsvollsten bei niedrigen Temperaturen, schwacher bis mittlerer Kopplungsstärke und starken elektrischen Feldern wird. Wir finden zudem Hinweise darauf, dass das Quantensystem durch die Existenz einer Badresonanz effektiver angeregt wird.

Als weiteres Beispiel für eine Nichtgleichgewichtsumgebung betrachten wir die optische Antwort von Wasser auf einen intensiven Puls im Terahertzbereich durch Analyse des Kerr-Effekts. Dazu verwenden wir eine Matrixmethode auf Basis einer Euler-Langevin Gleichung für die Rotationsbewegung eines Wassermoleküls und vergleichen die theoretischen Vorhersagen mit experimentellen Messungen. Wir finden eine grobe qualitative Übereinstimmung sowie einen starken Einschlag des permanenten Dipolmoments auf das entstehende Signal. Erste Analysen lassen vermuten, dass eine bessere Übereinstimmung mit den experimentellen Daten durch getriebene Badeffekte erreicht werden kann.

Wir schließen die Dissertation mit einem Ausblick auf potenzielle Anwendungen und eine Erweiterung des Formalismus zu parametrisch getriebenen Bädern. Wir hoffen,

dass die Ergebnisse in dieser Dissertation zu weiterer Forschung im Bereich getriebener Quantenbäder führt und neuartige Anwendungen inspirieren kann.

## Published and unpublished results

This work is based on the following published articles:

- H. Grabert, P. Nalbach, J. Reichert, and M. Thorwart, “Nonequilibrium Response of Nanosystems Coupled to Driven Quantum Baths”, *The Journal of Physical Chemistry Letters* **7**, 2015–2019 (2016),
- J. Reichert, P. Nalbach, and M. Thorwart, “Dynamics of a quantum two-state system in a linearly driven quantum bath”, *Physical Review A* **94**, 032127 (2016),
- P. Zalden, L. Song, X. Wu, H. Huang, F. Ahr, O. D. Mücke, J. Reichert, M. Thorwart, P. K. Mishra, R. Welsch, R. Santra, F. X. Kärtner, and C. Bressler, “Molecular polarizability anisotropy of liquid water revealed by terahertz-induced transient orientation”, *Nature Communications* **9**, 2142 (2018).

The following novel results contained within this thesis have not been published yet

- The derivation of the quantum Langevin equation in Part 4.
- The derivation of the two-sphere geometry result in the quantum-dot metal-nanoparticle setup in Part 4. This calculation was originally done by Prof. Hermann Grabert.
- The entirety of Part 6. This includes the derivation of the influence functional for a linearly driven bath, the emergence of the non-Markovian force, the strong coupling, non-zero temperature dynamics for dipolar bath driving and the outlook to parametric bath driving.
- The outlook and detailed discussion of water dynamics with respect to the Kerr effect in Part 7.
- Most of the results and discussions that appear in the appendix which includes the discussion of different Onsager geometries and the preliminary analyses of the transition probability and extensions to the Kerr effect theory of Part 7.

# Contents

<b>1</b>	<b>Introduction: Driven quantum baths</b>	<b>1</b>
<b>2</b>	<b>Quantum dissipation and system-bath models</b>	<b>4</b>
2.1	Decoherence and relaxation . . . . .	4
2.1.1	Golden rule rates . . . . .	7
2.1.2	Dephasing . . . . .	9
2.1.3	Detailed balance . . . . .	10
2.2	System-bath models . . . . .	11
2.2.1	The Caldeira-Leggett model . . . . .	12
2.2.2	Bath spectral density . . . . .	15
2.2.3	The spin-boson model . . . . .	19
2.3	Some solution methods . . . . .	24
2.3.1	Quantum master equations . . . . .	24
2.3.2	Path integral methods . . . . .	28
2.3.3	Other methods . . . . .	31
<b>3</b>	<b>The Onsager model and driven quantum systems</b>	<b>34</b>
3.1	Electrodynamics in materials . . . . .	34
3.1.1	Macroscopic Maxwell equations . . . . .	34
3.1.2	Electrostatic boundary conditions . . . . .	37
3.1.3	Dynamic polarization . . . . .	38
3.1.4	Refractive index and dielectric function . . . . .	39
3.1.5	Nonlinear effects and Kerr effect . . . . .	41
3.1.6	Molecular polarizability . . . . .	43
3.2	The Onsager solvation model . . . . .	45
3.2.1	Continuum solvation models . . . . .	46
3.2.2	Electrostatics for the Onsager sphere . . . . .	47
3.2.3	Connection to system-bath models . . . . .	50
3.3	Driven dissipative quantum systems . . . . .	51
3.3.1	General features . . . . .	51

3.3.2	Dipolar coupling to a time-dependent electric field . . . . .	53
3.3.3	Transition probabilities of a driven two-state system . . . . .	54
3.3.4	Linear response theory . . . . .	58
3.3.5	Optical Bloch equations . . . . .	59
3.3.6	Floquet theory . . . . .	61
<b>4</b>	<b>Linear response of nanosystems in a linearly driven bath</b>	<b>63</b>
4.1	The driven bath Hamiltonian . . . . .	63
4.2	Quantum Langevin dynamics for a linearly driven bath . . . . .	64
4.2.1	Caldeira-Leggett model . . . . .	65
4.2.2	Spin-boson model . . . . .	66
4.2.3	Evaluation of the effective force . . . . .	67
4.3	Polarizable molecule immersed in water . . . . .	69
4.3.1	Water in the THz regime . . . . .	71
4.3.2	Linear response of a polarizable molecule . . . . .	72
4.3.3	Dynamic polarizability . . . . .	74
4.4	Interacting quantum-dot metal-nanoparticle setup . . . . .	77
4.4.1	Quantum dots and plasmons . . . . .	79
4.4.2	The two-sphere geometry . . . . .	80
4.4.3	Linear response of the quantum dot . . . . .	82
4.4.4	Evaluation of the linear response . . . . .	84
4.5	Conclusion of Part 4 . . . . .	86
<b>5</b>	<b>The non-Markovian force and quantum master equation approach</b>	<b>88</b>
5.1	The non-Markovian force . . . . .	88
5.1.1	The effective force . . . . .	91
5.1.2	Redefined Hamiltonian . . . . .	93
5.1.3	Characterization of the non-Markovian force . . . . .	94
5.2	Adiabatic-Markovian master equation approach . . . . .	97
5.2.1	Liouville space quantum master equation . . . . .	97
5.2.2	Born approximation . . . . .	98
5.2.3	Adiabatic-Markovian approximation . . . . .	101
5.2.4	Rates and Bloch equations . . . . .	103
5.3	Two-state system dynamics . . . . .	106
5.3.1	Validity of the nonequilibrium Bloch equations . . . . .	106
5.3.2	Zero temperature rates and bath state . . . . .	107
5.3.3	Time-dependent dynamics . . . . .	108
5.3.4	Response spectra . . . . .	111
5.4	Conclusion of Part 5 . . . . .	115



<b>6</b>	<b>Driven influence functional and strong coupling dynamics</b>	<b>117</b>
6.1	The path integral formulation and the non-interacting blip approximation	117
6.1.1	Closed expressions for the system dynamics . . . . .	119
6.1.2	The non-interacting blip approximation (NIBA) . . . . .	125
6.1.3	Dynamics within the NIBA . . . . .	127
6.2	Formulation for a linearly driven bath . . . . .	129
6.2.1	The influence functional for a linearly driven bath . . . . .	129
6.2.2	Initial correlations and emergence of the non-Markovian force	132
6.2.3	NIBA dynamics for a linearly driven bath . . . . .	134
6.2.4	Parametrically driven baths . . . . .	143
6.3	Conclusion of Part 6 . . . . .	144
<b>7</b>	<b>THz Kerr effect dynamics in liquid water</b>	<b>146</b>
7.1	Kerr effect dynamics . . . . .	146
7.1.1	Microscopic description . . . . .	147
7.1.2	Euler-Langevin description . . . . .	148
7.1.3	Wigner's D-functions . . . . .	150
7.1.4	Matrix formulation of the dynamic Kerr effect . . . . .	152
7.1.5	Exact solution for isotropic diffusion . . . . .	154
7.2	Implementation for liquid water . . . . .	155
7.2.1	The case of liquid water . . . . .	155
7.2.2	Resulting dynamics . . . . .	158
7.2.3	Possible corrections . . . . .	162
7.3	Conclusion of Part 7 . . . . .	165
<b>8</b>	<b>Summary and outlook</b>	<b>167</b>
	<b>Appendix A Mathematical identities and definitions</b>	<b>169</b>
	<b>Appendix B Cavity and reaction field for a layered sphere and an ellipsoid</b>	<b>172</b>
	<b>Appendix C Evaluation of correlators in the Liouville space formalism</b>	<b>177</b>
	<b>Appendix D Transition probabilities from the nonequilibrium Bloch equations</b>	<b>180</b>
	<b>Appendix E Evaluation of the path integrals</b>	<b>182</b>
	<b>Appendix F Corrections to the THz Kerr effect in water due to interactions and bath driving</b>	<b>186</b>

## Introduction: Driven quantum baths

The statistical equilibrium by itself is an idealized time-independent state. However, even simple things such as driving a current through a wire or heating up a metal drives the substance out of its thermal equilibrium state for a time. In fact, any time-dependent force creates a nonequilibrium situation in principle [4]. It is for this simple reason that understanding nonequilibrium phenomena represents a focal point for physical inquiry. While transport problems and chemical reaction kinetics [5–7] are probably the most well known examples, novel methods of quantum control such as the emergence of topological phases from driving [8, 9] or light-induced superconductivity [10, 11] are also applications related to nonequilibrium phenomena.

In the easiest case, the dynamics out of equilibrium can be rendered by expansion of the density matrix around the equilibrium state with only small deviations originating from external stimuli [5]. Well known formulae such as Ohm’s law can be derived using this simple picture [12]. Another class of approaches is given by semiclassical descriptions based on the early work on statistical physics, such as the Boltzmann, Fokker-Planck and Smoluchowski equations, which describe the time evolution of the partition function by way of particle collisions or diffusive processes [7, 13]. Today, sophisticated schemes such as renormalization group methods (e.g. [14–16]), the Keldysh formalism [17, 18] or specialized simulation techniques (e.g. [19, 20]) are commonplace.

This work is concerned with a particular class of phenomenological descriptions called *system-bath models*. Therein, a physical problem is partitioned into a system of interest and a surrounding environment. The latter is represented through one or many large reservoirs, called baths, usually assumed to be in thermal equilibrium. In contrast to the ordinary treatment in statistical physics and thermodynamics, these (heat) baths are modeled explicitly through microscopic degrees of freedom. This allows to describe the reequilibration of a quantum system or to investigate the competition between driving, damping and decoherence in its dynamics. Collected under the label *Quantum Dissipation*, these models have been used in the past to analyze the behavior of quantum dots in order to find suitable conditions for quantum computing [21–23], the decay of excitons in biological complexes [24–26] or the low-temperature tunneling dynamics in glasses [27–30]. In fact, their versatility and the inherently microscopic approach

makes them a highly useful and successful framework to develop appropriate models for a variety of physical applications (see [31–33] and the references therein).

As a principle, however, the bath degrees of freedom are kept in thermal equilibrium, even while the system can be perturbed by strong external driving forces. This is mandated only for cases where any coupling to the external force can be neglected or the thermalization times are comparably fast such that any deviation from the original equilibrium is negligible on the relevant time scales. This dissertation presents collected works concerned with extending the system-bath framework to the situation of driven bath modes and investigates their effect on the dynamics of a system of interest.

Indeed, how environmental driving (or a nonequilibrium environment in general) impacts the response of physical systems has been the question in a variety of physical applications and more formal work on the issue has garnered attention in recent years. For instance, Grabert and Frey showed that current fluctuations, which act as bath driving contributions, produce additional noise sources in the case of tunneling junctions [34–36]. Furthermore, molecular dynamics simulations of liquid water imply that strong THz pulses can be used as an efficient heating mechanism and succeed to transfer energy into distinct modes of immersed molecules [37–39]. Driven baths have also been used for quantum cosmology [40], proposed as a model for the (instantaneous) normal modes in liquids [41, 42] and as a potential way to analyze surface enhanced Raman scattering or increase the efficacy of chemical reactions [1, 43].

In this dissertation, we focus our attention on the case of bilinear driving with classical fields and show that the system-bath framework leads to the creation of an additional force component which acts on the system of interest. This new force represents the full nonequilibrium dynamics of the bath and does not lead to a change of its fluctuation spectrum. We show that the resulting *effective force* qualitatively changes the response of the system of interest and paves the way for further development in the field of driven quantum baths. We also outline ways to extend to the parametrically driven case and discuss a possible application in nonlinear optics.

The setup of the thesis follows this outline. We start with an introduction to system-bath models in Part 2. This includes a discussion of the two most relevant toy models (the Caldeira-Leggett and spin-boson models) as well as a general introduction to relaxation and decoherence phenomena. Since system-bath models are by themselves problems of many-body physics, we outline a few sophisticated solution methods. Two of which (master equations and the path integral approach) are discussed in more detail and are applied to the problem in subsequent chapters.

Part 3 concerns classical electrodynamics and the dynamics of driven quantum systems. Particular focus lies on linear and nonlinear dielectric phenomena where we introduce both terminology and the relevant molecular quantities of interest. This chapter also introduces continuum solvation models which describe the environment on the basis of its dielectric properties. One particularly simple implementation, the

Onsager sphere model, will be discussed in more detail and allows us to define the spectral characteristics of our baths. Finally, we present a brief introduction to driven quantum systems on the basis of a generic two-state system. We show how its dynamics can be framed by transition probabilities and we give a short account of linear response theory and the optical Bloch equations.

We start with the discussion of driven quantum baths in Part 4, based on a first original paper on the topic [1]. Here, we introduce the notion of dipolar bath driving and evaluate the dynamics on the basis of a quantum Langevin approach. We go on to determine the corrected linear response for two particular nanosystems. Specifically, a polarizable molecule immersed in water driven by a THz field source and a quantum-dot metal-nanoparticle setup excited by an optical laser field. The Onsager sphere model will be used to quantify the resulting force.

Part 5 is concerned with generalizing the resulting force contribution and elucidates its connection to nonequilibrium dynamics. In this part, we show how the effective force can be introduced on the level of the Hamiltonian and reflects the nonequilibrium state of the bath due to external driving of the bath modes. We then present and utilize an established master equation approach for a coupled two-state system. This allows us to derive a response function where the effective force is taken into account in a nonlinear way. This part is based on a second publication on the topic [2].

Part 6 translates the problem into the path integral language. We derive the driven influence functional and show how the effective force emerges naturally from this approach. The dynamics of a coupled two-state system are then derived by way of the non-interacting blip approximation which allows us to investigate the high temperature, strong system-bath coupling regimes. Specifically, we look at the resulting dynamics in four different coupling and temperature ranges and compare to what was found in the preceding chapters. Finally, we briefly discuss the generalizing case of parametrically driven baths as an outlook for future research. This part of the thesis contains novel work which has not been published yet.

In Part 7, we look at a particular experimental realization where external preparation of the environment by a pulse changes the response of a dynamical quantity. Specifically, we look at the theoretical treatment and analysis of the Kerr effect, a nonlinear electric effect which induces birefringence in an otherwise isotropic liquid. We implement the theory for the case of water and compare our results to recent measurements in the terahertz regime. The chapter closes with an outlook, where we discuss possible improvements and also briefly consider the effect of bath driving contributions. This chapter contains work published in a recent collaborative paper [3].

We close this work with Part 8, which contains a summary of the work done in this dissertation and presents an outlook for future implementations of bath driving. Particular focus will be given to physical applications, where bath driving may play an important role to describe the underlying physical phenomena.

## Quantum dissipation and system-bath models

Environments are ubiquitous in physical applications. From the coupling of elementary particles to the electromagnetic field to the interaction of biomolecules with the surrounding water, small functional entities usually couple to a macroscopic number of peripheral degrees of freedom which together constitute an environment or *bath* as in “heat bath”. A large environment leads to ordinary damping in the form of relaxation as well as to the loss of quantum features in a process called decoherence [44–46]. Both phenomena are the subject of dissipative quantum mechanics, a field concerned with methods designed to mimic and explain the underlying dynamics of open quantum systems and related applications (see, e.g., [33, 47]). In this part of the thesis we are going to present some basic ideas of dissipative quantum mechanics and discuss methods to tackle the emerging many-body physics.

We start with a short introduction to decoherence and relaxation effects in the quantum realm and give some simple expressions for relaxation dynamics on the basis of golden rule rates. The second section introduces system-bath models. Specifically, we discuss the spin-boson and Caldeira-Leggett models which constitute the minimal models of dissipative quantum mechanics. Both will be instrumental for our discussion of the effect of a driven bath. This section also contains a brief introduction to spectral densities. Finally, we close this part with a third section that will discuss some approximate solution methods for the system-bath problem with a focus on master equation and path-integral approaches. This part of the thesis is largely based on the books by Nitzan [5], Weiss [33] and Caldeira [31] which should be consulted for more details on the subject.

### 2.1 Decoherence and relaxation

The Hamiltonian time evolution of quantum mechanics is reversible and an isolated atom will experience the same dynamics, no matter the sign of the time arrow. This observation stands in contrast to the presence of irreversibility and the absence of quantum effects in macroscopic systems. The answer to this dilemma is found in the presence of an environment: coupling many external degrees of freedom to a

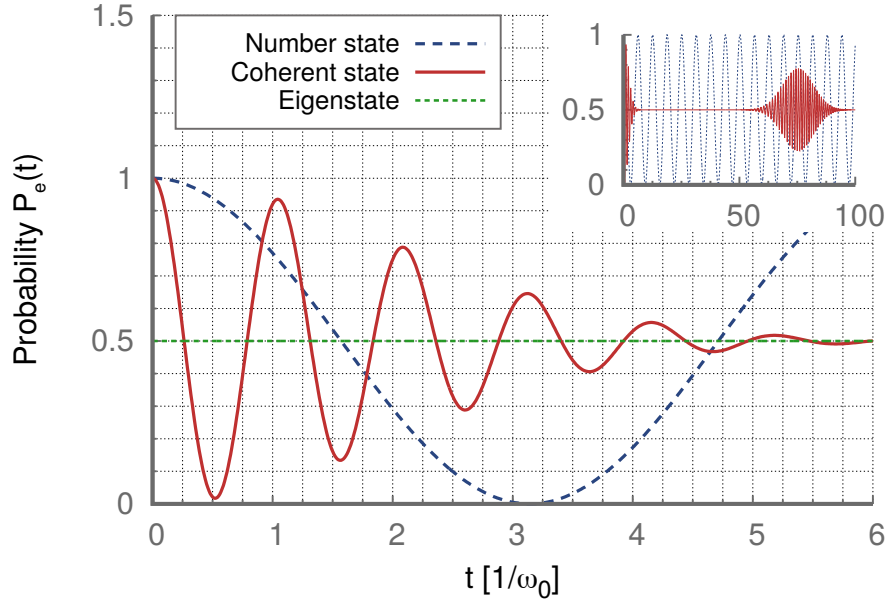


**Figure 2.1:** Dynamics of the Jaynes-Cummings model (JCM) based on the formulas in Zimmermann and Wauer [48] and Meystre and Sargent [49] for three different initial conditions. The plot shows the probability  $P_e(t)$  of finding the system in the excited state of the two-state system (TSS). We assumed resonance (the detuning is zero) and set the coupling constant to  $M = 0.5\Delta$ , where  $\Delta$  is the TSS splitting. No dynamics are observed for the case when the JCM starts in an eigenstate (green dotted line). Zero detuning gives an even superposition between excited and non-excited state such that the value  $1/2$  is obtained from projection. Regular oscillations are found when starting in a state with fixed photon number ( $n = 0$ , blue dashed line). This is an eigenstate of the uncoupled system but a superposition state of the full JCM, showcasing what is known as quantum beats. Starting with the oscillator in a coherent state (modulus  $|\alpha| = 6.0$ ; red solid line) leads to a quick collapse from dephasing but also to periodic revivals after some time (inset). This implies that only macroscopic environments can lead to irreversibility.

quantum system leads to energy transfer, while the interaction leads to a process called *decoherence*. The latter means that superposition states decay as a large environment constantly measures the state of the quantum system, thus restricting it to certain basis states. For this reason, decoherence is often cited as the answer to the Schrödinger’s cat thought experiment [50]. Of course, coupling a system to a large environment does not mean that their combination shows irreversibility or loses its quantum mechanical nature; Irreversibility arises, because we restrict our observation to the small quantum system and its Poincaré recurrence time is practically infinite for large environments. One can think of classical statistical mechanics where the system gets “lost in phase-space” over time [5].

Understanding the precise nature of both effects is important for a variety of ap-

plications. For instance, irreversibility means damping and knowledge of the time scales involved is highly important when driving systems or in order to ensure specific deexcitation pathways. Examples include lasers, where an excitation has to quickly decay into a radiative pathway in order to produce a population inversion [51, Chapter 1] or rhodopsin, the molecule responsible for photon detection in the retina, whose excited state persists much longer in its biological environment than without it - likely to ensure efficient signal transduction [26, 52]. In turn, understanding and quantifying decoherence is particularly important when considering quantum computational applications. Here, superposition states are used to store information so any decay whatsoever must be avoided when performing calculations [53]. In addition, low decoherence can lead to long-lived oscillations (an example of so-called quantum beats, see below) which have been discussed as a method to enhance energy transfer in the Fenna-Matthews-Olson complex, a protein which plays a crucial role for photosynthesis in green bacteria [54, 55]. While this was subsequently all but disproven at ambient temperatures [56, 57], the latter showcases the need for detailed investigations into the matter.

In this context, an illuminating (counter) example is provided by the Jaynes-Cummings model (JCM), where a two-state system is coupled to a single bosonic mode [49]. Such a situation pertains, for instance, to Rydberg atoms placed in optical cavities [58, 59]. In this case, the two-state system represents two highly excited states of the atom and the bosonic mode represents the distinguished frequency of the electric field determined by the cavity. The environment of the atom then consists only of a single degree of freedom which allows for emission or absorption of a single photon with a specific frequency. For the JCM, the exact dynamics can be determined analytically [48, 49, 59] and examples are shown in Figure 2.1 for three different initial conditions.

Starting with the two-state system in an excited state and the bosonic mode in the ground state, leads to periodic energy exchange between the two without any conceivable loss. As expected, an eigenstate of the JCM shows no dynamics. One might, however, suppose that the infinite number of states accessible to the mode would make a difference if they were included in a superposition. In fact, by placing the mode in a coherent state (that is, a superposition of energy eigenstates) recurring collapses and revivals in the quantum dynamics of the two-state system can be observed. This is because the states associated with different photon numbers (energies) interfere. For long enough times the system returns to random periodic energy exchanges [49]. However, the initial collapse gives a clue on the nature of decoherence: a sufficiently dense set of states with different eigenenergies suppresses quantum coherence by way of interference. What is notably still absent from this picture is loss of energy, which can only occur when more degrees of freedom are present as an energy sink. As we will see, system-bath models describe the environment with both a large number of degrees of freedom as well as a dense set of states characterized by a continuous frequency

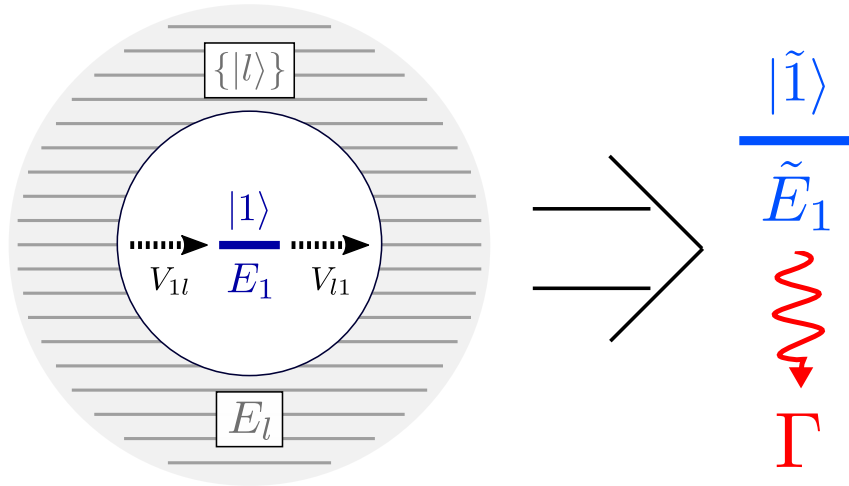


**Figure 2.2:** Graphical representation of the toy model for relaxation given in Equation (2.1). A state  $|1\rangle$  with energy  $E_1$  couples to a continuum of states  $\{|l\rangle\}$  (gray sphere) with energies  $E_l$  (gray lines) via the couplings  $V_{1l}$  and  $V_{l1}$ . Equation (2.4) shows that the effect of the environment on the state  $|1\rangle$  consists in a shift of its energy (quantities denoted by a tilde) as well as the presence of relaxation ( $\Gamma$ ).

distribution.

Damping and decoherence effects commonly appear in the context of three dynamical features [60, Chapter 3.8]:

**Relaxation:** Reequilibration of a system with its environment, or, more generally, decay of an excited state. Relaxation generally implies energy loss and damping.

**Dephasing:** Decay of phase coherence between quantum states due to energy loss to the environment. This implies a decay of superposition states and is synonymous with decoherence.

**True dephasing:** Decay of phase coherence between quantum states without energy loss to the environment. This implies a decay of superposition states and is also synonymous with decoherence.

In the following, we will discuss these features in more detail which yields some general insights into the dynamics we can expect. We start with relaxation in particular, and present the so-called *golden rule* results in the following.

### 2.1.1 Golden rule rates

A simple way to model relaxation dynamics is by way of the *golden rule*. The golden rule is a general formulation for transition probabilities per unit-time in first-order



perturbation theory, when the system is subject to a periodic perturbation [5, 61]. In this subsection, we demonstrate how relaxation arises on the basis of a minimal model where we will encounter some general features of system-bath dynamics. The model itself and the corresponding calculation follows the book by Nitzan [5, Chapter 9.1].

Specifically, we assume a single state  $|1\rangle$  with energy  $E_1$  coupled to a continuum of states  $\{|l\rangle\}$  with energies  $E_l$ . They are described by the Hamiltonian

$$H = E_1|1\rangle\langle 1| + \sum_l E_l|l\rangle\langle l| + \sum_l [V_{1l}|l\rangle\langle 1| + V_{l1}|1\rangle\langle l|], \quad (2.1)$$

where  $V_{ij}$  describes the interaction between states  $i$  and  $j$ . The resulting model is depicted in Figure 2.2. The dynamics of the Hamiltonian (2.1) can be found by way of Green's function methods. In particular, we consider the matrix element  $c_1(t) = \langle 1|\Psi(t)\rangle$  for a wavefunction  $|\Psi\rangle$  with initial condition  $|\Psi(0)\rangle = |1\rangle$ .  $|c_1(t)|^2$  then gives the probability of the system to remain in state  $|1\rangle$  at time  $t$ . Utilizing the Schrödinger equation and performing a Laplace transformation yields

$$c_1(t) = -\frac{1}{2\pi i} \int_{-\infty}^{\infty} dE G_{11}(E + i\epsilon) e^{-\frac{i}{\hbar}Et} \quad \text{with} \quad \epsilon \rightarrow 0^+. \quad (2.2)$$

Here,  $G_{11}(z)$  labels the Green's function of state  $|1\rangle$  in Laplace space

$$G_{11}(E) = \lim_{\epsilon \rightarrow 0} \frac{1}{E + i\epsilon - E_1 - B_1(E)}. \quad (2.3)$$

$B_1(E)$  labels the self-energy which encodes the effect of the continuum onto the single state. It is a common quantity in many-particle physics that encodes influence of many-body effects as an effective one-particle potential [62]. It is given here as

$$B_1(E) = \lim_{\epsilon \rightarrow 0} \sum_l \frac{|V_{1l}|^2}{E - E_1 + i\epsilon} = \Lambda_1(E) + (i/2)\Gamma_1(E). \quad (2.4)$$

The second equality used the Sokhotski–Plemelj identity (A.3) to separate real and imaginary part as

$$\Lambda_1(E) = \mathcal{P} \sum_l \frac{|V_{1l}|^2}{E - E_l}, \quad (2.5)$$

$$\Gamma_1(E) = 2\pi \sum_l |V_{1l}|^2 \delta(E - E_l). \quad (2.6)$$

The self-energy in Equation (2.4) renormalizes the resonant energies  $E_l$  into complex quantities. The real-part leads to a direct shift of the frequency, while the imaginary part introduces damping by providing a finite width  $\Gamma$  to the underlying Lorentzian structure

of the Green's function. Both are general features, which we will encounter throughout this thesis when considering system-bath models. In fact, one may also think of the classical damped harmonic oscillator where next to damping of the amplitude, the oscillation frequency is also renormalized by the damping constant [63]. The imaginary part of the self-energy (2.6) depends on the density of states, weighted by a squared coupling. Later, this quantity will be referred to as the *spectral density* of the model. It also implies that a convenient choice of this quantity or the density of states can lead to comparably simple solutions. For the case of a constant density of states, such that  $\Gamma_1(E)/2\pi = \sum_l |V_{1l}|^2 = \overline{|V_{1l}|^2}$  and  $\Lambda_1 = 0$ , we quickly find

$$|c_1(t)|^2 = e^{-k_1 t}, \quad (2.7)$$

with rate constant

$$k_1 = \frac{\Gamma_1}{\hbar} = \frac{2\pi}{\hbar} \overline{|V_{1l}|^2}. \quad (2.8)$$

The constant in Equation (2.8) is an example of a golden rule rate, which depends on the squared mean coupling and implies a simple exponential decay of the probability to stay in state  $|1\rangle$ . This is the simplest case of relaxation, where the system decays exponentially from an excited state. Far from a purely academic exercise, exponential decays are commonly found in physical measurements [5] and we will encounter similar behaviors throughout this thesis.

### 2.1.2 Dephasing

In order to illustrate how dephasing (decoherence) arises, we present an argument taken from May and Kühn [60, page 86 ff.]. We consider a state  $|\Psi(t)\rangle$ , which can be expanded in energy eigenstates  $|n\rangle$  for the energies  $E_n$ . The time-dependent Schrödinger equation then leads to the following representation:

$$|\Psi(t)\rangle = \sum_n c_n(t) |n\rangle = \sum_n c_n(t_0) e^{\frac{i}{\hbar} E_n (t-t_0)} |n\rangle, \quad (2.9)$$

with expansion coefficients  $c_n(t) = \langle n | \Psi(t) \rangle$ . Equation (2.9) gives the time evolution of a state by way of phases which depend on the eigenenergies of the Hamiltonian. The actual number of the phases involved depends on the expansion coefficient of the initial state. If it is an energy eigenstate, only a single phase is involved. If it is not, it will be a superposition state and more phases will contribute.

We will now consider the probability of the system to still be found in  $|\Psi(t_0)\rangle$  at time  $t$ , the survival probability  $P_s(t)$ . Using Equation (2.9) we find

$$P_s(t) = |\langle \Psi(t_0) | \Psi(t) \rangle|^2 = \sum_{n,m} |c_n(t_0) c_m(t_0)|^2 e^{-i\omega_{nm}(t-t_0)}. \quad (2.10)$$

Here,  $\omega_{nm} = (E_n - E_m)/\hbar$  is the difference of frequencies associated with the eigenenergies. Equation (2.10) shows that a sum of phases determines the survival probability. On one hand, this means that when the initial state only contains a few states  $n$ , the survival probability will fluctuate and the system will periodically return to its initial-state with some probability – a feature known as *quantum beats*, which arise naturally because the system starts in a superposition state. On the other hand, if the superposition encompasses a large amount of states  $n$ , the various phases will interfere increasingly with time, leading to a rapid decline of the survival probability. Since the terms essentially run out of phase, this decay of superpositions is also known as *dephasing*. For very long times, the system will settle into a value determined by the time-independent part  $\sum_n |c_n(t_0)|^4$  [60, page 89].

This simple argument explains what we saw in the dynamics of the JCM in Figure 2.1: the more states are initially involved in a superposition, the more complete a collapse becomes and the longer revivals take [49]. In contrast, by starting in the excited state with a fixed photon number, only two eigenstates are involved in the expansion, thus creating periodic fluctuations. Starting in an eigenstate showed no dynamics as expected. Quantum beats were visible for both superposition states.

Dephasing and true dephasing appear with rates similar to (2.8) in a Born-Markov type master equation treatment. In this approach, the system is characterized by a density matrix where non-diagonal elements give superposition states involved in a mixed state and the rates apply to. The dephasing rate (see Section 2.3.1 below) is given as half of the relaxation rate, whereas true dephasing is related to the zero-frequency response of the environment. The latter implies that this is an elastic process without energy exchange [5, 60, 64].

### 2.1.3 Detailed balance

Finally, we address the question of how a state equilibrates with the environment. As seen in the example of Section 2.1.1, an excited state will decay if enough unoccupied states are present. However, for finite temperature one should expect equilibration with the environment at some finite value, determined by the Boltzmann factor. Indeed, for a two-state system with states  $|1\rangle$  and  $|2\rangle$  which only couple to each other through the bath, one finds the following relation between the golden rule rates [60]

$$\frac{k_{1\rightarrow 2}}{k_{2\rightarrow 1}} = e^{-\frac{(E_1 - E_2)}{k_B T}}. \quad (2.11)$$

Here, the subscripts give the direction of relaxation between the states (the *forward* and *backward* rates). This condition is known in the context of system-bath models as *detailed balance*. Detailed balance is expected for Markovian approximations when the bath is in thermal equilibrium [5, Chapter 8.3][17, Chapter 10.4] and is a direct consequence of assuming that the system equilibrates with its environment. Detailed

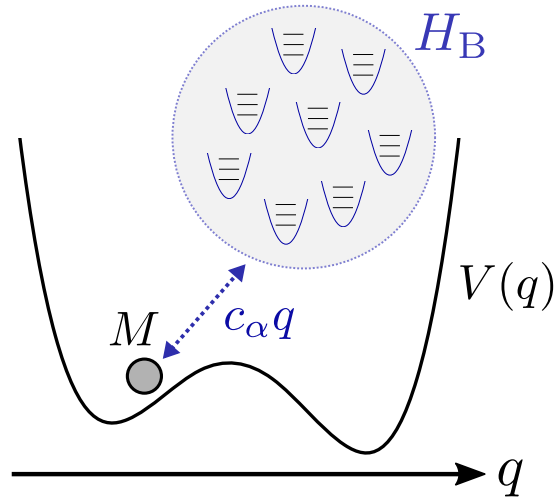


**Figure 2.3:** Graphical representation of the Caldeira-Leggett model. A one-dimensional quantum particle (small circle) of mass  $M$  and position  $q$  moves in a potential  $V(q)$ . The bath is described by the Hamiltonian  $H_B$  (large gray circle) which models the environment as a collection of harmonic oscillators (blue potentials). The particle couples bilinearly to the bath through its position  $q$  with coupling constants  $c_\alpha$ .

balance is not fulfilled in some approximation schemes, such as the Lindblad master equation method [5, page 390].

## 2.2 System-bath models

System-bath models provide a simple way to model decoherence and relaxation dynamics of quantum systems. In this section, we present the two most well-known minimal models which will provide the basis for our discussion of driven bath effects. We start with the so-called Caldeira-Leggett model which describes a one-dimensional particle in contact with a harmonic environment. The dynamics of this particle can be framed by way of a quantum Langevin equation. This approach naturally leads to the definition of a spectral density which parametrizes the environment within system-bath formulations. We will show that the imaginary part of the environmental susceptibility can be used to obtain the spectral density. Furthermore, we elucidate the impact of Lorentzian-shaped spectral densities which can be used to model specific modes in the environment. Lastly, we introduce the spin-boson model, which describes system-bath dynamics on the basis of a coupled two-state system.

## 2.2.1 The Caldeira-Leggett model

We start our discussion of system-bath models with the so-called Caldeira-Leggett model (CLM). It describes a one-dimensional quantum particle in a potential coupled to a collection of harmonic oscillators. A graphical representation is shown in Figure 2.3. As we will see, the dynamics of this simple model already leads to damping and fluctuations for the quantum particle and mimics the behavior found in macroscopic systems. The model is also highly useful for the discussion of metastable problems: if the potential is a double-well, transitioning between wells can be parametrized by the coordinate of the particle. The model can then be used to gauge the impact of dissipation on barrier crossing or tunneling, for instance in the case of chemical reaction dynamics [5, 6]. In addition, the model emerges naturally in case of superconducting quantum interference devices (SQUIDs), where the magnetic flux across a gap in a superconducting ring follows the dynamics of the model when external current fluctuations are taken into account [33, Chapter 3][31, Chapter 3.4]. The Hamiltonian of the CLM ( $H$ ) is given by a sum of a system part ( $H_S$ ), a bath part ( $H_B$ ), coupling terms ( $H_{SB}$ ) and a so-called counter term ( $H_C$ ) as

$$H = H_S + H_B + H_{SB} + H_C. \quad (2.12)$$

The system-Hamiltonian is a one-dimensional particle of mass  $M$  with position operator  $q$  and momentum operator  $p$  in a position-dependent but (for now) time-independent potential  $V(q)$ , i.e.,

$$H_S = \frac{p^2}{2M} + V(q). \quad (2.13)$$

The bath part consists of  $N$  uncoupled harmonic oscillators with masses  $m_\alpha$ , frequencies  $\omega_\alpha$  and position and momentum operators  $x_\alpha$  and  $p_\alpha$ . Specifically,

$$H_B = \sum_{\alpha=1}^N \frac{1}{2} \left[ \frac{p_\alpha^2}{m_\alpha} + m_\alpha \omega_\alpha^2 x_\alpha^2 \right]. \quad (2.14)$$

This rather simple choice of modeling for the environment reflects the notion that the equilibrium state of an individual mode is not significantly perturbed such that a harmonic approximation can be made [5, Chapter 6.5].

The coupling term is given through a simple bilinear structure which relates the position operators of the oscillators and the quantum particle via oscillator-dependent coupling constants  $c_\alpha$  as

$$H_{SB} = -q \sum_{\alpha=1}^N c_\alpha x_\alpha. \quad (2.15)$$

The bilinear choice for  $H_{\text{SB}}$  implies that the environment is large so the average coupling to a single mode in a geometrically macroscopic environment can be assumed as weak [33, page 18]. Note that this does not imply a weak interaction between system and bath as the total effect takes into account the contribution of all modes. As we will see below, the linear dependence on the oscillator position is also relevant in its own right as it allows to integrate out the environment and obtain terms which mimic ordinary macroscopic damping. It is also worthy to note, that the dependence on system operators in  $H_{\text{SB}}$  can be more arbitrary. This can be used, for instance, to describe the interaction with translationally-invariant environments or to model the behavior of two Brownian particles [33, page 19][31]. However, in this thesis we restrict ourselves to the simple bilinear form given above.

Finally, the counter-term represents a normalization of the system potential in such a way, that  $V(q)$  is not qualitatively altered from the interaction with the oscillators and only its dissipative effects remain. It depends on  $q^2$  by way of

$$H_C = q^2 \sum_{\alpha=1}^N \frac{c_\alpha^2}{2m_\alpha \omega_\alpha^2}. \quad (2.16)$$

### **Quantum Langevin equation**

The dynamics of the Caldeira-Leggett model can be cast into the form of a simple quantum analogue of the classical Langevin equation, simply called the *quantum Langevin equation* (QLE). It follows directly from the Heisenberg equations of motion for the position and momentum of the particle. By combination of the two, the position operator is found to satisfy

$$M \frac{d^2 q(t)}{dt^2} + \frac{dV(q)}{dq} + q(t) \sum_{\alpha=1}^N \frac{c_\alpha^2}{m_\alpha \omega_\alpha^2} = \sum_{\alpha=1}^N c_\alpha x_\alpha(t). \quad (2.17)$$

Similarly, the position operator of a single oscillator  $x_\alpha$  has to conform to

$$m_\alpha \frac{d^2 x_\alpha(t)}{dt^2} + m_\alpha \omega_\alpha^2 x_\alpha(t) = c_\alpha q(t). \quad (2.18)$$

Equation (2.18) is the equation of motion for a forced harmonic oscillator with external force  $c_\alpha q(t)$ . It can be solved by way of standard Green's function methods to obtain [65, Chapter 2.2]

$$\begin{aligned} x_\alpha(t) &= x_\alpha(t_0) \cos[\omega_\alpha(t - t_0)] + \frac{p_\alpha(t_0)}{m_\alpha \omega_\alpha} \sin[\omega_\alpha(t - t_0)] \\ &+ \frac{c_\alpha}{m_\alpha \omega_\alpha} \int_{t_0}^t ds q(s) \sin[\omega_\alpha(t - s)]. \end{aligned} \quad (2.19)$$

where  $t_0$  labels the initial time point. Result (2.19) can be inserted into Equation (2.17) to yield the dynamics of the quantum particle as

$$\begin{aligned} M \frac{d^2 q(t)}{dt^2} + \frac{dV(q)}{dq} + q(t) \sum_{\alpha=1}^N \frac{c_\alpha^2}{m_\alpha \omega_\alpha^2} \\ = \xi(t - t_0) + \sum_{\alpha=1}^N \frac{c_\alpha^2}{m_\alpha \omega_\alpha} \int_{t_0}^t ds q(s) \sin [\omega_\alpha(t - s)]. \end{aligned} \quad (2.20)$$

Equation (2.20) determines the dynamics of the system in the quantum analogue of a Newtonian equation of motion. The homogeneous part of Equation (2.19) has been absorbed into the term  $\xi(t - t_0)$  and the homogeneous part gives the last term on the right hand side. This represents a retarded  $q$ -dependent force. We will see later that its structure represents the linear response to the perturbation by the bath. Finally, a partial integration yields the QLE

$$\begin{aligned} M \frac{d^2 q(t)}{dt^2} + \frac{dV(q)}{dq} + M \int_{t_0}^t ds \gamma(t - s) \left( \frac{dq(s)}{ds} \right) \\ = \xi(t - t_0) - M \gamma(t - t_0) q(t_0). \end{aligned} \quad (2.21)$$

Equation (2.21) recreates the dynamics of the classical Langevin equation in the quantum realm: the first additional term introduces damping by way of a time-nonlocal damping kernel  $\gamma(t)$ , while the contribution  $\xi(t)$  is a fluctuating force. The damping kernel is given by

$$\gamma(t) = \Theta(t) \frac{1}{M} \sum_{\alpha=1}^N \frac{c_\alpha^2}{m_\alpha \omega_\alpha^2} \cos [\omega_\alpha t]. \quad (2.22)$$

Here, the Heaviside function  $\Theta(t)$  is explicitly included as  $\gamma(t)$  is a causal quantity. The fluctuating force is given by

$$\xi(t) = \sum_{\alpha=1}^N c_\alpha \left[ x_\alpha(t_0) \cos [\omega_\alpha t] + \frac{p_\alpha(t_0)}{m_\alpha \omega_\alpha} \sin [\omega_\alpha t] \right]. \quad (2.23)$$

$\xi(t)$  depends on the initial values of the bath operators which are usually drawn from thermal equilibrium. This directly implies Gaussian fluctuations as

$$\langle \xi(t) \rangle_{\text{B}} = \text{Tr}_{\text{B}} [\xi(t) \rho_{\text{B}}^{\text{eq}}] = 0, \quad (2.24)$$

where  $\rho_{\text{B}}^{\text{eq}} = \exp(-\beta H_{\text{B}}) / \mathcal{Z}_{\text{B}}$  is the canonical distribution operator of the uncoupled bath with inverse temperature  $\beta$  and partition function  $\mathcal{Z}_{\text{B}}$ .  $\text{Tr}_{\text{B}}[\dots]$  signifies a trace

over bath states. The fluctuations fulfill a colored noise relation given by the autocorrelation function

$$\begin{aligned} \langle \xi(t)\xi(t') \rangle_{\text{B}} &= \hbar L(t-t') = \hbar [L'(t-t') + iL''(t-t')] \\ &= \sum_{\alpha=1}^N \frac{\hbar c_{\alpha}^2}{2m_{\alpha}\omega_{\alpha}} \left[ \coth\left(\frac{\hbar\omega_{\alpha}\beta}{2}\right) \cos(\omega_{\alpha}(t-t')) - i \sin(\omega_{\alpha}(t-t')) \right]. \end{aligned} \quad (2.25)$$

Here, we assumed  $t > t'$  and introduced the function  $L(t) = L'(t) + iL''(t)$  as a shorthand. Equation (2.25) is the reason for non-Markovian effects which are absent in the classical equation where white noise is often assumed [31, Chapter 5.1][33, Chapter 2]. As in the classical case, the fluctuation spectrum (2.25) determines the resulting dissipative dynamics.

The additional term  $\gamma(t-t_0)q(t_0)$  in Equation (2.21) is called the initial slip and gives a force contribution which depends on the initial position of the quantum particle  $q(t_0)$ . It can be absorbed into the random-force operator such that the fluctuations now occur around  $q(t_0)$  instead of zero. In principle, the bath can then be chosen to be in equilibrium with the particle located at this position to restore Gaussian fluctuations [65, Chapter 2.2][31, Chapter 5.1]. Finally, it should also be noted that the partial integration from Equation (2.20) to (2.21) led to the cancellation of the counter-term.

### 2.2.2 Bath spectral density

The fluctuating force and the damping kernel depend on summations over each oscillator. A convenient parameterization is given by way of the so-called *spectral density*

$$J(\omega) = \frac{\pi}{2} \sum_{\alpha=1}^N \frac{c_{\alpha}^2}{m_{\alpha}\omega_{\alpha}} \delta(\omega - \omega_{\alpha}). \quad (2.26)$$

Using Equation (2.26) directly leads to

$$\gamma(t) = \Theta(t) \frac{2}{M\pi} \int_0^{\infty} d\omega \frac{J(\omega)}{\omega} \cos(\omega t), \quad (2.27)$$

while the fluctuation spectrum (2.25) becomes

$$L(t) = \frac{1}{\pi} \int_0^{\infty} d\omega J(\omega) \left[ \coth\left(\frac{\hbar\omega\beta}{2}\right) \cos(\omega t) - i \sin(\omega t) \right]. \quad (2.28)$$

The spectral density (2.26) represents the density of states for the oscillators weighted by the coupling constants and is only nonzero for positive frequencies. It describes the response to an excitation of the bath at a certain frequency and is the most important way that the bath can be parametrized within system-bath models. This is usually done



by assuming the bath to be large and the states of the bath to be dense such that the spectral density can be written as a function of frequency. A particular choice reads

$$J(\omega) \approx \eta \left( \frac{\omega^s}{\omega_c^{s-1}} \right) e^{-\omega/\omega_c}. \quad (2.29)$$

Here,  $\eta$  is a prefactor which determines the strength of the system-bath interaction. The exponential in (2.29) regularizes the function for high frequencies with a cutoff frequency  $\omega_c$ . This reflects inertial effects of the underlying physical makeup of the bath, for instance molecular vibrations which have a finite mass and thus will not react to excitations at large enough frequencies. The main point, however, is the validity of the power-law behavior at low frequencies. In practice, this means  $\omega_c$  is taken to be smaller than the Fermi, Drude or Debye frequencies but much larger than the frequency scales of the system we are interested in [33, Chapter 3.1] [31, Chapter 5.1]. Because of this, the limiting case  $\omega_c \rightarrow \infty$  is often considered at the end of the calculation [33, Chapter 3.1][31].

Finally, the factor  $\omega^s$  describes the low-frequency dynamics on the basis of the parameter  $s$ . The denominator is used to secure the correct dimension and may also contain a different frequency scale [31, 33]. For  $s = 1$ , Equation (2.29) is referred to as an *Ohmic* spectral density. For this particular case and with large values of  $\omega_c$ , the damping kernel becomes instant by

$$\gamma(t) = \frac{2\eta}{M} \delta(t), \quad (2.30)$$

which recreates a simple Stokes friction term in the QLE (2.21), as

$$M \int_{t_0}^t \gamma(t-s) \left( \frac{dq(s)}{ds} \right) ds = \eta \left( \frac{dq(t)}{dt} \right). \quad (2.31)$$

Note that the  $\delta$ -function counts only half due to the upper bound of the integral [31, 33]. Equation (2.30) recreates the typical form of the classical Langevin equation for a particle in a viscous fluid. In an electrical circuit, Equation (2.31) can also be identified with friction from a (series) resistor, hence the name “Ohmic” [33].

### ***Environmental susceptibility***

The spectral density (2.29) is a phenomenological choice, appropriate in many cases [33]. However, the spectral density of a given environment can also be found by experimental means, for instance from optical line-narrowing experiments [66, 67] or photon-echo measurements [68]. It can also be determined directly from the autocorrelation function in molecular dynamics simulations [69]. In this section, we show that the spectral

density can be connected to the environmental susceptibility which will ultimately allow us to use the dielectric function as a modeling prescription in Part 3 of this thesis.

The following argument is based on the book by Caldeira [31, Chapter 5.1]. We start with the Fourier transform of Equation (2.18)

$$x_\alpha(\omega) = -\frac{c_\alpha}{m_\alpha(\omega^2 - \omega_\alpha^2)}q(\omega). \quad (2.32)$$

In Equation (2.17), we have seen that the bath influences the system by way of a collective coordinate  $\sum_\alpha c_\alpha x_\alpha(t)$ . Insertion of Equation (2.32) into its Fourier transform yields

$$\sum_{\alpha=1}^N c_\alpha x_\alpha(\omega) = -\sum_{\alpha=1}^N \frac{c_\alpha^2}{m_\alpha(\omega^2 - \omega_\alpha^2)}q(\omega) = \chi_{\text{env}}(\omega)q(\omega). \quad (2.33)$$

Here, the last equation introduced the environmental susceptibility  $\chi_{\text{env}}(\omega)$ . An inverse Fourier transform yields a convolution of  $\chi_{\text{env}}(t)$  and  $q(t)$  in the time domain. This structure is characteristic for linear response and introduces a retarded structure which also implies causality for  $\chi_{\text{env}}(t)$ . The susceptibility can now be rewritten as

$$\chi_{\text{env}}(\omega) = \sum_{\alpha=1}^N \frac{c_\alpha^2}{2m_\alpha\omega_\alpha} \left( \frac{1}{\omega + \omega_\alpha} - \frac{1}{\omega - \omega_\alpha} \right). \quad (2.34)$$

Since the response has to be causal, an infinitesimally positive imaginary part  $i\epsilon$  is introduced in the denominators. Using the Sokhotski–Plemelj identity (A.3), the imaginary part is given by

$$\text{Im} [\chi_{\text{env}}(\omega)] = \frac{\pi}{2} \sum_{\alpha=1}^N \frac{c_\alpha^2}{m_\alpha\omega_\alpha} [\delta(\omega - \omega_\alpha) - \delta(\omega + \omega_\alpha)], \quad (2.35)$$

which directly gives

$$\text{Im} [\chi_{\text{env}}(\omega)] = J(\omega) \quad \text{for } \omega_\alpha > 0. \quad (2.36)$$

Note that the requirement of a positive frequency directly follows from assuming positive excitation energies for the harmonic oscillators [31]. In the next part of this thesis, we will apply Equation (2.36) to a simple dielectric solvation model and use it to determine the spectral density.

### ***Lorentzian spectral densities***

Next to the generic form introduced in Equation (2.29), another class of spectral densities is given by Lorentzians. Such spectral densities can arise, for instance, in the case of

a leaky optical cavity and can generally be used as a modeling prescription when environmental modes are considered [70, 71]. Because of their more intricate frequency dependence, one speaks of *structured* baths. For our purposes, we restrict ourselves to a single Lorentzian and define the following spectral density

$$J(\omega) = \frac{\kappa\Gamma\Omega^2\omega}{(\omega^2 - \Omega^2)^2 + (\Gamma\omega)^2}. \quad (2.37)$$

Evidently, Equation (2.37) gives a peaked structure located at frequency  $\Omega$  with width  $\Gamma$ . The parameter  $\kappa$  is a measure for the system-bath interaction strength. Note that the low-frequency behavior is also linear in  $\omega$ , similar to (2.29) for the Ohmic case.

In principle, the form (2.37) can be used as a generic model for resonances in the environment much like the spectral density introduced in (2.29) for ordinary structureless environments. However, the Lorentzian form (2.37) also permits an exact mapping where the bath can be replaced by a single harmonic oscillator in contact with a bath described by an Ohmic spectral density. This has been used, for instance, to obtain more accurate approximation schemes [72, 73]. In the following, we present a short derivation of this mapping taken from a paper by Garg et al. [74]. We start with the system-bath Hamiltonian of the CLM with an Ohmic spectral density of the form (2.29). However, we also include a harmonic oscillator coupled in between bath and system such that the total Hamiltonian is given by

$$H = \frac{p^2}{2M} + V(q) + \frac{1}{2} \left[ \frac{P^2}{M_O} + M_O\Omega^2(q - Q)^2 \right] + \sum_{\alpha=1}^N \frac{1}{2} \left[ \frac{p_\alpha^2}{m_\alpha} + m_\alpha\omega_\alpha^2 x_\alpha^2 \right] - Q \sum_{\alpha=1}^N c_\alpha x_\alpha + \sum_{\alpha=1}^N \frac{c_\alpha^2 Q^2}{2m_\alpha\omega_\alpha^2}. \quad (2.38)$$

Here,  $P$  and  $Q$  label momentum and position operators of the harmonic oscillator and  $M_O$  gives its mass. The last two terms give the interaction and counter-term for the bath. For simplicity, the quantum particle is assumed to interact with the oscillator on the basis of a shifted harmonic potential. In analogy to the derivation of the QLE in the previous subsection, we write down the Heisenberg equations of motion for the position operators to find

$$M \frac{d^2 q(t)}{dt^2} = -\frac{dV(q)}{dq} - M_O\Omega^2(q(t) - Q(t)), \quad (2.39)$$

$$M_O \frac{d^2 Q(t)}{dt^2} = M_O\Omega^2(q(t) - Q(t)) + \sum_{\alpha=1}^N c_\alpha \left( x_\alpha(t) - \frac{c_\alpha Q(t)}{m_\alpha\omega_\alpha^2} \right), \quad (2.40)$$

$$m_\alpha \frac{d^2 x_\alpha(t)}{dt^2} = c_\alpha Q(t) - m_\alpha\omega_\alpha^2 x_\alpha(t). \quad (2.41)$$

We now apply a Fourier transformation with frequency  $\omega$ , which allows us to solve (2.40) and (2.41) algebraically. Insertion into Equation (2.39) then yields

$$\chi_{\text{env}}(\omega)q(\omega) = M_O\Omega^2(q(\omega) - Q(\omega)) = M_O\Omega^2 \left[ \frac{L(\omega)}{M_O\Omega^2 + L(\omega)} \right] q(\omega), \quad (2.42)$$

with

$$L(\omega) = -\omega^2 \left[ M_O + \sum_{\alpha=1}^N \frac{c_\alpha^2}{m_\alpha \omega_\alpha^2 (\omega_\alpha^2 - \omega^2)} \right]. \quad (2.43)$$

The second term of  $L(\omega)$  is related to the spectral density of the bath. Using the form (2.29) for the Ohmic case yields

$$L(\omega) = -\omega^2 \left[ M_O + \frac{2}{\pi} \int_0^\infty d\omega' \frac{1}{\omega'^2 - \omega^2} \frac{J(\omega')}{\omega'} \right] = -\omega^2 M_O + i\eta\omega. \quad (2.44)$$

Equation (2.42) introduced the environmental susceptibility for the quantum particle as in Equation (2.33). This definition allows us to obtain the corresponding spectral density by taking the imaginary part. An infinitesimal imaginary part has to be added to  $\omega$  as well in order to ensure causality. With Equation (2.36) we finally get

$$J_{\text{eff}}(\omega) = \text{Im} [\chi_{\text{env}}(\omega)] = \frac{\eta\omega\Omega^4}{(\Omega^2 - \omega^2)^2 + (\frac{\eta\omega}{M_O})^2}. \quad (2.45)$$

Equation (2.45) is a Lorentzian spectral density of the form (2.37) with  $\Gamma = \eta/M_O$  and  $\kappa = M_O\Omega^2$ . This directly implies weak coupling strength for small widths and vice versa. Similar arguments can be found for the spin-boson model (see below) and we will exploit these relationships in Part 5.

We have now shown that the intermediate oscillator in contact with a structureless bath can be replaced by a bath with a Lorentzian spectral density. Our argument rested on the identification of a suitable environmental susceptibility, which was possible because of the harmonic potentials involved. Indeed, the analysis presented here amounts to including the oscillator in the bath and performing a normal mode analysis. The subsequent changes in the coupling to the system lead to the Lorentzian form [74].

### 2.2.3 The spin-boson model

The second minimal model we consider investigates the system-bath interaction on the basis of a quantum two-state system (TSS), and is therefore called the *spin-boson model* (SBM). Specifically, the model exchanges the system and system-bath coupling Hamiltonians encountered in Equation (2.13) and (2.15) for the CLM by defining

$$H_S = \frac{\Delta}{2}\sigma_x + \frac{\epsilon}{2}\sigma_z \quad (2.46)$$

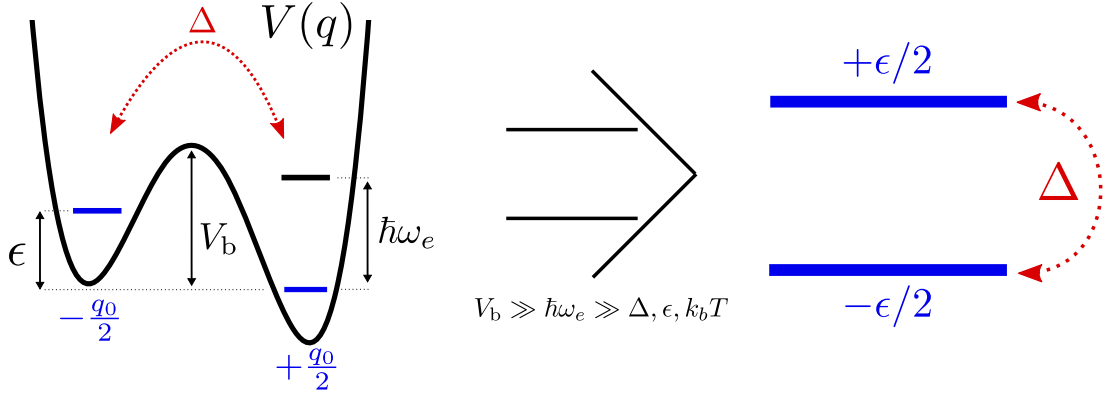


**Figure 2.4:** Emergence of the spin-boson model from a double well potential. The double well  $V(q)$  is characterized by two minima at  $\pm q_0/2$  separated by a barrier of height  $V_b$ . The characteristic ground states of the minima (blue lines) differ in energy by the amount  $\epsilon$  and possess the tunneling energy scale  $\Delta$ .  $\hbar\omega_e$  gives the separation of a ground state to the corresponding first excited state. For large barrier height, low temperature and large separation to excited states, the potential can be approximately reduced to the two ground states only, giving rise to a two-state description with coupling  $\Delta$ .

and

$$H_{SB} = -\frac{q_0}{2}\sigma_z \sum_{\alpha=1}^N c_{\alpha}x_{\alpha} = -\frac{\sigma_z}{2} \sum_{\alpha=1}^N \hbar\lambda_{\alpha} [b_{\alpha} + b_{\alpha}^{\dagger}]. \quad (2.47)$$

Here,  $\sigma_i$  are Pauli-matrices and  $q_0$  is a discrete position related to the states  $\sigma_z = \pm 1$ . The second equation of (2.47) uses the description by creation and annihilation operators with coupling constant  $\lambda_{\alpha} = q_0 c_{\alpha} (\sqrt{2\hbar\omega_{\alpha}m_{\alpha}})^{-1}$ . Note that our definition of  $H_S$  in Equation (2.46) differs by a minus sign from the usual convention (this changes the equilibrium values (2.51) and (2.52), for instance). Furthermore, the coupling Hamiltonian (2.47) represents the simplest possible form of the system-bath coupling in the SBM. More complicated terms, such as couplings to  $\sigma_x$  and/or to multiple baths, are possible and lead to more intricate dynamics [75–77]. For simplicity, we generally use the coupling (2.47) in this thesis.

The spin-boson model follows naturally as a limiting case of the CLM for a double-well potential: if the ground states of the two wells are sufficiently separated from any excited states and the temperature is also low in contrast to the spacing and the barrier height, only their ground states will become relevant for the dynamics. The energy scale  $\Delta$  then determines the tunneling matrix element between the two minima and  $\epsilon$  gives the difference in energy [33, 78]. A graphical representation is shown in Figure 2.4. As such, the spin-boson model has been applied mainly for the description of tunneling problems, for instance of impurities in glasses at low temperatures [27–30], as a model

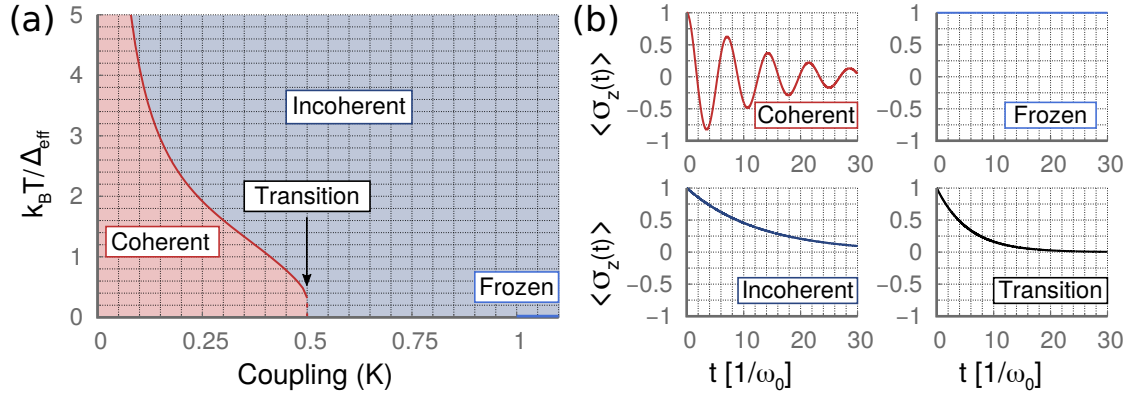


**Figure 2.5:** Typical behavior of the spin-boson model based on the non-interacting blip approximation for the symmetric case ( $\epsilon = 0$ ) [31, 33]. (a) Typical regimes and associated behaviors shown against coupling  $K$  given in Equation (2.56) and temperature rescaled by the renormalized TSS splitting  $\Delta_{\text{eff}}$ . The transition temperature curve  $T^*$  has been obtained from Weiss [33, Equation (22.20)]. (b) Typical dynamics of  $\langle \sigma_z(t) \rangle$ . The plots assume  $\langle \sigma_z(0) \rangle = 1$ ,  $\hbar\omega_c/k_B T \gg 1$  and an Ohmic spectral density. More details can be found in Section 6.1.3 and Weiss [33, Chapter 22].

for atomic force microscopy [79] or as a description of electron transfer reactions [33, Chapter 20][5, Chapter 16]. Furthermore, no complete analytic solution exists for the SBM outside of specific parameter ranges (for comparison, the CLM is exactly solvable for a harmonic potential or a free particle [33]). The SBM has therefore been a focus for the investigation of approximation methods and more elaborate numerical treatments, as well (see e.g. [73, 80, 81]). In fact, the list of applications of this model is rather extensive and we refer to the book by Weiss [33] and the review by Grifoni and Hänggi [32, Chapter 11.1] for more details on its use.

In the following, we discuss some of the dynamics encountered in the SBM as a general example of the dynamics in a system-bath model.

### Typical dynamics of the SBM

In order to understand the dynamics of the SBM, it is useful to look at the dynamics of the uncoupled TSS first. By diagonalization of Equation (2.46) and use of the Schrödinger equation, one finds

$$\langle \sigma_x(t) \rangle = \frac{\epsilon \Delta}{E^2} [1 - \cos(Et/\hbar)], \quad (2.48)$$

$$\langle \sigma_y(t) \rangle = -\frac{\Delta}{E} \sin(Et/\hbar), \quad (2.49)$$

$$\langle \sigma_z(t) \rangle = \frac{\epsilon^2}{E^2} + \frac{\Delta^2}{E^2} \cos(Et/\hbar), \quad (2.50)$$

where we assumed that the system starts in the excited state,  $\langle \sigma_z(t_0) \rangle = 1$ , and  $E = \sqrt{\Delta^2 + \epsilon^2}$  is the characteristic eigenenergy of  $H_S$ . Unsurprisingly, we see regular oscillations in the dynamics of all Pauli matrices. These are quantum beats, created because we start in a state that is not an eigenstate to  $H_S$  but rather to  $\sigma_z$  only. In contrast, if  $\Delta = 0$  the state does not change, as expected. Going back to the SBM, the system-bath coupling of Equation (2.47) couples to the system through the operator  $\sigma_z$  which implies that the bath aims to localize the state of the TSS in one of the two wells. In fact, if  $\Delta = 0$ , we have that  $[H_S, H_{SB}] = 0$  such that no relaxation occurs. However, dephasing can still be found and the model is then known as the *independent boson model* [82][33, Chapter 22.4]. If  $\Delta \neq 0$ , we can expect to see oscillations in  $\langle \sigma_z(t) \rangle$  again. As it turns out, their existence is strongly tied to both the coupling strength and the temperature. For the case of an Ohmic spectral density of the form (2.29) and a symmetric system with  $\epsilon = 0$ , the different regimes are shown exemplary in Figure 2.5 on the basis of results from the non-interacting blip approximation (see Section 6.1.3 and [31, Chapter 10] [33, Chapters 21 and 22] for more details).

Three different regions can be identified: coherent oscillations, incoherent (exponential) decay and a frozen-in state which occurs for strong coupling at zero temperature. The coherent and incoherent regimes are divided by a temperature curve  $T^*$  which scales with the inverse coupling for very small values. For high temperature and small coupling, the incoherent regime is characterized by a relaxation rate which scales with the inverse of the temperature such that the decay becomes more sluggish, the hotter the bath becomes. At coupling  $K = 1/2$  (see Equation (2.56) for a definition) a transition between coherent oscillations and incoherent behavior occurs even at zero temperature. At this point, an exact temperature-independent exponential decay can be found. Inside the coherent regime, smaller couplings and lower temperature lead to less damped and more long-lasting oscillations until the simple cosine of Equation (2.50) is obtained for zero coupling. Lastly, for very strong coupling and zero temperature, the system is localized and the particle cannot tunnel between the two wells.

A nonzero  $\epsilon$  complicates this picture, as the eigenstates of the TSS already introduce a measure of localization into  $\sigma_z$ . The most obvious result is a change of the equilibrium positions for the  $\langle \sigma_i(t) \rangle$ . Specifically, one obtains for weak damping [33, Chapter 21.3.2]

$$\langle \sigma_x(\infty) \rangle = -\frac{\Delta}{E} \tanh\left(\frac{E}{2k_B T}\right), \quad (2.51)$$

$$\langle \sigma_z(\infty) \rangle = -\frac{\epsilon}{E} \tanh\left(\frac{E}{2k_B T}\right). \quad (2.52)$$

Equations (2.51) and (2.52) show that  $E$  becomes the relevant energy scale for most considerations. It is a common practice to include this effect by diagonalizing  $H_S$  which naturally introduces  $E$ , but also leads to a more complicated coupling Hamiltonian from the rotation [83][33, Chapter 3.3]. We will utilize this method in Part 5. A non-zero  $\epsilon$

can also arise when considering external forces, as we will discuss more in the next part of this thesis [32, 33]. A more detailed account on the effect of a non-zero  $\epsilon$  can be found in the book by Weiss [33]. We also stress that our discussion here was based on the behavior for an Ohmic spectral density. Choosing other forms adds an additional layer of complexity to the model (see e.g. [33, Chapter 22.1.2]).

In closing, the SBM shows a rich and complicated behavior in the parameter space determined by temperature and coupling. In particular, we focus on the coherent regime in most parts of this thesis.

### ***Definitions for the SBM***

Finally, we give some general definitions of the spin-boson model which deviate from the presentation for the Caldeira-Leggett case. First, by use of Equation (2.26) the coupling Hamiltonian (2.47) automatically leads to the spectral density

$$\mathcal{J}(\omega) = \frac{\pi \hbar}{q_0^2} \sum_{\alpha=1}^N \lambda_{\alpha}^2 \delta(\omega - \omega_{\alpha}). \quad (2.53)$$

When we discuss the SBM, we usually work with a rescaled density given by

$$J(\omega) = \pi \sum_{\alpha=1}^N \lambda_{\alpha}^2 \delta(\omega - \omega_{\alpha}), \quad (2.54)$$

which has a dimension of a frequency. This definition deviates from the definition used in Weiss [33] by a factor of  $\pi$ , where the spectral density for the SBM is denoted as  $G(\omega)$ .

In Figure 2.5, the dimensionless coupling constant  $K$  relates to the parameterization in Equation (2.29) for the Ohmic case via

$$J(\omega) = 2K\pi\omega \exp[-\omega/\omega_c]. \quad (2.55)$$

This means that  $J(\omega)/\pi \propto 2K\omega$  which coincides with the usual definition from Leggett et al. [78]. This coupling can be traced back to the coupling strength  $\eta$  by

$$K = \frac{\eta q_0^2}{2\pi \hbar}. \quad (2.56)$$

The mapping of the Lorentzian density in the last section also has to be adapted for the SBM. We refer to Section 5.1, where an appropriate mapping is shown in Equation (5.5). Lastly, we note that we often work with the frequency  $\omega_0$  associated with the tunneling energy  $\Delta = \hbar\omega_0$ . This quantity will appear regularly in this thesis to parametrize the time variable.



## 2.3 Some solution methods

In order to obtain actual dynamics of a system-bath model, approximations have to be made. This is because system-bath models are still many-body problems with a large number of degrees of freedom. For this reason, a multitude of approximate solution methods have been developed. In this section, we present the basic ideas behind master equation approaches and the path integral formulation. Both methods will be further developed and utilized in the next parts of this thesis to parametrize the dynamics of the driven bath problem. We close this section with a brief overview of some additional solution methods.

### 2.3.1 Quantum master equations

Quantum master equations describe first order differential equations of the time-dependent density matrix of the system. These equations usually emerge as perturbative solutions of the system-bath problem for the assumption of comparably weak system-bath coupling. However, correlations between bath and the system will still build up over time. In the easiest case, these are neglected entirely which gives rise to a *Born-Markov quantum master equation*, valid for weak coupling and fast decay of memory. Its most famous implementation has been the so-called *Redfield equation* which has been developed to explain relaxation phenomena of nuclear spins in NMR spectroscopy [5, 60, 84]. Aside from this, master equations can also be derived in a variety of other ways and with varying complexity, for instance on the basis of projection operator techniques, such as the Nakajima-Zwanzig equation [5, Chapter 10], by deriving the functional forms required of a semi-group in what has been known as Lindblad formalism [85] or by utilizing time-nonlocal kernel structures [85, 86]. Furthermore, the approximations involved can be relaxed even within a Born-Markov treatment, for instance by calculating and adding non-Markovian corrections [25] or by rotating the Hamiltonian and doing perturbation theory in a different coupling [73]. In this section, we aim to provide a short derivation of a fairly general Born-Markov-type master equation and comment on the structure, the approximations and the solutions involved. Since we will derive these dynamical equations in more detail on the basis of a Liouville-space formulation in Part 5, we will only present the most important steps here. Our presentation is largely based on the books by Cohen-Tannoudji [64] and Nitzan [5] which should also be consulted for more details. For further reading, we also like to mention the derivation found in Breuer and Petruccione [85, Chapter 3.3].

#### *Born-Markov quantum master equation*

We start with the Liouville-von-Neumann equation for a generic system-bath Hamiltonian of the type (2.12) that is not explicitly dependent on time. The combined density

matrix of system and bath,  $W(t)$ , then fulfills

$$\frac{d\tilde{W}(t)}{dt} = -\frac{i}{\hbar}[\tilde{H}_{\text{SB}}(t), \tilde{W}(t)], \quad (2.57)$$

where we formulated the equation in the interaction picture, signified by a tilde. Therein, a generic operator  $\mathcal{O}$  has a time dependence given by  $\tilde{\mathcal{O}}(t) = e^{(i/\hbar)(H_{\text{S}}+H_{\text{B}})t} \mathcal{O} e^{-(i/\hbar)(H_{\text{S}}+H_{\text{B}})t}$ . Equation (2.57) can formally be integrated and the result reinserted to yield an expression in second order of  $H_{\text{SB}}$ ,

$$\begin{aligned} \tilde{W}(t) - \tilde{W}(t_0) = & -\frac{i}{\hbar} \int_{t_0}^t dt' [\tilde{H}_{\text{SB}}(t'), \tilde{W}(t_0)] \\ & - \frac{1}{\hbar^2} \int_{t_0}^t dt' \int_{t_0}^{t'} dt'' [\tilde{H}_{\text{SB}}(t'), [\tilde{H}_{\text{SB}}(t''), \tilde{W}(t'')]]. \end{aligned} \quad (2.58)$$

Again, we are interested in the behavior of the small system only. In terms of the density matrix, this information is encoded within the so-called *reduced density matrix* of the system,  $\rho_{\text{S}}(t)$ , which emerges after a trace over bath states as

$$\rho_{\text{S}}(t) = \text{Tr}_{\text{B}}[W(t)]. \quad (2.59)$$

With  $\rho_{\text{S}}(t)$  the dynamics of a system observable can be obtained from the corresponding averages  $\langle \mathcal{O}(t) \rangle_{\text{S}} = \text{Tr}_{\text{S}}[\mathcal{O}\rho_{\text{S}}(t)]$ . Thus, a trace over bath states in Equation (2.58) yields

$$\begin{aligned} \tilde{\rho}_{\text{S}}(t) - \tilde{\rho}_{\text{S}}(t_0) = & -\frac{i}{\hbar} \int_{t_0}^t dt' \text{Tr}_{\text{B}} \left[ [\tilde{H}_{\text{SB}}(t'), \tilde{W}(t_0)] \right] \\ & - \frac{1}{\hbar^2} \int_{t_0}^t dt' \int_{t_0}^{t'} dt'' \text{Tr}_{\text{B}} \left[ [\tilde{H}_{\text{SB}}(t'), [\tilde{H}_{\text{SB}}(t''), \tilde{W}(t'')]] \right]. \end{aligned} \quad (2.60)$$

Equation (2.60) is exact but due to the existence of the full density matrix on the right-hand side not solvable. In order to progress, a split of time scales is assumed, where the correlation time of the bath  $\tau_{\text{c}}$  is taken to be much smaller than the typical time that characterizes the evolution of the system  $\tau_{\text{S}}$ . In essence, this argument is similar to those in the classical Langevin equation: a heavy particle is subject to collisions from the environment, much faster than the typical time on which the particle moves and damping (as a consequence of lots of collisions) occurs. For our purposes, this permits a host of subsequent approximations based on the idea that correlations between system and bath vanish rapidly [64]. Specifically, we can evaluate Equation (2.60) for a time frame  $\delta t$  with  $\tau_{\text{S}} \gg \delta t \gg \tau_{\text{c}}$  which permits us to use a coarse-grained description for the dynamics of the system. This implies that we can assume  $\tilde{W}(t'') \approx \tilde{W}(t_0)$  on the right-hand side of Equation (2.60) because neither the density matrix of the system

nor the bath will change appreciably for sufficiently small coupling and  $\tau_S \gg \delta t$ . In addition, we assume the density matrix to factorize as

$$\tilde{W}(t_0) = \tilde{\rho}_S(t_0) \otimes \tilde{\rho}_B(t_0) = \tilde{\rho}_S(t_0) \otimes \rho_B^{\text{eq}}. \quad (2.61)$$

Here,  $\rho_B$  is assumed constant which follows from the fact that the bath itself is huge and will not be perturbed much by the system. In addition, we have assumed thermal equilibrium for the bath via

$$\rho_B^{\text{eq}} = \frac{1}{\mathcal{Z}} e^{-\beta H_B}, \quad (2.62)$$

for which the bath density matrix also commutes with the unperturbed time evolution of the bath. The factorization in Equation (2.61) assumes that no correlations exist between system and bath at  $t_0$ . In fact, correlations that build up can be shown to vanish on a time scale  $\tau_c$  and can therefore be neglected for the evaluation over time scales  $\delta t$ . Lastly, we write  $H_{SB}$  as a simple product of operators in the subspaces,

$$H_{SB} = -A \otimes R, \quad (2.63)$$

where  $A$  is an operator in the system subspace and  $R$  in the bath subspace. This choice reflects the typical bilinear couplings of the Caldeira-Leggett and spin-boson models (see Equations (2.15) and (2.47)). For simplicity, we assume that the average  $\langle \tilde{R}(t) \rangle_B = \text{Tr}_B[R \rho_B^{\text{eq}}] = 0$ . Putting all of those arguments into Equation (2.60) shows that only the second term will be nonzero and is defined by bath correlators

$$C(t' - t'') = \langle \tilde{R}(t') \tilde{R}(t'') \rangle_B = \text{Tr}_B[\tilde{R}(t' - t'') \tilde{R}(0) \rho_B^{\text{eq}}], \quad (2.64)$$

where the second equation used the cyclical invariance of the trace. In case of the system-bath models discussed, Equation (2.64) directly yields the fluctuation spectrum found in Equation (2.28). The real part then describes the symmetric autocorrelation function and the imaginary part gives the bath response function. However, next to the correlator and its complex conjugate, combinations of system operators emerge from the double commutator. Because of this, a representation in matrix elements of system-eigenstates (labeled as  $a, b, c, d$ ) is commonly used. Ultimately, one finds the following form of the Born-Markov master equation:

$$\frac{d\rho_{S,ab}(t)}{dt} = -i\omega_{ab} \rho_{S,ab}(t) + \sum_{c,d} \mathcal{R}_{abcd} \rho_{S,cd}(t). \quad (2.65)$$

Equation (2.65) is a general form of the Redfield equation [5, Chapter 10], which is just a linear differential equation with constant coefficients  $\mathcal{R}_{abcd}$  and a phase contribution depending on the transition frequencies  $\omega_{ab} = \omega_a - \omega_b$ . In order to arrive at

Equation (2.65), the coarse-grained evaluation over  $\delta t$  was used to approximate the instantaneous change of the density matrix. This implies, again, that only dynamics beyond  $\tau_c$  are considered. In addition, we employed the so-called *secular approximation*. This approximation neglects small terms, where differences of transition frequencies multiplied with time frames  $\Delta t = t - t_0 \sim \tau_S$  are large. Lastly, due to the rapidly decaying integration kernels, the boundaries of the integrals could be sent to infinity as well, removing any additional time dependence. With these arguments Equation (2.65) is approximated for predictions on time scales longer than  $\tau_S$  only [64].

### Resulting dynamics

According to Equation (2.65) the diagonal elements of the density matrix (which are just the populations of the states) evolve as [64, Chapter IV C.]

$$\frac{d\rho_{S,aa}(t)}{dt} = \sum_{c \neq a} [\Gamma_{c \rightarrow a} \rho_{S,cc}(t) - \Gamma_{a \rightarrow c} \rho_{S,aa}(t)]. \quad (2.66)$$

Here,  $\Gamma$  are transition rates from states  $a$  to  $c$  and vice versa. They are given by thermally averaged golden rule rates as (cf. Equation (2.8))

$$\Gamma_{c \rightarrow a} = \frac{2\pi}{\hbar} \sum_{n,n'} \frac{e^{-\beta E_n}}{\mathcal{Z}} |\langle a, n' | H_{SB} | c, n \rangle|^2 \delta(E_n + E_c - E_{n'} - E_a). \quad (2.67)$$

As such, the populations decay with a rate defined by the golden rule and exponential damping is obtained. However, Equation (2.67) also contains transitions into the states which fill up the populations. By equating both, a steady state is obtained and we recover detailed balance conditions as in Equation (2.11).

The non-diagonal elements of the reduced density matrix are often referred to as *coherences*. They fulfill

$$\frac{d\rho_{S,ab}(t)}{dt} = -i\omega_{ab} \rho_{S,ab}(t) - [\Gamma_{ab} + i\Delta_{ab}] \rho_{S,ab}(t). \quad (2.68)$$

Here, two new terms define the dynamics:  $\Gamma_{ab}$  gives rates which turn out to be similar to (2.67). However, a characteristic factor of  $1/2$  emerges for terms where the system changes its state and which are referred to as non-adiabatic contributions. This is an example of dephasing, where damping of coherences implies the decay of superposition states. The corresponding adiabatic contributions do not change the state of the bath and are determined by  $J(0)$ . These give rise to pure dephasing. The second new term, defined by  $\Delta_{ab}$ , gives an imaginary contribution which can be factorized into the transition frequency  $\omega_{ab}$ . This amounts to a frequency renormalization as predicted in Section 2.1.1. Finally, it should be noted that interactions between non-diagonal elements and populations are neglected in the secular approximation.

## *Approximations*

Up to now we have applied quite a few approximations. While all of them can be motivated by rapid decay of correlations between system and bath, we summarize the three most important ones in the following:

**Perturbative expansion (Born approximation):** in general, we require weak system-bath coupling for Equation (2.58) to be useful. However, it can be shown that the small parameter of the expansion includes  $\tau_c$  such that small enough correlation times can also be used to motivate the expansion. Nevertheless, weak coupling ensures that no correlations can build up [64, Chapter IV B.3, D].

**The Markov approximation:** the Markov approximation assumes no memory effects in the bath from interaction with the system and vice versa. This is essentially a formal statement about the size of the reservoir and only treating dynamics beyond  $\tau_c$ . If the correlations decay fast enough, no memory is retained in the coarse-grained description and the density matrix can be assumed to be constant over the time scale when the correlations are non-zero. Together with the Born approximation this amounts to an iterative summation of second-order terms (see Section 5.2.2). This also implies that the coefficients  $\mathcal{R}_{abcd}$  can be assumed as time-independent [5][64, Chapter IV].

**The secular approximation:** the secular approximation is a statement about the size of contributions in  $\mathcal{R}_{abcd}$ . It states that those terms where the difference of transition frequencies multiplied with  $\Delta t \sim \tau_S$  is large, will be small and can be neglected [64, Chapter IV][60, Chapter 3.8.3]. In a sense, this argument is reminiscent of results in ordinary quantum perturbation theory which yields terms with an inverse dependence on frequency differences. In fact, the secular approximation is similar to the rotating wave approximation in quantum optics that we will encounter in the next part of this thesis [85].

While these approximations seem drastic, they successfully yield both dephasing and relaxation contributions, give a simple description of typical system-bath dynamics and also permit an extension to driven systems or more involved treatments. We will apply a Born-Markov description to a driven bath in Part 5 and discuss these approximations and the emerging dynamics in more detail.

### **2.3.2 Path integral methods**

Another way to formulate the dynamics of the reduced density matrix is provided by way of Feynman's path integral description. Its advantage lies in analytical formulations of the system-bath problem. In particular, contributions from the path integral can

be summed up and brought into the form of an exact master equation, which can be exploited in approximation schemes. The so-called *non-interacting blip approximation* (NIBA), for instance, allows to find the dynamics for high temperatures and strong coupling. Presented at length in the 1987 seminal paper by Leggett et al. [78], this approximation has been used in the analysis of various problems (e.g. [87–89]) and has also seen some extensions over the years [33, 65]. We will derive the non-interacting blip approximation in Part 6 and use it to find the strong-coupling dynamics of a driven bath. Another interesting result of the path-integral description is a numerical implementation called *quasiadiabatic propagator path integral method* (QUAPI). Here, the analytical formulation through path integrals is used for an iterative solution over small time slices  $dt$  based on the assumption of sufficiently decaying bath autocorrelation functions. Since the method itself is numerically exact, it naturally includes memory effects, is usable for arbitrary coupling strengths and can also be readily extended to driven systems. However, the method is computationally expensive and its implementation rather complicated such that its applicability is limited [65, 90–92].

In the following, we derive the basics of the path integral formulation based on the presentation by Weiss [33]. We start with the combined density matrix of system and bath,  $W(t)$ . We assume that this density matrix factorizes into system and bath parts at some time  $t_0$ , just as in Equation (2.61). Specifically,  $W(t_0) = \rho_S(t_0) \otimes \rho_B^{\text{eq}}$ , where  $\rho_S$  is the reduced density matrix of the system. We also assume the bath to be in thermal equilibrium with its density matrix given by  $\rho_B^{\text{eq}}$  in Equation (2.62). The time evolution of  $W(t)$  between  $t_0$  and  $t$  can be written by way of time evolution operators,  $U(t, t_0)$ , such that

$$W(t) = U(t, t_0)W(t_0)U^\dagger(t, t_0). \quad (2.69)$$

Similar to the previous subsection, we want to obtain the reduced density matrix of the system at time  $t$  which emerges from a trace over bath states. We now use the Hamiltonian of the Caldeira-Leggett model in Section 2.2.1. This reduces our system to a single coordinate  $q$  and describes the bath as harmonic oscillators with positions  $x_\alpha$ . We collect the latter in variables  $\mathbf{x}$  for brevity. A matrix element of the reduced density matrix can then be written as

$$\begin{aligned} \rho_S(q_f, q'_f, t) &= \langle q_f | \rho_S(t) | q'_f \rangle = \int d\mathbf{x}_f \langle q_f, \mathbf{x}_f | W(t) | q'_f, \mathbf{x}_f \rangle \\ &= \int dq_i \int dq'_i \int d\mathbf{x}_f \int d\mathbf{x}_i \int d\mathbf{x}'_i K(q_f, \mathbf{x}_f, t; q_i, \mathbf{x}_i, t_0) \\ &\quad * \langle q_i, \mathbf{x}_i | W(t_0) | q'_i, \mathbf{x}'_i \rangle K^*(q'_f, \mathbf{x}_f, t; q'_i, \mathbf{x}'_i, t_0). \end{aligned} \quad (2.70)$$

Here,  $K(\dots)$  denotes the Feynman propagator which describes the matrix element of the time evolution operator as  $K(b, t; a, t_0) = \langle b | U(t, t_0) | a \rangle$ . Integrals over  $\mathbf{x}$  designate

integrations over each oscillator coordinate  $x_\alpha$ . As usual, the Feynman propagator can be discretized by splitting up the time interval from  $t_0$  to  $t$  into a large number  $M$  of infinitesimally small segments  $\delta t$ . Subsequent insertion of the identity allows for a formulation as a path integral [61],

$$K(q_f, \mathbf{x}_f, t; q_i, \mathbf{x}_i, t_0) = \int_{q_i}^{q_f} \mathcal{D}q \int_{\mathbf{x}_i}^{\mathbf{x}_f} \mathcal{D}\mathbf{x} e^{\frac{i}{\hbar}(S_S[q] + S_B[\mathbf{x}] + S_{SB}[q, \mathbf{x}])}, \quad (2.71)$$

where the measures stand in for  $M$  integrations over the intermediate position eigenvalues and the boundaries give the positions at the endpoints of the path. The exponentials contain the actions  $S[\dots]$  given by

$$S_B[\mathbf{x}] = \int_{t_0}^t ds \sum_{\alpha=1}^N \frac{1}{2} \left[ m_\alpha \dot{x}_\alpha^2(s) - m_\alpha \omega_\alpha^2 x_\alpha^2(s) \right], \quad (2.72)$$

$$S_{SB}[q, \mathbf{x}] = \int_{t_0}^t ds \sum_{\alpha=1}^N \left[ c_\alpha x_\alpha(s) q(s) - \frac{c_\alpha^2 q^2(s)}{2m_\alpha \omega_\alpha^2} \right], \quad (2.73)$$

$$S_S[q] = \int_{t_0}^t ds \left[ \frac{M \dot{q}^2(s)}{2} - V[q(s)] \right]. \quad (2.74)$$

Here, a dot signifies a derivative in time. Insertion of Equation (2.71) into Equation (2.70) allows us to find the reduced density matrix by way of a propagating function  $J_{FV}(\dots)$  according to

$$\rho_S(q_f, q'_f, t) = \int dq_i \int dq'_i J_{FV}(q_f, q'_f, t; q_i, q'_i, t_0) \rho_S(q_i, q'_i, t_0). \quad (2.75)$$

The propagating function is given by

$$J_{FV}(q_f, q'_f, t; q_i, q'_i, t_0) = \int_{q_i}^{q_f} \mathcal{D}q \int_{q'_i}^{q'_f} \mathcal{D}q' e^{\frac{i}{\hbar}(S_S[q] - S_S[q'])} F_{FV}[q, q'], \quad (2.76)$$

with the *Feynman-Vernon influence functional*  $F_{FV}[q, q']$  given by

$$F_{FV}[q, q'] = \int d\mathbf{x}_f \int d\mathbf{x}_i \int d\mathbf{x}'_i \int_{\mathbf{x}_i}^{\mathbf{x}_f} \mathcal{D}\mathbf{x} \int_{\mathbf{x}'_i}^{\mathbf{x}'_f} \mathcal{D}\mathbf{x}' \quad (2.77)$$

$$* e^{\frac{i}{\hbar}[S_{SB}[q, \mathbf{x}] - S_{SB}[q', \mathbf{x}']]} e^{\frac{i}{\hbar}[S_B[\mathbf{x}] - S_B[\mathbf{x}']]} \rho_B^{\text{eq}}(\mathbf{x}_i, \mathbf{x}'_i).$$

The Feynman-Vernon influence functional describes the interaction between two paths a system can take and results from the interaction with the bath. In a procedure going

back to Feynman and Vernon Jr. [93], the path integrals and boundary integrations in (2.77) can be evaluated to yield

$$F_{\text{FV}}[q, q'] = \exp \left[ -\frac{1}{\hbar} \int_{t_0}^t dt' \int_{t_0}^{t'} dt'' \{ L(t' - t'')q(t'') - L^*(t' - t'')q'(t'') \} \right. \\ \left. * \{ q(t') - q'(t') \} - \frac{i}{\hbar} \frac{\mu}{2} \int_{t_0}^t dt' \{ q^2(t') - q'^2(t') \} \right]. \quad (2.78)$$

Here  $L(t)$  is the fluctuation spectrum found in Equation (2.28) and  $\mu = M\gamma(0)$  originates from the counter-term. Details of the calculation can be found in Appendix E of this thesis, in the book by Weiss [33, Chapter 5] and in the review by Grabert and Ingold [94]. The imaginary part of Equation (2.78) leads to damping while the real part gives rise to decoherence [33]. For the simple bath of uncoupled harmonic oscillators in thermal equilibrium we also note that  $L(t)$  only depends on the difference of  $t'$  and  $t''$ . Equation (2.75) together with the influence functional (2.78) thus gives the full solution of the system-bath problem on the basis of path integrals.

Within the QUAPI method,  $F_{\text{FV}}[q, q']$  is parametrized in a basis of discrete position eigenstates dubbed the DVR-basis [65]. Together with finite time steps this allows to formulate the problem using finite matrices and one obtains an exact recurrence relation for the reduced density matrix. More details are found in the thesis by Thorwart [65] or in the original papers by Makri and Makarov [91, 92]. In contrast, the NIBA approximation for the spin-boson model parametrizes the influence functional via center-of-mass (sojourns) and relative coordinates (blips) where interactions of the latter are subsequently disregarded. Details for this are found in the book by Weiss [33, Chapter 21] and in Part 6.

### 2.3.3 Other methods

In this subsection, we mention a few additional solution methods. As we will not go into detail, this subsection is only intended as a short overview without claim of completeness. The cited literature can be used as a starting point for a more in-depth look into the different subjects.

#### *Hierarchical equations of motion (HEOM)*

The HEOM approach constructs the reduced density matrix from a hierarchy of differential recurrence relations. This hierarchy follows from introducing additional terms into the exact path integral expressions. Their order defines auxiliary density matrices, which can be connected to each other by differentiation. The zeroth order gives the exact reduced density matrix. It turns out that for very high orders the coupling between the matrices effectively vanishes such that the hierarchy can be truncated. By



iteratively solving the hierarchy from top to bottom it is therefore possible to obtain the reduced density matrix numerically. More details can be found in Ishizaki and Tanimura [95] and the original papers on the subject [96, 97].

### ***Renormalization group methods***

Renormalization group (RG) methods formalize the idea that bath degrees of freedom are integrated out in order to obtain the dynamics of the system only. Specifically, RG methods systematically decrease the number of degrees of freedom by iteratively absorbing their effect in specific quantities, leading to effective Hamiltonians. RG methods can then be understood as mapping procedures which can be used to obtain solutions on the basis of solvable effective models. The most well known example of their use concerns the emergence of universality near a critical point where many different physical systems exhibit the same functional dependence. In terms of RG this was successfully explained by showing that different systems map to the same effective model [98–100]. Practically, the actual procedure can be implemented in a variety of different ways. For instance on the basis of sophisticated path integral and diagrammatic descriptions (FRG) [14, 100, 101] or numerically via sequential diagonalization and truncation of the resulting state-space (NRG and DMRG) [15, 16, 102].

### ***Multiconfigurational time-dependent Hartree methods (MCTDH)***

MCTDH methods are a staple of numerical methods which have become increasingly popular for chemical physicists. In addition to density functional methods for electronic degrees of freedom, MCTDH can be used to describe the behavior of nuclear dynamics in molecules. The method is based on a variational ansatz for the wave-function as a superposition of products of time-dependent single-particle states (a so-called *Hartree product*). By using the Schrödinger equation and specific variational constraints, differential equations for the single-particle functions can be obtained. A similar ansatz can also be used to obtain the reduced density matrix. Still, the method is approximate as the ansatz itself neglects correlations. However, the degree of approximation is linked to the number of products involved, thus allowing for controlled accuracy and numerical effort. In contrast to previous Hartree-like treatments, MCTDH allows to describe more degrees of freedom, making it interesting for problems in dissipative quantum mechanics as well. For instance, the method has been used in the analysis of an ion in contact with a Bose condensate [103] and has been applied to the spin-boson model as well [104]. More information can be found in the book by Meyer et al. [105] and the reviews by Beck et al. [106] and Worth et al. [107].

### ***Stochastic Schrödinger equations***

As an alternative to the formulation by path integrals or reduced density matrices, system-bath models can also be analyzed using a framework of stochastic pure states. These states are constructed as solutions of Schrödinger equations which include a stochastic force. The reduced density matrix then follows as the ensemble average over projectors onto the states for the different realizations. The Schrödinger equations are constructed either by formulating the stochastic states in the basis of coherent states or by way of propagators which follow from path integral expressions [108, 109]. Recently, this ansatz was extended with ideas from the HEOM method in the so-called *hierarchy of pure states* (HOPS) approach. This new method replaces a functional derivative, which naturally appears in the stochastic Schrödinger equations, with a hierarchy of differential recurrence relations. By iteratively solving the hierarchy, the solutions converge faster with more accurate results [110].

## **The Onsager model and driven quantum systems**

After we introduced the ideas behind dissipative quantum systems in the last part, we proceed with the discussion of driven quantum systems. Our main focus will lie on the interaction with a classical electric field and, in particular, on the dipole approximation. This approach is particularly convenient for system-bath models, as a simple electrostatic cavity model can be employed to mimic environmental solvation and model the associated spectral density. The setup of this chapter is oriented along these core ideas: we begin by recalling the basics of classical electrodynamics with a focus on the macroscopic description in materials. In the second section, we introduce the notion of solvation models and discuss the so-called Onsager model. We proceed in Section 3 with a short introduction to driven dissipative quantum systems including linear response theory and the optical Bloch equations. This chapter is largely based on books on the subject matter [5, 49, 111–117].

### **3.1 Electrostatics in materials**

As a general rule, electrodynamic interactions are among the most important interactions for physical systems. In the form of driving fields from a laser or the Coulomb interaction with the environment (for instance in a polar solvent), they also prove to be particularly important for system-bath descriptions of molecules. Therefore, this section will give a presentation of classical electrodynamics with a focus on macroscopic fields in materials. This allows us to introduce the notion of a dynamic polarization and we discuss usual forms of the dielectric function. We proceed with a short summary of nonlinear effects and the Kerr effect in preparation for our analysis in Part 7. Finally, we introduce some molecular quantities which determine the interaction with electric fields on the microscopic level.

#### **3.1.1 Macroscopic Maxwell equations**

What happens when electrical fields act on a material? In conducting materials such as metals electric fields excite conduction electrons which gives rise to currents and magnetic fields. In non-conducting materials, however, electrons are bound and cannot

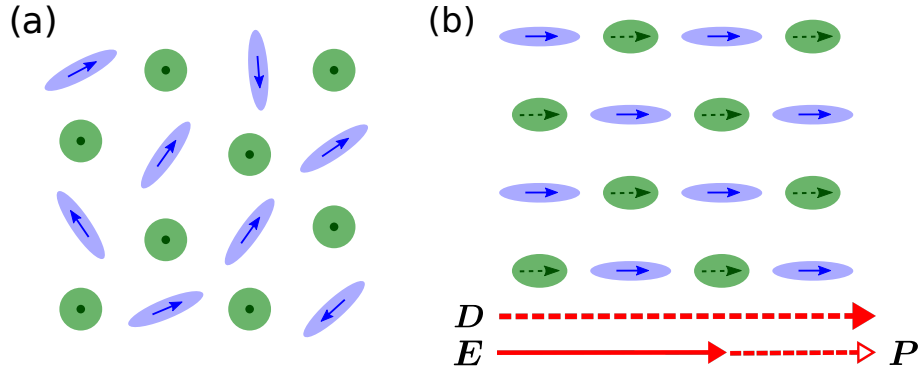


**Figure 3.1:** Depiction of polarization in a dielectric. (a) A dielectric consists of electrically neutral molecules (green spheres) and molecules with permanent dipole moments (blue ovals and arrows), which are initially unoriented. (b) Upon application of an external field (the dielectric displacement  $\mathbf{D}$ ), dipole moments are induced in the neutral molecules (dashed green arrows) while the molecules with permanent dipole moment rotate into the direction of the field. The dielectric becomes polarized with polarization  $\mathbf{P}$ . This usually amounts to shielding and the measurable electric field  $\mathbf{E}$  inside the material is smaller than  $\mathbf{D}$  (red arrows). In a simple linear approximation the relative dielectric constant determines the size of this effect.

separate or flow as easily. This means, an electric field that is not too strong merely induces molecular dipole moments by deforming the electron cloud inside the molecules or it reorients permanent moments across the material. This is known as dielectric polarization and the corresponding materials as dielectrics. A magnetic field, on the other hand, may induce or reorient magnetic moments which gives rise to a macroscopic magnetization. Both ideas are formalized by introducing appropriate fields which take into account the effect of external sources as well as the internal effects from polarization or magnetization. Naturally, this description cannot be valid on the molecular scale as the fields created by the molecules or atoms will vary too strongly. Their quantized nature also has to be taken into account. However, the definition of macroscopic fields allows for an easy formulation by way of modified Maxwell equations which describe a coarse-grained picture where molecular details are neglected. In the following,  $\epsilon_0$  gives the vacuum permittivity,  $\mu_0$  the vacuum permeability while boldfaced quantities designate vectors. With this in mind, we define the displacement field  $\mathbf{D}(\mathbf{r}, t)$  as

$$\mathbf{D}(\mathbf{r}, t) = \epsilon_0 \mathbf{E}(\mathbf{r}, t) + \mathbf{P}(\mathbf{r}, t), \quad (3.1)$$

where  $\mathbf{P}(\mathbf{r}, t)$  is the polarization which follows from the average molecular dipole-moment  $\mathbf{p}_{\text{mol}}$  in a small volume around  $\mathbf{r}$ , multiplied by their number density  $N$  [111,

$$\mathbf{P}(\mathbf{r}, t) = N \mathbf{p}_{\text{mol}}(\mathbf{r}, t). \quad (3.2)$$

Definition (3.1) implies that the total electric field  $\mathbf{E}(\mathbf{r}, t)$  in the material is modified because of shielding or enhancement by the molecular dipoles. The displacement field then gives the unmodified field contribution created by real charges only. The relationship between these quantities and the two primary origins of dielectric polarization are depicted exemplarily in Figure 3.1. Similarly, we can also define a magnetization by way of magnetic moments  $\mathbf{m}_{\text{mol}}$  as [111, 115]

$$\mathbf{M}(\mathbf{r}, t) = N \mathbf{m}_{\text{mol}}(\mathbf{r}, t). \quad (3.3)$$

The magnetizing field is then defined as

$$\mathbf{H}(\mathbf{r}, t) = \mu_0^{-1} \mathbf{B}(\mathbf{r}, t) - \mathbf{M}(\mathbf{r}, t). \quad (3.4)$$

It can be shown that the fields  $\mathbf{D}(\mathbf{r}, t)$  and  $\mathbf{H}(\mathbf{r}, t)$  fulfill the Maxwell equations,

$$\nabla \cdot \mathbf{D}(\mathbf{r}, t) = \rho_{\text{free}}(\mathbf{r}, t), \quad (3.5)$$

$$\nabla \cdot \mathbf{B}(\mathbf{r}, t) = 0, \quad (3.6)$$

$$\nabla \times \mathbf{E}(\mathbf{r}, t) = -\frac{\partial \mathbf{B}(\mathbf{r}, t)}{\partial t}, \quad (3.7)$$

$$\nabla \times \mathbf{H}(\mathbf{r}, t) = \mathbf{j}_{\text{free}}(\mathbf{r}, t) + \frac{\partial \mathbf{D}(\mathbf{r}, t)}{\partial t}. \quad (3.8)$$

Here, the subscript *free* designates that only non-bound charges and currents are taken into account. Any changes in both the charge and the current distribution are absorbed into the definitions of  $\mathbf{H}$  and  $\mathbf{D}$  such that they describe unperturbed fields created by external charges and currents only. The measurable magnetic and electric fields ( $\mathbf{E}$  and  $\mathbf{B}$ ) are changed by the corrections from  $\mathbf{P}$  and  $\mathbf{M}$ . Their sign, behavior and size give rise to different classifications of materials such as ferromagnetic or paraelectric substances. In this thesis, we will work with the ordinary dielectric or paraelectric cases, where no polarization occurs at zero field [115]. As can be seen from Equations (3.1) and (3.4), the contribution of  $\mathbf{P}$  and  $\mathbf{M}$  may also change the associated direction of the fields and can depend on the fields inside the material in a complicated manner. In the easiest case, they can be assumed as linear and isotropic such that polarization and magnetization become simple proportionalities. That is, for linear dielectrics and linear magnetizations, we have that

$$\mathbf{P}(\mathbf{r}, t) \approx \varepsilon_0 \chi_e \mathbf{E}(\mathbf{r}, t), \quad (3.9)$$

$$\mathbf{M}(\mathbf{r}, t) \approx \chi_m \mathbf{H}(\mathbf{r}, t), \quad (3.10)$$

where  $\chi_e$  and  $\chi_m$  are called *electric and magnetic susceptibility* respectively. Inserted in Equations (3.1) and (3.4), these are often grouped together as new constants

$$\mathbf{D}(\mathbf{r}, t) = \varepsilon_0(1 + \chi_e)\mathbf{E}(\mathbf{r}, t) = \varepsilon_0\varepsilon_r\mathbf{E}(\mathbf{r}, t), \quad (3.11)$$

$$\mathbf{B}(\mathbf{r}, t) = \mu_0(1 + \chi_m)\mathbf{H}(\mathbf{r}, t) = \mu_0\mu_r\mathbf{H}(\mathbf{r}, t), \quad (3.12)$$

where  $\varepsilon_r$  is the *relative permittivity* (sometimes called the relative dielectric constant) and  $\mu_r$  the *relative permeability*. Both quantities are evidently dimensionless.

In the following, we restrict ourselves to the discussion of electrostatic problems where  $\mathbf{j}_{\text{free}}(\mathbf{r}, t) = 0$  and no magnetization exists. Nevertheless, we will later also use a time-dependent electric field while we neglect the impact of the dielectric displacement current in Equation (3.8). This reduces the problem to a purely electrostatic one.

### 3.1.2 Electrostatic boundary conditions

The usual boundary conditions for electrostatic or magnetostatic problems are altered in materials. Here, we outline the results for electrostatic problems in the linear regime and neglect any time dependence for the time being. First, Equation (3.11) implies that we can define the potential of the electric field as usual, that is  $\mathbf{E}(\mathbf{r}) = -\nabla\Phi(\mathbf{r})$ . Insertion of Equation (3.11) into Equation (3.5) yields the associated Poisson equation,

$$\Delta\Phi(\mathbf{r}) = -\frac{\rho_{\text{free}}(\mathbf{r})}{\varepsilon_0\varepsilon_r}. \quad (3.13)$$

This means that the overall solution methods to electrostatic problems remain the same but for an additional factor  $\varepsilon_r$ . Thus, the boundary conditions between two dielectric surfaces 1 and 2 can be derived from Equations (3.5) and (3.7) as usual by considering the tangential and perpendicular component of the electric field at the boundary [111, 112]. Specifically, we find continuity of the potential,

$$\Phi_1(\mathbf{r})|_{\text{boundary}} = \Phi_2(\mathbf{r})|_{\text{boundary}}, \quad (3.14)$$

and a jump in the derivative along the normal  $\mathbf{n}$ ,

$$\varepsilon_{r,1}\frac{\partial\Phi_1(\mathbf{r})}{\partial\mathbf{n}} - \varepsilon_{r,2}\frac{\partial\Phi_2(\mathbf{r})}{\partial\mathbf{n}} = \sigma_{\text{free}}(\mathbf{r}). \quad (3.15)$$

Only the last equation is modified by the existence of the relative permittivities of the two dielectrics,  $\varepsilon_{1,r}$  and  $\varepsilon_{2,r}$ , and by evaluating the surface charge density  $\sigma$  only for free charges.

### 3.1.3 Dynamic polarization

Up to this point, we have not only worked in the isotropic linear approximation, but also neglected any kind of spatial or time dependence within the response of the dielectric. By keeping both isotropy and linearity in  $\mathbf{E}$ , we can write the polarization of Equation (3.9) by way of an integral for a time and space-dependent linear electric susceptibility  $\chi_e(\mathbf{x}, \mathbf{x}'; t, t')$ , according to [5, 49, 117]

$$\mathbf{P}(t, \mathbf{x}) = \varepsilon_0 \int d^3x' \int_{-\infty}^t dt' \chi_e(\mathbf{x}, \mathbf{x}'; t, t') \mathbf{E}(\mathbf{x}', t'). \quad (3.16)$$

Here,  $\chi_e$  now relates the two positions  $\mathbf{x}$  and  $\mathbf{x}'$  as well as the times  $t$  and  $t'$ . For the case of homogeneity in space and time, only the difference of the respective variables is important such that

$$\mathbf{P}(t, \mathbf{x}) = \varepsilon_0 \int d^3x' \int_{-\infty}^t dt' \chi_e(\mathbf{x} - \mathbf{x}'; t - t') \mathbf{E}(\mathbf{x}', t'). \quad (3.17)$$

In this thesis, we usually neglect the spatial dependence and argue that the electric field is assumed to vary little across the length of the physical system of interest. This means, we use a localized response given by  $\chi_e(\mathbf{x} - \mathbf{x}'; t - t') = \chi_e(t - t')\delta(\mathbf{x} - \mathbf{x}')$  [5]. In terms of the time variable, Equation (3.17) describes the case in which the electric field changes faster than the response of the dielectric such that the polarization follows the field with a delay. This can happen, for instance, when the molecules forming the dielectric reorient in the direction of a fast oscillating field. The inertia of the molecules will then naturally introduce a delay into the response of the dielectric. An instantaneous response (such as as fast reaction of a molecule's electron cloud) can also be included by way of an appropriate  $\delta$ -function. It should be noted that this physical picture introduces a notion of causality, in that the response must follow after the perturbation and cannot occur beforehand. This is reflected mathematically by having  $\chi_e(\tau) = 0$  for  $\tau < 0$ . Together with the localized response, a Fourier transformation to frequency space turns Equation (3.17) into a simple proportionality given by

$$\mathbf{P}(\omega) = \varepsilon_0 \chi_e(\omega) \mathbf{E}(\omega). \quad (3.18)$$

Equation (3.18) recreates Equation (3.9) except with an additional frequency dependence. This implies that in the absence of currents and magnetic fields, we can apply the ordinary solution methods of electrostatics to find the resulting fields. Naturally, the complete absence of currents (especially the displacement current) is an approximation which we motivate by their relative weakness for weak, slowly varying fields and the (essentially) non-conducting nature of dielectric materials. We apply these principles in the next section to solve the Onsager sphere model.

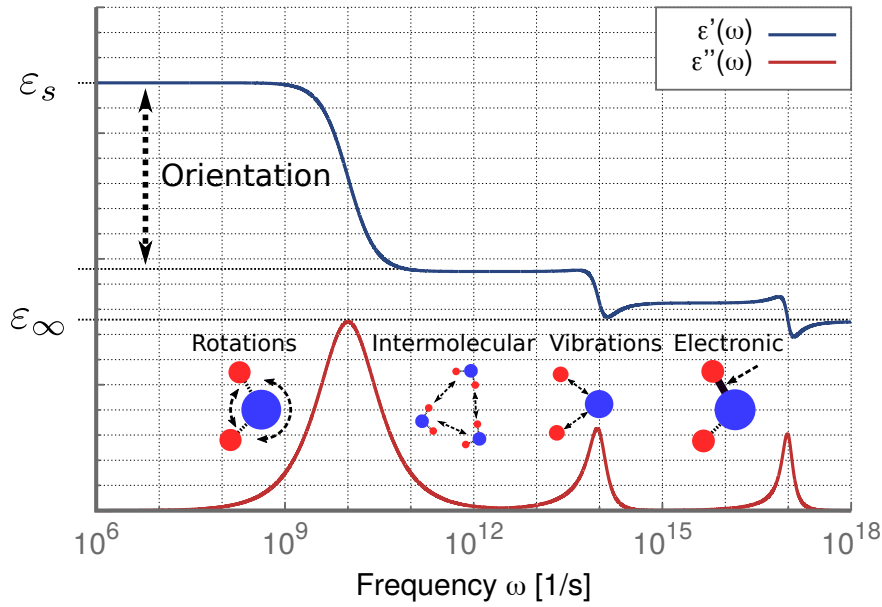


**Figure 3.2:** Typical behavior of a dielectric function  $\varepsilon(\omega)$  for molecules in the condensed phase at different probing frequencies [113]. The plot is constructed from a Debye-type peak and two Lorentzian resonances (see Equations (3.20) and (3.34)). The former corresponds to typical dynamics related to orientation of molecules while the latter models specific molecular resonances as shown exemplary for water molecules in the relevant frequency range. The real part  $\varepsilon'(\omega)$  shows a characteristic peak-antipeak structure at resonance and determines the phase of an incoming beam of light. The imaginary part  $\varepsilon''(\omega)$  produces clearly visible peaks which correspond to damping. The step-like structure of  $\varepsilon'(\omega)$  shows that for increasing frequency degrees of freedom stop to contribute and for frequencies too high only nuclear effects will eventually remain.

### 3.1.4 Refractive index and dielectric function

In Equation (3.16) we saw that the polarization could be written by way of a time-dependent susceptibility. In this subsection, we note that this time dependence can also be absorbed into the dielectric permittivity found in Equation (3.11). In frequency space, it is then usually referred to as the dielectric function  $\varepsilon(\omega)$  defined by

$$\mathbf{D}(\omega) = \varepsilon_0[1 + \chi_e(\omega)]\mathbf{E}(\omega) = \varepsilon_0\varepsilon(\omega)\mathbf{E}(\omega). \quad (3.19)$$

Note that we have defined  $\varepsilon(\omega)$  without a factor  $\varepsilon_0$  so that it is equivalent to the relative permittivity. The dielectric function is an experimentally accessible quantity which characterizes dielectric materials [113]. Its actual size and behavior depends on the material and the frequency range probed. For instance, polar compounds in the condensed phase tend to show recurring structures which can be understood by molecular resonances separated by almost constant regions. An example is shown in



Figure 3.2. The resonances can usually be distinguished by three regimes: rotational excitations which correspond to beam energies in the meV-range, vibrational excitations which occur in the infrared and electronic resonances at visible and UV frequencies in the eV-range [113]. The dielectric function can also be used for solids and we will make use of  $\varepsilon(\omega)$  to model a plasmonic resonance on the surface of a metallic nanoparticle in the next part of the thesis.

The dielectric function has different forms for different frequency regimes and whether or not polarization is caused by reorientation of permanent dipoles, induced dipole moments, molecular excitations or the presence of conductivity [111, 113]. For our purposes, we note Lorentzians as common structures, which we will discuss in more detail in Section 4.3, and the so-called *Debye relaxation* type given by

$$\varepsilon(\omega) = \varepsilon_\infty + \frac{\varepsilon_s - \varepsilon_\infty}{1 - i\omega\tau}. \quad (3.20)$$

Here,  $\varepsilon_s$  gives a constant contribution at zero frequency, whereas  $\varepsilon_\infty$  describes the high (infinite) frequency limit. The form (3.20) assumes the dielectric as a collection of non-interacting dipoles that all relax with the same time scale  $\tau$  and is often used as a simple description for orientational polarization in condensed systems [113, Chapter VIII]. It can be derived with the methods outlined in Part 7 [13] or it can be seen as a phenomenological approach by assuming exponential decay of the polarization on the time scale  $\tau$  [5, Chapter 15.2][113, §53]. This also implies that Equation (3.20) will be valid at frequencies below  $\sim 10^{16}$  Hz [5, pages 50 and 51] where effects from induced dipole moments are practically instantaneous and captured within  $\varepsilon_\infty$ . More involved descriptions and extensions for multiple relaxation times are also possible, such as the Cole-Cole or the Havriliak–Negami formula [113, §55] [118]. An experimentally measured fit for a real dielectric function is provided in the next part (Equation (4.26)) for the dielectric response of water in the terahertz regime [119, 120].

The imaginary part of  $\varepsilon(\omega)$  leads to damping, while the real part changes the phase velocity of an incoming electromagnetic wave. This can be made manifest by noting that the refractive index of a material with  $\mu_r = 1$  can be obtained by [111, 113]

$$n(\omega) = \sqrt{1 + \chi_e(\omega)} = \sqrt{\varepsilon(\omega)} = n'(\omega) + in''(\omega). \quad (3.21)$$

Here, we split  $n$  into its real part ( $n'$ ) and its imaginary part ( $n''$ ), while we note that the index is now frequency-dependent. Insertion of (3.21) into a plane wave, propagating in a direction  $x$  with wave number  $k$ , frequency  $\omega$  and amplitude  $E_0$ , leads to

$$E(x, t) = E_0 e^{ikx - i\omega t} = E_0 e^{-i\omega\left(t - \frac{nx}{c}\right)} = E_0 e^{-i\omega\left(t - \frac{xn'(\omega)}{c}\right) - \frac{2\pi xn''(\omega)}{\lambda_0}}, \quad (3.22)$$

where  $c$  is the speed of light in vacuum. Equation (3.22) describes a wave with a phase velocity  $v_p = c/n'(\omega)$  and exponential damping characterized by  $n''(\omega)$  and the position

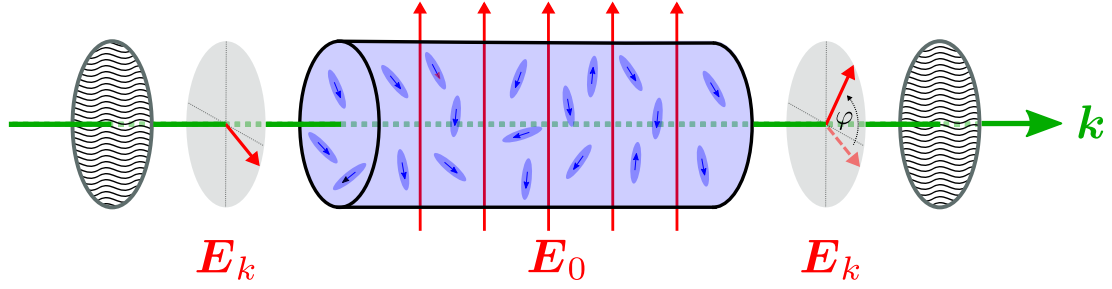


**Figure 3.3:** Schematic depiction of a Kerr cell. A light beam (green arrow) with propagation-direction  $\mathbf{k}$  and electric field  $\mathbf{E}_k$  is sent through a polarizer (gray grates) and enters a cell with a Kerr medium (blue cylinder). Perpendicular to the beam, an electric field  $\mathbf{E}_0$  acts on the medium in the cell and changes the refractive index along its direction. This leads to a change in the polarization of the beam (angle  $\varphi$ ). A second polarizer can now be used to shut out or permit the beam by way of  $\mathbf{E}_0$ .

$x$  in relation to the vacuum wavelength  $\lambda_0$ . The modulus of Equation (3.20) directly leads to the Lambert-Beer law, where the intensity of an electromagnetic wave decays exponentially with the thickness of the sample [111, 113]. In this thesis, the dielectric function  $\varepsilon(\omega)$  will play a prominent role and we will use it extensively to model different environments in our system-bath description.

### 3.1.5 Nonlinear effects and Kerr effect

After discussing the rather simple picture of a linear isotropic dielectric, we will outline a few basics of nonlinear dielectrics in this subsection. In particular, we will discuss the so-called *Kerr effect* which will be a topic in Part 7. As we have seen in Equation (3.18), we treated the response in the linear regime by way of a frequency-dependent susceptibility  $\chi_e(\omega)$ . However, the assumption of linearity is based on comparably weak fields and there is ultimately no reason to think that the response of the material may not follow a more complicated dependence. In order to approximate the behavior for stronger fields, one can straightforwardly extend the polarization to higher orders [49, 116, 117]

$$\begin{aligned} \hat{P}_i(\omega) = & \varepsilon_0 \sum_{j=1}^3 \chi_{ij}^{(1)}(\omega; \omega_1) \hat{E}_j(\omega_1) + \varepsilon_0 \sum_{j,k=1}^3 \chi_{ijk}^{(2)}(\omega; \omega_1, \omega_2) \hat{E}_j(\omega_1) \hat{E}_k(\omega_2) \\ & + \varepsilon_0 \sum_{j,k,l=1}^3 \chi_{ijkl}^{(3)}(\omega; \omega_1, \omega_2, \omega_3) \hat{E}_j(\omega_1) \hat{E}_k(\omega_2) \hat{E}_l(\omega_3) + \dots \end{aligned} \quad (3.23)$$

Here, we omitted the subscript  $e$  such that  $\chi^{(n)}$  labels the expansion coefficient of  $n$ -th order and used  $ijkl$  to label components of vectors and tensors. The equation thus

includes the tensorial nature of susceptibilities and covers anisotropic materials. We did, however, not include summations over perturbations and the like such that Equation (3.23) should still be seen as approximate. Moreover, the equation describes the relationship between monochromatic components of the field, i.e.  $E(t) = \sum_j \hat{E}(\omega_j) e^{i\omega_j t}$ , which means the equation is not directly formulated in frequency space. Nevertheless, Equation (3.23) shows that amplitudes in different directions as well as frequency components of an electric field  $\mathbf{E}$  combine to create the  $i$ -th component of the polarization with frequency  $\omega$ . In principle, this is already the heart of nonlinear optics: the different possibilities of combining frequencies, for instance by summation and subtraction, as well as the coupling of different directions ultimately give rise to a variety of nonlinear effects. For instance, sum-frequency generation is a second-order process which creates the frequency  $\omega$  by way of a simple addition  $\omega = \omega_1 + \omega_2$ . This can be directly exploited in optical setups to create an output beam of desired frequency and direction by combining two appropriate inputs. Other examples include difference frequency generation, self-(de)focusing and the Pockels and Kerr effects. Still, their relative weakness and symmetry considerations restrict the number of important nonlinear effects [116]. Due to phase matching conditions and the high field strengths involved, most applications are also restricted to laser optics where these effects are used to create certain frequencies or shorten the beam. The resulting beams can then be used for such things as signal transduction in optical fibers or LASIK surgeries to improve eyesight. An overview of the various applications can be found in the review by Garmire [121].

The rather simple expansion performed in Equation (3.23) can be motivated by quantum mechanical perturbation theory: coupling to an electric field automatically creates terms in a perturbative expansion that depend inversely on the differences between transition and external driving frequencies. The possible combinations lead to the structures seen in Equation (3.23) at the corresponding orders. It also makes manifest that some effects will be smaller if the associated differences are large. While this argument is sketchy, it directly illuminates that the combinations of frequencies and directions follow from energy and momentum conservation of photons and the transitions involved in the full quantum mechanical treatment. More details and a more involved discussion can be found in the usual literature [49, 116, 117].

In the following, we focus on the *Kerr effect* which we will analyze for liquid water in Part 7. The Kerr effect describes an intensity-dependent correction to the refractive index of the material. This leads to birefringence and a change in the direction of polarization of an incoming beam of light. This was exploited in the past as an ultrafast shutter mechanism by way of the Kerr cell, illustrated in Figure 3.3 [116, 122]. Today, its impact is mostly visible in laser physics, where the Kerr effect can be used for such things as mode locking or to create solitons in optical fibers [116, 123–125]. The Kerr effect is described by a third-order nonlinear polarization such as [116]

$$\hat{P}_x^{\text{KE}}(\omega) \propto \varepsilon_0 \chi_{xxxx}^{\text{KE}(3)}(\omega; \omega', -\omega', \omega) \hat{E}_z(\omega') \hat{E}_z^*(\omega') \hat{E}_x(\omega). \quad (3.24)$$

Here, we have assumed that an (optical) field of frequency  $\omega$  occurs in the  $x$  direction. A second electric field with frequency  $\omega'$  occurs in  $z$ -direction. It is clear from the structure of Equation (3.24), that the intensity of the field in  $z$ -direction changes the refractive index for the field in  $x$ -direction. We can see this explicitly by insertion of Equation (3.24) into Equation (3.1) and using Equation (3.21) for the nonlinear susceptibility. For small changes to the refractive index, we find [116][117, Chapter 4.1]

$$\Delta n \approx \frac{3\chi^{(3)} I_z(\omega')}{2n(\omega')n(\omega)c\varepsilon_0}, \quad (3.25)$$

where  $c$  is the speed of light in vacuum,  $n(\omega)$  the refractive index at the given frequency and  $I_z(\omega')$  is the intensity of the field in  $z$ -direction. We have also omitted the dependencies of  $\chi^{(3)}$  for brevity. The phenomenon described by Equation (3.25) is known as the *optical Kerr effect* (OKE) or the AC Kerr effect [116]. If the driving field is static, that is  $\omega' = 0$ , the change in refractive index is often written as [113, 116]

$$\Delta n = n_{\parallel} - n_{\perp} = n_z - n_x = \lambda_0 K E^2(0), \quad (3.26)$$

with the Kerr constant  $K$  and the probing wavelength  $\lambda_0$  [113, 126]. This case is known as the DC or *static Kerr effect*. Both effects lead to a shift in the polarization of a beam with field components in both  $z$  and  $x$  direction, as depicted in Figure 3.3.

It can be shown that terms of even order in the expansion (3.23) vanish for materials with inversion symmetry [116, 117]. This implies that the Kerr effect is especially important for centrosymmetric materials such as gases, liquids and amorphous solids where second-order contributions are zero [127]. In this case, the OKE can also be used as a spectroscopic method since the Kerr effect is sensitive to reorientational dynamics of molecular dipoles (cf. Part 7). By measuring the OKE response of a substance to an ultrafast driving pulse, one is able to resolve the microscopic dynamics or quantify molecular parameters. OKE spectroscopy is also sensitive to Raman-active intra- and intermolecular modes, making it particularly useful to explore condensed matter systems [128–130]. In Part 7, we present a theoretical description of OKE dynamics based on single-particle rotational diffusion [13, 131] and use it to analyze recent experimental measurements on the *Terahertz Kerr effect* on liquid water [3].

### 3.1.6 Molecular polarizability

Lastly, we introduce the *molecular polarizability*. The molecular polarizability  $\alpha_{\text{mol}}$  defines the relationship between an external electric field and the (induced) dipole moment of a molecule. Again, the simplest case is a linear relationship with the local electric field  $\mathbf{E}_{\text{loc}}$  which gives the field that acts on a single molecule inside a material [111, 117]

$$\mathbf{p}_{\text{mol}} = \alpha_{\text{mol}} \mathbf{E}_{\text{loc}}. \quad (3.27)$$

Note that Equation (3.27) can be easily generalized to the anisotropic case, where  $\alpha_{\text{mol}}$  is promoted to a three-dimensional tensor. By assuming that  $\mathbf{p}_{\text{mol}}$  represents an averaged quantity, Equation (3.27) can be used to obtain the polarization via Equation (3.2). This assumption also permits us to evaluate the local electric field which contains corrections from the difference between the continuum description to the actual field on the molecular level. It can be connected to the macroscopic polarization to yield the so-called *Clausius-Mosotti equation* [111]

$$\alpha_{\text{mol}} = \frac{3\varepsilon_0}{N} \left( \frac{\varepsilon_r - 1}{\varepsilon_r + 2} \right), \quad (3.28)$$

where  $N$  is the number density of molecular dipoles in the material. This result introduces a local-field correction given by an additional factor of  $(\varepsilon_r + 2)/3$  for the linear susceptibility [117]. The Clausius-Mosotti equation can also be rewritten by substituting the refractive index of Equation (3.21) and is then known as the *Lorentz-Lorenz equation*. Furthermore, by comparing Equation (3.18), we can see that we are similarly able to ascribe a time dependence to the molecular polarizability, leading to

$$\mathbf{p}_{\text{mol}}(\omega) = \alpha_{\text{mol}}(\omega) \mathbf{E}_{\text{loc}}(\omega). \quad (3.29)$$

We will exploit the relationship (3.29) in the next chapter to model a polarizable molecule in a driven bath. Next, we note that (3.29) can also be expanded to higher orders, known as *hyperpolarizabilities*. The dipole moment can then be written as [112, 113, 117]

$$\begin{aligned} p_{i,\text{mol}}(\omega) = & \mu_i(\omega) + \sum_{j=1}^3 \alpha_{ij}(\omega; \omega_1) \hat{E}_j(\omega_1) + \sum_{j,k=1}^3 \beta_{ijk}(\omega; \omega_1, \omega_2) \hat{E}_j(\omega_1) \hat{E}_k(\omega_2) \\ & + \sum_{j,k,l=1}^3 \gamma_{ijkl}(\omega; \omega_1, \omega_2, \omega_3) \hat{E}_j(\omega_1) \hat{E}_k(\omega_2) \hat{E}_l(\omega_3) + \dots \end{aligned} \quad (3.30)$$

Here, we wrote the equation for a component  $i$  and introduced the hyperpolarizabilities  $\beta$  and  $\gamma$ . In preparation for our treatment in Part 7, we also included a *permanent molecular dipole moment*  $\mu$ . The advantage of the description in Equation (3.30) lies in the inclusion of local field effects and the focus on molecular quantities in contrast to the macroscopic description in Equation (3.23).

Finally, we introduce a simple modeling prescription for the molecular polarizability usually referred to as the *Lorentz oscillator model* [114, 132]. The model treats the dielectric as a collection of forced and uncoupled harmonic oscillators for the electrons in a molecule and can be seen as a shorthand for the deformation of their electronic cloud. The classical equation of motion for a single electron under a periodic perturbation by a monochromatic electric field follows as [111, 114, 132]

$$m_e \frac{d^2 \mathbf{r}(t)}{dt^2} + m_e \Gamma \frac{d\mathbf{r}(t)}{dt} + m_e \omega_0^2 \mathbf{r}(t) = -e \mathbf{E}_0 e^{-i\omega t}. \quad (3.31)$$

Here,  $m_e$  is the electron mass,  $\mathbf{r}(t)$  the position,  $\Gamma$  a damping factor (for instance from collisions or radiative losses),  $\omega_0$  the frequency of the oscillator and  $\mathbf{E}_0$  the amplitude of the electric field with frequency  $\omega$ . Since a forced oscillator settles into the external frequency after a while, we can set  $\mathbf{r}(t) \approx \mathbf{r}_0 e^{-i\omega t}$  and focus on the particular solution. Insertion yields for the dipole moment

$$\mathbf{p}_{\text{mol}} = -e\mathbf{r}(t) = \frac{e^2 \mathbf{E}_0}{m_e(\omega_0^2 - \omega^2 - i\Gamma\omega)} e^{-i\omega t}, \quad (3.32)$$

which gives the polarizability as

$$\alpha_{\text{mol}}(\omega) = \frac{e^2}{m_e(\omega_0^2 - \omega^2 - i\Gamma\omega)}. \quad (3.33)$$

Note that this derivation assumed that the local field in Equation (3.32) is equal to the external field. Equation (3.33) is an ordinary Lorentzian excitation spectrum with particular resonances of the electronic cloud.  $\alpha_{\text{mol}}(\omega)$  is connected to the dielectric function via Equations (3.18) and (3.19) such that these Lorentzian structures also appear in  $\varepsilon(\omega)$ . Specifically, one finds the *Drude form* [111]

$$\varepsilon(\omega) = 1 + \frac{Ne^2}{\varepsilon_0 m_e} \sum_j \frac{f_j}{\omega_j^2 - \omega^2 - i\Gamma\omega}. \quad (3.34)$$

Here,  $j$  labels the atoms in the dielectric and the variable  $f_j$  describes the so-called oscillator strength which gives the number of electrons with resonant frequency  $\omega_j$ . In a quantum mechanical treatment the  $f_j$  are given by matrix elements of transition dipole moments and the  $\omega_j$  are transition frequencies between states [114, 132]. While the model itself is simplistic, the resulting form of the dielectric function in Equation (3.34) is fairly general and can be specified further for special cases such as conducting metals or liquids like water [111]. We will see examples for both cases in the next part of this thesis.

## 3.2 The Onsager solvation model

In this section, we will discuss the Onsager solvation model and provide a detailed calculation for a simple spherical geometry. We begin by outlining the basic idea behind continuum solvation models and provide a short introduction to the concept. Further reading can be found in the lengthy reviews by Tomasi et al. [133–135], the books by Böttcher [112, 113] and Mennucci and Cammi [136].

### 3.2.1 Continuum solvation models

As implied in Part 2, one of the most important applications for system-bath models is the description of molecules in a solvent. In general, solvent molecules can react to the presence of a polar solute with shielding, electron transfer, distortion of internal charges and chemical bonding, all of which can change the molecular properties or the observed spectra of the solute [5, 112, 137]. This situation is ubiquitous when it comes to liquids and also particularly important for biological systems where proteins and their functional groups are naturally immersed in water or embedded within a specific molecular environment [5, 26]. However, properly treating solution amounts to the evaluation of a quantum mechanical many-body problem which can only be done approximately, if at all [133, 138]. A particularly simple treatment, originally developed by Onsager, Kirkwood and Born [139–141], has proven popular instead: the solvent is described as a continuous dielectric such that a solute interacts with its environment by way of effective electric fields. The solute is modeled as a charge distribution placed inside a cavity, which stands in for the molecular radius. The electric field of the solute polarizes the dielectric, giving rise to a so-called *reaction field* that acts back onto the solute, describing the interaction between the system and its environment. This class of simple (semi-) classical models is known as continuum solvation models [112, 135].

Over the years, such things as the actual shape of the cavity for different molecules (ellipsoidal, spherical, molecule-shaped etc.) [26, 112, 134, 135], its size [112, 142, 143], the detailed charge distribution [134, 135] and various quantum mechanical improvements (of the solute and even by explicitly taking into account a limited number of solvent molecules) have been considered [133, 134, 144]. Continuum solvation models have been used in conjunction with quantum chemical methods to predict molecular parameters such as the dipole moment in solution [144–147], to explain reaction rates of chemical reactions [5, 136], surface enhanced Raman scattering (SERS) [134, 148] or energy transfer in biological systems [26, 52].

Nevertheless, the simplest models still serve as a useful analytical tool to gain physical insight into the impact of solvation on molecular properties. For our purposes, we note that McKenzie et al. [26, 52] used simple spherical geometries in conjunction with spin-boson models as a proxy for the description of relaxation and energy transfer dynamics in biological systems. Recently, the effect of a time-dependent cavity radius coupled to a spin-boson model has also been considered for the solution of certain iron complexes whose solvation shell changes size when the complex switches spin states [149, 150]. Both applications showcase that coupling simple system-bath descriptions and continuum solvation models allows for the construction of useful minimal models which can be connected to experimentally measurable quantities by way of their dielectric properties.

In the following, we derive the effective electric fields for the case of a point dipole in a spherical cavity - a description which we will refer to as the *Onsager model*. We

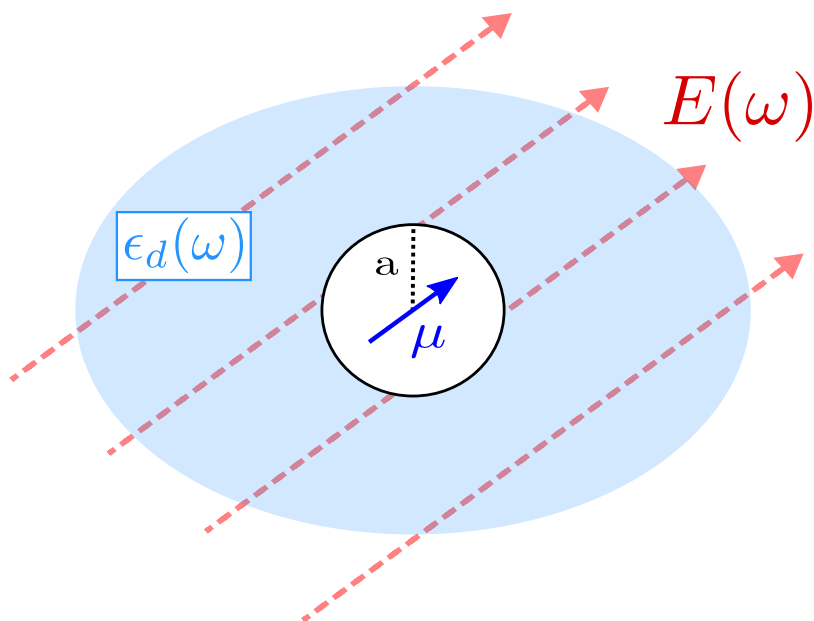


**Figure 3.4:** *The Onsager solvation model. Solvent effects are modeled by a continuum approach where the environment of a molecule is given by an infinite dielectric with dielectric function  $\epsilon_d(\omega)$ . The molecule is represented by a dipole  $\mu(\omega)$  located at the center of a spherical cavity with radius  $a$ . An electric field  $E(\omega)$  acts on the setup. The dipole becomes subject to two field contributions: a reaction field from interaction with the dielectric which leads to damping and a dressed driving field originating from  $E(\omega)$ , known as the cavity field.*

will outline how the emerging fields can be used to quantify the spectral density of Equation (2.26) and we shall see later that they also allow us to quantify the effect of bath-driving contributions. As noted, more complicated cavity shapes can make for more accurate models and additional results for a layered model and an ellipsoidal cavity can be found in Appendix B.

### 3.2.2 Electrostatics for the Onsager sphere

In this subsection, we outline the electrostatic calculation in the Onsager sphere model for vanishing external field. Similar calculations can be found in the literature [111, 112], where our proceedings will largely follow the derivation outlined in a paper by McKenzie and Gilmore [26]. In the original publication by Onsager [141] an external field is also taken into account. This situation is outlined in Part 4, where we will interpret the additional term (the *cavity field*) as an effective bath driving contribution.



We start by assuming a spherical molecule with radius  $a$  and permanent dipole moment  $\mu$ . It is placed inside a dielectric with relative permittivity  $\varepsilon_d(\omega)$ . The molecule itself is assumed to be a cavity in the dielectric with  $\varepsilon_c(\omega) = 1$  and a point dipole located at its center oriented into the  $z$ -direction. This dipole, its direction and the associated forces can then be seen as a minimal model for the behavior of a solvated molecule. The model is depicted in Figure 3.4.

In order to find the dynamics, we neglect any currents and only focus on the impact of the polarization. As discussed in Section 3.1.3, we can then work in frequency space where we only have to solve the Poisson Equation (3.13) in the different dielectric regions. Since we assume that no free charges exist, the problem reduces to the evaluation of the Laplace equation,

$$\Delta\Phi(\mathbf{r}, \omega) = 0, \quad (3.35)$$

at position  $\mathbf{r}$ . The problem has a spherical symmetry so it is advantageous to work in spherical coordinates characterized by the two angles  $\theta$  and  $\varphi$  and the distance from the origin  $r$ . In this case, the Laplace equation can be solved by expanding the potential in a series of spherical harmonics [111]. We have

$$\Phi(r, \theta, \varphi, \omega) = \sum_{l=0}^{\infty} \sum_{m=-l}^{m=+l} \left[ A_{lm}(\omega)r^l + \frac{B_{lm}(\omega)}{r^{l+1}} \right] Y_{lm}(\theta, \varphi), \quad (3.36)$$

where  $Y_{lm}(\theta, \varphi)$  label the spherical harmonics. We can simplify this expansion, as the direction of the dipole imposes a cylindrical (azimuthal) symmetry on the problem such that the dependence on  $\varphi$  vanishes. Equation (3.36) then reduces to

$$\Phi(r, \theta, \omega) = \sum_{l=0}^{\infty} \left[ A_l(\omega)r^l + \frac{B_l(\omega)}{r^{l+1}} \right] P_l(\cos(\theta)), \quad (3.37)$$

where the  $P_l(x)$  are Legendre-polynomials. The corresponding derivative in  $r$ -direction is given by

$$\frac{\partial\Phi(r, \theta, \omega)}{\partial r} = \sum_{l=0}^{\infty} \left[ lA_l(\omega)r^{l-1} - (l+1)\frac{B_l(\omega)}{r^{l+2}} \right] P_l(\cos(\theta)). \quad (3.38)$$

The potential (3.37) can be determined from the boundary conditions of the model. First, the potential has to obey the general boundary conditions (3.14) and (3.15) at the boundary between the two dielectric regions. We find for the potential inside the cavity  $\Phi_c$  and in the dielectric  $\Phi_d$  that

$$\Phi_d(r = a) = \Phi_c(r = a), \quad (3.39)$$

$$\varepsilon_d(\omega) \frac{\partial\Phi_d(\mathbf{r}, \omega)}{\partial r} \Big|_{r=a} = \frac{\partial\Phi_c(\mathbf{r}, \omega)}{\partial r} \Big|_{r=a}. \quad (3.40)$$

Moreover, we assume that the potential has to vanish at infinity and recreates the field of the point dipole near the origin

$$\Phi_d(r \rightarrow \infty) = 0, \quad (3.41)$$

$$\Phi_c(r \rightarrow 0) = \frac{\mu(\omega)}{4\pi\epsilon_0 r^2} \cos(\theta). \quad (3.42)$$

Note that all the boundary conditions in Equations (3.39) to (3.42) depend only on the radial coordinate  $r$ , due to the spherical nature of the boundary. This drastically simplifies the following calculation. We start by noticing that  $P_1(x) = x$  and all Legendre polynomials are linearly independent. This directly leads to the observation that only the  $l = 1$  component of Equation (3.37) is important. Indeed, if we use the conditions (3.41) and (3.42), we directly find

$$A_1^d(\omega) = 0, \quad B_1^c(\omega) = \frac{\mu(\omega)}{4\pi\epsilon_0}, \quad A_{l \neq 1}^d(\omega) = 0, \quad B_{l \neq 1}^c(\omega) = 0. \quad (3.43)$$

Here,  $c$  and  $d$  label the coefficients for the corresponding potentials. If we insert the coefficients for  $l \neq 1$  into the conditions (3.39) and (3.40) we quickly obtain that  $B_{l \neq 1}^d = 0$  and  $A_{l \neq 1}^c = 0$ , as well. Therefore, we only need to consider the two equations for the radial coefficients with  $l = 1$ , given by

$$A_1^c(\omega)a + \frac{\mu(\omega)}{4\pi\epsilon_0 a^2} = \frac{B_1^d(\omega)}{a^2}, \quad (3.44)$$

$$\left[ A_1^c(\omega) - 2\frac{\mu(\omega)}{4\pi\epsilon_0 a^3} \right] = -2\epsilon_d(\omega) \frac{B_1^d(\omega)}{a^3}. \quad (3.45)$$

Combining (3.44) and (3.45) quickly leads to

$$B_1^d(\omega) = \frac{\mu(\omega)}{4\pi\epsilon_0} \left[ \frac{3}{2\epsilon_d(\omega) + 1} \right], \quad (3.46)$$

$$A_1^c(\omega) = -2\frac{\mu(\omega)}{4\pi\epsilon_0 a^3} \chi_o(\omega), \quad (3.47)$$

where we have defined the frequency-dependent *Onsager susceptibility*,

$$\chi_o(\omega) = \frac{\epsilon_d(\omega) - \epsilon_c(\omega)}{2\epsilon_d(\omega) + \epsilon_c(\omega)} = \frac{\epsilon_d(\omega) - 1}{2\epsilon_d(\omega) + 1}. \quad (3.48)$$

Insertion of (3.45) and (3.46) then yields for the potential inside the cavity

$$\Phi_c(r, \theta, \omega) = \frac{\mu(\omega)}{4\pi\epsilon_0 r^2} \cos(\theta) - \left[ \frac{\mu(\omega)}{2\pi\epsilon_0 a^3} \chi_o(\omega) \right] r \cos(\theta). \quad (3.49)$$

Equation (3.49) has two contributions: the first one gives the field of the dipole itself while the latter describes an effective field pointing along the direction of the dipole. It is caused by the reaction of the dielectric to  $\mu(\omega)$  and is therefore referred to as the *reaction field*. In the next subsection, we show that this leads to damping and can be directly compared to the terms that arose in Part 2.

### 3.2.3 Connection to system-bath models

The reaction field in Equation (3.49) implies a force in the  $z$ -direction. In the time domain, the component along  $z$  can be easily calculated as

$$\begin{aligned} QE_z(t) &= Q \int_{-\infty}^t dt' \chi_o(t-t') \frac{\mu(t')}{2\pi\epsilon_0 a^3} \\ &= q(t)\gamma(0) - \int_{-\infty}^t dt' \gamma(t-t') \frac{dq(t')}{dt'}, \end{aligned} \quad (3.50)$$

where  $Q$  is the separated charge of the dipole and  $q(t)$  its (time-dependent) length. To obtain the second equality, we have performed a partial integration with  $\gamma(t)$  defined as

$$\gamma(t) = \frac{Q^2}{2\pi\epsilon_0 a^3} \int_t^{\infty} dt' \chi_o(t'). \quad (3.51)$$

As we can see, Equation (3.50) creates an effective damping term characterized by the damping-kernel in (3.51). In this way, the structure of the Onsager model automatically leads to terms similar to those found in the quantum Langevin Equation (2.21). In fact, we can directly argue that the susceptibility  $\chi_o(\omega)$  defined in Equation (3.48) can be seen as the environmental response of Equation (2.33). This allows us to derive the corresponding spectral density by taking the imaginary part as per Equation (2.36). We directly see that

$$J(\omega) = \frac{Q^2}{2\pi\epsilon_0 a^3} \text{Im}[\chi_o(\omega)]. \quad (3.52)$$

Hence, we have now directly modeled an environment through its experimentally accessible dielectric function  $\epsilon(\omega)$ . We will use this connection extensively throughout this thesis. Finally, we note that the partial integration in (3.50) introduces an additional term which acts as a potential renormalization by  $\gamma(0)$  if the potential is harmonic. This is the static response of the dielectric to the dipole in the cavity, similar to the potential renormalization obtained in the Caldeira-Leggett model of Section 2.2.1. It can also be treated by defining an appropriate counter-term.

Finally, we emphasize that the equivalence in this section holds because we effectively considered a one-dimensional model by aligning the dipole to the  $z$ -direction

and the spherical cavity creates a cylindrical symmetry. If this is not the case, the direction of the dipole and its relative orientation to the cavity has to be considered. This case is discussed briefly in Boettcher [112, Chapter IV] and also implies that a proper connection to a system-bath model can only be made in such a case if the system-bath description is extended to multiple spatial dimensions.

### **3.3 Driven dissipative quantum systems**

In this section, we discuss dissipative quantum systems under the influence of external driving forces. Since the field itself is vast and general features are hard to identify, we will largely stick to a presentation of a few selected methods. Nevertheless, the tools we develop in this part of the thesis will suffice for our analysis in the next chapters. We start this section with a brief introduction to driven dissipative quantum systems, based on the review by Grifoni and Hänggi [32] where a more detailed discussion can be found. Afterwards, we present the dipolar coupling of a classical field to a quantum system and proceed to discuss its impact on transition probabilities. In the next two subsections we present two particular methods, namely linear response theory and the optical Bloch equations. The former is a general scheme for weakly driven systems while the latter takes dissipation into account explicitly. We close this part with a short description of Floquet theory which is an important tool for periodically driven problems. Since we will mostly look at the example of a driven two-state system (TSS) throughout, our focus will implicitly lie on the spin-boson model. The content on driven systems is largely taken from the books by Meystre and Sargent [49], Boyd [117] and Shankar [61], whereas the dissipative aspects include content from the books by Nitzan, Weiss and Caldeira [5, 31, 33]

#### **3.3.1 General features**

A general approach to driven quantum systems is to study the different time scales of the problem. In order to illustrate this idea, it is useful to consider the simple example of a classical harmonic oscillator under the influence of (sufficiently small) damping and a sinusoidal driving force. Assuming that the oscillator is initially dislocated from its rest position, it will start to swing in some manner before it eventually settles into an oscillation determined by the external perturbation alone. The latter is what is usually referred to as a steady-state, which labels a dynamic equilibrium situation [5]. This happens because the homogeneous solution is exponentially damped while the inhomogeneous part has an amplitude with a Lorentzian structure [63]. For earlier times, both contributions mix and lead to a comparably complicated behavior. For the case of a slowly varying force, the undriven frequency determines the initial time-evolution. All in all, we can see the influence of three distinct time scales: one associated with the frequency of the undriven system, another with the external perturbation

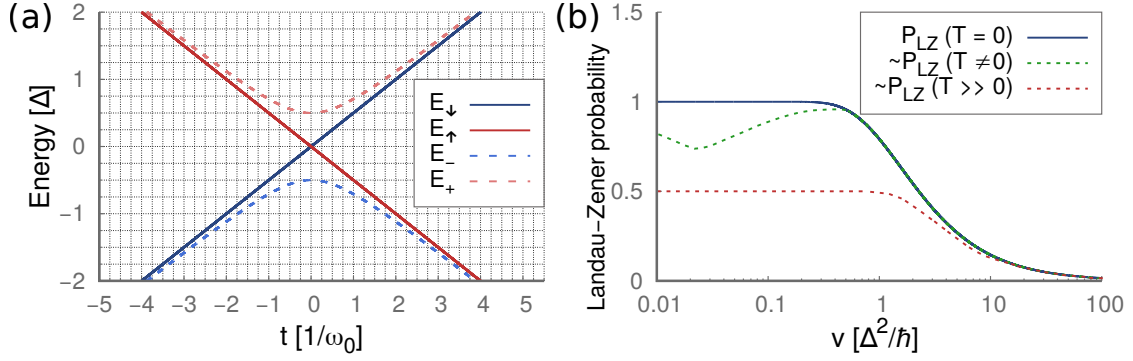


**Figure 3.5:** Energies and transition probabilities in the Landau-Zener-Stückelberg model. (a) Eigenenergies of the two-state system of Equation (2.46) in the Landau-Zener model where  $\epsilon(t) = vt$ . For vanishing  $\Delta$ , the eigenstates are those of  $\sigma_z$  and the energies of the two states  $E_{\uparrow,\downarrow} = \mp vt/2$  (solid lines) cross. If  $\Delta \neq 0$ , the eigenstates are different and their energies  $E_{\pm} = \pm\sqrt{\Delta^2 + (vt)^2}/2$  show an avoided crossing structure (dotted lines). In the infinite past and future both descriptions overlap as  $\Delta$  becomes negligible to  $\epsilon(t)$ . In order to stay in the ground state, the system has to switch states. (b) Landau-Zener probability for the system to stay in the ground state  $P_{LZ}$  versus the velocity  $v$ . Faster speeds result in a suppression. When dissipative effects are included, the probability shows a strong temperature dependence (dotted lines). Note that the probabilities for non-zero temperature are only rough sketches (denoted by a tilde) based on the results in Nalbach and Thorwart [151] where the associated numerical results can be found.

and lastly the time scale of the damping process. Their competition gives rise to the different regions seen in the dynamics.

In the quantum case similar arguments can often be made. The prototypical example is the so-called *Landau-Zener-Stückelberg model* [5, 32, 152–154]. Here, a two-state system is subject to a driving force linear in time. This can, for instance, serve as a toy model for the progression of a reaction coordinate or a collision process between two molecules [5, Chapter 2.4]. Within the TSS description of Equation (2.46) the force couples to the bias energy such that  $\epsilon(t) = vt$ . The energy spectrum over time is depicted in panel (a) of Figure 3.5. Assuming that the system is in the ground state of  $\sigma_z$  in the far past, one usually asks about the probability of finding the system in the ground state in the far future. Because the energy of the two states change and eventually cross, this requires the system to switch states. It turns out, that this probability depends exponentially on the value  $\Delta/|v|$  where larger speeds suppress the probability for a transition [5, 151]. This is shown in Figure 3.5 panel (b). One may imagine, that the system exhibits typical quantum beats when  $\epsilon(t)$  becomes comparable to  $\Delta$ . If  $\epsilon(t)$  changes too quickly, the system does not have enough time to “beat” and the system is trapped in the state it started in and ends up in the excited state. In turn, slower speeds allow for the system to switch into the new ground state.

When adding dissipative effects to the Landau-Zener model its dynamics become more complicated. Initially, the system is in the ground state such that it can interact with the bath only when thermally populated bath modes are available whose energy correspond to the momentary splitting energy. The characteristic time scale of this interaction then depends on the temperature, the cutoff frequency and the velocity  $v$  [151]. Most importantly, the bath leads to relaxation and the competition between the two time scales determines the change in probability. For low temperatures, the resonant time scale is fairly small such that the impact of the bath is restricted to lower speeds. In fact, the transition probability exhibits a clear dent, showing that comparably slow driving gives the system enough time to equilibrate during the crossing. For faster speeds, the effect becomes negligible and the exponential decay is restored. For higher temperatures, the dent grows more and more pronounced until the curve becomes essentially flat at the equilibrium value up to very high speeds [83, 151]. A stronger coupling strength does not invalidate this simple analysis and can be roughly explained by the same mechanism [151].

In contrast to this rather simplistic approach, systems can show highly nontrivial effects when both driving and dissipation is present. For instance, tunneling problems can exhibit resonances in a driven steady-state for particular values of the relaxation strength, called *quantum stochastic resonances* [32, Chapter 3.2.2]. Driving can also completely suppress tunneling in what is known as *coherent destruction of tunneling* [32, Chapter 3.2.2] (cf. Section 2.2.2). All examples we mentioned, showcase that the interaction between driving and dissipation can strongly impact the dynamics of a system. However, more general features are hard to identify which is why we now turn to the actual description of driven and driven dissipative systems in the following.

### 3.3.2 Dipolar coupling to a time-dependent electric field

The interaction of a quantum system with an electric field can be quickly obtained by canonical quantization. In particular, we can couple an electric field to a dipole moment by recalling the appropriate energy term [5, 49]

$$H_{\text{int}}(t) = -\boldsymbol{\mu} \cdot \mathbf{E}(t). \quad (3.53)$$

Here, the dipole moment  $\mu$  is now promoted to an operator while the field  $E(t)$  is still a function. This is a semiclassical ansatz as the field itself has to be quantized for a true quantum description. It turns out that the electromagnetic field can be described by a bath of harmonic oscillators [33, 155]. For this reason, system-bath descriptions are also ubiquitous in quantum optics (see, e.g., [49, 64]).

However, we will stick to a semiclassical description in this thesis which can be used for fields of high intensity where the number of photons is large [5, 49]. Per definition, Equation (3.53) also merely recreates the interaction with a dipole and not with higher

moments which can play a role in more complicated charge distributions. However, the dipolar case is the term of lowest order and we will only use dipolar coupling schemes throughout this thesis.

Still, the question of how exactly a quantum system exhibits a dipole moment remains. For a simple one-dimensional dipole of one elementary charge, we may write the dipole operator as  $\mu = ex$  with position operator  $x$ . We can rewrite the position by way of creation and annihilation operators in the case of a harmonic oscillator. In this case, it directly follows that only matrix elements between two different energy eigenstates are non-zero (Equation (A.7)). For a two-state system representing the two lowest states, this implies that only non-diagonal elements of the density matrix  $\rho$  can contribute in this basis. We find [49]

$$\langle \mu(t) \rangle = \text{Tr}[\mu(t)\rho] = \mu_{12}\rho_{12} + \mu_{21}\rho_{21}, \quad (3.54)$$

where  $|1\rangle$  designates the lower and  $|2\rangle$  the higher-lying state with subscripts denoting the associated matrix elements. In this way, we can see that a coupling of dipolar type (3.53) couples to transitions and we can include the coupling to the spin-boson model of Equation (2.46) by making the asymmetry  $\epsilon$  of the system time-dependent

$$H_S(t) = \frac{\Delta}{2}\sigma_x + \frac{\epsilon(t)}{2}\sigma_z. \quad (3.55)$$

Comparison with Figure 2.4 implies that the coupling changes the difference in energy between the two ground states of a double well. In general, driving can also occur in the tunnel coupling which is related to a modulation of the barrier height [32]. In practice, driving of  $\Delta$  or  $\epsilon$  is chosen according to the underlying physical system. For our purposes, we will largely stick to the case of a time-dependent  $\epsilon$ .

Nevertheless, a direct consequence of Equation (3.55) is already visible: since driving induces transitions by changing the eigenstates and eigenenergies of the two-state system, we can expect that an initial state will likely not be an eigenstate to the momentary system. This implies that the state becomes a superposition of momentary eigenstates such that some kind of quantum beat must occur as per our discussion in Sections 2.1.2 and 2.2.3. We will see an example of this in the following.

### 3.3.3 Transition probabilities of a driven two-state system

In quantum optics, a particularly interesting quantity are transition probabilities which give the time-dependent probability of a transition between states induced by an external driving field. In general, this is done by evaluating the expansion coefficients of a wave-function  $|\Psi(t)\rangle$ . In case of a two-state system, we can write

$$|\Psi(t)\rangle = c_1(t)|1\rangle + c_2(t)|2\rangle = C_1(t)e^{-i\omega_1 t}|1\rangle + C_2(t)e^{-i\omega_2 t}|2\rangle, \quad (3.56)$$

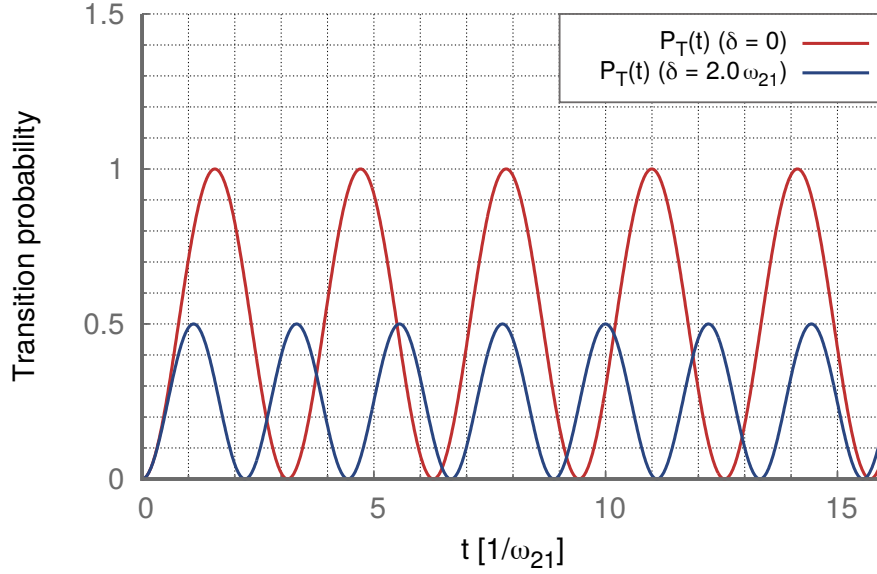


**Figure 3.6:** Transition probability as predicted by the Rabi formula of Equation (3.61) for two values of the detuning  $\delta$  and a Rabi frequency of  $R_0 = 2\omega_{21}$ . The Rabi formula predicts periodic oscillations of the transition probability depending on time or on the length of a rectangular pulse. At resonance, the system can be fully excited for certain pulse lengths (red curves). For nonzero detuning, the amplitudes become smaller and the oscillations become more rapid (blue curves).

where  $c_n(t) = \langle n | \Psi(t) \rangle$  are probability amplitudes and  $|n\rangle$  are the energy eigenstates. The second equation redefined the expansion coefficients as  $C_n(t)$  which include a phase based on the eigenenergies  $\hbar\omega_n$ . This amounts to a formulation in the interaction picture. To get a transition probability, we have to assume that the system is initially in the lowest energy state, i.e.,  $c_1(0) = C_1(0) = 1$ . The transition probability can then be obtained by solving the Schrödinger equation for the coefficients and taking their modulus squared as

$$P_T = |c_2(t)|^2 = |C_2(t)|^2 = 1 - |c_1(t)|^2 = 1 - |C_1(t)|^2. \quad (3.57)$$

However, even for two-state systems, analytic solutions for arbitrary driving pulses do not exist. Notable exceptions are rectangular pulses and monochromatic fields for which exact solutions can be derived. Approximate solutions have also been developed for Gaussian and similarly shaped pulses. In the following, we give a few results within the so-called rotating-wave approximation and first-order perturbation theory to showcase the general behavior for a monochromatic beam. This part will be based on the presentation in Meystre and Sargent [49]. In the second part, we give approximate results for more involved driving schemes.



### Monochromatic driving

We start with results for sinusoidal driving, derived using first-order time-dependent perturbation theory. The Hamiltonian is assumed to consist of a time-independent part and a time-dependent perturbation  $H = H_0 + V(t)$ . The interaction has the form

$$V(t) = V_0 \cos(\omega_e t) = \frac{\mu E_0}{2} (e^{i\omega_e t} + e^{-i\omega_e t}), \quad (3.58)$$

where  $\omega_e$  is the external driving frequency,  $V_0$  is a time-independent operator and also includes factors which determine the strength of the interaction. The second equation translates this into the language of the simple dipolar coupling introduced in (3.53) with dipole operator  $\mu$  and field strength  $E_0$  where the field has been assumed to occur parallel to the dipole moment. An iterative integration of the Schrödinger equation yields in first order of  $V$  [49]:

$$C_2(t) \approx -i \frac{V_{21}}{2\hbar} \left[ \frac{e^{i(\omega_{21} + \omega_e)t} - 1}{i(\omega_{21} + \omega_e)} + \frac{e^{i(\omega_{21} - \omega_e)t} - 1}{i(\omega_{21} - \omega_e)} \right], \quad (3.59)$$

where  $\omega_{21} = \omega_2 - \omega_1$  and  $V_{21} = \langle 2|V_0|1\rangle$ . The structure of (3.59) has two contributions which depend on the sum and the difference of the transition and the external driving frequency. When  $\omega_{21} \approx \omega_e$  one can neglect the first term in favor of the latter to obtain the transition probability as

$$P_T = |C_2(t)|^2 \approx R_0^2 \frac{\sin^2\left[(\omega_{21} - \omega_e)\frac{t}{2}\right]}{(\omega_{21} - \omega_e)^2}. \quad (3.60)$$

Here, we used Equation (3.58) to define  $R_0 = \mu_{12}E_0/\hbar$  as the so-called *Rabi flopping frequency* and wrote  $\mu_{21}$  for the matrix element of the dipole-moment operator [49, Chapter 3.2 and 3.3]. As we suspected, Equation (3.60) shows that the field rotates the TSS eigenstates with a certain period. Because we evaluated  $C_2(t)$ , we obtain periodic maxima and minima when they are either parallel or perpendicular to the excited state of the unrotated system. This means that the two-state system shows a coherent phase relationship with the external perturbation. At this stage, we can also easily include the effect of more states by introducing an integration over possible splitting frequencies with a corresponding weight function - a spectral density. One ends up with golden rule rates from Section 2.1.1 for a well-peaked structure and slowly varying density of states [49, Chapter 3.2]. It is also possible to include damping in a phenomenological way, which leads to an additional exponential damping term  $\exp(-\gamma t)$  in Equation (3.60). Such a damping process then defines relaxation to low-lying states which do not take part in the two-state dynamics we consider [49, Chapter 4.1].

Result (3.60) is valid for weak perturbations and for the case of working near resonance. The latter assumption is referred to as the *rotating-wave approximation*

(RWA) which argues that rapidly oscillating terms in the dynamics can be neglected. A non-perturbative result can also be derived on the basis of the RWA alone, where the counter-rotating terms are neglected already in the perturbation (3.58). One finds [49, Chapter 3.3]

$$P_T = |C_2(t)|^2 \approx \frac{R_0^2}{R_0^2 + \delta^2} \sin^2 \left[ \sqrt{R_0^2 + \delta^2} \left( \frac{t}{2} \right) \right]. \quad (3.61)$$

Equation (3.61) is referred to as the *Rabi formula* with the detuning,  $\delta = \omega_{21} - \omega_e$ , quantifying the difference to resonance conditions. The Rabi formula exhibits the same  $\sin^2$  dependence as Equation (3.60) but also predicts a dependence of the frequency on the field strength. This behaviour is known as *Rabi oscillations* [156, 157], which are shown exemplarily in Figure 3.6 for two values of  $\delta$ .

Before proceeding, we note that the result (3.59) also underscores the reasoning done in Section 3.1.5 for a finite number of nonlinear optical effects per order. For more than two states, terms as in (3.59) appear where the transition frequencies are given by combinations between the different levels. Only those combinations that fit to the external frequency will be relevant and the rest can be neglected [116].

### ***Pulsed driving***

Up until now, we have only considered monochromatic driving with a practically infinite duration. We now focus on the behavior of pulse-shaped driving, which is highly relevant for many state-of-the-art laser applications and for the preparation of quantum states. Hence, this subject has also been a focus of extended research over the years [156–159] and we will outline some simple results here.

We start by noting that pulses usually include a carrier frequency which gives rise to a distinct plane-wave [51]. This allows us to use the description (3.58) and apply the RWA. The remaining time-dependent profile is then absorbed into a time-dependent Rabi frequency  $R(t) = R_0 f(t)$  with a pulse-shape function  $f(t)$ . For resonant driving, such that  $\delta = 0$ , the population transfer after conclusion of the pulse is determined by the area of the pulse alone. Specifically [156],

$$P_T = \sin^2 \left( \frac{A}{2} \right), \quad (3.62)$$

with the pulse-area

$$A = R_0 \int_{-\infty}^{\infty} dt f(t). \quad (3.63)$$

For a rectangular pulse, where  $R(t) = R_0$  in an interval  $0 \leq t \leq T$ , the Rabi formula (3.61) is recovered with time  $t$  replaced by the duration of the pulse  $T$ . This

is valid even for nonzero detuning [157]. The squared sine dependence on the area of (3.62) shows that the transition probability will be maximized for rectangular pulses when  $R_0 T = \pi$ . Pulses that reach maximum population transfer are therefore known as  $\pi$ -pulses [157].

As noted previously, analytic solutions in the RWA for arbitrary pulse-shape functions with non-zero detuning do not exist. A notable exception is a sech-shaped pulse which multiplies an additional factor of  $\sim \text{sech}^2(A\delta/2R_0)$  to Equation (3.62) [156, 160, 161]. For other bell-shaped pulses, Rabi oscillations persist while the amplitude of the transition probability and the location of the zeroes depend on the exact behavior of the pulse-wings and the activation and deactivation behavior of the pulse [156, 157]. We are most interested in Gaussian pulses, for which approximate solutions have been found [157, 159, 161]. In particular, for large  $\alpha = R(t)/\delta$  an involved approximation scheme yields an additional factor  $\sim \text{sech}^2(s[\ln(\alpha)]^{-1/2})$  multiplied to a squared sine with a detuning and pulse length dependent factor  $s$  [161]. This predicts Rabi oscillations but also a slow growth for the amplitude for smaller detuning or larger driving strength, which is also seen experimentally and numerically [156, 159, 161]. Finally, we note that pulse-shaped driving is often treated on the basis of a time-dependent rotation into a momentary eigenbasis (the so-called adiabatic basis) where we will see an example of in Part 5 (see e.g. [157]).

### 3.3.4 Linear response theory

A particularly easy method to analyze time-dependent quantum systems is given by way of linear response theory. In linear response, the time-dependent perturbation is assumed to be weak such that any deviations are linear in its strength. This permits us to find the lowest order corrections to expectation values of observables. Note that this method is based on the density matrix formalism and is therefore applicable to mixed states as well. Our presentation in the following is taken largely from the book by Nitzan [5, Chapter 11].

We start by assuming that the Hamiltonian of a quantum system can be split into a bare part  $H_0$  and a time-dependent perturbation  $V(t)$ . The Liouville equation of motion is then given by

$$\frac{\partial \rho(t)}{\partial t} = \frac{i}{\hbar} [H_0 + V(t), \rho(t)], \quad (3.64)$$

where  $\rho(t)$  is the density matrix of the system under study. We now assume the system to be in thermal equilibrium before  $V(t)$  is activated by setting

$$\rho(-\infty) = \rho^{\text{eq}} = \frac{e^{-\beta H_0}}{\text{Tr} e^{-\beta H_0}}. \quad (3.65)$$

Here,  $\beta$  gives the inverse temperature. We can progress similarly to the derivation of the master equation in Section 2.3.1 and formally integrate Equation (3.64). We then

approximate  $\rho(t) \approx \rho^{\text{eq}}$  at first order to find

$$\rho(t) = \rho^{\text{eq}} - \frac{i}{\hbar} \int_{-\infty}^t dt' e^{-\frac{i}{\hbar} H_0(t-t')} [V(t'), \rho^{\text{eq}}] e^{\frac{i}{\hbar} H_0(t-t')}. \quad (3.66)$$

We can now use Equation (3.66) to derive the change in an observable  $\mathcal{O}$ . To do this, we note that  $\langle \mathcal{O}(t) \rangle = \text{Tr}[\mathcal{O}\rho(t)]$  and obtain after a few manipulations [5]

$$\langle \mathcal{O}(t) \rangle - \langle \mathcal{O} \rangle^{\text{eq}} = -\frac{i}{\hbar} \int_{-\infty}^t dt' \text{Tr}[\delta\tilde{\mathcal{O}}(t-t') [V(t'), \rho^{\text{eq}}]], \quad (3.67)$$

where  $\delta\mathcal{O} = \mathcal{O} - \langle \mathcal{O} \rangle^{\text{eq}}$ . The tilde denotes the interaction picture. For simplicity we now assume that  $V = -AF(t)$ , where  $F(t)$  is a time-dependent function and  $A$  is a system operator. This choice mimics the dipolar coupling of Equation (3.53). By reordering, we finally obtain

$$\begin{aligned} \langle \mathcal{O}(t) \rangle - \langle \mathcal{O} \rangle^{\text{eq}} &= \frac{i}{\hbar} \int_{-\infty}^t dt' \langle [\delta\tilde{\mathcal{O}}(t-t'), A] \rangle^{\text{eq}} F(t') \\ &= \int_{-\infty}^{\infty} dt' \chi_{\mathcal{O}A}(t-t') F(t'). \end{aligned} \quad (3.68)$$

Here, the expectation value  $\langle [\delta\tilde{\mathcal{O}}(t-t'), A] \rangle^{\text{eq}}$  was combined into the susceptibility  $\chi_{\mathcal{O}A}(t-t')$  in the last equation, which is sometimes also written as the *retarded Green's function*  $G(t, t')$  (cf. Equation (4.20)). Note that both imply causality.

We achieved two things at this stage: First, the time dependence of an observable is now encoded in an integral over an equilibrium average, which can be easily calculated. Any deviation from equilibrium is only linearly dependent on the strength of the perturbation  $F(t)$ , which implies weak perturbations of the equilibrium state of the system. Second, we have now rather belatedly shown the typical linear response structure we have already seen in Part 2 (e.g. in Equations (2.20) and (2.33)) and we directly argued for when discussing the time-dependent polarization in Equation (3.17). However, we should note that Equation (3.68) also assumes an equilibrium distribution such that a dependence on  $t-t'$  arises in the argument. We will calculate linear response spectra in the next chapters.

### 3.3.5 Optical Bloch equations

The next method we discuss is known as the optical Bloch equations. In contrast to the simple perturbative approach in the last subsection, the Bloch equations couple driving with a Born-Markov master equation treatment and can thus naturally include damping and dephasing (decoherence) within the description. The presentation here is based on the books by Nitzan [5, Chapter 10] and Cohen-Tannoudji et al. [64, Chapter V].

In principle, we already have all that we need to extend the master equation treatment of Section 2.3.1 with driving terms. To see this, we note that for a two-state system Equations (2.66) and (2.68) become

$$\dot{\rho}_{11}(t) = \Gamma \rho_{22}(t), \quad (3.69)$$

$$\dot{\rho}_{22}(t) = -\Gamma \rho_{22}(t), \quad (3.70)$$

$$\dot{\rho}_{12}(t) = i\omega_r \rho_{12}(t) - (\Gamma/2) \rho_{12}(t), \quad (3.71)$$

$$\dot{\rho}_{21}(t) = -i\omega_r \rho_{21}(t) - (\Gamma/2) \rho_{21}(t), \quad (3.72)$$

where we set the backward rate  $\Gamma_{1 \rightarrow 2}$  to zero and used  $\Gamma_{12} = \Gamma_{21} = \Gamma/2$  with  $\Gamma_{2 \rightarrow 1} = \Gamma$ . We also wrote  $\dot{x}(t) = dx(t)/dt$  as a shorthand and used  $\rho(t)$  for the reduced density matrix of the system. The frequency shifts from the interaction with the bath were included in the renormalized two-level frequency  $\omega_r$ . Equations (3.69) to (3.72) manifestly fulfill conservation of probability as  $\dot{\rho}_{11} + \dot{\rho}_{22} = 0$  and Hermiticity as  $\dot{\rho}_{12} = \dot{\rho}_{21}^*$ .

As master equations recreate the effect of a bath, it is straightforward to include driving via a macroscopic field as per Equation (3.55). Specifically, for a monochromatic beam where  $\varepsilon(t)/2 = \mu E_0 \cos(\omega_e t)$ , we can use the Liouville equation to obtain driving terms such as

$$\dot{\rho}_{11}(t) \propto -iR_0 \cos(\omega_e t) [\rho_{21}(t) - \rho_{12}(t)], \quad (3.73)$$

with the Rabi frequency  $R_0 = \mu_{12} E_0 / \hbar$ . We can simplify further by using the rotating-wave approximation, as described in Section 3.3.3, and neglect rapidly oscillating terms. Equation (3.73) then turns into

$$\dot{\rho}_{11}(t) \propto -iR_0 [e^{i\omega_e t} \rho_{21}(t) - e^{-i\omega_e t} \rho_{12}(t)]. \quad (3.74)$$

Results for terms in  $\dot{\rho}_{21}(t)$  follow similarly. Insertion into Equations (3.69) to (3.72) then yields the so-called *optical Bloch equations*

$$\dot{\tilde{\rho}}_{11}(t) = -i(R_0/2) [\tilde{\rho}_{21}(t) - \tilde{\rho}_{12}(t)] + \Gamma \tilde{\rho}_{22}(t), \quad (3.75)$$

$$\dot{\tilde{\rho}}_{22}(t) = i(R_0/2) [\tilde{\rho}_{21}(t) - \tilde{\rho}_{12}(t)] - \Gamma \tilde{\rho}_{22}(t), \quad (3.76)$$

$$\dot{\tilde{\rho}}_{12}(t) = i\delta \tilde{\rho}_{12}(t) - i(R_0/2) [\tilde{\rho}_{22}(t) - \tilde{\rho}_{11}(t)] - (\Gamma/2) \tilde{\rho}_{12}(t), \quad (3.77)$$

$$\dot{\tilde{\rho}}_{21}(t) = -i\delta \tilde{\rho}_{21}(t) + i(R_0/2) [\tilde{\rho}_{22}(t) - \tilde{\rho}_{11}(t)] - (\Gamma/2) \tilde{\rho}_{21}(t). \quad (3.78)$$

Here, we have switched to a rotating frame by defining  $\tilde{\rho}_{12}(t) = \rho_{12}(t)e^{-i\omega_e t}$  and  $\tilde{\rho}_{21}(t) = \rho_{21}(t)e^{i\omega_e t}$ , while  $\tilde{\rho}_{11}(t) = \rho_{11}(t)$  and  $\tilde{\rho}_{22}(t) = \rho_{22}(t)$ . This also introduces the detuning, defined as in Section 3.3.3 as  $\delta = \omega_r - \omega_e$ . As every Hermitian two-by-two

matrix can be constructed from the three Pauli matrices and the identity, Equations (3.75) to (3.78) can be rewritten for the Pauli matrices to yield

$$\frac{d}{dt}\langle\sigma_z(t)\rangle = -\delta\langle\sigma_y(t)\rangle - (\Gamma/2)\langle\sigma_z(t)\rangle, \quad (3.79)$$

$$\frac{d}{dt}\langle\sigma_y(t)\rangle = \delta\langle\sigma_z(t)\rangle - R_0\langle\sigma_x(t)\rangle - (\Gamma/2)\langle\sigma_y(t)\rangle, \quad (3.80)$$

$$\frac{d}{dt}\langle\sigma_x(t)\rangle = R_0\langle\sigma_y(t)\rangle - \Gamma\langle\sigma_x(t)\rangle - (\Gamma/2). \quad (3.81)$$

Note that we have used our convention for the spin-boson model (3.55) and exchanged  $\sigma_z$  and  $\sigma_x$  in contrast to the literature results [5, Chapter 10.5.2][64, Chapter V.A.4].

The Bloch equations are valid near resonance due to the rotating wave approximation but also assume comparably slow driving by way of  $R_0 \ll \omega_r$  which also follows from the comparably fast decay of correlations in the reservoir. This constraint originates from the fact that any modifications of the transition rates  $\Gamma$  due to driving are neglected in this treatment [64]. In contrast to the master equation results, couplings between coherences and populations exist in Equations (3.75) to (3.78) such that the result cannot be formulated purely by transition rates between the two states (cf. Equation (2.66)) [64]. Instead, the typical dynamics associated with the Bloch equations depend on the competition between the driving and damping - much as we argued in Section 3.3.1. In the simplest case, where  $\delta = 0$  and damping is strong such that  $\Gamma \gg R_0 \rightarrow 0$ , one obtains exponential damping determined by  $(1/2)\Gamma$  and  $\Gamma$ . In the opposite regime, where  $\Gamma \ll R_0$ , the system oscillates with the Rabi frequency in addition to damping with  $(3/4)\Gamma$  and  $(1/2)\Gamma$ . In addition, steady state solutions can be found which predict a Lorentzian structure about  $\delta$  with half-width  $\sqrt{(\Gamma^2/4) + (R_0^2/2)}$ . Moreover, the population of the upper state is proportional to  $R_0^2/4$  which shows that very intense pulses will merely equalize the two levels [64].

In Part 5, we will explicitly derive Bloch equations for a driven bath on the basis of an adiabatic treatment of the driving processes. Ultimately, we obtain results similar to Equations (3.79) to (3.81) but with time-dependent rates.

### 3.3.6 Floquet theory

In addition to the two methods outlined, we mention Floquet theory as an important approach for the analysis of problems involving external driving forces. In Floquet theory, the external perturbation is assumed to be periodic in time, for instance from a monochromatic field or a pulsed laser. The wavefunction of the quantum system can then be written as a time-periodic analogue to a Bloch wave where a *quasi-energy* plays the role of the crystal momentum. The Floquet functions then fulfill a time-independent Schrödinger equation for each quasi-energy which can be solved by the usual methods. An intrinsic advantage of this ansatz is that secular terms are avoided while periodicity

is automatically secured. For instance, it is possible to use Floquet theory to derive approximate solutions for a two-state system under monochromatic driving without recourse to the RWA [32, Chapter 3.2]. The ansatz can also be extended to non-periodic driving schemes [32, Chapter 2.4]. As we will not use this method in this thesis, we refer to the review by Grifoni and Hänggi [32] and the references therein for more details.

## Linear response of nanosystems in a linearly driven bath

In this chapter we will take a first look at the impact of driven baths onto the dynamics of coupled systems. Our method of choice will be the Langevin Equation presented in Part 2. We derive the dynamics for dipolar bath driving on the basis of the Caldeira-Leggett model in the first section and show that the result can be cast into the form of an additional time-dependent force component for the system under study. In the second section, we quantify this force contribution by use of the Onsager solvation model as discussed in Part 3. Our stated aim follows in the next two sections: We investigate the linear response of two particular physical nanosystems and show that bath driving qualitatively changes the associated response spectrum. The results presented herein provide a strong physical motivation to further investigate and develop the theoretical foundations of the dynamics in driven baths. The results in this part of the thesis are based on our work in Grabert et al. [1].

### 4.1 The driven bath Hamiltonian

A simple way to characterize the dissipative dynamics of a physical system lies in the formulation of appropriate system-bath models. Thus, we presented two particular minimal models in Section 2.2: the Caldeira-Leggett and the spin-boson model. We also discussed how a classical electric field can couple to a quantum system in Section 3.3. Bath driving can then be introduced in a very intuitive manner by coupling the bath operators to a field in the spirit of Equation (3.53). For a simple bosonic bath of  $N$  oscillators, we therefore introduce the general driven bath Hamiltonian:

$$\begin{aligned}
 H_B^{\text{Dr}}(t) = H_B + H_{\text{IB}}(t) &= \sum_{\alpha=1}^N \frac{1}{2} \left[ \frac{p_\alpha^2}{m_\alpha} + m_\alpha \omega_\alpha^2 x_\alpha^2 \right] + \sum_{\alpha=1}^N f_\alpha(x_\alpha, p_\alpha, t) \\
 &= \sum_{\alpha=1}^N \hbar \omega_\alpha \left[ b_\alpha^\dagger b_\alpha + \frac{1}{2} \right] + \sum_{\alpha=1}^N f'_\alpha(b_\alpha, b_\alpha^\dagger, t).
 \end{aligned} \tag{4.1}$$

Again, the bath is represented by a collection of harmonic oscillators, now driven



by an unspecified function  $f_\alpha(\dots, t)$  which couples to the position and momentum operators of the associated oscillators. In the second line, we rewrote the Hamiltonian using the appropriate creation and annihilation operators  $b_\alpha$  and  $b_\alpha^\dagger$  of an oscillator mode (see Equation (A.5)). The function  $f_\alpha$  introduced by the additional driving term  $H_{\text{IB}}(t)$  can be specified to contain terms which explicitly describe the interaction of the oscillators with a magnetic or electric field, as long as we assume that the sample is small in comparison to the wavelength of the external fields. In this work, we largely restrict ourselves to a simple linear coupling of the form

$$f_\alpha(x_\alpha, p_\alpha, t) = -d_\alpha x_\alpha F(t), \quad (4.2)$$

where we sequestered the time dependence into a (real) function  $F(t)$ . The coupling to each oscillator is represented by separate coupling constants  $d_\alpha$ . The choice of Equation (4.2) recreates the effect of Equation (3.53), that is, the oscillators effectively represent dipoles which couple to a classical electric field  $F(t)$ . In fact, we may see the above description as a simple model for the polarization of a molecular environment: as briefly discussed in Part 3, molecules in an electric field of comparably low frequency rotate to orient their permanent dipole moments into the direction of the field. If we neglect any spatial dependence, we can restrict the process to one dimension, where the position  $x_\alpha$  acts as a measure for the overall orientation into the direction of the field. Since the bath modes are assumed to be harmonic as usual, we also implicitly assume that only small deviations from equilibrium are induced by the external driving process. Equation (4.2) coupled with (4.1) provides us with a suitable first look into the effect of a driven bath and we use

$$\begin{aligned} H_{\text{B}}^{\text{Dr}}(t) &= \sum_{\alpha=1}^N \frac{1}{2} \left[ \frac{p_\alpha^2(t)}{m_\alpha} + m_\alpha \omega_\alpha^2 x_\alpha^2 \right] - \sum_{\alpha=1}^N d_\alpha F(t) x_\alpha \\ &= \sum_{\alpha=1}^N \hbar \omega_\alpha \left[ b_\alpha^\dagger b_\alpha + \frac{1}{2} \right] - \sum_{\alpha=1}^N \hbar \mu_\alpha F(t) (b_\alpha + b_\alpha^\dagger), \end{aligned} \quad (4.3)$$

where we have defined the coupling  $\mu_\alpha$  for the description using annihilation and creation operators. In the next section, we evaluate the dynamics following Equation (4.3) using the quantum Langevin Equation. Also note that we neglect the zero-point energy as it will not play a role in our analysis.

## 4.2 Quantum Langevin dynamics for a linearly driven bath

With the driven bath Hamiltonian of Equation (4.3) at hand, we can investigate the effect of a driven bath by using the quantum Langevin Equation (QLE) discussed in Section 2.2.1. The total system-bath Hamiltonian is now given by

$$H(t) = H_{\text{S}} + H_{\text{SB}} + H_{\text{B}}^{\text{Dr}}(t) + H_{\text{E}}(t), \quad (4.4)$$

where the term  $H_E(t)$  contains additional driving terms which act onto the system only. In the following, we evaluate the dynamics for the linearly driven bath of Equation (4.3) for both the Caldeira-Leggett and the spin-boson models discussed in Section 2.2. We will then proceed to use the Onsager sphere model of Section 3.2 to characterize the resulting effects.

### 4.2.1 Caldeira-Leggett model

Following Equations (4.4) and (2.13) the total Hamiltonian reads

$$\begin{aligned}
H(t) = & \frac{p^2}{2M} + V(q) - q \sum_{\alpha=1}^N c_{\alpha} x_{\alpha} + q^2 \sum_{\alpha=1}^N \frac{c_{\alpha}^2}{2m_{\alpha}\omega_{\alpha}^2} \\
& + \sum_{\alpha=1}^N \frac{1}{2} \left[ \frac{p_{\alpha}^2}{m_{\alpha}} + m_{\alpha}\omega_{\alpha}^2 x_{\alpha}^2 \right] - F(t) \left[ d_0 q + \sum_{\alpha=1}^N d_{\alpha} x_{\alpha} \right],
\end{aligned} \tag{4.5}$$

where we use a simple dipolar coupling  $H_E(t) = -d_0 F(t) q(t)$  to model the impact of the field  $F(t)$  on the system. We find the Heisenberg Equation of motion for the oscillator positions as

$$m_{\alpha} \frac{d^2 x_{\alpha}(t)}{dt^2} + m_{\alpha} \omega_{\alpha}^2 x_{\alpha}(t) = c_{\alpha} q(t) + d_{\alpha} F(t). \tag{4.6}$$

Equation (4.6) is similar in form to the usual result of Equation (2.18) but with the homogeneity shifted as  $c_{\alpha} q(t) \rightarrow c_{\alpha} q(t) + d_{\alpha} F(t)$ . As such, the bath operators still follow the dynamics of forced oscillators and we can directly substitute the new homogeneity in Equation (2.19). We obtain

$$\begin{aligned}
x_{\alpha}(t) = & x_{\alpha}(t_0) \cos [\omega_{\alpha}(t - t_0)] + \frac{p_{\alpha}(t_0)}{m_{\alpha}\omega_{\alpha}} \sin [\omega_{\alpha}(t - t_0)] \\
& + \frac{1}{m_{\alpha}\omega_{\alpha}} \int_{t_0}^t ds [d_{\alpha} F(s) + c_{\alpha} q(s)] \sin [\omega_{\alpha}(t - s)],
\end{aligned} \tag{4.7}$$

which differs from the previous result only by a new field-dependent term. We perform the same manipulations as in Section 2.2.1 to arrive at the associated quantum Langevin equation

$$\begin{aligned}
M \frac{d^2 q(t)}{dt^2} + \frac{dV(q)}{dq} + M \int_{t_0}^t ds \gamma(t - s) \frac{dq(s)}{ds} \\
= \xi(t - t_0) + d_0 F(t) + \int_{t_0}^t ds \lambda(t - s) F(s),
\end{aligned} \tag{4.8}$$

where  $\gamma(t)$  is the damping kernel defined in Equation (2.22) and  $\xi(t)$  is the fluctuating force of Equation (2.23) where we also included the initial-slip term for brevity. Equation (4.8) shows that a linearly driven bath merely introduces a correction to the driving force experienced by the system. This also meshes well with our expectations from Part 3, where we saw that polarization leads to a correction of the underlying field inside a dielectric and therefore also to the force experienced by a quantum system. The new total force is now given as

$$F_{\text{eff}}(t) = d_0 F(t) + \int_{t_0}^t ds \lambda(t-s) F(s). \quad (4.9)$$

Here, the correction from bath-driving is characterized by a force kernel

$$\lambda(t) = \sum_{\alpha=1}^N \frac{c_\alpha d_\alpha}{m_\alpha \omega_\alpha} \sin[\omega_\alpha t] = \frac{2}{\pi} \int_0^\infty d\omega \bar{J}(\omega) \sin[\omega t]. \quad (4.10)$$

In the second equation we have introduced an effective spectral density  $\bar{J}(\omega)$  defined in analogy to Equation (2.26) by

$$\bar{J}(\omega) = \frac{\pi}{2} \sum_{\alpha=1}^N \frac{c_\alpha d_\alpha}{m_\alpha \omega_\alpha} \delta(\omega - \omega_\alpha), \quad (4.11)$$

which incorporates both the system-bath couplings  $c_\alpha$  as well as the coupling constants between the force and the bath  $d_\alpha$ .

#### 4.2.2 Spin-boson model

Equation (4.9) represents a general result, valid for any potential choice of the system, as long as the system-bath coupling remains linear in the bath position operators. For this reason, we can proceed in a similar manner for the spin-boson Hamiltonian defined by Equations (2.46) and (2.47). We also include a direct driving term that couples to the spin-boson model according to (3.55). In total, we have

$$H(t) = \frac{\Delta}{2} \sigma_x + \frac{\epsilon}{2} \sigma_z - q_0 \frac{\sigma_z}{2} \sum_{\alpha=1}^N c_\alpha x_\alpha + \sum_{\alpha=1}^N \frac{1}{2} \left[ \frac{p_\alpha^2}{m_\alpha} + m_\alpha \omega_\alpha^2 x_\alpha^2 \right] - \frac{F(t)}{2} \left[ d_0 \sigma_z + \sum_{\alpha=1}^N d_\alpha x_\alpha \right], \quad (4.12)$$

where it should be noted that we scaled the force by a factor of two to account for the definitions in the system Hamiltonian. The Heisenberg equations of motion for the

Pauli matrices are then given by

$$\frac{d\sigma_x}{dt} = -\frac{\sigma_y(t)}{\hbar} \left[ \epsilon - d_0 F(t) - q_0 \sum_{\alpha=1}^N c_\alpha x_\alpha(t) \right], \quad (4.13)$$

$$\frac{d\sigma_y}{dt} = -\frac{\Delta}{\hbar} \sigma_z(t) + \frac{\sigma_x(t)}{\hbar} \left[ \epsilon - d_0 F(t) - q_0 \sum_{\alpha=1}^N c_\alpha x_\alpha(t) \right], \quad (4.14)$$

$$\frac{d\sigma_z}{dt} = \frac{\Delta}{\hbar} \sigma_y(t). \quad (4.15)$$

Insertion of Equation (4.7) into Equations (4.13), (4.14) and (4.15) yields the time-evolution for the Pauli matrices in the driven bath as

$$\frac{d\sigma_x}{dt} = -\frac{\sigma_y(t)}{\hbar} \left[ \epsilon_{\text{eff}}(t) - \bar{\xi}(t) - \frac{q_0^2}{2} \int_{t_0}^t ds \chi(t-s) \sigma_z(s) \right], \quad (4.16)$$

$$\frac{d\sigma_y}{dt} = -\frac{\Delta}{\hbar} \sigma_z(t) + \frac{\sigma_x(t)}{\hbar} \left[ \epsilon_{\text{eff}}(t) - \bar{\xi}(t) - \frac{q_0^2}{2} \int_{t_0}^t ds \chi(t-s) \sigma_z(s) \right], \quad (4.17)$$

$$\frac{d\sigma_z}{dt} = \frac{\Delta}{\hbar} \sigma_y(t), \quad (4.18)$$

where we have defined  $\bar{\xi}(t)$  from the homogeneous part of Equation (4.7) and combined the integrand of (2.20) into a single kernel  $\chi$ . As expected, the effect of a driven bath is now included via an effective asymmetry  $\epsilon_{\text{eff}}(t)$  which determines the time evolution of the Pauli matrices. It is given by

$$\epsilon_{\text{eff}}(t) = \epsilon - d_0 F(t) - \frac{q_0}{2} \int_{t_0}^t ds \lambda(t-s) F(s). \quad (4.19)$$

The effective time-dependent asymmetry includes the effect of the direct driving contribution, as well as the bath driving which is determined by the kernel of Equation (4.10) and the effective spectral density of (4.11). Note that we will encounter the bath driving term usually with  $\lambda(s-t)$  later, as the minus in Equation (4.19) can be conveniently absorbed into the sine found in Equation (4.10).

### 4.2.3 Evaluation of the effective force

As we have seen in Equations (4.9) and (4.19), linear bath driving introduces a correction to the external force experienced by the system which gives rise to a new total force.

Naturally, linear response theory, as discussed in Section 3.3.4, can be applied with respect to this extended force, as well. In particular, what we aim for in this part of the thesis is a description following Equation (3.68) via

$$\langle \mathcal{O}(t) \rangle - \langle \mathcal{O} \rangle_0 \approx \frac{1}{\hbar} \int_{-\infty}^{\infty} dt' G(t, t') F_{\text{eff}}(t'). \quad (4.20)$$

Here, the retarded Green's function  $G(t, t')$  is defined similarly to the susceptibility in Equation (3.68) and we have used the subscript 0 to indicate that the expectation values are evaluated for the undriven case.

Equation (4.20) requires us to compute both  $G(t, t')$  for the observable  $\mathcal{O}$  as well as the full effective force  $F_{\text{eff}}(t)$ . While the former amounts to the solution of the (undriven) system-bath problem and we can apply any of the methods outlined in Part 2, the evaluation of the effective force itself is potentially more involved. The reason for this lies in its dependence on the effective spectral density of Equation (4.11) which is an a priori unknown quantity. As we have seen in Part 2, however, the bath spectral density of Equation (2.26) can be connected to phenomenological quantities by use of the environmental susceptibility according to Equation (2.36). In particular, we saw later that the dielectric function can be used to model the spectral density in Equation (3.52). This was done on the basis of the Onsager model where the resulting reaction field was assumed to represent the response of the bath to the system in question. Similarly, we can obtain an effective external driving field from the same model which allows us to specify the total effective force. We do this by tweaking the boundary condition in Equation (3.41) to

$$\Phi_{\text{d}}(\omega, r)|_{r \rightarrow \infty} = -E(\omega)r \cos(\theta), \quad (4.21)$$

which represents an external field in the  $z$ -direction [111]. Since this external field permeates both the dielectric as well as the cavity, the resulting field inside the cavity will be dressed by the interaction with the dielectric. Following the steps in Section 3.2.2, we obtain the total potential in the cavity as

$$\Phi_{\text{c}}(r, \theta, \omega) = - \left[ 2 \frac{\mu(\omega)}{4\pi\epsilon_0 a^3} \chi_o(\omega) + [1 + \chi_o(\omega)] E(\omega) \right] r \cos(\theta) + \frac{\mu(\omega)}{4\pi\epsilon_0 r^2} \cos(\theta). \quad (4.22)$$

Again, the first term represents the reaction field and the last term the potential created by the dipole. The second term represents the corrected influence from external driving in the setup and is commonly referred to as the *cavity field* in the literature [135, 145, 162]. We can directly argue in the same way as before that the contributions in  $\Phi_{\text{c}}(r, \theta, \omega)$  give rise to a classical equation of motion reminiscent of the Langevin

dynamics for a one-dimensional particle. Using  $\mu(t) = Qq(t)$  for a dipole with charge  $Q$  and separation  $q(t)$ , the total field is modified into

$$E_{\text{tot}}(t) = \frac{Q}{2\pi\epsilon_0 a^3} \int_{t_0}^t ds \chi_r(t-s)q(s) + \int_{t_0}^t ds \chi_c(t-s)E(s), \quad (4.23)$$

where the first term contains the contribution of the reaction field characterized by  $\chi_r(t)$  and the latter contains the cavity field characterized by  $\chi_c(t)$ . The integral boundaries imply causality and the absence of dynamics before  $t_0$ . In the case of Equation (4.23) the Fourier transforms  $\chi_c(\omega) = 1 + \chi_o(\omega)$  and  $\chi_r(\omega) = \chi_o(\omega)$  are defined by the Onsager susceptibility of Equation (3.48). The correction from the cavity field possesses the same structure as the effective force by comparison to Equation (4.9). Thus, we can directly state that

$$F_{\text{eff}}(t) = Q \int_{t_0}^t ds \chi_c(t-s)E(s) = QE(t) + Q \int_{t_0}^t ds \chi_o(t-s)E(s). \quad (4.24)$$

Comparison with (4.9) also shows that  $\lambda(t) = Q\chi_o(t)$ . Or in other words,

$$\bar{J}(\omega) = (2\pi\epsilon_0 a^3/Q)J(\omega). \quad (4.25)$$

As such, the use of the Onsager model allows us to consider the new effective spectral density of Equation (4.11) as directly proportional to the ordinary bath spectral density. Similar results can also be obtained in different geometries like a layered dielectric sphere as shown in Appendix B and will also appear in the quantum-dot metal-nanoparticle setup discussed below. This implies that the result (4.25) is a general manifestation of linear bath driving and we will explicitly assume a proportionality for the calculations in Parts 5 and 6. However, Equation (4.24) predicts a separability into a direct driving and a retarded force contribution, which is not always true in more complicated geometries.

### 4.3 Polarizable molecule immersed in water

With the dynamics of the linearly driven bath problem at hand and a way to characterize the resulting force, we can now ask about the impact of a driven bath on the linear response spectra in specific physical problems. As outlined in the introduction, this effect is usually taken as negligible as external driving tends to be tuned to the system modes under study and strongly off-resonant to the environment (cf. our discussion of driven quantum systems in Section 3.3). Therefore, we aim to gauge the impact of bath driving on the response of physical model systems by explicitly utilizing problems where resonant environmental modes may play a role.

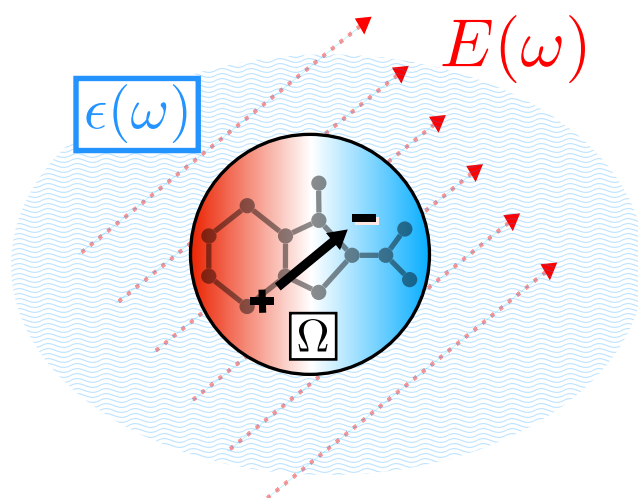


**Figure 4.1:** Toy model for a polarizable molecule in water. The probe molecule is represented by a spherical Onsager cavity with radius  $a$  and is assumed to contain a single harmonic polarizability mode at frequency  $\Omega$ . The surrounding water is characterized by its dielectric function  $\epsilon(\omega)$  given in Equation (4.26). A time-dependent electric field  $E(\omega)$  acts on both.

First, we look at the most paradigmatic problem related to driven baths: a molecule immersed in a solvent - as, in general, a molecule cannot be excited by an external source without perturbing the solvent as well. Specifically, we consider a polarizable molecule immersed in water while both are excited by a THz field source. This rather specific problem garnered attention in view of recent advances in THz spectroscopy methods which allows for a more thorough investigation of this frequency regime at higher field strengths [123, 163, 164]. For instance, recent studies on the THz-induced Kerr effect were conducted in an effort to determine the sign of the anisotropy of the molecular polarizability of various solvent molecules such as water [3, 165, 166]. In addition, the dielectric function of water in this regime is still highly debated and THz spectroscopy methods are seen as a way to gain additional information about their physical origin [118–120]. Most importantly, however, recent molecular dynamics simulation studies suggest an efficient heating mechanism present for liquid water in the THz regime which can also be used to excite specific molecular modes of immersed molecules [37–39]. While these studies do not target specific environmental modes and achieve their heating mainly through sheer intensity, the energy of THz photons can be used to couple to rotational modes and modes corresponding to weak intermolecular forces [163], as well. This turns the problem into an interesting example for the application of our driven bath approach.

In the following, we employ a simple toy model shown exemplarily in Figure 4.1. We consider a polarizable molecule with a harmonic polarizability mode resonant to

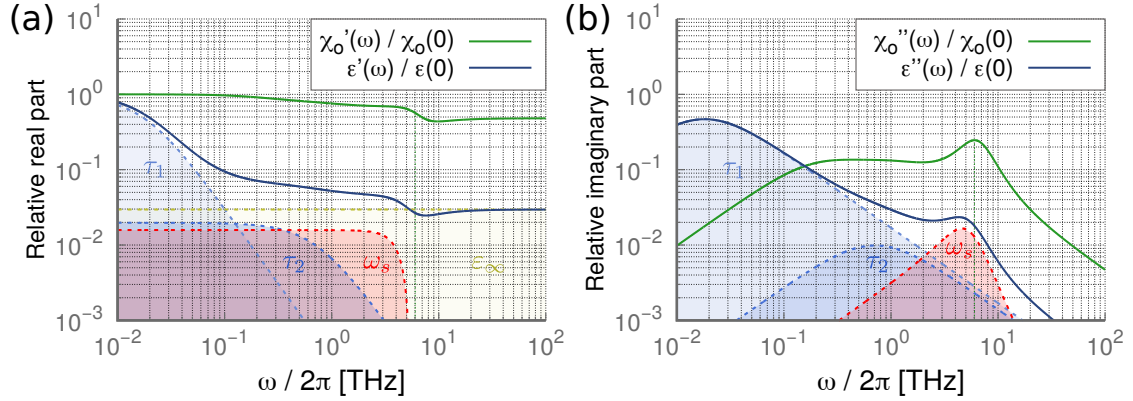


**Figure 4.2:** The dielectric function  $\varepsilon(\omega)$  for water given by Equation (4.26) and the corresponding Onsager susceptibility  $\chi_o(\omega)$  given by Equation (3.48). The real parts  $\varepsilon'$  and  $\chi_o'$  are depicted in (a), whereas the imaginary parts  $\varepsilon''$  and  $\chi_o''$  are shown in (b). The shaded regions give the contributions from each term in Equation (4.26). The intermolecular stretching mode (red shaded region) leads to a clearly visible peak in the imaginary parts, albeit slightly shifted to about 6 THz for  $\chi_o''(\omega)$ .

a specific THz frequency and characterize the environment by the dielectric function of water in this regime. The molecule itself is represented by a spherical Onsager cavity where polarization creates a dipole moment, such that we are able to use the quantification laid out in Section 4.2.3. This reduces the problem to a forced harmonic oscillator which permits us to easily obtain analytic results for the linear response in the long-time limit.

### 4.3.1 Water in the THz regime

The usual energy spectrum of THz photons lies in the meV-range with wave numbers ranging from  $3.3 \text{ cm}^{-1}$  to about  $334 \text{ cm}^{-1}$ . This places the excitation energies close to the thermal energy at room temperature. Characteristic excitations in this regime are therefore rather low in energy and are most commonly represented by low-lying molecular and weak intermolecular excitations characterized by dynamics in the picosecond regime. Specifically, rotational and low-lying vibrational degrees of freedom of large molecules as well as collective excitations of supramolecular complexes of small interacting molecules are usually found [163]. Water falls into the second category, where hydrogen bonding in the liquid phase allows for collective dynamics to emerge. The dynamics of its dielectric function in the THz regime are commonly associated with three relaxation times at about 0.1 ps, 1 ps and 8.3 ps. While their exact microscopic origin is still debated, the first is attributed to dynamic breaking and reforming of hydrogen bonds while the next fastest process corresponds to rotational relaxation of free or weakly bound water molecules. The slowest process has by far the highest



contribution and is thought to correspond to collective reorientational phenomena, i.e., dynamics of water molecules within the whole hydrogen-bond network. In addition, intermolecular modes may also contribute [118, 120, 167, 168].

Yada et al. probed the dynamics of liquid water using THz attenuated total reflection time-domain spectroscopy in order to parametrize the resulting dielectric function [119, 120]. We utilize their result parametrized according to

$$\varepsilon(\omega) = \frac{\Delta\varepsilon_1}{1 - i\omega\tau_1} + \frac{\Delta\varepsilon_2}{1 - i\omega\tau_2} + \frac{A_s}{\omega_s^2 - \omega^2 - i\omega\gamma_s} + \varepsilon_\infty, \quad (4.26)$$

with parameters given by  $\Delta\varepsilon_1 = 73.9$ ,  $\tau_1 = 8.76$  ps,  $\Delta\varepsilon_2 = 1.56$ ,  $\tau_2 = 0.224$  ps,  $A_s = 35.1 \times (2\pi)^2$  THz<sup>2</sup>,  $\omega_s = 5.3 \times (2\pi)$  THz,  $\gamma_s = 5.4 \times (2\pi)$  THz and  $\varepsilon_\infty = 2.34$ . The dielectric function clearly exhibits two Debye relaxation backgrounds of the type seen in Equation (3.20) corresponding to overdamped dynamics of rotational modes. The Lorentzian contribution (cf. Equation (3.34)) represents a characteristic intermolecular collective stretching mode at 5 THz which can be excited in the relevant frequency region. The last term represents electronic and any other dynamics much faster than the typical picosecond scale we consider. We have omitted another Lorentzian contribution from an intermolecular librational mode at about 15 THz as we will focus on the dynamics created by the stretching mode. The dielectric function (4.26) and the corresponding Onsager susceptibility (3.48) are shown in Figure 4.2. As expected, the mode creates a pronounced peak in the corresponding susceptibility and, thus, also in the spectral density. However, the peak is shifted slightly to about 6 THz.

### 4.3.2 Linear response of a polarizable molecule

After discussing the dielectric properties of the environment, we are now in the position to model a suitable probe. As shown in Section 3.1.6, the (isotropic) molecular polarizability can be modeled by a simple Lorentz oscillator model for the electrons in a molecule. In general, multiple modes may contribute as implied in Equation (3.34). The dynamic polarizability  $\alpha(\omega)$  of a single mode then gives rise to an induced dipole moment  $\mu(\omega)$  by way of Equation (3.29), that is

$$\mu(\omega) = \alpha(\omega)E(\omega). \quad (4.27)$$

Here, we have neglected any spatial dependence and local field corrections and have reduced the electric field to a single component. In this way, the dynamic polarizability represents the linear response to the electric field  $E(\omega)$  in the frequency domain. We now consider only a single mode at frequency  $\Omega$ . As before, we define the dipole moment as  $\mu(t) = eq(t)$ , where  $e$  is an elementary charge and  $q(t)$  a coordinate which describes the charge separation in our molecular probe. Utilizing the Caldeira-Leggett

model we explicitly use a harmonic potential

$$V(q) = \frac{1}{2}M\Omega^2q^2(t), \quad (4.28)$$

as suggested by Equation (3.31). This gives rise to the quantum Langevin Equation

$$\begin{aligned} \ddot{\mu}(t) + \Omega^2\mu(t) &= \frac{e}{M}\xi(t-t_0) + \frac{e^2}{2M\pi\epsilon_0a^3} \int_{t_0}^t ds \chi_r(t-s)\mu(s) \\ &+ \frac{e^2}{M} \int_{t_0}^t ds \chi_c(t-s)E(s), \end{aligned} \quad (4.29)$$

where we have directly inserted the definition of the resulting reaction- and cavity field contributions from Equation (4.23).  $\xi(t)$  is given by the homogeneous part of Equation (4.7) and we abbreviated time derivatives by dots. In order to obtain the linear response, we consider the average of Equation (4.29) such that  $\langle \xi(t) \rangle = 0$ . This follows by setting  $\langle \dots \rangle = \text{Tr}[\dots \rho(t_0)]$  and assuming that the initial density matrix  $\rho(t_0)$  factorizes into system and bath parts with the bath in thermal equilibrium. We get

$$\begin{aligned} \langle \ddot{\mu}(t) \rangle + \Omega^2\langle \mu(t) \rangle &= \frac{e^2}{2M\pi\epsilon_0a^3} \int_{t_0}^t ds \chi_r(t-s)\langle \mu(s) \rangle \\ &+ \frac{e^2}{M} \int_{t_0}^t ds \chi_c(t-s)E(s). \end{aligned} \quad (4.30)$$

Next, we apply a Fourier transformation and consider the long-time limit such that  $t_0 \rightarrow -\infty$ . This allows us to write the integrals as products in frequency space to obtain

$$\langle \mu(\omega) \rangle = \frac{e^2}{M} \frac{\chi_c(\omega)E(\omega)}{[\Omega^2 - \omega^2 - \frac{e^2}{2M\pi\epsilon_0a^3}\chi_r(\omega)]}. \quad (4.31)$$

Equations (4.31) and (4.27) show that the dynamic polarizability in frequency space is given by

$$\alpha(\omega) = \frac{e^2}{M} \frac{\chi_c(\omega)}{\Omega^2 \left[ 1 - \frac{\alpha_0}{2\pi\epsilon_0a^3}\chi_r(\omega) \right] - \omega^2}, \quad (4.32)$$

where we have used  $\alpha_0 = e^2/(M\Omega^2)$  as the static polarizability of the mode  $\Omega$ . The ratio in the denominator then gives a ratio between a polarizability volume (cf. Equation (7.2)) and the volume associated with the Onsager sphere. For a monochromatic field of the form  $E(t) = E_0 \cos(\omega_e t)$ , the dipole moment in the time domain becomes

$$\langle \mu(t) \rangle = \frac{e^2 E_0}{M} \text{Re} \left[ \frac{\chi_c(\omega_e) e^{-i\omega_e t}}{\Omega^2 \left[ 1 - \frac{\alpha_0}{2\pi\epsilon_0a^3}\chi_r(\omega_e) \right] - \omega_e^2} \right]. \quad (4.33)$$

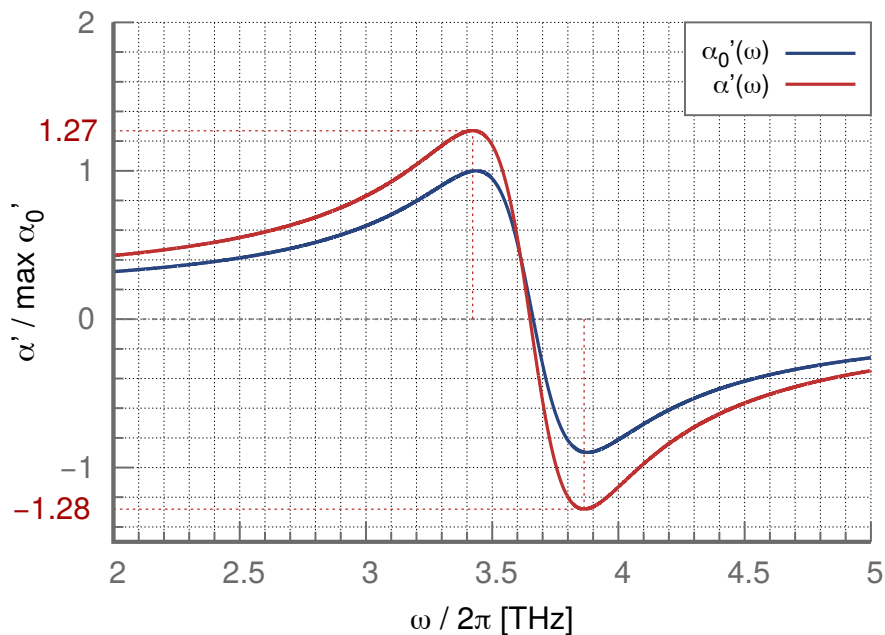


**Figure 4.3:** Real part of the dynamic polarizability  $\alpha(\omega) = \alpha'(\omega) + i\alpha''(\omega)$  given in Equation (4.34) (red line) in contrast to the result without bath driving (blue line). Both results have been scaled by the maximum of the result without bath driving to enable a comparison. Bath driving leads to an enhancement of the driving effect as seen from its increased peak height. However, bath driving also introduces a slight asymmetry into the corresponding peaks (red numbers).

Equation (4.33) shows a proportionality given by  $\langle \mu(t) \rangle = \text{Re}[\alpha(\omega_e)E_0e^{-i\omega_e t}]$ . The dynamic polarizability  $\alpha(\omega)$  therefore gives a suitable measure of the linear response of the problem.

### 4.3.3 Dynamic polarizability

We are now going to characterize the dynamic polarizability in Equation (4.32) for the case of water. In order to start, we need to specify the probe molecule. We set our probe frequency to  $\Omega = 4.5$  THz or about  $150 \text{ cm}^{-1}$ . This places the polarizability mode in the vicinity of the intermolecular stretching peak that appears in Equation (4.26), such that mutual excitation becomes possible in principle. Numerous examples of molecular modes in a similar frequency range exist [169, 170]. Examples include stretching modes of small halocarbons [171], e.g. in solid  $\text{Cl}_4$ , a torsional mode of acetaldehyde [172] or a deformation in the ring-methyl bond in toluene [173]. These examples also allow us to settle for potential Onsager radii: most involve fairly small molecules and we can use values for the geometric parameters in the few Angstrom range. Polarizabilities differ more strongly. For instance, typical values for  $\alpha_0/4\pi\epsilon_0$  are about  $1.5 \text{ \AA}^3$  for water,

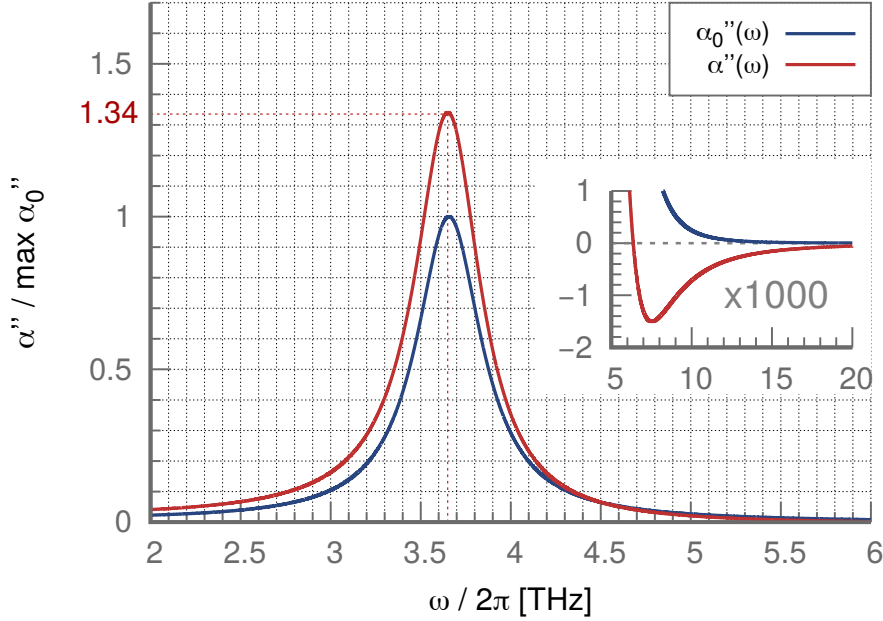


**Figure 4.4:** Imaginary part of the dynamic polarizability  $\alpha(\omega) = \alpha'(\omega) + i\alpha''(\omega)$  given in Equation (4.34) (red line) in contrast to the result without bath driving (blue line). Both results have been scaled by the maximum of the result without bath driving to enable a comparison. Bath driving leads to an enhancement of the absorbance as seen from its increased peak height (red number). However, bath driving also shifts the result downward and produces a small negative undershoot beyond the resonance (inset).

about  $2.5 \text{ \AA}^3$  for methane and about  $10 \text{ \AA}^3$  for benzene [174, 175]. Using an average bond length of  $a = 2 \text{ \AA}$  as a gauge of the Onsager radius, we can see that the prefactor  $2\alpha_0/4\pi\epsilon_0 a^3$  is of the order of 1. However, this factor only determines the frequency shift of the associated response peaks and gives an overall scaling factor, which will not play a role since we will only consider relative quantities later. Therefore, we set  $2\alpha_0/4\pi\epsilon_0 a^3 = 1$  for simplicity in the following.

We also need to choose the particular geometry of the Onsager solvation model in order to specify the cavity and reaction field components. For the simple spherical geometry of Figure 4.1, we can directly use the results from Section 4.2.3 to obtain

$$\alpha(\omega) = \frac{e^2}{M} \frac{1 + \chi(\omega)}{\Omega^2 \left[ 1 - \frac{\alpha_0}{2\pi\epsilon_0 a^3} \chi(\omega) \right] - \omega^2}, \quad (4.34)$$

where  $\chi(\omega) = [\epsilon(\omega) - 1]/[2\epsilon(\omega) + 1]$  is the Onsager susceptibility of the environment according to Equation (3.48) with  $\epsilon(\omega)$  given for water by Equation (4.26). This gives a spectral density  $J(\omega) = (e^2/2\pi\epsilon_0 a^3) \text{Im}[\chi(\omega)]$  via Equation (3.52). We also note that

the change introduced by bath driving can be included as

$$\alpha(\omega) = [1 + \chi(\omega)]\alpha_0(\omega), \quad (4.35)$$

where  $\alpha_0(\omega) = \frac{e^2}{M} \left\{ \Omega^2 \left[ 1 - \frac{\alpha_0}{2\pi\epsilon_0 a^3} \chi(\omega) \right] - \omega^2 \right\}^{-1}$  gives the dynamic polarizability without the bath-driving contribution. Figures 4.3 and 4.4 show the dynamic polarizability together with the results without bath driving as described by Equation (4.35). Evidently, driving enhances the overall response of the system in question by a factor of about 30% both in the real and the imaginary part. This implies an overall stronger signal related to polarizability responses of suitable molecules when bath driving is included. This result already shows that bath driving in a structured bath can, in principle, be used to enhance the response properties of modes in a probe. However, the argument proves to be more subtle: the coupling to the bath also introduces qualitative changes to the spectrum, as seen in the inset of Figure 4.4 that shows a negative undershoot beyond the resonance. In addition, a new asymmetry in the resonance peaks of the real part can also be observed. Both features can be quantified by separating (4.35) into its real and imaginary part. Denoting real parts by a prime and imaginary parts by two primes, we find

$$\alpha'(\omega) = \frac{1 + \chi'(\omega)}{\Lambda^2} \left[ 1 - \frac{\omega^2}{\Omega^2} - V_f \chi'(\omega) \right] - \frac{V_f}{\Lambda^2} [\chi''(\omega)]^2, \quad (4.36)$$

$$\alpha''(\omega) = \frac{V_f}{\Lambda^2} \chi''(\omega) + \frac{\chi''(\omega)}{\Lambda^2} \left[ 1 - \frac{\omega^2}{\Omega^2} \right]. \quad (4.37)$$

The results for the undriven bath read

$$\alpha'_0(\omega) = \frac{1}{\Lambda^2} \left[ 1 - \frac{\omega^2}{\Omega^2} - V_f \chi'(\omega) \right], \quad (4.38)$$

$$\alpha''_0(\omega) = \frac{V_f}{\Lambda^2} \chi''(\omega), \quad (4.39)$$

where we wrote the dimensionless volume fraction as  $V_f = \alpha_0/2\pi\epsilon_0 a^3$ . The symbol  $\Lambda$  contains the Lorentzian characteristic of the response

$$\Lambda^2 = \alpha_0^{-1} \left\{ \left[ 1 - \frac{\omega^2}{\Omega^2} - V_f \chi'(\omega) \right]^2 + [V_f \chi''(\omega)]^2 \right\}. \quad (4.40)$$

A comparison shows that the additional contribution from bath driving mixes real and imaginary part. This leads to both an enhancement in the real part by a factor of  $1 + \chi'(\omega)$  as well as a downward shift proportional to  $[\chi''(\omega)]^2$ . The latter produces the asymmetry. In the imaginary part, bath driving produces a possible sign related to the

position of the frequency with respect to the resonance. Hence, bath driving always leads to a sign change within the simple spherical model, but only if the frequency is larger than the frequency of the resonance. Furthermore, the emergence of a negative sign is independent of the actual dielectric function of the environment because the impact of  $\chi'(\omega)$  cancels in Equation (4.37).

This is an interesting result, as a comparison with the solution for the Lorentz oscillator model of Equation (3.33) suggests that this changes the sign of the damping constant. In contrast to ordinary damping, bath driving seems to effectively modulate the constant for this model, such that energy is deposited in the system at the right driving frequency via the bath itself. Unfortunately, this would also predict exponentially rising solutions in the simple forced oscillator model and could point to limitations of our simplistic approach. On the other hand, we can translate the linear polarizability above to a refractive index by use of the Clausius-Mosotti equation (3.28). A sign change of the imaginary part could then imply a change in the sign of the exponential decay of a probe beam according to (3.22). In other words, the system seems to emit radiation and strengthens the external field instead of showing absorption. Such a situation was shown to be possible for nonlinear oscillators when looking at classical models for lasing by Borenstein and Lamb Jr. [176]. They argued that this was possible because the nonlinearity introduced couplings between phase and amplitude, not present in an ordinary harmonic oscillator. We may suppose that the coupling between real and imaginary part of the polarizability introduced by bath driving plays a similar role. Another possible explanation may be found in the so-called Fano effect which describes interference of scattering amplitudes between a discrete state and a continuum and eventually gives rise to similarly asymmetric or inverted lineshapes [177–179]. A more detailed analysis should be considered in future research.

#### **4.4 Interacting quantum-dot metal-nanoparticle setup**

The second application we consider concerns colloidal semiconductor quantum dots in the vicinity of metallic nanoparticles. *Colloidal quantum dots* describe nanometer-sized solid-state structures that display discrete electronic states similar to molecules or atoms. The size dependence of these features and their sensitivity to environmental conditions has led to a surge in research into potential applications. Examples include light-emitting diodes (LEDs) or solar panel setups where their high tunability is exploited to increase emission or absorption yields [180–184]. The addition of metallic nanoparticles introduces electromagnetic interactions between dot and nanoparticle which is seen as another way to enhance and control their dynamics. In particular, the coupling to collective surface excitations of conduction electrons called *plasmons* has been a focus of recent research [185]. Plasmonic excitations have been discussed as efficient single-photon sources [186, 187], for biosensing [188] and to further boost light-emitting diodes

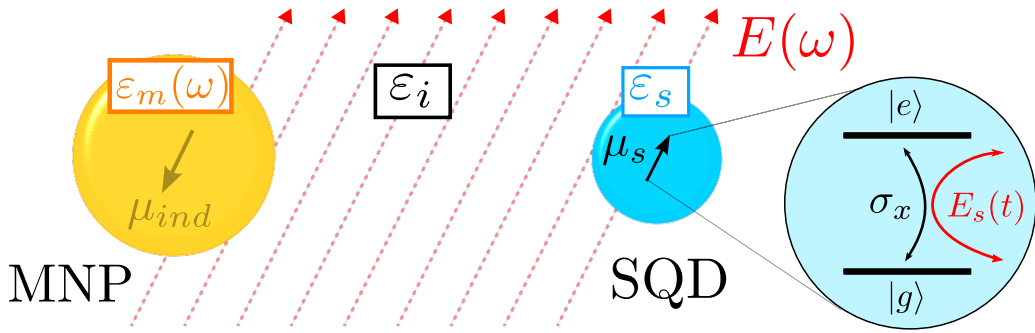


**Figure 4.5:** Toy model for a colloidal semiconductor quantum dot (SQD) interacting with a metallic nanoparticle (MNP). Both are modeled as dielectric spheres immersed in a dielectric medium. All regions are then characterized by their corresponding dielectric constants or functions ( $\epsilon$ ). The interaction is constrained to dipole-dipole interactions between an induced dipole moment in the MNP and a dipole in the quantum dot. The latter is modeled as a two-state system where transitions between a ground  $|g\rangle$  and excited state  $|e\rangle$  produce a dipole moment that couples to an effective field  $E_s$  inside the dot. The field originates from interactions with the MNP as well as with an external electric field  $E(\omega)$  which perturbs both the dot and the MNP. The latter effect introduces bath-driving contributions.

and solar-cell yield [189, 190]. The theoretical description usually treats the problem on the basis of classical electrodynamics which may include multipole effects and gives rise to distinct features such as the Fano effect [179, 191–193]. In this section we aim to model the problem on the basis of a simple system-bath approach and investigate the impact of bath driving contributions using the linear response of a quantum dot.

Our toy model is summarized in Figure 4.5. We apply the system-bath approach by looking at the interaction of a semiconductor quantum dot (SQD) with a single metallic nanoparticle (MNP) which we treat as a dynamical bath. The plasmon is included via the Drude model [111, 194] for the dielectric function of the nanoparticle which entails a structured spectral density. In contrast to the previous section, the quantum dot is assumed to constitute a two-state system, allowing for a description on the basis of the spin-boson model. The quantum dot then interacts with the mode by way of electric fields and we restrict ourselves to dipole-dipole interactions. Finally, we are going to apply the Onsager description by assuming a simplified geometry where the dot and the nanoparticle are modeled as dielectric spheres. Since the resulting geometry is more involved than the simple cavity we considered up until now, we explicitly derive the corresponding reaction- and cavity field components in a separate subsection. We start with a discussion of the underlying model.

### 4.4.1 Quantum dots and plasmons

In general, bulk materials exhibit a continuum of electronic states due to the large number of particles involved. In the simplest case, these states are arranged in bands due to the repeating crystal structure of the material and define the material as a conductor, semiconductor or an insulator. If a band is not filled or no separation to an empty band exists, electrons can be excited easily and a current can be induced. If a measurable energetic gap exists between a full and an empty band, more voltage is required to induce a flow of current. For many semiconductors in use, this gap is of the order of an electron volt which corresponds to wave lengths in the visible spectrum. In nanometer-sized semiconductor particles the fewer number of atoms imply that the bands start to unravel at the edges and transitions between discrete states can be observed. This quasi-zero-dimensional behavior gives rise to the term quantum dot. Since the exact energy of these transitions depends on the size, they can be fine-tuned across the visible spectrum [180, 181].

For a minimal model, we restrict ourselves to the lowest state of the conduction band and the highest of the valence band and assume that no other states of the dot take part in the dynamics. This allows us to describe the dot as a simple two-state system. Its interaction with the electric field is then modeled by coupling the transition matrix element to a classical field. Specifically, we use the system Hamiltonian

$$H_S = \frac{\hbar\omega_0}{2}\sigma_z - \mu\sigma_x E_s(t), \quad (4.41)$$

where the effective field  $E_s(t)$  contains all influences from the driven bath, as well as the direct coupling to an external electric field. Equation (4.41) deviates from our convention for the spin-boson model up to this point, in order to better fit the physical picture: the external field induces transitions between two states in the lower and higher band and does not just perturb the tunneling dynamics as implicitly assumed in the usual convention. In effect, we employ the driven spin-boson model, discussed in Equation (4.12), but exchange the roles of  $\sigma_x$  and  $\sigma_z$  such that the dynamics between the two conventions should not be different. Finally, we have also replaced  $\epsilon$  by its frequency  $\omega_0$  here and have absorbed a factor of two in the definition of  $E_s$ .  $\mu$  then represents the interband optical transition matrix element between the two states of the dot (cf. Equation (3.54)).

The bath is represented by the metallic nanoparticle. For optical frequencies nanoparticles made of noble metals such as gold or silver are often used [195]. In classical electrodynamics a dipole moment in a quantum dot will lead to the redistribution of free charges in a metal, leading to the creation of mirror charges. From an electrostatic perspective, only infinite conductive planes will create perfect mirror charges [111] such that multipole effects will enter from the limited geometry of the nanoparticles. Next to the redistribution of electrons, the charge fluctuations on the dot and the external field may induce additional resonant oscillations of conduction electrons called



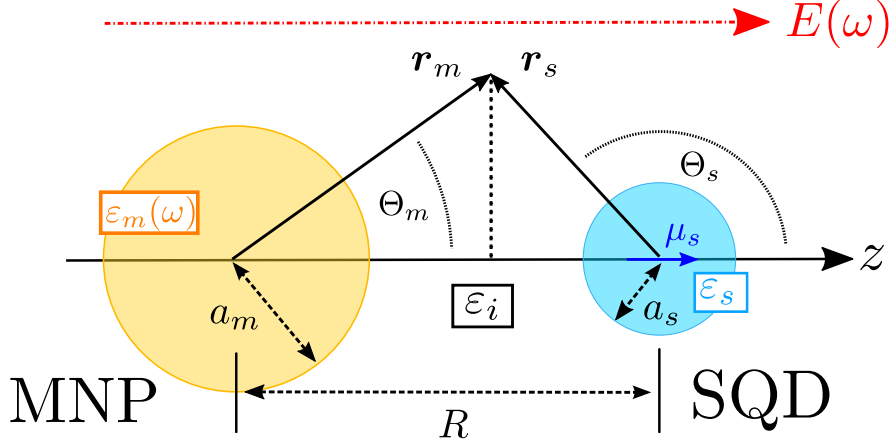


**Figure 4.6:** Geometric parameters of the simple two-sphere Onsager model of Figure 4.5 for the interaction between a semiconductor quantum dot (SQD) and a metallic nanoparticle (MNP). The two spheres are separated by a distance  $R$  with radii and dielectric constants given by  $a_s$  and  $\epsilon_s$  and  $a_m$  and  $\epsilon_m(\omega)$ , respectively. The intermediate space is characterized by the dielectric constant  $\epsilon_i$  and an external electric field  $E(\omega)$  applied parallel to the  $z$ -axis. The problem can be treated on the basis of the vectors  $\mathbf{r}_s$  and  $\mathbf{r}_m$  and their angles to the  $z$ -axis,  $\Theta_s$  and  $\Theta_m$ .

plasmons. These oscillations represent fluctuations in the electronic charge density and can be thought of as charge density waves on the metallic surface. A common approximation is done on the basis of the Drude-Sommerfeld model [190, 194] which predicts a Lorentzian excitation spectrum by describing the conduction electrons as a noninteracting gas of free particles. Specifically, it allows us to write the dielectric function inside the nanoparticle as [111, Chapter 7.5][194]

$$\epsilon_m(\omega) = 1 - \frac{\omega_p^2}{\omega^2 + i\Gamma\omega}, \quad (4.42)$$

where  $\omega_p$  is the plasma frequency and the relaxation time is given by  $\tau_D = 1/\Gamma$  that represents the inverse width of the resonance peak. In order to find the spectral density of the problem, we are now tasked with finding the environmental susceptibility for the geometry of our model.

#### 4.4.2 The two-sphere geometry

We consider the simplified geometry shown in Figure 4.6 and apply the same methods as in Section 3.2. The nanoparticle and the quantum dot are modeled as dielectric spheres with a specific distance  $R$ . The dot features the dielectric constant  $\epsilon_s$  and radius  $a_s$  while the nanoparticle is modeled by the dynamic dielectric function  $\epsilon_m(\omega)$  of Equation (4.42) with the radius  $a_m$ . Both spheres are immersed in a dielectric medium

with dielectric constant  $\varepsilon_i$ . The problem is assumed to have a cylindrical symmetry along the  $z$ -direction which is parallel to both the external field  $E(\omega)$  as well as the separation between the two spheres. The dipole  $\mu_s(\omega)$  is assumed to be pointlike as usual and to be oriented along the  $z$ -axis as well.

In order to apply the system-bath approach to the problem at hand, we have to determine the corresponding electrostatic reaction and cavity fields inside the quantum dot. Since we aim to keep the analysis simple, we restrict ourselves to dipole-dipole interactions and apply the generic condition of small radii  $a/R \ll 1$ . We start by defining the relevant vectors and orientations according to Figure 4.6 to find the geometric conditions

$$r_m \cos \Theta_m = R + r_s \cos \Theta_s, \quad (4.43)$$

$$r_s \sin \Theta_s = r_m \sin \Theta_m, \quad (4.44)$$

with  $r_m$  and  $r_s$  being the moduli of the generic vectors  $\mathbf{r}_s$  and  $\mathbf{r}_m$ . This gives rise to the connection

$$r_m^2 = r_s^2 + R^2 + 2r_s R \cos \Theta_s \quad (4.45)$$

between  $r_s$  and  $r_m$ . As usual, we are tasked with finding the electrostatic potential  $\Phi$  in the different dielectric regions. Based on the generic structure for a potential with cylindrical symmetry in Equation (3.37), we make an ansatz for the potential inside the dot  $\Phi_s$ , the metallic nanoparticle  $\Phi_m$  and in the intermediate region  $\Phi_i$ , according to

$$\Phi_s(r_s, \Theta_s) = A_i^s + \left[ A_1^s r_s + \frac{\mu_s(\omega)}{4\pi\varepsilon_0 r_s^2} \right] \cos \Theta_s, \quad (4.46)$$

$$\Phi_m(r_m, \Theta_m) = A_i^m + A_1^m r_m \cos \Theta_m, \quad (4.47)$$

$$\Phi_i(r_s, \Theta_s, r_m, \Theta_m) = \left[ -E(\omega)r_s + \frac{B_1^i(\omega)}{r_s^2} \right] \cos \Theta_s + \frac{C_1^i}{r_m^2} \cos \Theta_m, \quad (4.48)$$

where the potentials are expressed in the spherical coordinates of the dot and the metallic particle, respectively. We have truncated the series of spherical harmonics at  $l = 1$  due to the spherical symmetry and the assumption of dipolar interactions only. In the intermediate region, we assumed the metallic particle to be represented by a contribution of dipolar type, emerging from an induced dipole moment located at the center of the MNP. Furthermore, we have already included the external electric field  $E(\omega)$  and the dipole of the SQD  $\mu_s(\omega)$ . The boundary conditions for the potentials are

given by

$$\Phi_i(r_s = a_s) = \Phi_s(r_s = a_s), \quad (4.49)$$

$$\Phi_i(r_m = a_m) = \Phi_m(r_m = a_m), \quad (4.50)$$

$$\varepsilon_i \frac{\partial \Phi_i}{\partial r_s}(r_s = a_s) = \varepsilon_s \frac{\partial \Phi_s}{\partial r_s}(r_s = a_s), \quad (4.51)$$

$$\varepsilon_i \frac{\partial \Phi_i}{\partial r_m}(r_m = a_m) = \varepsilon_m(\omega) \frac{\partial \Phi_m}{\partial r_m}(r_m = a_m). \quad (4.52)$$

Putting together Equations (4.46) to (4.48) and the conditions (4.49) to (4.52) yields the field inside the SQD via  $A_1^s = -E_s(\omega)$ . We find

$$\begin{aligned} E_s(\omega) = & (1 + \chi_s)E(\omega) + 2\chi_s \frac{\mu_s(\omega)}{4\pi\varepsilon_0 a_s^3} - 2\frac{a_m^3}{R^3}(1 + \chi_s)\chi_m(\omega)E(\omega) \\ & + 4\frac{a_s^3 a_m^3}{R^6}(1 + \chi_s)\chi_m(\omega) \left[ \chi_s E(\omega) + (1 - 2\chi_s) \frac{\mu_s(\omega)}{4\pi\varepsilon_0 a_s^3} \right]. \end{aligned} \quad (4.53)$$

In order to arrive at Equation (4.53), we have neglected terms of higher order than  $a^6/R^6$ , have approximated  $\cos \Theta_{m/s}/r_{m/s}^2 \approx (1/R^3) [\pm R - 2r_{s/m} \cos \Theta_{s/m}]$  and have used  $[1 - x]^{-1} \approx 1 + x$  where  $x$  depends on  $a_m^3 a_s^3 / R^6$ . The Onsager susceptibilities describe the interfaces as

$$\chi_s = \frac{\varepsilon_i - \varepsilon_s}{2\varepsilon_i + \varepsilon_s} \quad \text{and} \quad \chi_m(\omega) = \frac{\varepsilon_i - \varepsilon_m(\omega)}{2\varepsilon_i + \varepsilon_m(\omega)}. \quad (4.54)$$

Using the convention that  $\mu_s(\omega) = \mu\sigma_x(\omega)$  and separating the prefactor  $2\mu/(4\pi\varepsilon_0 a_s^3)$  as in Equation (4.23), we find

$$\chi_r(\omega) = \chi_s - 2\frac{a_s^3 a_m^3}{R^6}(1 + \chi_s)(1 - 2\chi_s)\chi_m(\omega), \quad (4.55)$$

while the cavity field is characterized by

$$\chi_c(\omega) = \left[ 1 + \chi_s - 2\frac{a_m^3}{R^3}(1 + \chi_s)\chi_m(\omega) \left( 1 - 2\chi_s \frac{a_s^3}{R^3} \right) \right]. \quad (4.56)$$

#### 4.4.3 Linear response of the quantum dot

Having determined the cavity and the reaction field in Equations (4.55) and (4.56), the effective force is directly provided by Equation (4.23). As such, we are now faced with the issue of determining the linear response of Equation (4.20) for the spin-boson model. This requires us to determine the retarded Green's function of the system which

can only be done approximately. We will explicitly derive a response function for the spin-boson model later in Part 5 on the basis of a master equation framework. For simplicity, however, we defer to the literature in this section. In particular, Gan et al. [73] use a specific unitary transformation of the Hamiltonian after which they apply the Born approximation in order to derive explicit results for the retarded Green's function. In addition to supplying us with a suitable result, their method improves upon simpler schemes by allowing for a wider parameter range even while still assuming weak coupling between system and bath. For the system given by Equation (4.41), their result reads

$$G(\omega) = + \frac{\omega - \omega_0 - R(\omega) - i\gamma(\omega)}{[\omega - \omega_0 - R(\omega)]^2 + [\gamma(\omega)]^2} \Theta(\omega) \\ + \frac{\omega + \omega_0 + R(-\omega) + i\gamma(-\omega)}{[\omega + \omega_0 + R(-\omega)]^2 + [\gamma(-\omega)]^2} \Theta(-\omega), \quad (4.57)$$

which represents (in our convention) the Fourier transform of the Green's function  $G(t) = -i\Theta(t)\text{Tr}\{\rho_S^{\text{eq}}[\sigma_x(t), \sigma_x]\}$  and is valid for zero temperature and weak coupling. In order to find the actual form of the self-energy contributions  $R(\omega)$  and  $\gamma(\omega)$ , we have to derive the spectral density of the model. By application of Equation (2.36) while noting an additional factor of  $2\mu$  from Equation (4.41), we obtain

$$\hbar J(\omega) = \frac{(2\mu)^2}{4\pi\varepsilon_0 a_s^3} \text{Im}[\chi_r(\omega)] = \kappa \frac{\Gamma\omega_r^2\omega}{(\omega^2 - \omega_r^2)^2 + \Gamma^2\omega^2}. \quad (4.58)$$

Here, we have inserted the dielectric function of Equation (4.42) and have defined  $\omega_r = \omega_p/\sqrt{2\varepsilon_i + 1}$ . Note that the spectral density  $J(\omega)$  of Equation (4.58) gives the rescaled spectral density of Equation (2.54). The prefactor  $\kappa$  includes all geometrical parameters as

$$\kappa = \frac{\mu^2}{4\pi\varepsilon_0} \frac{6^3\varepsilon_i^2\varepsilon_s a_m^3}{(2\varepsilon_i + \varepsilon_s)^2(2\varepsilon_i + 1)R^6}. \quad (4.59)$$

The quantities  $R(\omega)$  and  $\gamma(\omega)$  are then defined as

$$R(\omega) = \frac{\kappa\omega_r\omega_0^2}{2\hbar(\omega - \omega_r)(\omega_r + \omega_0)^2}, \quad (4.60)$$

$$\gamma(\omega) = \frac{\omega_0^2}{(\omega_0 + \omega)^2} J(\omega), \quad (4.61)$$

where we have assumed for simplicity that  $\Gamma\omega \rightarrow 0$  for the calculation of  $R(\omega)$ . The effective driving field follows from the equations of motion as

$$E_{\text{eff}}(t) = \int_{-\infty}^{\infty} dt' \chi_c(t-t') E(t') \\ = E(t) + \int_{-\infty}^{\infty} dt' \lambda(t-t') E(t'). \quad (4.62)$$

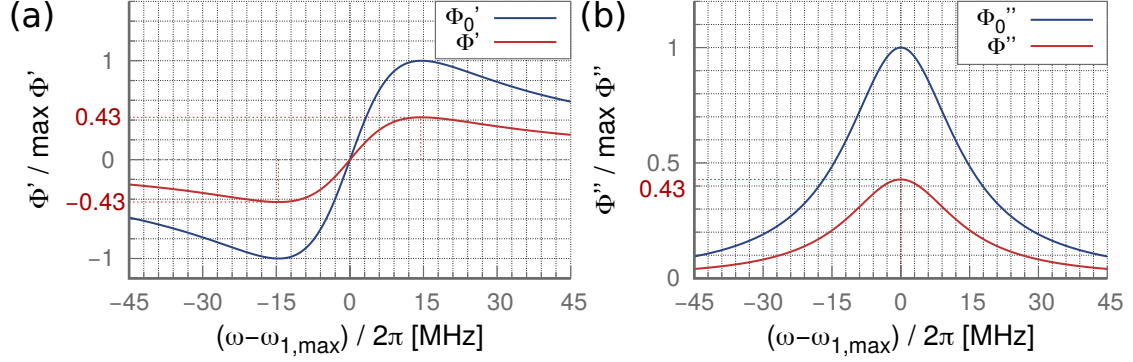


**Figure 4.7:** Real (a) and imaginary part (b) of the linear response  $\Phi(\omega) = \Phi'(\omega) + i\Phi''(\omega)$  given in Equation (4.65), evaluated around the shifted two-state splitting frequency  $\omega_{1,\max} \approx \omega_0$ . The full response (red) is shown in contrast to the bare result  $\Phi_0(\omega)$  where both driving contributions are not included (blue). Both curves have been normalized to the maximum of the bare result. At the two-state frequency, the response is suppressed by a factor of 0.43 in both real and imaginary part (red numbers).

Equation (4.62) shows a direct driving contribution that has been separated from the cavity field by defining  $\lambda(\omega) = \chi_c(\omega) - 1$ . Once more, the kernel  $\lambda(t)$  represents the effect of bath driving. The effective driving field of the problem in Fourier space then follows as

$$E_{\text{eff}}(\omega) = [1 + \lambda(\omega)]E(\omega). \quad (4.63)$$

We are now in the position to calculate the linear response of the setup. As before, we restrict ourselves to the case of monochromatic driving, i.e.,  $E(t) = E_0 \cos(\omega_e t)$ . This allows us to obtain the average of  $\mu_s = \mu\sigma_x$  as

$$\begin{aligned} \langle \mu_s(t) \rangle &= -\frac{\mu^2}{\hbar} \int_{-\infty}^{\infty} dt' G(t-t') E_{\text{eff}}(t') \\ &= \text{Re} \left[ -\frac{\mu^2}{\hbar} G(\omega_e) [1 + \lambda(\omega_e)] E_0 e^{-i\omega_e t} \right]. \end{aligned} \quad (4.64)$$

We can read off the extended linear response as

$$\Phi(\omega) = -\frac{\mu^2}{\hbar} G(\omega) [1 + \lambda(\omega)] \quad (4.65)$$

#### 4.4.4 Evaluation of the linear response

As before, we aim to evaluate Equation (4.65) and discuss the emerging results in contrast to the response without bath driving effects. To do so, we have to find suitable

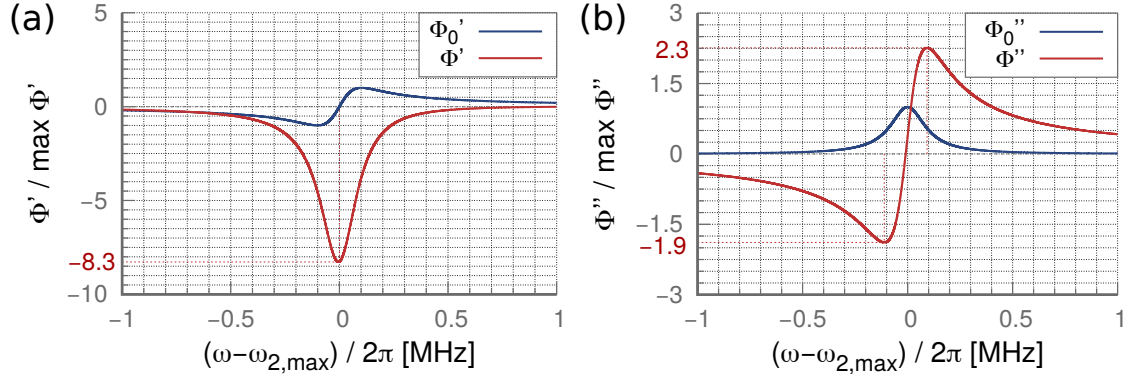


**Figure 4.8:** Real (a) and imaginary part (b) of the linear response  $\Phi(\omega) = \Phi'(\omega) + i\Phi''(\omega)$  given in Equation (4.65), evaluated around the shifted plasmon frequency  $\omega_{2,max} \approx \omega_r$ . The full response (red) is shown in contrast to the bare result  $\Phi_0(\omega)$  where bath driving contributions are not included (blue). Both curves have been normalized to the maximum of the bare result. The response at the plasmon frequency is strongly altered with a complete exchange of real- and imaginary part and evident quantitative enhancement (red numbers).

parameters for the physical problem. First, our general energy scale has to be in the optical regime, i.e., has to have values in the low eV-range. For typical gold nanoparticles, the dielectric function can be modeled with a plasma frequency of  $\hbar\omega_p = 8.5$  eV and a Debye relaxation time of  $\tau_D = 14$  fs [194]. Similarly, CdSe nanocrystals can be used to model the SQD. In accordance, we set the excitonic energy gap to  $\hbar\omega_0 = 2.5$  eV and choose the dielectric constant of the SQD as  $\varepsilon_s = 6.0$  [191, 196]. The surrounding medium is assumed to be empty such that  $\varepsilon_i = 1$ . This particular choice of energies reflects our desire to retain comparable energy scales between the bath mode and the system. Indeed, with these parameters the renormalized energy scale of the bath mode turns out to be  $\hbar\omega_r \approx 2\hbar\omega_0$ , which is reasonably close to investigate the impact of the driven bath mode. Lastly, the dimensions of the setup have been chosen as  $a_s = 0.65$  nm,  $a_m = 7.5$  nm and  $R = 20$  nm in line with typical values [191, 196]. Note that this choice is constrained by the dipole approximation used to derive the cavity and reaction field above. Utilizing all parameters leads to an extremely small coupling strength of  $\kappa \approx 10^{-8}\hbar\omega_0$  for a dipole of 1 Debye which fulfills the requirement of low coupling strength required by Equation (4.57).

The resulting dynamical response is shown in Figures 4.7 and 4.8 at the two relevant frequencies. Given the small coupling constant, the resonant frequencies are not shifted appreciably and we can state  $\omega_1 \approx \omega_0$  and  $\omega_2 \approx \omega_r$ . The first frequency corresponds to the two-state splitting in the dot. As in case of the polarizable molecule, no significant qualitative changes can be observed for the parameter range we utilize except for a broad scaling of peak height. Instead of an enhancement, however, both real and imaginary part are suppressed by about 43% in contrast to the case without bath driving.

This suggests that bath driving effects interfere with the response characteristics at this frequency. In contrast, the second frequency corresponds to the plasmonic mode in the bath and we may therefore expect a stronger impact at this frequency. The response clearly supports this notion as the peak height is increased by an order of magnitude in the real part and a factor of four in the imaginary part. Additionally, an almost complete exchange of real and imaginary part can be observed. This can be made manifest by splitting the response into real and imaginary part as before. We quickly find

$$\Phi'(\omega) = -\frac{\mu^2}{\hbar} \{G'(\omega)[1 + \lambda'(\omega)] - G''(\omega)\lambda''(\omega)\} , \quad (4.66)$$

$$\Phi''(\omega) = -\frac{\mu^2}{\hbar} \{G''(\omega)[1 + \lambda'(\omega)] + G'(\omega)\lambda''(\omega)\} , \quad (4.67)$$

where we denoted real parts with a prime and imaginary parts with two. The second terms of (4.66) and (4.67) couple imaginary and real parts via the complex function  $\lambda(\omega)$ , whereas the first lead to a scaling of the response peaks. Again, we may interpret the negative imaginary part as a sign of emission, whose detailed origin has to be discussed in future research. Nevertheless, we may suppose that the bounded nature of the TSS may give rise to a population inversion such that the usual conditions for lasing are fulfilled.

## 4.5 Conclusion of Part 4

Throughout this part of the thesis, we have established our first major result: a linearly driven bath creates an additional force component onto the system in question. We have seen that this force is determined by a retarded kernel  $\lambda(t)$  which can be formulated in a convenient way by introducing a secondary spectral density  $\bar{J}(\omega)$  given in Equation (4.11). This additional spectral density depends on the coupling constants of the force to the bath modes and is an a priori unknown quantity. By utilizing the Onsager solvation model, we were able to connect the additional force component to the emerging Onsager cavity field. This approach allowed us to derive a simple proportionality between the two spectral densities and enabled us to investigate the impact of this new force component. In this chapter, our method of choice was the evaluation of the extended linear response for two particular nanosystems. Specifically, we have investigated the response of a polarizable molecule immersed in water and subjected to radiation in the THz-regime, as well as an interacting quantum-dot metal-nanoparticle setup driven by optical laser fields. Both cases represent physical systems where pronounced bath modes indicate the possibility for the bath to interact with the driving field as well. Utilizing the basic models of quantum dissipation, we have treated the polarizable molecule as a forced harmonic oscillator and applied the spin-boson model to the quantum-dot metal-nanoparticle setup. The resulting response spectra show an enhancement or

suppression as well as qualitative changes which can be explained by a mixing of real and imaginary part mediated by the Fourier-transformed kernel  $\lambda(\omega)$ . Indeed, the effects were so profound that the imaginary part of the response became negative, suggesting that the system is able to emit radiation due to energy transfer from the driven bath.

This part of the thesis has shown that bath driving changes the dynamics associated with driven quantum systems, leading not only to an enhancement or suppression of response signals but also to a qualitatively different response behavior when bath driving is considered. Bath driving may thus constitute a novel way of exciting and controlling dissipative quantum systems, for instance by tuning the driving frequency to the selected bath modes. At this point, such a statement is somewhat surprising given that we restricted ourselves to purely linear effects throughout, most notably by using a dipolar coupling between bath and driving field and by only considering the extended linear response of the quantum system. In the following parts of this thesis, we will try to relax some of these assumptions and investigate their impact onto the dynamics of coupled systems.



## The non-Markovian force and quantum master equation approach

In the last chapter, we saw that a system in contact with a linearly driven bath experiences a new retarded force component which adds to an already present direct driving force. The linear response for the case of two nanosystems in contact with a structured bath was seen to be qualitatively altered due to this new force component. In this part of the thesis, we aim to develop a more complete picture of the problem by introducing this effective force on the level of the Hamiltonian. This procedure will enable us to show not only that this force fully encodes the nonequilibrium dynamics of the bath but also allows us to derive and investigate a nonlinear response function by way of a specific master equation approach [83, 197]. This part of the thesis is based on published results by the author [2].

### 5.1 The non-Markovian force

We start from the spin-boson model for dipolar bath driving given in Equation (4.12)

$$\begin{aligned}
 H(t) = H_0 + H_{\text{IB}}(t) &= \frac{\hbar\omega_0}{2}\sigma_x - \frac{\sigma_z}{2} \sum_{\alpha=1}^N \hbar\lambda_{\alpha}(b_{\alpha} + b_{\alpha}^{\dagger}) \\
 &+ \sum_{\alpha=1}^N \hbar\omega_{\alpha}b_{\alpha}^{\dagger}b_{\alpha} - \frac{F(t)}{2} \sum_{\alpha=1}^N \hbar\mu_{\alpha}(b_{\alpha} + b_{\alpha}^{\dagger}).
 \end{aligned} \tag{5.1}$$

Here, we used the description in terms of annihilation and creation operators for the bath Hamiltonian and removed the zero-point energy contribution. In order to keep our analysis simple, we also set the asymmetry  $\epsilon = 0$  and disregard the direct driving contribution to the two-state system for the time being. We note the definition  $\Delta = \hbar\omega_0$  from Section 2.2.3, inserted here as the characteristic frequency  $\omega_0$  will appear throughout this part of the thesis to parametrize the time variable. The spectral density

of the bath is given by Equation (2.54) as

$$J(\omega) = \pi \sum_{\alpha=1}^N \lambda_{\alpha}^2 \delta(\omega - \omega_{\alpha}). \quad (5.2)$$

In this part of the thesis, we consider two kinds of spectral densities

$$J^{(1)}(\omega) = \frac{\eta\omega}{\omega_c} e^{-\omega/\omega_c}, \quad (5.3)$$

$$J^{(2)}(\omega) = \kappa \frac{\Gamma\Omega^2\omega}{(\omega^2 - \Omega^2)^2 + (\Gamma\omega)^2}. \quad (5.4)$$

Equation (5.3) describes an ordinary Ohmic spectral density as seen in Equation (2.29). Equation (5.4) is a Lorentzian density as given by Equation (2.37) which represents the kind of structured baths we already considered for the two nanosystems in the previous chapter (cf. Equation (4.58)). In contrast to the definition in Equation (2.29), the cutoff frequency  $\omega_c$  has been used here to rescale the density (5.3) such that  $\eta$  and  $\kappa$  have the same dimension of a frequency. We will also make use of the mapping procedure outlined in Section 2.2.2. Specifically, the undriven Hamiltonian  $H_0$  with the Lorentzian spectral density (5.4) is equivalent to [72–74]

$$\begin{aligned} H_0 = & \frac{\hbar\omega_0}{2}\sigma_x - \hbar g\sigma_z(B + B^\dagger) + \hbar\Omega B^\dagger B \\ & + \sum_{\alpha=1}^{N'} \hbar\omega'_\alpha b_\alpha^\dagger b'_\alpha + (B + B^\dagger) \sum_{\alpha=1}^{N'} \hbar\lambda'_\alpha (b'_\alpha + b_\alpha^\dagger), \end{aligned} \quad (5.5)$$

where the annihilation and creation operators  $B$  and  $B^\dagger$  describe a single harmonic oscillator with energy  $\hbar\Omega$  coupled to a bath with an Ohmic spectral density of the form (2.29) with prefactor  $\eta' = \Gamma/(2\Omega)$ . The coupling to the system is given by  $g = \sqrt{\kappa\Omega/8}$ . We also omitted a potential renormalization term here.

### ***Pulsed bath driving scheme***

In the previous chapter we considered the response to a simple monochromatic AC driving field in the long-time limit. This led to fairly simple expressions where we could read off the corrected linear response directly. In this part of the thesis, we extend our analysis to pulse-shaped bath driving schemes, where the perturbation is constrained to a specific time span. This will allow us to investigate cases where the coupling time and the time of onset of the perturbation differ. As we shall see, this also yields insights about the nature of the effective force and the resulting bath states. Most importantly, we will use our results to show that the new force component fully encodes the memory

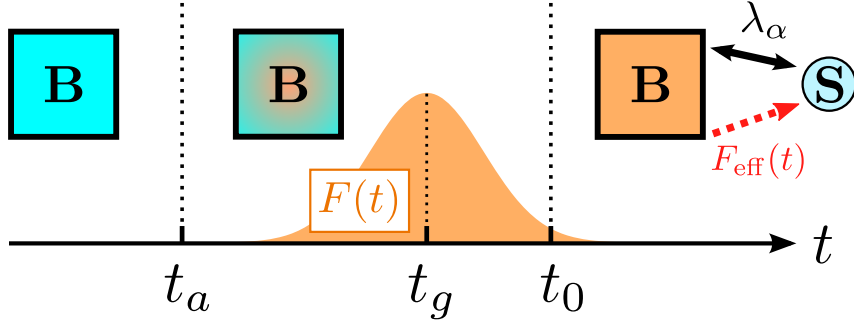


**Figure 5.1:** General setup of the pulse-shaped bath driving scheme we consider. The bath (B) is in equilibrium until time  $t_a$ , when the bath driving force  $F(t)$  is activated. Subsequently, the bath is driven out of equilibrium (orange color) by a pulse centered at some time  $t_g$  (orange Gaussian). The system (S) is coupled to the driven bath at time  $t_0$ . In this part of the thesis, we consider a generic spin-boson model with coupling  $\lambda_\alpha$ . As shown, the driven bath induces an additional effective force  $F_{\text{eff}}(t)$  on the system.

of the bath by explicitly analyzing the case where the system is coupled to a bath already subject to driving at an earlier time.

Our general setup is depicted in Figure 5.1. Three times are now relevant: the time of the onset of the perturbation  $t_a$  after which  $F(t)$  is nonzero, the time  $t_g$  where the perturbation is centered and the coupling time  $t_0$  when we (instantaneously) couple system and bath. We assume factorizing initial conditions, i.e., the combined density matrix  $W(t)$  of system and bath is given as a product until the coupling time is reached (cf. Equation (2.61)). Thus,

$$W(t \leq t_0) = \rho_S(t) \otimes \rho_B(t), \quad (5.6)$$

where  $\rho_S(t)$  designates the reduced density matrix of the system and  $\rho_B(t)$  the corresponding reduced density matrix of the bath. The bath is assumed to be in equilibrium until activation of the driving force, i.e.,

$$\rho_B(t \leq t_a) = \rho_B^{\text{eq}} = e^{-\beta H_B} / \mathcal{Z}. \quad (5.7)$$

Here, the temperature is encoded in  $k_B T = 1/\beta$  and  $\mathcal{Z}$  is the equilibrium partition function of the decoupled bath. Following  $t_a$ , the bath is driven out of equilibrium and  $\rho_B(t)$  becomes a nonequilibrium distribution. The bath degrees of freedom are then subject to the driven bath Hamiltonian (4.3), which reads here

$$H_B^{\text{eff}}(t) = H_B + H_{\text{IB}}(t) = \sum_{\alpha=1}^N \hbar \omega_\alpha b_\alpha^\dagger b_\alpha - \frac{F(t)}{2} \sum_{\alpha=1}^N \hbar \mu_\alpha (b_\alpha + b_\alpha^\dagger). \quad (5.8)$$

Finally, we consider two particular pulse shapes for the field  $F(t)$ : a  $\delta$ -shaped and a Gaussian driving pulse, described by

$$F^{(1)}(t) = \omega_0^{-1} \delta(t - t_a), \quad (5.9)$$

$$F^{(2)}(t) = \frac{\omega_0^{-1}}{\sqrt{2\pi\sigma^2}} e^{-\frac{(t-t_g)^2}{2\sigma^2}}. \quad (5.10)$$

The area of both pulses is normalized to  $\omega_0^{-1}$  and  $F(t)$  is set to be dimensionless. For the Dirac pulse we also note that  $t_g$  and  $t_a$  coincide. These particular pulse shapes permit for relatively simple expressions for the resulting effective force.

### 5.1.1 The effective force

We are now ready to introduce the effective force. To do so, we evaluate the Heisenberg equation of motion for the bath operator  $b_\alpha$ , subject to the time evolution described by Equation (5.8). In the following, we denote Heisenberg operators with a tilde and consider the interval  $[0, t]$  with  $t \geq t_a \geq 0$  for simplicity.  $\tilde{b}_\alpha(t)$  then fulfills

$$\frac{d\tilde{b}_\alpha(t)}{dt} + i\omega_\alpha \tilde{b}_\alpha(t) - i \frac{\mu_\alpha F(t)}{2} = 0, \quad (5.11)$$

which can be solved to yield

$$\tilde{b}_\alpha(t) = \tilde{b}_\alpha^0(t) + \frac{1}{2} K_\alpha(t, t_a). \quad (5.12)$$

The first term denoted by  $\tilde{b}_\alpha^0(t)$  gives the undriven time evolution

$$\tilde{b}_\alpha^0(t) = b_\alpha e^{-i\omega_\alpha t}, \quad (5.13)$$

while  $K_\alpha$  couples to the identity and describes the driving-induced term

$$K_\alpha(t, t_a) = i \int_{t_a}^t dt' e^{i\omega_\alpha(t'-t)} \mu_\alpha F(t'). \quad (5.14)$$

The corresponding equation for  $\tilde{b}_j^\dagger(t)$  can be obtained from Hermitian conjugation. The new driving term  $K_\alpha(t, t_a)$  displaces the operator from its equilibrium position at zero. This follows since

$$\langle \tilde{b}_j(t) \rangle_{\text{B}}^{\text{eq}} = \langle \tilde{b}_\alpha^0(t) \rangle_{\text{B}}^{\text{eq}} + \langle K_\alpha(t, t_a)/2 \rangle_{\text{B}}^{\text{eq}} = K_\alpha(t, t_a)/2, \quad (5.15)$$

where we have used  $\langle \tilde{b}_\alpha^0(t) \rangle_B^{\text{eq}} = 0$ . This also means that (bath-) averages of the coupling operator no longer vanish as we have

$$\begin{aligned} \langle H_{\text{SB}} \rangle_B(t) &= -\frac{\sigma_z}{2} \sum_{\alpha=1}^N \hbar \lambda_\alpha \langle \tilde{x}_\alpha(t) \rangle_B^{\text{eq}} \\ &= -\frac{\sigma_z}{2} \text{Re} \left[ \sum_{\alpha=1}^N \hbar \lambda_\alpha K_\alpha(t, t_a) \right] \equiv \frac{\sigma_z}{2} \hbar F_{\text{eff}}(t), \end{aligned} \quad (5.16)$$

where we have introduced the dimensionless (Heisenberg) position operator  $\tilde{x}_j(t) = \tilde{b}_j(t) + \tilde{b}_j^\dagger(t)$ . Equation (5.16) defines the effective force  $F_{\text{eff}}(t)$  as

$$\begin{aligned} F_{\text{eff}}(t) &= \Theta(t - t_0) \text{Im} \left[ \frac{1}{\pi} \int_0^\infty d\omega \bar{J}(\omega) \int_{t_a}^t dt' F(t') e^{i\omega(t'-t)} \right] \\ &= \Theta(t - t_0) \frac{1}{\pi} \int_0^\infty d\omega \bar{J}(\omega) \int_{t_a}^t dt' F(t') \sin[\omega(t' - t)]. \end{aligned} \quad (5.17)$$

In the second equation, we have used that  $F(t)$  and  $\bar{J}(\omega)$  must be real. We have also explicitly noted the time dependence of the system-bath coupling constants in a Heaviside function. Evidently, the effective force coincides with what we found in Part 4. However,  $F_{\text{eff}}$  is not a force but defined as a frequency here such that  $\hbar F_{\text{eff}}$  gives an effective time-dependent asymmetry (as in Equation (4.19)).  $\bar{J}(\omega)$  is defined in accordance with Equation (5.2) as

$$\bar{J}(\omega) = \pi \sum_{\alpha=1}^N \mu_\alpha \lambda_\alpha \delta(\omega - \omega_\alpha). \quad (5.18)$$

Lastly, we note that Equation (5.16) denotes the nonequilibrium bath average and not just the case for equilibrium. This follows because the time evolution of the bath density matrix can be factored out into the coupling operators until an equilibrium average remains. Specifically,

$$\begin{aligned} \langle H_{\text{SB}} \rangle_B(t) &= \text{Tr}_B [H_{\text{SB}} \rho_B(t)] = \text{Tr}_B [H_{\text{SB}} U(t) \rho_B(0) U^\dagger(t)] \\ &= \text{Tr}_B [U^\dagger(t) H_{\text{SB}} U(t) \rho_B^{\text{eq}}] = \langle \tilde{H}_{\text{SB}}(t) \rangle_B^{\text{eq}}. \end{aligned} \quad (5.19)$$

Here, we have denoted the time evolution operator with the Hamiltonian (5.8) as  $U(t)$ , used the cyclical invariance of the trace and assumed  $\rho_B(0) = \rho_B^{\text{eq}}$ . The simple procedure outlined here will also allow us to rewrite the correlation functions that appear in the perturbative expansion as equilibrium averages.

### 5.1.2 Redefined Hamiltonian

By introducing the effective force via Equation (5.16) we can exploit perturbative methods for our purposes. In particular, we saw in Section 2.3.1 that Born-Markov master equation approaches are based on perturbation theory in the system-bath coupling Hamiltonian. The resulting dynamics for the system are then determined by bath correlation functions (cf. Equation (2.64)). As we have seen in Equation (5.16), linear bath driving induces a time-dependent shift on the dynamics of the coupling operator. If we subtract this shift by a suitable redefinition in the Hamiltonian, we can recover the dynamics rendered by an undriven bath. This approach is not particularly new, as it is commonly used in master equation approaches for time-independent problems when  $\langle H_{\text{SB}} \rangle = \text{const}$  [5]. In our case, we add zero to Equation (5.1) by choosing

$$\begin{aligned} H(t) &= H(t) - \langle H_{\text{SB}} \rangle_{\text{B}}(t) + \langle H_{\text{SB}} \rangle_{\text{B}}(t) \\ &= H_{\text{S}}^{\text{eff}}(t) + H_{\text{SB}}^{\text{eff}}(t) + H_{\text{B}}^{\text{eff}}(t), \end{aligned} \quad (5.20)$$

with  $H_{\text{B}}^{\text{eff}}(t)$  given in Equation (5.8). As a first consequence, the system-bath coupling operator becomes

$$H_{\text{SB}}^{\text{eff}}(t) = -\frac{\sigma_z}{2} \sum_{\alpha=1}^N \hbar \lambda_{\alpha} x_{\alpha}^{\text{eff}}(t), \quad (5.21)$$

with  $x_{\alpha}^{\text{eff}}(t) = x_{\alpha} - \langle \tilde{x}_{\alpha}(t) \rangle_{\text{B}}^{\text{eq}}$ . In addition, the system Hamiltonian also becomes time-dependent as

$$H_{\text{S}}^{\text{eff}}(t) = \frac{\hbar \omega_0}{2} \sigma_x + \frac{\hbar F_{\text{eff}}(t)}{2} \sigma_z. \quad (5.22)$$

With this redefinition, the shifted Heisenberg position operator now includes only the free time evolution as  $\tilde{x}_{\alpha}^{\text{eff}}(t) = \tilde{x}_{\alpha}(t) - \langle \tilde{x}_{\alpha}(t) \rangle_{\text{B}}^{\text{eq}} = \tilde{x}_{\alpha}^0(t)$ . Consequently, the bath autocorrelation function remains unchanged compared to the equilibrium case of Equation (2.25). For later purposes, we note that its real part defines the symmetric bath autocorrelation function  $B_{\text{C}}(t, s)$  as

$$\begin{aligned} B_{\text{C}}(t, s) &= \sum_{\alpha, \alpha'=1}^N \frac{\lambda_{\alpha} \lambda_{\alpha'}}{2} \langle \{ \tilde{x}_{\alpha}^{\text{eff}}(t), \tilde{x}_{\alpha'}^{\text{eff}}(s) \} \rangle_{\text{B}}^{\text{eq}} \\ &= \sum_{\alpha=1}^N \lambda_{\alpha}^2 \coth \left( \frac{\beta \hbar \omega_{\alpha}}{2} \right) \cos[\omega_{\alpha}(t - s)], \end{aligned} \quad (5.23)$$

where  $\{\cdot, \cdot\}$  denotes the anticommutator. The imaginary part gives the bath response function  $B_R(t, s)$  as

$$\begin{aligned} B_R(t, s) &= \sum_{\alpha, \alpha'=1}^N \frac{\lambda_\alpha \lambda_{\alpha'}}{2} i \langle [\tilde{x}_\alpha^{\text{eff}}(t), \tilde{x}_{\alpha'}^{\text{eff}}(s)] \rangle_B^{\text{eq}} \\ &= \sum_{\alpha=1}^N \lambda_\alpha^2 \sin[\omega_\alpha(t - s)]. \end{aligned} \quad (5.24)$$

Coming back to (5.22), the effective force now appears as an effective asymmetry of the two-state system, consistent with our expectation from Equation (4.19). We can also see from the explicit form in Equation (5.17) that the force includes the full driven time evolution in the interval  $[t_a, t]$ . Together with Equations (5.23) and (5.24) this implies that the force encodes the nonequilibrium properties of the bath. This conclusion is not new as we have already derived it by way of the quantum Langevin equation in the last part of this thesis. However, we can now extend this argument to the case where bath driving sets in prior to the coupling time  $t_0$ , as depicted in Figure 5.1, where the system couples to an already driven bath. The force itself will then be zero until time  $t_0$  as it depends on the coupling constants between system and bath. However, for  $t > t_0$ , the effective force still includes the time interval down to  $t_a$  when the force was first activated. Thus, the force encodes the history, or memory, of the bath since the activation of the driving force. It is for this reason, that we can refer to the effective force given in Equation (5.17) as a *non-Markovian force*. Note that this only describes the force component introduced by bath driving and we did not take direct driving of the system into account in this chapter.

### 5.1.3 Characterization of the non-Markovian force

Before proceeding to evaluate the dynamics, we will take a look at the behavior of the non-Markovian force given in Equation (5.17). We analyze the force for an Ohmic and a Lorentzian effective spectral density given by

$$\bar{J}^{(1)}(\omega) = \frac{\bar{\eta}\omega}{\omega_c} e^{-\omega/\omega_c} \quad \text{and} \quad \bar{J}^{(2)}(\omega) = \bar{\kappa} \frac{\Gamma\Omega^2\omega}{(\omega^2 - \Omega^2)^2 + (\Gamma\omega)^2}. \quad (5.25)$$

Here, we chose the same form as the spectral densities in Equations (5.3) and (5.4) but signified the prefactor with an additional bar. This choice is based on our conclusion in Section 4.2.3 where we saw that the Onsager sphere model can be used to derive a direct proportionality between the ordinary spectral density and the effective spectral density (Equation (4.25)). We will explicitly make use of this connection in the next Section. Evaluation of the effective force yields

$$F_{\text{eff}}^\delta(t) = -\frac{1}{\pi\omega_0} \int_0^\infty d\omega \bar{J}(\omega) \sin[\omega(t - t_a)], \quad (5.26)$$

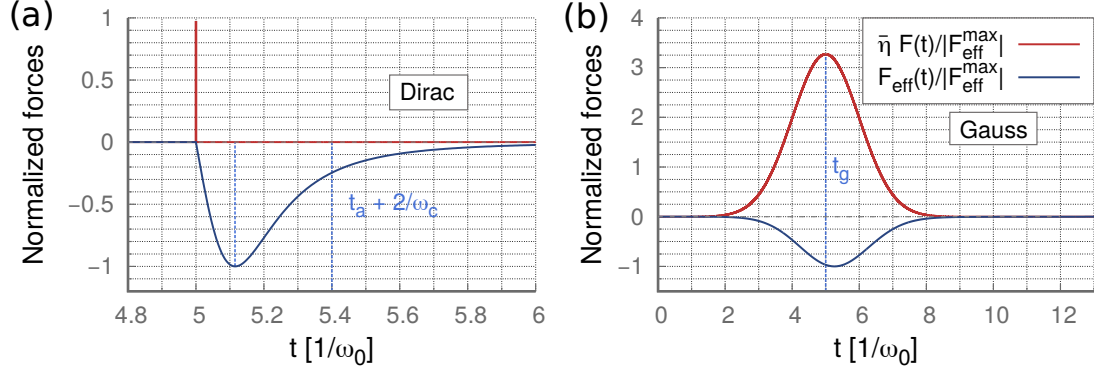


**Figure 5.2:** Normalized effective force  $F_{\text{eff}}(t)$  (blue) and direct bath driving force  $\bar{\eta}F(t)$  (red) for the Ohmic density  $\bar{J}^{(1)}(\omega)$  driven by a Dirac  $\delta$ -pulse (a) and a Gaussian pulse (b). Both pulses are centered at  $t_g = 5\omega_0^{-1}$  while the Gaussian starts at  $t_a = 0$ . The bath is characterized by a cutoff frequency  $\omega_c = 5\omega_0$ . The interaction strength of the Dirac pulse is set as  $\bar{\eta} = 2\omega_0$  while the Gaussian has a strength  $\bar{\eta} = 6\omega_0$  and a width  $\sigma = \omega_0^{-1}$ . Both quantities are normalized with respect to the maximum of the effective forces.

for the  $\delta$ -pulse of Equation (5.9) and

$$F_{\text{eff}}^g(t) = \text{Im} \left[ \frac{1}{2\pi\omega_0} \int_0^\infty d\omega \bar{J}(\omega) e^{-\frac{\omega^2\sigma^2}{2} - i\omega(t-t_g)} \text{erfc}(\zeta_t) \right], \quad (5.27)$$

for the Gaussian pulse of Equation (5.10). We assumed  $t > t_0$  in both cases and used  $\zeta_t = (i\omega\sigma^2 - t + t_g)/\sqrt{2\sigma^2}$  while  $\text{erfc}(z)$  designates the complementary error function. For the Ohmic density of Equation (5.25), the integral in Equation (5.26) can also be solved analytically to yield

$$F_{\text{eff}}^{\delta,(1)}(t) = -\frac{2\bar{\eta}\omega_c}{\pi\omega_0} \frac{\omega_c(t-t_a)}{[1 + \omega_c^2(t-t_a)^2]}. \quad (5.28)$$

The explicit driving pulses  $F(t)$  and the resulting non-Markovian forces are shown in Figure 5.2 for the Ohmic spectral density  $\bar{J}^{(1)}(\omega)$  for the parameters indicated. In this case, the profile of the non-Markovian force follows the original pulse closely, albeit with a lower peak strength. A clear retardation can also be observed. In the case of the  $\delta$ -pulse both retardation and subsequent decay follow on a time scale  $1/\omega_c$  as can be seen from the analytic solution. The latter result is reasonable, as the cutoff is the only distinguished frequency scale in the absence of a pronounced mode in the bath. Hence, similar deviations occur for the Gaussian on that time scale but are overshadowed by the comparably large width of the original pulse. This implies that the new force becomes effectively instantaneous with  $F(t)$  for large cutoffs. In this case the non-Markovian force simply gives a correction to the strength of a direct driving pulse.



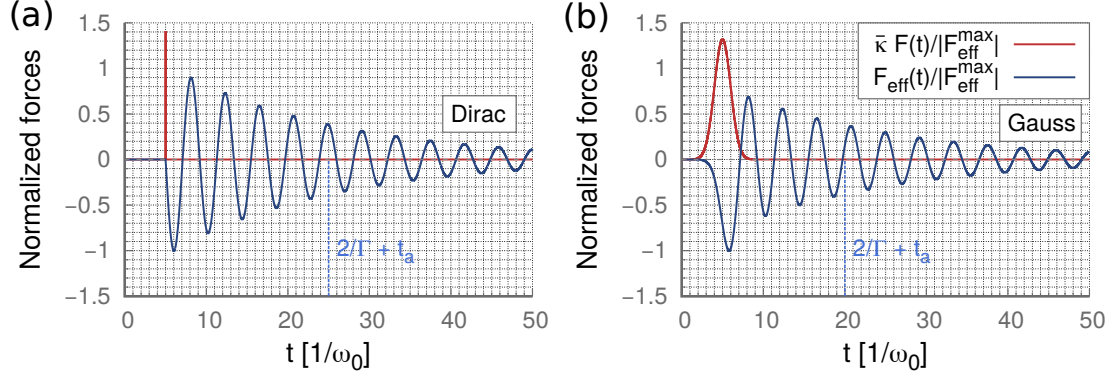


**Figure 5.3:** Normalized effective force  $F_{\text{eff}}(t)$  (blue) and direct bath driving force  $\bar{\kappa}F(t)$  (red) for the Lorentzian density  $\bar{J}^{(2)}(\omega)$  driven by a Dirac  $\delta$ -pulse (a) and a Gaussian pulse (b). Both pulses are centered at  $t_g = 5\omega_0^{-1}$  while the Gaussian starts at  $t_a = 0$ . The bath is characterized by the parameters  $\Omega = 1.5\omega_0$  and  $\Gamma = 0.1\omega_0$ . The interaction strength of the Dirac pulse is set to  $\bar{\kappa} = 2\omega_0$ , while the Gaussian has a strength  $\bar{\kappa} = 6\omega_0$  and a width  $\sigma = \omega_0^{-1}$ . Both quantities are normalized with respect to the maximum of the effective forces.

The Lorentzian cases are shown in Figure 5.3. Their main feature is a comparably long-lived pattern of exponentially decaying oscillations. These can be successfully fitted by the function

$$F_{\text{eff}}^{(2)}(t) \approx -A \sin(\Omega t) e^{-\Gamma t/2}, \quad (5.29)$$

where  $A$  is a fit parameter. Evidently, the force is governed by the interaction with the mode and is strongly reminiscent of the behavior of a damped harmonic oscillator with frequency  $\Omega$  and friction proportional to  $\Gamma/2$ . This observation is in line with the mapped Hamiltonian in Equation (5.5) if we utilize Equation (2.31): the friction term of the oscillator is then proportional to  $\hbar\eta'/q_0^2 \propto \Gamma/2$  which directly gives the correct time scale. As such, a TSS in a Lorentzian bath experiences a force chiefly governed by the oscillating bath mode. The Lorentzian density may also be simplified in the case of very narrow resonances as a delta-function. This implies a simple sinusoidal behavior of the effective force in case of the  $\delta$ -pulse.

In contrast, changes in the pulse shapes themselves only lead to deviations on the time scale when the force is still active, which is why the first oscillation is contorted in the case of the Gaussian. For stronger damping (i.e. a broader mode) or comparably long-lasting forces these effects will become more important. Finally, the comparison between spectral densities supports the notion employed in the previous chapter, where we reasoned that bath driving could have a larger effect in baths with pronounced modes. In contrast, the effect from dipolar bath driving just recreates the original pulse with a different strength for structureless baths with a broad frequency response for which  $\omega_c$  is large.

## 5.2 Adiabatic-Markovian master equation approach

With the non-Markovian force of Equation (5.17) and the redefined Hamiltonian of Equation (5.19) at hand, we are now going to obtain the approximate dynamics for the two-state system (TSS). For this purpose, we introduce a specific master equation approach based on the works of Nalbach, Horner, Würger and others [25, 198–201]. Specifically, a master equation is derived in Liouville space on the basis of a superoperator formalism. Because we are dealing with a nonequilibrium bath, explicit care must be taken to include its time evolution. We will see that the effect of bath driving can be fully accounted for by the effective force within a simple Born approximation scheme. The dynamics is then obtained through the assumption of a fast decay of bath correlations in conjunction with a comparably slow force (the so-called *Adiabatic-Markovian approximation* [83, 197]).

### 5.2.1 Liouville space quantum master equation

We start our analysis by considering the Liouville-von Neumann equation for the combined density matrix of system and bath  $W(t)$  [5]

$$\frac{dW(t)}{dt} = -\frac{i}{\hbar}[H(t), W(t)] \equiv \mathcal{L}(t)W(t). \quad (5.30)$$

The last equation defined the time-dependent Liouvillian superoperator  $\mathcal{L}(t) \cdot = -(i/\hbar)[H(t), \cdot]$  which acts on operators in the product Hilbert space of system and bath. It can also be written as a sum of system, bath and system-bath coupling parts  $\mathcal{L}(t) = \mathcal{L}_S(t) + \mathcal{L}_B(t) + \mathcal{L}_{SB}(t)$ . A formal solution of Equation (5.30) can be formulated as

$$W(t) = \mathcal{T} \exp \left[ \int_{t_0}^t ds \mathcal{L}(s) \right] W(t_0) = \mathcal{U}(t, t_0)W(t_0), \quad (5.31)$$

where  $\mathcal{T}$  denotes the proper time ordering [202]. The last equation introduced the time evolution superoperator  $\mathcal{U}(t, t_0) = \mathcal{T} \exp \left[ \int_{t_0}^t ds \mathcal{L}(s) \right]$ . Following Equation (5.6), we have  $W(t_0) = \rho_S(t_0) \otimes \rho_B(t_0)$ . This allows us to obtain the reduced density matrix of the system by averaging over the bath states at coupling time (cf. Equation (2.59))

$$\rho_S(t) = \text{Tr}_B [\mathcal{U}(t, t_0)W(t_0)] = \mathcal{U}_{\text{eff}}(t, t_0)\rho_S(t_0). \quad (5.32)$$

Here, we have defined the effective time evolution superoperator of the reduced density matrix of the system  $\mathcal{U}_{\text{eff}}(t, t_0) = \text{Tr}_B [\mathcal{U}(t, t_0)\rho_B(t_0)] = \langle \mathcal{U}(t, t_0) \rangle_B$ . Next, we expand  $\mathcal{U}(t, t_0)$  into a Dyson series as [25]

$$\begin{aligned} \mathcal{U}(t, t_0) &= \mathcal{U}_0(t, t_0) + \int_{t_0}^t ds \mathcal{U}_0(t, s)\mathcal{L}_{SB}(s)\mathcal{U}_0(s, t_0) \\ &+ \int_{t_0}^t ds \int_{t_0}^s ds' \mathcal{U}_0(t, s)\mathcal{L}_{SB}(s)\mathcal{U}_0(s, s')\mathcal{L}_{SB}(s')\mathcal{U}_0(s', t_0). \end{aligned} \quad (5.33)$$

Here, the superoperator  $\mathcal{U}_0(t, t_0) = \mathcal{U}_S(t, t_0) \otimes \mathcal{U}_B(t, t_0)$  is the combined time evolution superoperator of system ( $\mathcal{U}_S(t, t_0)$ ) and bath ( $\mathcal{U}_B(t, t_0)$ ) without the system-bath coupling. Subsequent averaging yields the equivalent series for  $\mathcal{U}_{\text{eff}}(t, t_0)$  in the form

$$\begin{aligned} \mathcal{U}_{\text{eff}}(t, t_0) &= \mathcal{U}_S(t, t_0) + \int_{t_0}^t ds \mathcal{U}_S(t, s) \langle \mathcal{L}_{\text{SB}}(s) \mathcal{U}_0(s, t_0) \rangle_{\text{B}} \\ &+ \int_{t_0}^t ds \int_{t_0}^s ds' \mathcal{U}_S(t, s) \langle \mathcal{L}_{\text{SB}}(s) \mathcal{U}_0(s, s') \mathcal{L}_{\text{SB}}(s') \mathcal{U}(s', t_0) \rangle_{\text{B}}. \end{aligned} \quad (5.34)$$

In order to obtain Equation (5.34) we have utilized  $\langle \mathcal{U}_0(t, t_0) A(s) \rangle_{\text{B}} = \mathcal{U}_S(t, t_0) \langle A(s) \rangle_{\text{B}}$  for some operator  $A$ . This follows because the effect of  $\mathcal{U}(t)$  can be formulated as

$$\mathcal{U}(t)A = U(t)AU^\dagger(t), \quad (5.35)$$

where  $U(t)$  is the ordinary time evolution operator. Cyclic invariance of the trace then allows cancellation of  $\mathcal{U}_B(t, t_0)$ . Finally, combining Equations (5.32) with (5.34) leads to a quantum master equation in Liouville space given by

$$\begin{aligned} \frac{d\rho_S(t)}{dt} &= \mathcal{L}_S(t)\rho_S(t) + \langle \mathcal{L}_{\text{SB}}(t) \mathcal{U}_0(t, t_0) \rangle_{\text{B}} \rho_S(t_0) \\ &+ \int_{t_0}^t ds \langle \mathcal{L}_{\text{SB}}(t) \mathcal{U}_0(t, s) \mathcal{L}_{\text{SB}}(s) \mathcal{U}(s, t_0) \rangle_{\text{B}} \rho_S(t_0). \end{aligned} \quad (5.36)$$

Equation (5.36) is still exact as the full time evolution superoperator  $\mathcal{U}(s, t_0)$  is present on the right-hand side.

## 5.2.2 Born approximation

In order to find explicit the dynamics we need to approximate Equation (5.36). We note that the structure of the expansion is the same as in Equation (2.60). Neglecting higher order terms by setting  $\mathcal{U}(t) \approx \mathcal{U}_0(t)$  in the expectation value then similarly amounts to the Born approximation. To provide more details, this approximation is done on the basis of a cumulant expansion where only powers of second order correlations are taken into account [85, 198, 202]. This means that the infinite sum obtained by reinsertion of Equation (5.36) into itself is reduced to a kind of power series of the bath correlators found in Equation (2.64). This is a typical example for a resummation technique of many-body correlations and can be represented diagrammatically by keeping sequential one-loop diagrams. A detailed presentation is provided in the paper by Würger [198] and the doctoral thesis of Nalbach [202] for the equilibrium case. We are going to generalize the procedure here for the nonequilibrium case and approximate

$$\begin{aligned} &\langle \mathcal{L}_{\text{SB}}(t) \mathcal{U}_0(t, s) \mathcal{L}_{\text{SB}}(s) \mathcal{U}(s, t_0) \rangle_{\text{B}} \\ &\approx \langle \mathcal{L}_{\text{SB}}(t) \mathcal{U}_0(t, s) \mathcal{L}_{\text{SB}}(s) \mathcal{U}_B(s, t_0) \rangle_{\text{B}} \mathcal{U}_{\text{eff}}(s, t_0), \end{aligned} \quad (5.37)$$

where the average is performed with respect to  $\rho_B(t_0)$  which we assume to not be equal to  $\rho_B^{\text{eq}}$ . However, this assumption is intrinsically problematic as the resummation procedure can be motivated by the thermal Wick theorem where higher order thermal averages can be written as the sum of permutations of lower orders [62, 198]. By using the method in Equation (5.19), we can reduce the correlations to equilibrium averages once more. To see this, we start by considering the infinite Dyson series of  $\mathcal{U}_{\text{eff}}(t, t_0)$  which can be obtained by reinsertion of Equation (5.33) into itself and subsequent averaging. One finds that terms of the  $n$ -th power in  $\mathcal{L}_{\text{SB}}$  feature an  $n$ -th order correlator  $\Phi^{(n)}(\dots)$  which depends on  $n$ -time arguments plus the initial time  $t_0$ . They are given by

$$\begin{aligned} \Phi^{(n)}(s_n, s_{n-1}, \dots, s_2, s_1) = \\ \langle \mathcal{L}_{\text{SB}}(s_n) \mathcal{U}_0(s_n, s_{n-1}) \mathcal{L}_{\text{SB}}(s_{n-1}) \mathcal{U}_0(s_{n-1}, s_{n-2}) \dots \mathcal{L}_{\text{SB}}(s_1) \mathcal{U}_0(s_1, t_0) \rangle_B. \end{aligned} \quad (5.38)$$

Note that  $\Phi^{(n)}$  is still a superoperator which acts on operators inside the system Hilbert subspace. To proceed, we note that in our driving scheme we start from equilibrium at time  $t_a$ . This allows us to extract another time evolution superoperator via  $\rho_B(t_0) = \mathcal{U}_B(t_0, t_a) \rho_B^{\text{eq}}$  to recover an equilibrium average. This yields

$$\Phi^{(n)}(\dots) = \langle \dots \mathcal{L}_{\text{SB}}(s_1) \mathcal{U}_0(s_1, t_0) \rangle_B = \langle \dots \mathcal{L}_{\text{SB}}(s_1) \mathcal{U}_S(s_1, t_0) \mathcal{U}_B(s_1, t_a) \rangle_B^{\text{eq}}. \quad (5.39)$$

It is obvious that this step is only relevant when driving precedes the coupling, i.e. for  $t_a < t_0$ , as the bath is assumed to be in equilibrium prior to  $t_a$ .

While we now possess equilibrium averages, the nonequilibrium time evolution changes the correlation function and may either invalidate the perturbative expansion because of the shift done in Equation (5.21), or changes the time scales such that the Markov approximation becomes problematic. We can solve these issues in part by showing that the correlators reduce to the equilibrium case via application of Equation (5.20). While we will not provide a rigorous proof to all orders, we are going to show in the following how the time evolutions can be rearranged in second-order correlators in such a way that the results (5.23) and (5.24) reemerge and briefly discuss the case for fourth-order correlators.

### ***Second and fourth order bath correlations***

To check how the time evolution factorizes into the different operators, it is necessary to split the correlators of Equation (5.38) into system and bath parts. This is done by explicitly writing down the superoperators and evaluating the nested commutator structure encoded within the Liouvillians. The procedure is outlined in Appendix C and we only consider some exemplary terms. In particular, the second order correlator

$\Phi^{(2)}(t_2, t_1)$  yields a term

$$\begin{aligned} & \phi^{(2)}(t_2, t_1) \\ &= \sum_{\alpha, \alpha'=1}^N \lambda_\alpha \lambda_{\alpha'} \text{Tr}_B \left[ x_{\alpha'}^{\text{eff}}(t_2) U(t_2, t_1) x_\alpha^{\text{eff}}(t_1) U(t_1, t_a) \rho_B^{\text{eq}} U^\dagger(t_1, t_a) U^\dagger(t_2, t_1) \right], \end{aligned} \quad (5.40)$$

where  $U(t_j, t_i)$  are the time evolution operators of the bath with Hamiltonian (5.8). We can now exploit the cyclical invariance of the trace and insert  $\mathbb{1} = U(t_1, t_a) U^\dagger(t_1, t_a)$  to absorb the time dependence into the operators according to

$$\phi^{(2)}(t_2, t_1) = \sum_{\alpha, \alpha'=1}^N \lambda_\alpha \lambda_{\alpha'} \text{Tr}_B \left[ \tilde{x}_{\alpha'}^{\text{eff}}(t_2 - t_a) \tilde{x}_\alpha^{\text{eff}}(t_1 - t_a) \rho_B^{\text{eq}} \right]. \quad (5.41)$$

This procedure can be done similarly for the other ordering that appears from the commutators and Equations (5.23) and (5.24) emerge naturally (cf. Equations (C.5) and (C.6)). Before proceeding, it should be mentioned that the dependence on  $t_i - t_a$  in Equation (5.41) only applies to the free time evolution of the operators. This follows from the solution of the differential equation (5.11) where we can see that the driving contribution is unchanged when the interval  $[t_a, t]$  is considered. Therefore, the driving contribution cancels and the correlators only depend on the difference  $t_2 - t_1$ .

In fourth order, a total of 8 orderings can be found (see Equation (C.7)). By similar methods, one finds terms such as

$$\begin{aligned} \phi^{(4)}(t_4, t_3, t_2, t_1) &= \sum_{\alpha, \alpha', \alpha'', \alpha'''=1}^N \lambda_\alpha \lambda_{\alpha'} \lambda_{\alpha''} \lambda_{\alpha'''} \\ & * \text{Tr}_B \left[ \tilde{x}_{\alpha'''}^{\text{eff}}(t_4 - t_a) \tilde{x}_{\alpha''}^{\text{eff}}(t_3 - t_a) \tilde{x}_{\alpha'}^{\text{eff}}(t_2 - t_a) \tilde{x}_\alpha^{\text{eff}}(t_1 - t_a) \rho_B^{\text{eq}} \right], \end{aligned} \quad (5.42)$$

which coincides with the equilibrium result. It therefore stands to reason that the same procedure can be applied to arbitrary high order to regain simple equilibrium correlations. While this is not a strict proof, we note that this result must be exact as shown in the QLE treatment of the previous chapter where the only effect of a linearly driven bath is an additional force contribution. We shall also derive this result on the basis of path integrals in the next part of this thesis. However, this short calculation allows us to argue that additional time scales will not appear from the bath correlations, as these are completely absorbed in the effective force contribution.

### ***Born-approximated quantum master equation***

After arguing that the bath correlators retain their equilibrium result, we apply the Born approximation. We first note that the first-order term in the master equation

(5.36) vanishes because the shift of Equation (5.20) recreates Gaussian fluctuations. Specifically, we have

$$\langle \mathcal{L}_{\text{SB}}(t)\mathcal{U}_0(t, t_0) \rangle_{\text{B}} \propto \sum_{\alpha=1}^N \lambda_{\alpha} \langle \tilde{x}_j^{\text{eff}}(t - t_a) \rangle_{\text{B}}^{\text{eq}} = 0, \quad (5.43)$$

since the average position of an unperturbed oscillator is zero in equilibrium (Equation (A.7)). We finally arrive at the Born-approximated quantum master equation

$$\frac{d\rho_{\text{S}}(t)}{dt} = \mathcal{L}_{\text{S}}(t)\rho_{\text{S}}(t) + \int_{t_0}^t ds \mathcal{M}(t, s)\rho_{\text{S}}(s). \quad (5.44)$$

Here, the kernel  $\mathcal{M}(t, s)$  is defined by Equation (5.37) as

$$\mathcal{M}(t, s) = \langle \mathcal{L}_{\text{SB}}(t)\mathcal{U}_0(t, s)\mathcal{L}_{\text{SB}}(s)\mathcal{U}_{\text{B}}(s, t_0) \rangle_{\text{B}}. \quad (5.45)$$

While the bath correlators depend only on the difference  $t - s$ , the system part of Equation (5.45) is still subject to the non-Markovian force such that more simplifications cannot be made without further approximations. In other words, while we have simplified the coupling to the bath, we are still left with the problem of a driven system.

### 5.2.3 Adiabatic-Markovian approximation

In a simple approach applied by Nalbach to the dissipative Landau-Zener problem [83, 197] and previously also noted by Weiss [33, Chapter 23.2], a Markovian approximation can be connected with the assumption of slow external driving. This gives rise to time-dependent nonequilibrium Bloch equations. To find them, we return to the shifted Hamiltonian of Equation (5.20) and perform a rotation into the momentary eigenbasis of the system which we denote by a bar [83]. The system part then transforms as

$$\bar{H}_{\text{S}}(t) = R^{\dagger}(t)H_{\text{S}}^{\text{eff}}(t)R(t) = \frac{E(t)}{2}\tau_x, \quad (5.46)$$

with the time-dependent momentary eigenenergies  $E(t) = \hbar\sqrt{\omega_0^2 + [F_{\text{eff}}(t)]^2}$  and the  $\tau_i$  give the rotated Pauli matrices. The rotation is generated by the operator  $R(t) = \exp[i(\phi(t)/2)\sigma_y]$  with the phase  $\phi(t) = \arctan[F_{\text{eff}}(t)/\omega_0]$ . Similarly, the system-bath coupling Hamiltonian yields

$$\bar{H}_{\text{SB}}(t) = - \left( \frac{u(t)}{2}\tau_z + \frac{v(t)}{2}\tau_x \right) \sum_{\alpha=1}^N \hbar\lambda_{\alpha}x_{\alpha}^{\text{eff}}(t), \quad (5.47)$$

with the prefactors  $u(t) = \cos[\phi(t)]$  and  $v(t) = \sin[\phi(t)]$ . The rotations done in Equation (5.46) and (5.47) amount to a transformation into an adiabatic basis which

is known as a common approach to find the dynamics in driven quantum systems, as mentioned in Sections 2.2.3 and 3.3.3 [157].

The time-dependent rotation introduces an additional term in the time evolution of the density matrix. Specifically, for the rotated combined density matrix  $\bar{W}(t)$  the Liouville-von Neumann equation (5.30) becomes

$$\frac{d\bar{W}(t)}{dt} = -\frac{i}{\hbar} \left[ \frac{\hbar}{2} \left( \frac{d\phi(t)}{dt} \right) \tau_y + \bar{H}_S(t) + H_B^{\text{eff}}(t) + \bar{H}_{\text{SB}}(t), \bar{W}(t) \right]. \quad (5.48)$$

The time evolution of the bare system is then determined by the rotated system Hamiltonian and the derivative of the phase according to

$$\bar{H}'_S(t) = \bar{H}_S(t) + \frac{\hbar}{2} \left( \frac{d\phi(t)}{dt} \right) \tau_y. \quad (5.49)$$

This changes the free time evolution superoperator of the system into

$$\bar{\mathcal{U}}_S(t, t_0) = \exp \left[ \int_{t_0}^t ds \bar{\mathcal{L}}'_S(s) \right] = \exp \left[ \int_{t_0}^t ds \left( \bar{\mathcal{L}}_S(s) - \frac{i}{2} \left( \frac{d\phi(t)}{dt} \right) [\tau_y, \cdot] \right) \right], \quad (5.50)$$

where a bar over the Liouvillian signifies that it is constructed from the corresponding rotated Hamiltonians and we omitted the time ordering for brevity. The rotated kernel  $\bar{\mathcal{M}}$  is then given by

$$\bar{\mathcal{M}}(t, s) = \langle \bar{\mathcal{L}}_{\text{SB}}(t) \bar{\mathcal{U}}_0(t, s) \bar{\mathcal{L}}_{\text{SB}}(s) \mathcal{U}_B(s, t_0) \rangle_B. \quad (5.51)$$

As outlined in Section 2.3.1, the Markovian approximation involves well separated time scales of the system and the bath such that the memory of the bath decays much faster than any time scale of the system. In this way, the memory kernel  $\bar{\mathcal{M}}(t, s)$  is assumed to decay fast with increasing time difference  $t - s$ . This assumption allows us to move the reduced density matrix in front of the integral in Equation (5.44) as it does not change appreciably during the time frame when the integral is evaluated (cf. the text below Equation (2.60)). Driving does not change this picture as long as it is sufficiently slow in contrast to the bath. If the force occurs on the time scale of the system or changes even slower while the bath remains fast, the bath will effectively see a constant system – regardless of the time dependence rendered by the driving. This notion of adiabaticity of the force is thus compatible with the Markovian approximation [83]. This allows us to make simplifications inside the kernel  $\bar{\mathcal{M}}(t, s)$  according to

$$\bar{\mathcal{U}}_S(t, t_0) \approx \exp \left[ \bar{\mathcal{L}}_S(t)(t - t_0) \right], \quad (5.52)$$

$$\bar{\mathcal{L}}_{\text{SB}}(s) \approx \bar{\mathcal{L}}_{\text{SB}}(t), \text{ while keeping } x_j^{\text{eff}}(s). \quad (5.53)$$

As noted in the previous subsection, we have to keep the time dependence of  $x_j^{\text{eff}}(s)$  intact to preserve the equilibrium dynamics of the bath. Our approximations then only

affect the system dynamics and we neglect the time dependence introduced by the two prefactors in  $\bar{\mathcal{L}}_{\text{SB}}$ , i.e.  $u(s) \approx u(t)$  and  $v(s) \approx v(t)$ . In this way, the dynamics of bath and system inside the kernel depend only on the time difference along with a parametric dependence on  $t$ . We therefore write  $\bar{\mathcal{M}}(t, s) \approx \bar{\mathcal{M}}_{\text{AM}}(t, t - s)$ .

We are now able to proceed with the ordinary Markov approximation. First, we have to extract a fast time dependence from the reduced density matrix by switching to the interaction picture before it can be pulled from the integral [5, 64]. This is done in our formalism by [83]

$$\bar{\rho}_{\text{S}}(s) = \bar{\mathcal{U}}_{\text{S}}(s, t_0) \bar{\rho}'_{\text{S}}(s) \approx \exp[\bar{\mathcal{L}}_{\text{S}}(t)(s - t_0)] \bar{\rho}'_{\text{S}}(s), \quad (5.54)$$

which directly follows from Equation (5.35) and our approximation in Equation (5.52). We proceed to simplify the integral in Equation (5.44) by

$$\begin{aligned} \int_{t_0}^t ds \bar{\mathcal{M}}(t, s) \bar{\rho}_{\text{S}}(s) &\approx \int_0^{t-t_0} d\tau \bar{\mathcal{M}}_{\text{AM}}(t, \tau) \bar{\rho}_{\text{S}}(t - \tau) \\ &\approx \int_0^{t-t_0} d\tau \bar{\mathcal{M}}_{\text{AM}}(t, \tau) e^{\bar{\mathcal{L}}_{\text{S}}(t)(t-\tau-t_0)} \bar{\rho}'_{\text{S}}(t) \approx \left[ \int_0^{\infty} d\tau \bar{\mathcal{M}}_{\text{AM}}(t, \tau) e^{-\bar{\mathcal{L}}_{\text{S}}(t)\tau} \right] \bar{\rho}_{\text{S}}(t). \end{aligned} \quad (5.55)$$

Here, we have set  $\tau = t - s$  in the first step, have approximated  $\bar{\rho}'_{\text{S}}(t - \tau) \approx \bar{\rho}'_{\text{S}}(t)$  for the second and finally have extended the upper bound of the integral to infinity on the basis that the kernel decays fast in our approximation. Insertion into the rotated master Equation (5.44) finally leads to the *Adiabatic-Markovian quantum master equation* (cf. Equation (2.65))

$$\frac{d\bar{\rho}_{\text{S}}(t)}{dt} = \bar{\mathcal{L}}'_{\text{S}}(t) \bar{\rho}_{\text{S}}(t) + \bar{M}_{\text{AM}}(t) \bar{\rho}_{\text{S}}(t), \quad (5.56)$$

where we have defined the shorthand

$$\bar{M}_{\text{AM}}(t) = \left[ \int_0^{\infty} d\tau \bar{\mathcal{M}}_{\text{AM}}(t, \tau) e^{-\bar{\mathcal{L}}_{\text{S}}(t)\tau} \right]. \quad (5.57)$$

## 5.2.4 Rates and Bloch equations

Equation (5.56) yields the usual Bloch-Redfield rates which can be derived by a variety of methods for undriven systems and baths. For instance, by switching to Laplace space in Equation (5.34) and only taking into account the pole that belongs to the system frequency during the inverse transformation [25], via the Nakajima-Zwanzig



projector equation [5, Chapter 10] or by the derivation in Section 2.3.1 [64, Chapter IV]. In this part of the thesis, we derive these results by evaluating the kernel  $\bar{\mathcal{M}}_{\text{AM}}$  as matrices in the space of the system operators. We will then proceed to apply the secular approximation to derive nonequilibrium Bloch equations.

We start with the observation that we can construct the reduced density matrix from a basis spanned by the (rotated) Pauli matrices  $\tau_i$  and the identity operator  $\mathbb{1}_{2 \times 2}$ . The reduced density matrix can then be written as

$$\bar{\rho}_{\text{S}}(t) = \frac{1}{2} \left[ \mathbb{1}_{2 \times 2} - \sum_{i=1}^3 r_i(t) \tau_i \right] = \frac{1}{2} \begin{pmatrix} 1 \\ -r_x(t) \\ -r_y(t) \\ -r_z(t) \end{pmatrix}, \quad (5.58)$$

where the last equation has introduced the basis vectors

$$\mathbb{1}_{2 \times 2} = \begin{pmatrix} 1 \\ 0 \\ 0 \\ 0 \end{pmatrix}, \quad \tau_x = \begin{pmatrix} 0 \\ 1 \\ 0 \\ 0 \end{pmatrix}, \quad \tau_y = \begin{pmatrix} 0 \\ 0 \\ 1 \\ 0 \end{pmatrix}, \quad \tau_z = \begin{pmatrix} 0 \\ 0 \\ 0 \\ 1 \end{pmatrix}. \quad (5.59)$$

The prefactors then give the averages as

$$\langle \tau_i \rangle(t) = \text{Tr} [\tau_i \bar{\rho}_{\text{S}}(t)] = \frac{1}{2} \text{Tr} [\{\tau_i, \bar{\rho}_{\text{S}}(t)\}] = -\frac{1}{2} r_i(t) \text{Tr} [\mathbb{1}_{2 \times 2}] = -r_i(t). \quad (5.60)$$

Explicit evaluation yields  $\bar{\mathcal{L}}_{\text{SB}}(t)$  and  $\bar{\mathcal{U}}_{\text{S}}(t)$  as

$$\bar{\mathcal{U}}_{\text{S}}(t) = \begin{pmatrix} 1 & 0 & 0 & 0 \\ 0 & 1 & 0 & 0 \\ 0 & 0 & \cos \left[ \frac{E(t)}{\hbar} t \right] & -\sin \left[ \frac{E(t)}{\hbar} t \right] \\ 0 & 0 & \sin \left[ \frac{E(t)}{\hbar} t \right] & \cos \left[ \frac{E(t)}{\hbar} t \right] \end{pmatrix}, \quad (5.61)$$

$$\bar{\mathcal{L}}_{\text{SB}}(t) = \frac{i}{\hbar} \begin{pmatrix} 0 & \frac{v(t)}{2} \hat{f}(t) & 0 & \frac{u(t)}{2} \hat{f}(t) \\ \frac{v(t)}{2} \hat{f}(t) & 0 & -iu(t) \check{f}(t) & 0 \\ 0 & iu(t) \check{f}(t) & 0 & -iv(t) \check{f}(t) \\ \frac{u(t)}{2} \hat{f}(t) & 0 & iv(t) \check{f}(t) & 0 \end{pmatrix}, \quad (5.62)$$

where  $\bar{\mathcal{L}}_{\text{SB}}(t)$  contains superoperators of the bath coupling operator  $f(t) = \sum_{\alpha}^N \hbar \lambda_{\alpha} x_{\alpha}^{\text{eff}}(t)$  as defined in Equation (C.3). Matrix multiplication leads to the kernel

$$\bar{\mathcal{M}}_{\text{AM}} = - \begin{pmatrix} 0 & 0 & 0 & 0 \\ u^2 s B_{\text{R}} & u^2 c B_{\text{C}} & (-uvs B_{\text{C}}) & (-uvc B_{\text{C}}) \\ (uv[1-c] B_{\text{R}}) & (uvs B_{\text{C}}) & [u^2 + v^2 c] B_{\text{C}} & -v^2 s B_{\text{C}} \\ (-uvs B_{\text{R}}) & (-uvc B_{\text{C}}) & v^2 s B_{\text{C}} & v^2 c B_{\text{C}} \end{pmatrix}, \quad (5.63)$$

where we have omitted the time arguments and shorthanded  $c = \cos[(E(t)/\hbar)t]$  and  $s = \sin[(E(t)/\hbar)t]$ .  $B_R$  and  $B_C$  describe the bath response and the symmetric bath autocorrelation function as given in Equations (5.23) and (5.24). In the language of superoperators they emerge from

$$B_R(t-s) = -(2i\hbar^2)^{-1} \langle \check{f}(t) \mathcal{U}_B(t,s) \hat{f}(s) \mathcal{U}_B(s,t_0) \rangle_B \quad \text{and} \quad (5.64)$$

$$B_C(t-s) = (1/\hbar^2) \langle \check{f}(t) \mathcal{U}_B(t,s) \check{f}(s) \mathcal{U}_B(s,t_0) \rangle_B. \quad (5.65)$$

We now apply the secular approximation. As outlined in Part 2, the secular approximation neglects damping terms with certain frequency differences corresponding to a comparably rapid time evolution. This implies that these terms quickly average out with increasing time. For the two-state system, this happens ordinarily on a time scale of the order of  $\omega_0^{-1}$ . The only terms where this does not happen describe population transfer and dephasing [60, 64]. To apply the secular approximation, we therefore neglect couplings between off-diagonal and diagonal states. These appear as the matrix elements in Equation (5.63) marked by plain brackets ( $\cdot$ ). Multiplying the remaining factor from the Markov approximation still leaves a non-diagonal matrix. Switching to the basis of  $\bar{\mathcal{L}}_S(t)$  and neglecting any imaginary parts and emerging off-diagonals apart from the first element in the second line finally yields [83]

$$\bar{M}_{AM}(t) \approx \begin{pmatrix} 0 & 0 & 0 & 0 \\ -\gamma_0(t) & -\gamma_1(t) & 0 & 0 \\ 0 & 0 & -\gamma_2(t) & 0 \\ 0 & 0 & 0 & -\gamma_2(t) \end{pmatrix}, \quad (5.66)$$

with the elements

$$\gamma_0(t) = \frac{1}{2} J \left( \frac{E(t)}{\hbar} \right), \quad (5.67)$$

$$\gamma_1(t) = \frac{u^2(t)}{2} J \left( \frac{E(t)}{\hbar} \right) \coth \left( \frac{\beta E(t)}{2} \right), \quad (5.68)$$

$$\gamma_2(t) = \frac{\gamma_1(t)}{2} + v^2(t) \left[ J(\omega) \coth \left( \frac{\beta \hbar \omega}{2} \right) \right]_{\omega \rightarrow 0}. \quad (5.69)$$

The quantum master equation can then be written as

$$\frac{d\bar{\rho}_S(t)}{dt} = -\frac{i}{\hbar} [\bar{H}'_S, \bar{\rho}_S(t)] - \Gamma(t) [\bar{\rho}_S(t) - \bar{\rho}_S^{\text{eq}}(t)], \quad (5.70)$$

where  $\bar{\rho}_S^{\text{eq}} = \frac{1}{2} \left[ \mathbb{1}_{2 \times 2} - \tanh \left( \frac{\beta E(t)}{2} \right) \tau_x \right]$  and  $\Gamma(t) = \text{diag}(0, \gamma_1(t), \gamma_2(t), \gamma_2(t))$ . Insertion of the density matrix as given in Equation (5.58) leads to a set of differential

equations for its components. We find

$$\begin{aligned}
\dot{r}_x(t) &= -\gamma_1(t)[r_x(t) - r_x^{\text{eq}}(t)] + \dot{\phi}(t)r_z(t), \\
\dot{r}_y(t) &= -\gamma_2(t)r_y(t) - (E(t)/\hbar)r_z(t), \\
\dot{r}_z(t) &= -\gamma_2(t)r_z(t) + (E(t)/\hbar)r_y(t) - \dot{\phi}(t)r_x(t),
\end{aligned}
\tag{5.71}$$

where derivatives in time have been indicated by a dot. Equations (5.71) are typical examples of Bloch equations and correspond to Equations (3.79) to (3.81). The rates in Equations (5.68) and (5.69) are similar to those found in Section 2.3.1:  $\gamma_1$  is a golden rule relaxation rate which determines the populations for  $\tau_x$ , while  $\gamma_2$  is responsible for decoherence and a sum of dephasing and pure dephasing terms. What is notably absent are frequency renormalizations which were neglected in Equation (5.66).

Due to driving, the Bloch equations now depend parametrically on time via time-dependent rates  $\gamma(t)$ , momentary eigenenergies  $E(t)$  and the explicit dependence on the change of the dynamic phase  $\dot{\phi}(t)$ . This also entails a time-dependent equilibrium  $r_x^{\text{eq}}(t) = \tanh(\beta E(t)/2)$ . These nonequilibrium Bloch equations enable us to analyze some of the dynamics of the two-state system under the influence of the non-Markovian force. We explicitly note that this result only applies because of our procedure in Section 5.1.2, where we introduced the effective force in such a way that the bath correlators retain their equilibrium values during the Born approximation.

### 5.3

**Two-state system dynamics**

After framing the dynamics of the system by the nonequilibrium Bloch equations (5.71), we can now proceed to evaluate the resulting dynamics. We will make use of the same parameters as those indicated for the effective force in Section 5.1.3 such that a comparison is easily possible. In addition, we also restrict ourselves to the case of zero temperature for which allows us to make some statements about the emerging state of the bath. Before proceeding, we take a look at the validity of the Bloch equations for these parameters.

#### 5.3.1 Validity of the nonequilibrium Bloch equations

In the last section, we applied the usual Born, Markov and secular approximations while also assuming a comparably slow force. The general requirements of the Born and Markov approximations do not change. Specifically, we still have to assume weak system-bath coupling and rapidly decaying correlations as discussed in Section 2.3.1. We may gauge the validity of the secular approximation by considering the general requirement that terms can be neglected where  $|\omega_{ab} - \omega_{cd}|^{-1} \ll t - t_0$  with  $\omega_{ab}$  being frequency differences between states [60, Chapter 3.8.3]. In the momentary eigenbasis

$E(t)$  determines the largest time scale. Since  $E(t) \geq \hbar\omega_0$ , the assumption should still be valid for times longer than  $\omega_0^{-1}$ . The only terms for which this assumption fails are those where the difference is zero. These are the terms retained above [60, 64].

Lastly, the question of adiabaticity has to be posed. In the case of the Lorentzian bath, we saw that the non-Markovian force follows a behavior approximately described by Equation (5.29) where the only inverse time scales are  $\Omega$  and  $\Gamma/2$ . By choosing both on the order or smaller than  $\omega_0$  while still assuming a separation of time scales between bath and system, the assumption of a slow force is reasonable. However, the case is different for the ordinary Ohmic bath where we saw that the effective force is characterized by  $\omega_c$ . For the Gaussian case, the impact of  $\omega_c$  is overshadowed by the pulse width which can be chosen on the order of  $\omega_0$ , too. Still, for the  $\delta$ -pulse the force becomes effectively instant for large  $\omega_c$  (see Equation (5.28)). In order to investigate this particular case, we choose an intermediate value for  $\omega_c$  which should be large enough to serve as a cutoff but also small enough to extract some general information about the dynamics. In fact, the parameters used for Figures 5.2 and 5.3 have already been set to appropriate values such that the dynamics below correspond to the effective forces shown.

### 5.3.2 Zero temperature rates and bath state

Throughout this section we assume  $T = 0$  when evaluating the nonequilibrium Bloch equations. As the spectral densities in Equation (5.3) and (5.4) both vanish for  $\omega \rightarrow 0$ , the rates simplify to

$$\gamma_1(t) = \frac{u^2(t)}{2} J \left( \frac{E(t)}{\hbar} \right) \quad , \quad \gamma_2(t) = \frac{\gamma_1(t)}{2}. \quad (5.72)$$

More importantly, we are also able to determine the exact state of the bath at zero temperature. Specifically, linear bath driving produces coherent states  $|K_\alpha(t, t_a)\rangle$  with a time-dependent value determined by  $K_\alpha(t, t_a)$  seen in Equation (5.14). This follows because the shape of the effective bath Hamiltonian of Equation (5.8) frames the time evolution of forced oscillators which produces a coherent state from the ground state  $|0\rangle$  [203]. The time-dependent density matrix is then a direct product of projectors onto the coherent state for each oscillator, i.e.,

$$\rho_B(t) = U(t, t_a) \left[ \prod_{\alpha=1}^N |0\rangle\langle 0| \right] U^\dagger(t, t_a) = \prod_{\alpha=1}^N |K_\alpha(t, t_a)\rangle\langle K_\alpha(t, t_a)|. \quad (5.73)$$

We can gauge the value of  $K_\alpha$  at long times by considering its modulus. For values of  $t$  large compared to the pulse width while also neglecting  $t_a$ , we may formally insert the Fourier transform of the driving force  $F(\omega)$ . We find

$$|K_\alpha|^2 \approx \mu_\alpha^2 |F(\omega)|^2. \quad (5.74)$$

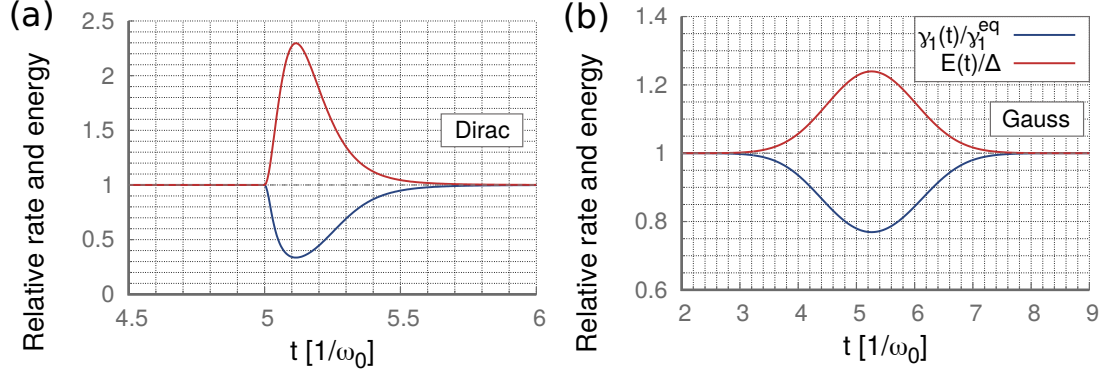


**Figure 5.4:** Time-dependent relaxation rate  $\gamma_1(t)$  of Equation (5.72) (blue) and momentary energy gap (red) for the Ohmic bath in relation to the equilibrium rate  $\gamma_1^{\text{eq}} = J^{(1)}(\omega_0)/2$  and the bare TSS energy scale  $\Delta$ . The parameters have been chosen the same as in Figure 5.2 with the coupling strength  $\eta = 0.05\omega_0$ .

For the simple case of the  $\delta$ -pulse in Equation (5.9), we have  $|F(\omega)| = \omega_0^{-1}$  which means that the modulus of the coherent state remains finite. Hence, the bath does not dephase over time by itself, as is expected given each mode is uncoupled such that the energy cannot be redistributed inside the bath. Nevertheless, interaction with the system may provide a way for the bath to reequilibrate via back-action and memory effects which are, however, neglected in the Born-Markov treatment. Indeed, the effective force includes the combined frequency response of all oscillators via  $\bar{J}(\omega)$ . As we saw in Figures 5.2 and 5.3, the effective force decays over time, suggesting that the system equilibrates with the driven bath because it includes this response.

### 5.3.3 Time-dependent dynamics

#### *Time-dependent rates*

The time-dependent rates are shown in Figures 5.4 and 5.5 in relation to the time-independent rates at  $t = 0$ . Since Equation (5.72) states that the dephasing rate reduces to half of the relaxation rate, we only consider the latter for the analysis. We also note that the prefactors of  $J(\omega)$  do not enter as we only show relative quantities.

First, the Ohmic bath shows a behavior similar to the effective force in Figure 5.2. While the rate for the  $\delta$ -pulsed bath only deviates considerably on a time scale  $(\omega_c)^{-1} = (1/5)\omega_0^{-1}$ , the rate for the Gaussian pulse follows the underlying driving profile. The momentary energy mimics this behavior, as it directly depends on the non-Markovian force. The most interesting feature, however, is that the rates are reduced in both cases. This behavior stems from the fact that the nonequilibrium Bloch equations describe both a decay into a momentary equilibrium state of higher energy as well

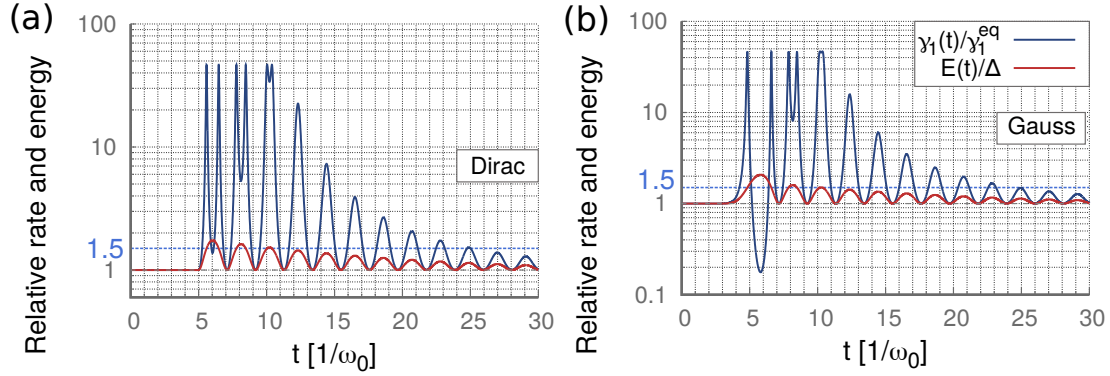


**Figure 5.5:** Time-dependent relaxation rate  $\gamma_1(t)$  of Equation (5.72) (blue) and momentary energy gap (red) for the Lorentzian bath in relation to the equilibrium rate  $\gamma_1^{\text{eq}} = J^{(2)}(\omega_0)/2$  and the bare TSS energy scale  $\Delta$ . The parameters have been chosen the same as in Figure 5.3 with the coupling strength  $\kappa = 0.05\omega_0$ .

as the change in eigenstates from the time-dependent rotation. At zero temperature, the mixing factor  $u$  will lead to a suppression of the rate because the eigenstate of the system is rotated away from the ground state of the TSS. In addition, bath states at the momentary eigenenergy  $E(t)$  must be available such that the spectral density also factors into the rate. For an Ohmic spectral density the frequency distribution is broad enough such that the effect from  $u$  will be the most relevant.

The Lorentzian bath shows a much more peculiar behavior: pairs of large spikes emerge where the rate is almost two magnitudes larger than the equilibrium rate. In between, the rate returns briefly to its equilibrium value. The momentary energy follows an oscillating behavior as expected from Equation (5.29). The spikes in the rate occur when the momentary energy remains above the threshold  $E(t) > \hbar\Omega$ . If the energy is lower, the splitting disappears and the enhancement rapidly becomes smaller. This behavior reflects the dependence of the rate on the spectral density of the bath at the momentary energy. Since the Lorentzian is strongly peaked, the large spectral weight will lead to an increase of the rate if the momentary energy falls on  $\Omega$ . As the momentary energy oscillates this situation can happen twice per oscillation, leading to visible pairs of spikes in the rate.

Similar to the non-Markovian force, the behavior between Gaussian and  $\delta$ -pulse only differs as long as the bath driving pulse is still active. However, in the Gaussian case the first oscillation shows a suppression of the rate in contrast to the  $\delta$ -pulse. This is also a consequence of the narrow Lorentzian which translates the small difference in the momentary energy to a large difference in the spectral weight. Therefore, the larger energy of the Gaussian leads to a smaller rate as the spectral density is sampled further away from the resonance.

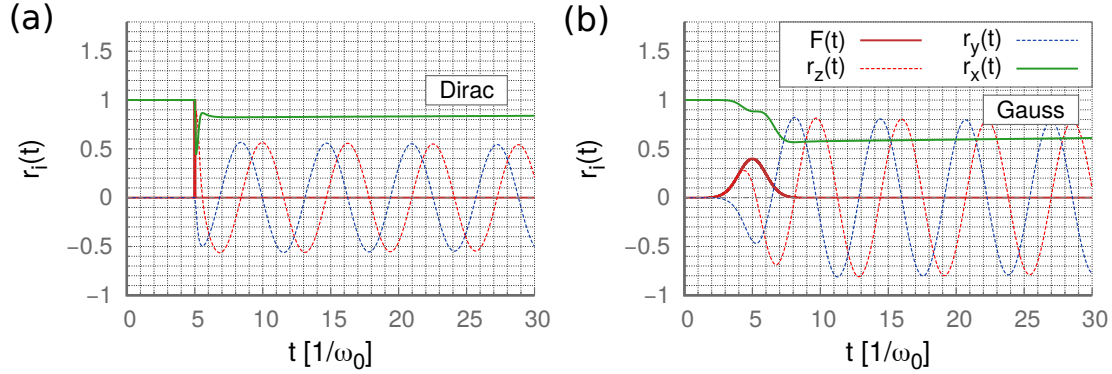


**Figure 5.6:** Averages of the Pauli matrices in the rotated system  $r_i(t)$  and external driving profile  $F(t)$  (red solid line) for the Ohmic density  $J^{(1)}(\omega)$  driven by a Dirac  $\delta$ -pulse (a) and a Gaussian pulse (b). The  $r_i(t)$  correspond to the unrotated system for long times and the decay to the ground state is visible in  $r_x(t)$  (green). The parameters used can be found in Figure 5.2, while we have chosen  $\eta = 0.05\omega_0$  and  $\omega_c = 5\omega_0$  for the bath.

### Populations and coherences

The resulting dynamics for the rotated averages  $r_i$  is shown in Figures 5.6 and 5.7. The system starts in the ground state and we plot the averages in the rotated system. This corresponds to  $r_x(0) = 1$  as per our definition in Equation (5.60). For very long times or before the onset of the pulse, these values correspond to the unrotated system as the effective force will be zero. In fact, the system relaxes back to the ground state as the populations show a slow but steady decline for longer times in all cases.

We can conclude at this point that bath driving can be used to excite a system. However, for the Ohmic cases this excitation is fairly small, in agreement with the suppressed rates and relatively quick conclusion of the non-Markovian force. The populations also follow the profile of the rates to some extent, with strong suppression corresponding to either excitation or a plateau-like behavior. Moreover, the system is not just excited but the coherences also become non-zero and oscillate regularly for longer times. In contrast, the Lorentzian cases show a more complicated behavior as we could suspect from the rates in Figure 5.5:  $r_x(t)$  not only fluctuates in conjunction with the non-Markovian force, but also shows additional frequency components which come from excitation of the underlying mode. We will see this explicitly in the next subsection. However, the rapid excitation and deexcitation of the system has no direct signature in the rates shown in Figure 5.5, except that the initial suppression in the Gaussian case seems to indicate a small plateau at  $t \approx 8.0 \omega_0^{-1}$ . Still, the Lorentzian bath seems to lead to a much larger and persistent excitation of the TSS.

With the population dynamics in hand, it is also possible to analyze the emerging transition probabilities according to Section 3.3.3. This serves as an additional test of

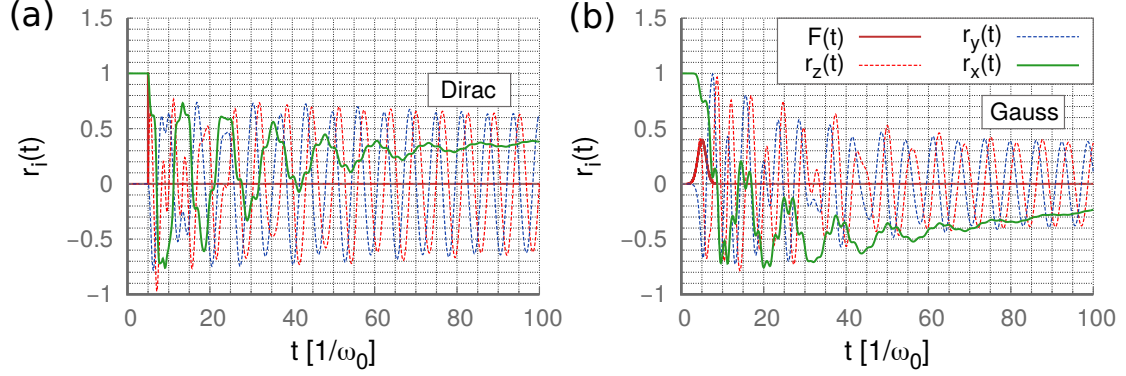


**Figure 5.7:** Averages of the Pauli matrices in the rotated system  $r_i(t)$  and external driving profile  $F(t)$  (red solid line) for the Lorentzian density  $J^{(2)}(\omega)$  driven by a Dirac  $\delta$ -pulse (a) and a Gaussian pulse (b). The  $r_i$  correspond to the unrotated system for long times and the decay to the ground state is visible in  $r_x(t)$  (green). The parameters used can be found in Figure 5.3, while we have chosen  $\kappa = 0.05\omega_0$ ,  $\Omega = 1.5\omega_0$  and  $\Gamma = 0.1\omega_0$  for the bath.

realistic calculations and can be found in Appendix D.

### 5.3.4 Response spectra

The time evolution described by the Bloch equations also allows us to determine an approximate response function of the system. To do so, we recall the definition on the basis of linear response theory done in Section 3.3.4. Specifically, we aim to evaluate (cf. Equation (3.68))

$$R(t, t_0) = \text{Tr}_S \{ i[\tilde{\sigma}_z(t, t_0), \sigma_z] \rho_S(t_0) \} = \text{Tr}_S \{ \sigma_z \mathcal{U}_{\text{eff}}(t, t_0) i[\sigma_z, \rho_S(t_0)] \}. \quad (5.75)$$

Equation (5.75) is the generalized response function for  $\sigma_z$  where one time point has been set to  $t_0$ . The reason for this choice is that we can easily derive  $R(t, t_0)$  by calculating  $\mathcal{U}_{\text{eff}}(t, t_0)$ . This is done by identifying  $R(t, t_0)$  as the expectation value of  $\sigma_z$  weighted by a time-dependent auxiliary density matrix  $\rho_r(t) = \mathcal{U}_{\text{eff}}(t, t_0) i[\sigma_z, \rho_S(t_0)]$  whose elements can be found by use of the Bloch equations. Since we aim to analyze the response in the original unrotated system,  $R(t, t_0)$  follows from a linear combination as

$$R(t, t_0) = -[u(t)r_z(t) + v(t)r_x(t)]. \quad (5.76)$$

Two remarks need to be made. First, setting one of the two time points to  $t_0$  is done in order to simplify the calculation. A more general result can be derived by taking additional corrections into account [202]. In order to obtain a first picture of the underlying excitation spectra, the calculation of  $R(t, t_0)$  still proves sufficient as we will see in the following. Second, the response function  $R(t, t_0)$  goes beyond linear



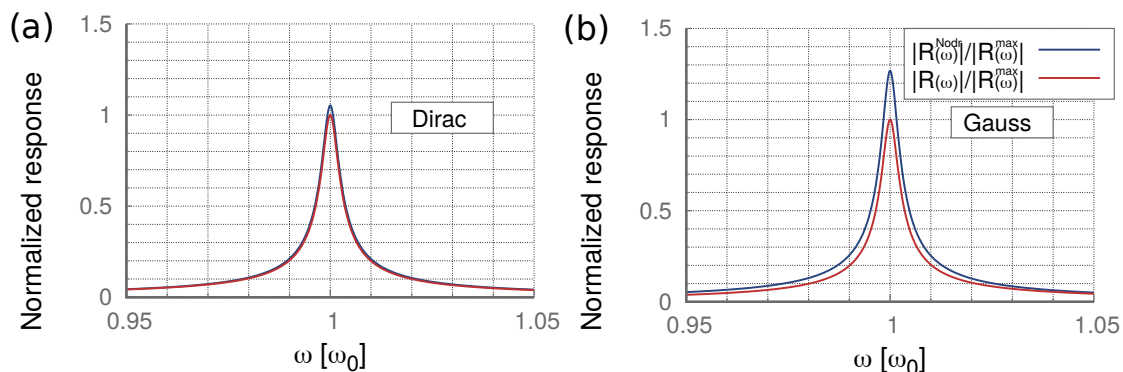


**Figure 5.8:** Magnitude of the frequency-dependent response  $|R(\omega)|$  obtained from Equation (5.75) (red) for the Ohmic spectral density  $J^{(1)}(\omega)$  versus the bare response (blue) at the two-state frequency  $\omega_0$ . Both results are normalized to the maximum of the driven response to allow for a comparison. The case for the  $\delta$ -pulse (a) shows almost no reduction of the peak while the peak is reduced by about 20% in case of the Gaussian pulse (b). In addition, the peak becomes slightly asymmetric. The parameters used are given below Figures 5.2 and 5.6.

response. This follows because we have specifically included the non-Markovian force on the level of the Hamiltonian and have derived an effective time evolution operator. The only assumptions made with respect to the force concern its relative time scale and the secular approximation, none of which rely on a series expansion in powers of its strength. In principle, the results may therefore include non-linear effects, as discussed in Section 3.1.5, and one can think of  $R(t, t_0)$  as the response function multiplying the amplitude of a direct driving force in a linear response description.

The response function is shown in Figures 5.8 to 5.10. Here, we have evaluated the dynamics for the same parameters as before and have performed a discrete Fourier transformation on the data in order to obtain the frequency-dependent response function  $R(\omega)$ . Specifically, the numerics yield the magnitude of the Fourier coefficients such that we effectively discuss  $|R(\omega)|$  in the following. The function is given relative to the response without bath driving effects.

The results around  $\omega_0$  are shown in Figure 5.8 for the Ohmic bath and in Figure 5.9 for the Lorentzian bath. We see similar results as in the previous chapter: the response is suppressed for the TSS when bath driving is taken into account. This is the case even for the simple Ohmic bath where the Gaussian pulse suppresses the response by a factor of about a third. In contrast, almost no difference is seen in case of the  $\delta$ -pulse. The Lorentzian bath sees a stronger suppression of about 40% in the  $\delta$ -case and about 60% in the case of the Gaussian. Similar to the results in Figure 4.4, a slight asymmetry between the left and the right flank is visible in all cases, except for the case of an Ohmic bath plus the  $\delta$ -pulse.

However, the Lorentzian cases show additional signatures of the underlying mode

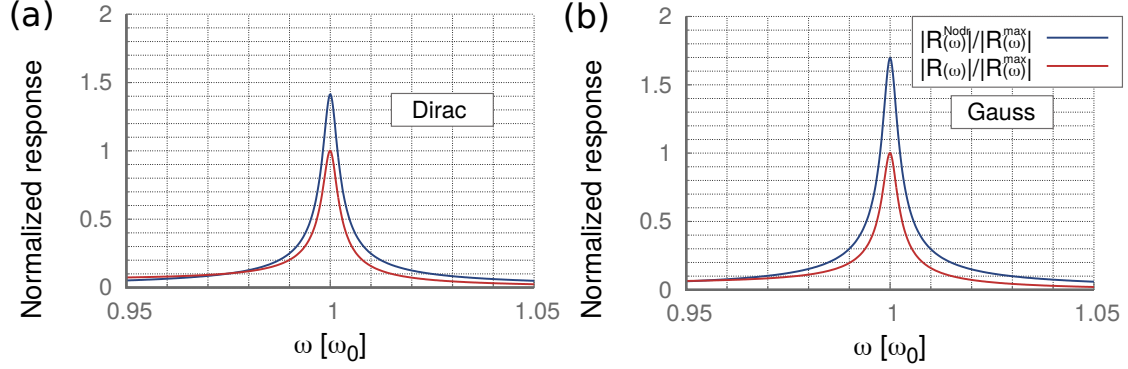


**Figure 5.9:** Magnitude of the frequency-dependent response  $|R(\omega)|$  obtained from Equation (5.75) (red) for the Lorentzian spectral density  $J^{(2)}(\omega)$  versus the bare response (blue) at the two-state frequency  $\omega_0$ . Both results are normalized to the maximum of the driven response to allow for a comparison. Both driving pulses lead to a reduction. In case of the  $\delta$ -pulse (a) by about 30% while the Gaussian pulse (b) reduces the peak by about 41%. Both peaks show a slight asymmetry. The parameters used are given below Figures 5.3 and 5.7.

which are clearly visible beyond the two-state frequency as shown in Figure 5.10 panels (a) and (b). A clearly defined peak arises at about  $\omega = 1.5\omega_0$  and a broad shoulder occurs between  $2\omega_0$  and  $2.5\omega_0$  from bath driving. The peak corresponds to the frequency of the bath mode  $\Omega$  and is a clear indication of its involvement. The shoulder, as well as the slightly dented flank of the peak, should similarly have its origin in different interactions of the two-state system with the mode. To answer this question, we consider the mapped Hamiltonian of Equation (5.5): for our choice of parameters, the coupling to the oscillator is about  $g \approx 0.1\omega_0$  while the spectral density of the Ohmic bath has a prefactor of  $\eta' = 1/30$ . The latter is still fairly small such that the dynamics is largely influenced only by the interplay between the oscillator and the TSS. In fact, we may consider the reduced (Jaynes-Cummings) Hamiltonian of system and oscillator, rendered by

$$H_{\text{TSS-HO}} = \frac{\hbar\omega_0}{2}\sigma_x - \hbar g\sigma_z(B^\dagger + B) + \hbar\Omega B^\dagger B, \quad (5.77)$$

as a way to find possible transitions which should be visible as peaks in the spectrum (cf. also our initial discussion in Section 2.1). The most relevant are indicated in Figure 5.10 (c), which relates the states of the Hamiltonian (5.77) for zero coupling ( $g = 0$ ). In contrast, the values obtained from exact diagonalization with non-zero  $g$  are shown in 5.10 (a) and (b) by dotted lines and are related to the bare transitions by the numbers indicated.

The transitions found do not completely coincide with the spectrum, which is reasonable in light of the approximations involved for the response function and the

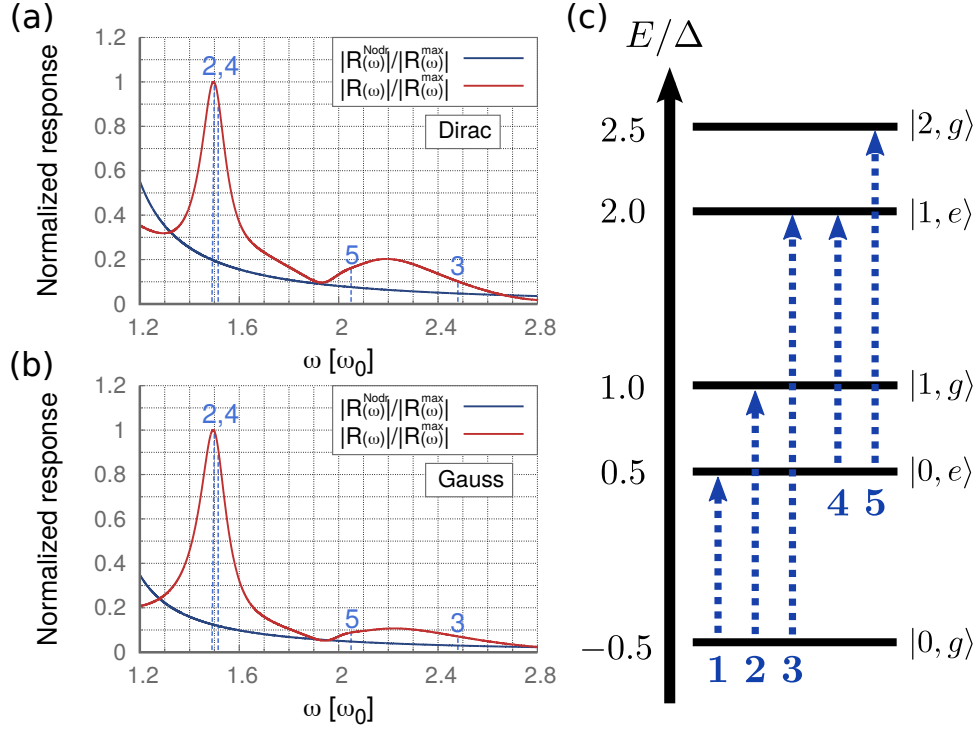


**Figure 5.10:** Magnitude of the frequency-dependent response  $|R(\omega)|$  obtained from Equation (5.75) (red) for the Lorentzian spectral density  $J^{(2)}(\omega)$  versus the bare response (blue) away from the two-state frequency  $\omega_0$ . Results are normalized to the maximum of the driven response to allow for a comparison. Both the  $\delta$ -pulse (a) as well as the Gaussian pulse (b) give rise to additional structures in the spectrum. The emerging peaks correspond well to energy gaps (blue dotted lines) obtained numerically from the Hamiltonian in Equation (5.77) with  $g = \sqrt{\kappa\Omega}/8 \approx 0.1\omega_0$  ( $\Omega = 1.5\omega_0$ ). The level diagram for  $g = 0$  (c) shows the corresponding transitions (blue dotted arrows). Here, the product state  $|n, s\rangle$  denotes the number state of the oscillator  $n$ , while  $s$  describes either the ground (g) or excited state (e) of the TSS. The parameters used are given below Figures 5.3 and 5.7.

existence of the bath which shifts the energy and broadens the peaks. Nevertheless, some of them are close enough and can be suspected to determine the spectra. In particular, we find the transitions number 3 and 5 to correspond to the edges of the shoulder, both of which describe processes involving (de-)excitation of the system and excitation of the oscillating mode. In contrast, ordinary excitation of the oscillator corresponds well to the peak at  $\Omega$ , even though a splitting between the two transitions (number 2 and 4) is not observed. Transition number 1 merely describes excitation of the TSS. The difference between the  $\delta$ -pulse and the Gaussian pulse mostly concerns the relative height of the contributions, where the  $\delta$ -pulse can be seen to excite the shoulder more strongly. This effect may be caused by their relative durations, which implies a broader frequency distribution for the  $\delta$ -pulse. The  $\delta$ -pulse may therefore

contain more components resonant to the higher-lying transitions than the Gaussian.

We can conclude that the driven bath qualitatively changes the response spectrum, similar to what we saw in the previous part of this thesis. While this effect is less pronounced in the case of the Ohmic bath, additional resonances appear in the Lorentzian case.

## 5.4 Conclusion of Part 5

In Part 5, we have expanded on the results of the previous chapter by discussing the force created by linear bath driving and evaluating the dynamics of the spin-boson model using a quantum master equation approach. We have introduced the effective force on the level of the Hamiltonian, where we saw that a simple shift by the average of the coupling Hamiltonian gives rise to the result of Equation (4.19). In fact, we found that the force included the effect of bath driving before the coupling to the system is switched on. This led us to conclude that the effective force completely describes the nonequilibrium properties of the bath, prompting the name *non-Markovian force*. With this additional knowledge at hand, we have used a quantum master equation treatment on the basis of a Born-Markov approximation. We reasoned that the shift in the coupling Hamiltonian automatically reduces the correlators to their equilibrium values such that the non-Markovian force proves to be the only effect from the driven bath. Next, we have obtained the dynamics of the two-state system on the basis of nonequilibrium Bloch equations, where we have used the Born, Markov and secular approximations together with the assumption of a comparably slow effective force. We have found, that the system becomes excited by the interaction with a driven bath alone and an evaluation of the response spectrum has confirmed qualitative changes reminiscent of the results in the previous chapter. Throughout, we have compared forces from a  $\delta$ -shaped and a Gaussian pulse as well as Ohmic and Lorentzian spectral densities. This comparison supported our assumption in Part 4, where bath driving in a Lorentzian bath was assumed to be more effective due to the excitation of a particular bath mode. Signatures of the latter were found throughout our analysis, whereas the driven Ohmic bath was overall less efficient in exciting the system. Most of the differences between the Gaussian and the  $\delta$ -pulse were found while the external driving pulse was still active such that any deviations were constrained to comparably short times. The most visible difference proved to be a comparably large excitation of transitions at higher energy for the  $\delta$ -pulse.

A particularly limiting constraint in our analysis was the restriction to small system-bath coupling strength as required by the Born-Markov approach. This is because we can expect the effect of a driven bath to be more profound for larger system-bath coupling strength. Indeed, the effective spectral density of Equation (5.18) is directly proportional to the system-bath couplings. Hence, we investigate the strong-coupling

non-zero temperature dynamics and derive the non-Markovian force using a path integral formulation in the next chapter.

## Driven influence functional and strong coupling dynamics

We have shown previously that a linearly driven bath creates an additional force that acts on an immersed quantum system. Specifically, we have seen that this new force encodes the nonequilibrium dynamics of the bath and have proceeded to call it a *non-Markovian force* for this reason. In addition, we have looked at the change in linear and nonlinear response, as well as the dynamics of the spin-boson model on the basis of a weak coupling approximation. We proceed to extend our investigation by addressing the problem of driven baths in terms of the path integral formulation in this chapter. We will show that the influence functional for a linearly driven bath leads to a term that can be directly identified with the non-Markovian force. However, the path integral formulation also enables us to investigate the resulting dynamics for the case of strong system-bath coupling within the so-called *non-interacting blip approximation* whose results we are going to derive in this chapter. Furthermore, Shao and Makri [41] and Hu and Matacz [40] already gave expressions for the influence functional for the case of a parametrically driven bath. We will briefly discuss their results as a cursory look into this more daunting problem. The results in this chapter have yet to be published.

### 6.1 The path integral formulation and the non-interacting blip approximation

We start this chapter with a brief review of the path integral results for the spin-boson model on the basis of the discussions found in Weiss [33], Grifoni and Hänggi [32] and the seminal paper by Leggett et al. [78]. Ultimately, we are going to obtain dynamics valid for strong system-bath coupling and/or high temperatures via the so-called *non-interacting blip approximation* (NIBA) [78]. In this chapter, we work with the driven spin-boson Hamiltonian defined by Equations (3.55) and (2.47), i.e. [33]

$$H(t) = \frac{\Delta}{2}\sigma_x + \frac{\epsilon(t)}{2}\sigma_z - q_0 \frac{\sigma_z}{2} \sum_{\alpha=1}^N c_{\alpha} x_{\alpha} + \sum_{\alpha=1}^N \frac{1}{2} \left[ \frac{p_{\alpha}^2}{m_{\alpha}} + m_{\alpha} \omega_{\alpha}^2 x_{\alpha}^2 \right]. \quad (6.1)$$

Here, we kept the particle position  $q_0$  as in Equation (2.47) and absorbed any driving contributions into a time-dependent asymmetry for the time being. In order to find its path integral formulation, we mimic the steps outlined in Section 2.3.2 and formulate the dynamics using a propagating function  $J_{\text{FV}}(\dots)$ . It connects the reduced density matrix at coupling time  $t_0$  to the matrix at time  $t$  via (cf. Equation (2.75))

$$\rho_{\sigma_f, \sigma'_f}(t) = \sum_{\sigma_i, \sigma'_i} J_{\text{FV}}(\sigma_f, \sigma'_f, t; \sigma_i, \sigma'_i, t_0) \rho_{\sigma_i, \sigma'_i}(t_0). \quad (6.2)$$

Here,  $\sigma_i$  and  $\sigma_f$  label initial and final density matrix elements and we have assumed complete factorization of system and bath density matrices at time  $t_0$  as in Equation (5.6). By discretizing the propagators the propagating function can be written as a path integral over effective spin paths according to

$$J_{\text{FV}}(\sigma_f, \sigma'_f, t; \sigma_i, \sigma'_i, t_0) = \int_{\sigma_i}^{\sigma_f} \mathcal{D}\sigma \int_{\sigma'_i}^{\sigma'_f} \mathcal{D}\sigma' A[\sigma] A^*[\sigma'] F_{\text{FV}}[\sigma, \sigma'], \quad (6.3)$$

where the spins  $\sigma(t), \sigma'(t) = \pm 1$  represent eigenvalues of the coupling operator  $\sigma_z$ . The transition amplitudes  $A[\sigma]$  describe the uncoupled time evolution of the two-state system (TSS) and may contain additional driving terms. The Feynman-Vernon influence functional  $F_{\text{FV}}[\sigma, \sigma']$  retains its form. This can be made manifest by recalling our discussion of the spin-boson model as a limiting case for low temperature and large barrier height in a double-well potential (cf. Figure 2.4). This means that we can directly insert the spin states by substituting  $q(t) = (q_0/2)\sigma(t)$  in Equation (2.78). We get

$$F_{\text{FV}}[\sigma, \sigma'] = \exp \left[ -\frac{1}{4} \int_{t_0}^t dt' \int_{t_0}^{t'} dt'' \{ \sigma(t') - \sigma'(t') \} \{ L(t' - t'') \sigma(t'') - L^*(t' - t'') \sigma'(t'') \} \right], \quad (6.4)$$

where the bath correlation function has been rescaled by  $\hbar/q_0^2$ . It is then given by Equation (2.28) for thermal equilibrium with the rescaled spectral density of Equation (2.54).

The two-state dynamics is obtained by forming specific linear combinations using the  $J_{\text{FV}}(\dots)$  [33, Chapter 21]. We have

$$\langle \sigma_z(t) \rangle = \sum_{\sigma_i, \sigma'_i} [J_{\text{FV}}(1, 1, t; \dots) - J_{\text{FV}}(-1, -1, t; \dots)] \rho_{\sigma_i, \sigma'_i}(t_0), \quad (6.5)$$

$$\langle \sigma_x(t) \rangle = \sum_{\sigma_i, \sigma'_i} [J_{\text{FV}}(1, -1, t; \dots) + J_{\text{FV}}(-1, 1, t; \dots)] \rho_{\sigma_i, \sigma'_i}(t_0), \quad (6.6)$$

$$\langle \sigma_y(t) \rangle = i \sum_{\sigma_i, \sigma'_i} [J_{\text{FV}}(1, -1, t; \dots) - J_{\text{FV}}(-1, 1, t; \dots)] \rho_{\sigma_i, \sigma'_i}(t_0). \quad (6.7)$$

Here, we have replaced the initial value combination  $\sigma_i, \sigma'_i, t_0$  by dots for brevity. Equations (6.4) to (6.7) can be written in a more convenient way by introducing center-of-mass and relative spin coordinates called *sojourns* and *blips* according to [33, 78]

$$\eta(t) = \frac{1}{2}(\sigma(t) + \sigma'(t)) \quad \textit{sojourn} \quad , \quad \xi(t) = \frac{1}{2}(\sigma(t) - \sigma'(t)) \quad \textit{blip}. \quad (6.8)$$

We note that blips and sojourns can only take values of  $\pm 1$  or 0. Insertion into Equation (6.4) and separation of  $L(t)$  into real and imaginary part yields

$$F_{\text{FV}}[\eta, \xi] = \exp \left[ - \int_{t_0}^t dt' \int_{t_0}^{t'} dt'' \xi(t') L'(t' - t'') \xi(t'') + i \xi(t') L''(t' - t'') \eta(t'') \right], \quad (6.9)$$

which frames the influence of the bath in terms of a blip-sojourn and a blip-blip interaction term. Since we have used the spin eigenvalues  $\sigma$  and  $\sigma'$  to label elements of the reduced density matrix, diagonal states correspond to a non-zero sojourn while off-diagonal states correspond to a non-zero blip. Thus, if the system is initially in the excited state  $\eta(t_0) = \eta_0 = +1$ , Equations (6.5), (6.6) and (6.7) can be written as [33]

$$\langle \sigma_z(t) \rangle = \sum_{\eta=\pm 1} \eta J_{\text{FV}}(\eta, t; \eta_0, t_0), \quad (6.10)$$

$$\langle \sigma_x(t) \rangle = \sum_{\xi=\pm 1} J_{\text{FV}}(\xi, t; \eta_0, t_0), \quad (6.11)$$

$$\langle \sigma_y(t) \rangle = i \sum_{\xi=\pm 1} \xi J_{\text{FV}}(\xi, t; \eta_0, t_0). \quad (6.12)$$

The summations are performed over the final states  $\xi(t)$  and  $\eta(t)$ . Equations (6.10) to (6.12) frame the dynamics of the system as propagations between blip and sojourn states.

### 6.1.1 Closed expressions for the system dynamics

With the parametrization in Equation (6.8) exact expressions for the two-state dynamics can be derived. We are going to sketch the usual derivation in the following, adapted from the book by Weiss [33, Chapter 21] where a more thorough discussion can be found. To make comparisons easier we retained the notation in large parts. Other presentations can be found in the original paper by Leggett et al. [78] and the review by Grifoni and Hänggi [32].

#### *Parametrization of blip and sojourn paths*

We start by noting that the spin-spin interaction rendered by the influence functional can be seen as a path between four different states because  $\sigma(t)$  and  $\sigma'(t)$  can only take



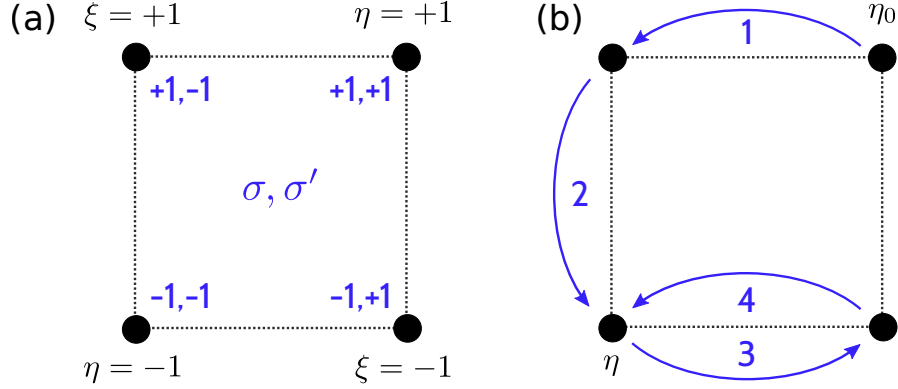


**Figure 6.1:** *Parametrization of the path integral by blip and sojourn states  $\xi$  and  $\eta$ . (a) The spins  $\sigma$  and  $\sigma'$  can only take the values  $\pm 1$  (blue numbers) which can be directly translated to values for blips and sojourns via Equation (6.8). If a sojourn is nonzero, the corresponding blip vanishes and vice versa. This gives rise to four effective blip and sojourn states, such that the spin paths can be parametrized by hopping along the sides of the resulting square. (b) Example of a path made out of  $n = 4$  jumps (blue numbers and arrows). The path starts from the initial sojourn  $\eta_0$ . In this case, an even number of jumps always results in a final sojourn and an odd number in a final blip. This picture was adapted from the presentation in Weiss [33, Chapter 21].*

the values  $\pm 1$  each. In terms of blips and sojourns, this means a constant switching between states where either blips or sojourns are zero. The resulting paths can be visualized as hopping along the sides of the square shown in Figure 6.1. They are parametrized by the number of jumps  $n$ , the times  $t_j$  when the jumps occur and the state of the sojourn or blip  $\eta_j$  or  $\xi_j$ . For instance, a sojourn-to-sojourn path may be written by way of Heaviside functions as

$$\eta^{(n)}(t') = \sum_{j=0}^n \eta_j [\Theta(t' - t_{2j}) - \Theta(t' - t_{2j+1})], \quad (6.13)$$

$$\xi^{(n)}(t') = \sum_{j=1}^n \xi_j [\Theta(t' - t_{2j-1}) - \Theta(t' - t_{2j})], \quad (6.14)$$

with  $\eta_j, \xi_j = \pm 1$  [78]. If we start in a sojourn, an even number of jumps always leads back into a sojourn (diagonal) state while an odd number results in a blip (off-diagonal) state. We can exploit this parametrization by partially integrating the exponent in

Equation (6.9) to obtain

$$F_{\text{FV}}[\eta, \xi] = \exp \left[ B[\xi(t_0), \eta(t_0), \xi(t)] \right] \quad (6.15)$$

$$* \exp \left[ \int_{t_0}^t dt' \int_{t_0}^{t'} dt'' \dot{\xi}(t') Q'(t' - t'') \dot{\xi}(t'') + i \dot{\xi}(t') Q''(t' - t'') \dot{\eta}(t'') \right].$$

Here, the function  $Q(t) = Q'(t) + iQ''(t)$  is the twice integrated bath autocorrelation function. In thermal equilibrium, we find

$$Q(t) = \frac{1}{\pi} \int_0^\infty d\omega \frac{J(\omega)}{\omega^2} \left\{ \coth \left( \frac{\hbar\omega\beta}{2} \right) [1 - \cos(\omega t)] + i \sin(\omega t) \right\}, \quad (6.16)$$

where  $J(\omega)$  is the rescaled spectral density of Equation (2.54).  $B[\eta(t_0), \xi(t_0), \xi(t)]$  describes boundary terms from the integration. They read [65]

$$B[\eta(t_0), \xi(t_0), \xi(t)] = -\xi(t) \int_{t_0}^t \left[ Q'(t-s) \dot{\xi}(s) + iQ''(t-s) \dot{\eta}(s) \right] ds$$

$$- \left[ Q'(t-t_0) \xi(t) - \int_{t_0}^t Q'(s-t_0) \dot{\xi}(s) ds \right] \xi(t_0) \quad (6.17)$$

$$- i \left[ Q''(t-t_0) \xi(t) - \int_{t_0}^t Q''(s-t_0) \dot{\xi}(s) ds \right] \eta(t_0).$$

We will now restrict ourselves to the sojourn-to-sojourn paths (6.13) and (6.14) which will eventually lead to a closed expression for the population dynamics via Equation (6.10). Insertion into the influence functional (6.15) for a given number of jumps  $n$  leads to a product. Specifically,

$$F_{\text{FV}}^{(n)}[\eta, \xi] = G_n[\xi] H_n[\xi, \eta], \quad (6.18)$$

where

$$G_n[\xi] = \exp \left[ - \sum_{j=1}^n Q'_{2j, 2j-1} - \sum_{j=2}^n \sum_{k=1}^{j-1} \Lambda_{j,k} \xi_j \xi_k \right] \quad (6.19)$$

represents the blip-blip interaction term and

$$H_n[\xi, \eta] = \exp \left[ i \sum_{k=0}^{n-1} \sum_{j=k+1}^n X_{j,k} \xi_j \eta_k \right] \quad (6.20)$$

gives the blip-sojourn interactions. The interaction parameters  $X_{i,j}$  and  $\Lambda_{i,j}$  are given by sums of the function  $Q(t)$  during the intervals between jumps, according to

$$\Lambda_{j,k} = Q'_{2j,2k-1} + Q'_{2j-1,2k} - Q'_{2j,2k} - Q'_{2j-1,2k-1}, \quad (6.21)$$

$$X_{j,k} = Q''_{2j,2k+1} + Q''_{2j-1,2k} - Q''_{2j,2k} - Q''_{2j-1,2k+1}, \quad (6.22)$$

where we have used the shorthand  $Q_{i,j} = Q(t_i - t_j)$ . Note that a different initial preparation of system and bath can be absorbed into a redefinition of  $X_{j,0}$  [33].

### *Driven system amplitudes*

After having rewritten the influence functional according to Equation (6.18), the next task is to find a similar parametrization for the system amplitudes which should also include any driving terms. We note that the amplitudes are determined by matrix elements of system propagators in the time slices that make up the path integral. For a time-dependent system Hamiltonian, we may approximate the time evolution operator  $U_S(\delta t)$  for a small time-slice  $\delta t = t_k - t_{k-1}$  as

$$\begin{aligned} U_S(\delta t) &= \mathcal{T} \exp \left[ -\frac{i}{\hbar} \int_{t_{k-1}}^{t_k} H_S(s) ds \right] \approx \exp \left[ -\frac{i}{\hbar} H_S(t_k) \delta t \right] \\ &= \exp \left[ -\frac{i}{\hbar} \left( \frac{\Delta}{2} \sigma_x + \frac{\epsilon(t_k)}{2} \sigma_z \right) \delta t \right]. \end{aligned} \quad (6.23)$$

Here, we have inserted the system Hamiltonian of the driven two-state system as given in Equation (6.1). We are interested in the matrix elements of eigenstates  $|\sigma_k\rangle$  of the coupling operator  $\sigma_z$  at time  $t_k$ . For small  $\delta t$ , we may write [65]

$$\begin{aligned} \langle \sigma_k | U_S(\delta t) | \sigma_{k-1} \rangle &\approx e^{-\frac{i}{\hbar} \frac{\epsilon(t_k)}{2} \sigma_{k-1} \delta t} \langle \sigma_k | e^{-\frac{i}{\hbar} \frac{\Delta}{2} \sigma_x \delta t} | \sigma_{k-1} \rangle \\ &\approx e^{-\frac{i}{\hbar} \frac{\epsilon(t_k)}{2} \sigma_{k-1} \delta t} \langle \sigma_k | \sigma_{k-1} \rangle - \frac{i\Delta}{2\hbar} \delta t \langle \sigma_k | \sigma_x | \sigma_{k-1} \rangle + \mathcal{O}(\delta t^2). \end{aligned} \quad (6.24)$$

Equation (6.24) shows that each time slice either contributes  $\exp[-(i/2\hbar)\epsilon(t_k)\sigma_{k-1}\delta t]$  if the state of the system does not change during  $\delta t$  or gives a factor of  $-(i\Delta/2\hbar)\delta t$  if the state of the system changes. The amplitude  $A[\sigma]$  represents the continuum limit for all time slices. Combined with its complex conjugate  $A^*[\sigma']$ , the weight to stay in a state is given by an exponential which depends on the difference of the paths, i.e, the

blip state. It can be written as

$$\begin{aligned}
B_m &= \exp \left[ -\frac{i}{\hbar} \sum_{k=1}^N \epsilon(t_k) \xi(t_{k-1}) (t_k - t_{k-1}) \right] = \exp \left[ -\frac{i}{\hbar} \sum_{j=1}^m \xi_j \int_{t_{j-1}}^{t_j} dt' \epsilon(t') \right] \\
&= \exp \left[ -i \sum_{j=1}^m \xi_j \vartheta(t_{j-1}, t_j) \right].
\end{aligned} \tag{6.25}$$

Here, we have rewritten the sum over  $N$  time slices into a sum over  $m$  blips with corresponding jump times  $t_j$ . The influence of driving is captured in a bias phase  $\vartheta(t, t')$  determined by an integral over the time-dependent asymmetry within the respective blips [32, 33]. For a time-independent bias, the integral can be carried out and the term is directly proportional to the duration of a blip  $\tau_j = t_j - t_{j-1}$ . If the state of the system changes between  $t_{k-1}$  and  $t_k$  the system switches from a sojourn into a blip or vice versa. The resulting weight per unit time can be written as [33]

$$-i \frac{\Delta}{2\hbar} [\xi(t_k) \eta(t_{k-1}) + \eta(t_k) \xi(t_{k-1})]. \tag{6.26}$$

The weight (6.26) contributes at each jump  $n$ , where one of the two combinations  $\xi\eta$  is  $\pm 1$ . While the sign of the latter depends on each jump the collective sign depends only on the boundary values for a sojourn-to-sojourn-path. This can be made manifest by considering that a sign can only occur when switching between  $\xi = 1$  and  $\eta = -1$  or  $\xi = -1$  and  $\eta = 1$ . The other transitions will not produce a sign. In order to progress from  $\eta = 1$  to  $\eta = -1$  along any path, one must pass these transitions an odd number of times. In contrast, staying in  $\eta = 1$  means passing none of the two transitions or passing them an even number of times (cf. Figure 6.1 (b)). Hence, the former leads to a net sign while the latter does not. This allows us to write the total factor as  $\eta_0 \eta (-1)^n (\Delta/2\hbar)^{2n}$ .

### ***Population dynamics and exact master Equation***

We are now left with changing the integral measure to account for the parametrization in blips and sojourns. All possible paths can be represented by a sum over the number of jumps between sojourns and blips  $n$ , the possibilities of arranging the time-ordered jump times  $t_j$  within the interval and the sojourn and blip states  $\xi_j$  and  $\eta_j$  [33, Chapter 21.2]. This allows us to replace

$$\int \mathcal{D}\sigma \int \mathcal{D}\sigma' \rightarrow \sum_{n=0}^{\infty} \sum_{\{\xi_j = \pm 1\}} \sum_{\{\eta_j = \pm 1\}} \int_{t_0}^t dt_n \int_{t_0}^{t_n} dt_{n-1} \cdots \int_{t_0}^{t_2} dt_1. \tag{6.27}$$

The curly brackets denote sums over all possible combinations of the  $\xi_j$  and  $\eta_j$ .

Putting everything into Equation (6.10) and using Equations (6.18) and (6.25) finally yields

$$\langle \sigma_z(t) \rangle = 1 + \sum_{n=1}^{\infty} \left( -\frac{1}{2} \right)^n \int_{t_0}^t \mathcal{D}_{2n}\{t_j\} \sum_{\{\xi_j=\pm 1\}} [B'_n F'_n - B''_n F''_n]. \quad (6.28)$$

Here,

$$F'_n + iF''_n = G_n \left[ \prod_{k=0}^{n-1} \cos(\phi_{k,n}) + i \sin(\phi_{0,n}) \prod_{k=1}^{n-1} \cos(\phi_{k,n}) \right]. \quad (6.29)$$

The phases  $\phi_{k,n} = \sum_{j=1+k}^n \xi_j X_{j,k}$  stem from the blip-sojourn interaction in Equation (6.20) while  $G_n$  gives the contribution of the blip-blip interaction of Equation (6.19). The factor  $B_n = B'_n + iB''_n$  is defined in Equation (6.25) and represents the effect of the time-dependent asymmetry. Finally, the integrations over the jump times of Equation (6.27) have been collected in a new functional integral defined as

$$\int_{t_0}^t \mathcal{D}_n\{t_j\} = \int_{t_0}^t dt_n \int_{t_0}^{t_n} dt_{n-1} \dots \int_{t_0}^{t_2} dt_1 \left( \frac{\Delta}{\hbar} \right)^n. \quad (6.30)$$

Similar expressions for the coherences and expressions for the propagating functions can be found in the book by Weiss [33].

The closed expression of Equation (6.28) can now be cast into the form of an exact master equation for the spin-boson problem. First, it is possible to formulate a generalized master equation for the conditional populations  $P(i, t; j, t_0)$  for switching from state  $j$  to state  $i$  between  $t_0$  and  $t$  as [204]

$$\dot{P}(i, t; j, t_0) = - \sum_{k=1}^S \int_{t_0}^t dt' K(i, t; k, t') P(k, t'; j, t_0), \quad (6.31)$$

where  $S$  is the maximum number of states. For the case of a two-state system, Equation (6.31) can be rewritten by forming linear combinations of the kernels  $K$  according to

$$\frac{d\langle \sigma_z(t) \rangle}{dt} = - \int_{t_0}^t dt' [K_z^{(a)}(t, t') - K_z^{(s)}(t, t') \langle \sigma_z(t') \rangle], \quad (6.32)$$

where the kernels  $K_z^{(s/a)}(t, t') = K(-1, t; -1, t') \pm K(1, t; 1, t')$ . The labels  $s$  and  $a$  refer to combinations that are symmetric or antisymmetric under inversion of  $\epsilon(t)$ . The kernels represent irreducible components of the correlations  $F'_n B'_n$  and  $F''_n B''_n$  which appear in Equation (6.28) [33, 78]. In fact, the kernels give a kind of self-energy which is usually defined as the irreducible contributions in a perturbative expansion by way

of the Dyson equation [62]. Therefore we need to rewrite the functions  $F'$  and  $F''$  in terms of irreducible clusters  $\tilde{F}$  defined according to

$$\tilde{F}_n''' B_n''' = F_n''' B_n''' - \sum_{j=2}^n \sum_{m_1, \dots, m_j} (-1)^j F_{m_1}' B_{m_1}' F_{m_2}' B_{m_2}' \dots F_{m_j}''' B_{m_j}''' \delta_{\sum_j m_j, n}, \quad (6.33)$$

where the  $m_j$  are summed over as positive integers. Equation (6.28) allows us to find the kernels by comparison as [33]

$$K_z^{(s/a)}(t, t') = \left(\frac{\Delta}{\hbar}\right)^2 F_1'''(t, t') B_1'''(t, t') + \sum_{n=2}^{\infty} (-1)^{n-1} \left(\frac{\Delta^2}{2\hbar^2}\right)^n * \int_{t'}^t dt_{2n-1} \int_{t'}^{t_{2n-1}} dt_{2n-2} \dots \int_{t'}^{t_3} dt_2 \sum_{\{\xi_j = \pm 1\}} \tilde{F}_n''' B_n'''. \quad (6.34)$$

Equation (6.32) in conjunction with Equation (6.34) represent exact results for the system by way of a generalized quantum master equation and provide the main result of this section. While both are not solvable, we will see how a simple truncation of the kernels can yield useful results in the next subsection. It should also be mentioned that the time-independent problem is often treated in Laplace space because the kernels (6.34) only depend on  $t - t'$  in this case such that convolutions can be exploited [31, 33]. As we are dealing with an explicitly time-dependent problem this route is not viable here and we will present the necessary results in the time domain.

### 6.1.2 The non-interacting blip approximation (NIBA)

As we have seen in Equation (6.32), the dynamics of the spin-boson problem can be cast in the frame of an exact generalized master equation which depends on a parametrization of the path integral in terms of sojourns and blips. In order to progress, we have to approximate. The easiest and most-well known approximation is the so-called *non-interacting blip approximation* (NIBA). The NIBA has been presented already in the seminal paper by Leggett et al. [78] which provided a cornerstone for the applicability and analysis of the spin-boson model. It rests on the assumption of strongly suppressed blips such that

the blip-blip interaction is set to  $\Lambda_{i,k} \approx 0$  and

the blip-sojourn interaction is  $X_{j,k} \approx X_{k+1,k} = Q''(t_{2k+2} - t_{2k+1})$ .

Such a situation can, for instance, arise for large system-bath coupling and/or high

temperatures for the case of Ohmic spectral densities. Then, the exponential decay in Equation (6.19) penalizes blips with respect to sojourns and the time spent in a sojourn becomes much larger than the time spent in a blip. For Ohmic environments, the NIBA can also be used with arbitrary coupling, if the temperature is high enough or in case of a symmetric system with weak coupling down to zero temperature (cf. Section 2.2.3) [31–33]. Since we already investigated the weak system-bath coupling regime in Part 4 and 5, we are interested mainly in the strong coupling case here. Within the NIBA, the influence functional of Equation (6.18) is approximated as

$$F_{\text{FV}}^{(n)}[\eta, \xi] \approx \prod_{j=1}^n \exp \left[ -Q'_{2j,2j-1} + iQ''_{2j,2j-1} \xi_j \eta_{j-1} \right]. \quad (6.35)$$

The important characteristic of Equation (6.35) is the factorization into one-blip contributions. This implies that the irreducible clusters defined in Equation (6.33) simplify. Specifically, we have that the influence clusters  $\tilde{F}$  become zero for all  $n > 1$ . This just leaves the  $F_1$  terms and we obtain a quantum master equation as [32, 33]

$$\begin{aligned} \frac{d\langle \sigma_z(t) \rangle}{dt} = & - \left( \frac{\Delta}{\hbar} \right)^2 \int_{t_0}^t dt' e^{-Q'(t-t')} \sin[Q''(t-t')] \sin[\vartheta(t, t')] \\ & - \left( \frac{\Delta}{\hbar} \right)^2 \int_{t_0}^t dt' e^{-Q'(t-t')} \cos[Q''(t-t')] \cos[\vartheta(t, t')] \langle \sigma_z(t') \rangle. \end{aligned} \quad (6.36)$$

Equations for the coherences can be obtained similarly [32, 33] as

$$\langle \sigma_y(t) \rangle = \frac{\hbar}{\Delta} \frac{d\langle \sigma_z(t) \rangle}{dt}, \quad (6.37)$$

$$\begin{aligned} \langle \sigma_x(t) \rangle = & - \left( \frac{\Delta}{\hbar} \right) \int_{t_0}^t dt' e^{-Q'(t-t')} \sin[Q''(t-t')] \cos[\vartheta(t, t')] \\ & + \left( \frac{\Delta}{\hbar} \right) \int_{t_0}^t dt' e^{-Q'(t-t')} \cos[Q''(t-t')] \sin[\vartheta(t, t')] \langle \sigma_z(t') \rangle. \end{aligned} \quad (6.38)$$

The impact of driving is encoded in the bias phase given by

$$\vartheta(t, t') = \frac{1}{\hbar} \int_{t'}^t dt'' \epsilon(t''). \quad (6.39)$$

Note that the results here differ from the literature by signs and  $\hbar$ , both of which enter from our slightly different definition of  $H_S(t)$  in Equation (6.1).

The NIBA results can also be obtained by way of a master equation approach together with a polaron transformation [205, 206]. In the next section, we will use Equations (6.36), (6.37) and (6.38) to showcase the dynamics of a linearly driven bath for the case of strong system-bath coupling and non-zero temperature. To facilitate comparisons, we briefly discuss some analytic results of the NIBA beforehand.

### 6.1.3 Dynamics within the NIBA

As discussed in Section 2.2.3, we can roughly expect two different types of behaviors for the dissipative two-state system: an overdamped (incoherent) case, for which the dynamics follows exponential decays and an underdamped case with long-lived damped oscillations. In fact, the NIBA expressions can be solved by using a Laplace transformation when no driving is present. This allows for a host of analytic expressions depending on the exact parameters of the problem and gives the regimes shown in Figure 2.5 [31, 33]. In this subsection, we present a few of those expressions and discuss the results of the NIBA. Specifically, we focus on the population dynamics of  $\langle \sigma_z(t) \rangle$  under the initial condition  $\langle \sigma_z(0) \rangle = 1$ . Further information and more involved treatments can be found in the book by Weiss [33, Chapter 22].

Before starting, we note that we assume an Ohmic spectral density of the form (2.29) and characterize the coupling strength using the prefactor  $K$  as defined in Equation (2.56). For the case of  $\beta \hbar \omega_c \gg 1$  (the so-called scaling limit) with  $\beta = 1/k_B T$ , we obtain [33]

$$Q(t) = 2K \ln \left( \frac{\beta \hbar \omega_c}{\pi} \sinh \left[ \frac{\pi |t|}{\hbar \beta} \right] \right) + i\pi K \operatorname{sgn}(t), \quad (6.40)$$

which is used to calculate all expressions below. Also note that, in contrast to the results in Weiss [33], we continue to use our definition of the spin-boson Hamiltonian in Equation (6.1) which introduces factors of  $\hbar^{-1}$  and different signs.

#### *Dynamics for a symmetric two-state system*

First, we consider the dynamics at zero temperature for the symmetric case with  $\epsilon = 0$  and no external driving. In this case, the population dynamics follows the so-called Mittag-Leffler function, a generalization of the exponential series, valid for  $K < 1$ . For  $K < 0.5$ , the sum can be split into a coherent and incoherent part and the system exhibits coherent oscillations. Indeed, one finds the dependence  $\langle \sigma_z(t) \rangle_{\text{coh}} \propto \cos(at) \exp(-bt)$  for the coherent part. The specific case of  $K = 0.5$  marks the transition between coherent and incoherent behavior. At this point the Mittag-Leffler function reduces to the exponential series and one obtains [31, 33]

$$\langle \sigma_z(t) \rangle = \exp \left( -\frac{\pi \Delta^2}{2 \hbar^2 \omega_c} t \right). \quad (6.41)$$

For the case  $1 > K > 0.5$ , only the incoherent part exists which implies a comparably sluggish decay. This is known to be false as the decay is exponential in reality [33]. In fact, the NIBA has been noted to be least reliable in this region [31]. For  $K \geq 1$ , the state of the system is frozen in. The reason for this behavior can be found in the frequency shift from the bath which renormalizes  $\Delta$  to  $\Delta_r$ . In this regime,  $\Delta_r$  becomes



zero which implies that the system localizes in one of the two wells as the effective tunneling matrix element vanishes [31, 33]. This is an example of the so-called *quantum Zeno effect* where continuous measurement of a quantum system blocks its decay [207, 208].

A non-zero temperature complicates the picture but does not necessarily change the underlying dynamics. The incoherent contribution becomes a series of exponentials which vanishes for zero system-bath coupling such that the dynamics for small  $K$  and low temperature is determined by the coherent oscillation alone [33]. The most profound difference is the existence of the transition temperature  $T^*(K)$  which marks the crossover between coherent and incoherent behavior as shown in Figure 2.5 (a). We refrain from discussing more details but note that an approximate formula for this temperature can be found in the book by Weiss [33, Equation (22.20)] or the original paper by Weiss et al. [209]. In the incoherent phase, the simplest expression can be found in the regime far above  $T^*$  and/or with large  $K$  where the decay is again a single exponential, i.e., [31, 33]

$$\langle \sigma_z(t) \rangle = \exp \left( -\frac{\sqrt{\pi}}{2} \frac{\Delta^2}{\hbar^2 \omega_c} \frac{\Gamma(K)}{\Gamma(K+1/2)} \left[ \frac{\pi}{\hbar \omega_c \beta} \right]^{2K-1} t \right). \quad (6.42)$$

Here,  $\Gamma(x)$  designates the gamma function. This form coincides with golden rule rates and is valid for  $k_B T \gg \Delta_r/K$ , with the renormalized tunneling matrix element given by  $\Delta_r = \Delta(\Delta/\hbar\omega_c)^{K/(1-K)}$  for  $K < 1$ . It is also generally valid for  $K > 1$  at any temperature as long as  $\hbar\omega_c$  is far larger than  $k_B T$  and  $\Delta$  [33, 78]. Both cases coincide with the region where the NIBA is always justified for an Ohmic spectral density: that is, either for  $K > 1$  or for arbitrary  $K$  with temperatures larger than  $k_B T \simeq \Delta$  [32].

### ***Impact of asymmetry and driving***

Solutions for a static asymmetry can be found in Laplace space for small system-bath coupling and moderate temperature, as well [33]. Here, the existence of a bias leads to different equilibrium values and gives more involved expressions (see Equations (2.51) and (2.52)). In particular, one obtains up to three temperature scales which determine the behavior together with a critical value of the asymmetry. However, the NIBA becomes invalid for an asymmetric system at low temperatures outside the regime of very weak system-bath coupling. The equilibrium values also become qualitatively incorrect at low temperatures [33].

Driving complicates the matter further, for instance, by inducing coherent oscillations in the incoherent regime through modification of the transition temperature [32]. Nevertheless, for a simple AC driving scheme a Fourier transformation of Equations (6.36), (6.37) and (6.38) can be performed, yielding solutions for the associated Fourier components. One finds a dependence on higher-order Bessel functions which indicate

that for large frequencies, blips are even better suppressed [33, Chapter 23]. For an Ohmic bath in the scaling limit at  $K = 1/2$  an exact solution for arbitrary driving can be derived [33, Chapter 23.1.4]. One finds,

$$\langle \sigma_z(t) \rangle = e^{-\frac{\pi \Delta^2}{2\hbar^2} \frac{t}{\omega_c}} + P_a(t), \quad (6.43)$$

which uses  $t_0 = 0$ . The additional term  $P_a(t)$  reads

$$P_a(t) = - \left( \frac{\Delta}{\hbar} \right)^2 e^{-\frac{\pi \Delta^2}{2\hbar^2} \frac{t}{\omega_c}} \int_0^t dt' \int_0^{t'} dt'' e^{\frac{\pi \Delta^2}{2\hbar^2} \frac{(t'+t'')}{2\omega_c}} \sin[\vartheta(t', t'')] e^{-Q'(t'-t'')}, \quad (6.44)$$

which contains the driving contribution and is responsible for the resulting steady state. In the next section, we will use the results presented here as a comparison to numerical results from Equation (6.36).

### *Markovian regime*

Finally, we comment on the parameter regime where Markovianity holds [33]. This regime is characterized by both small system-bath coupling and moderate temperature, which means that the perturbation theory behind the master equation treatments of Section 2.3.1 and Part 5 are valid. In particular, we have a temperature larger than the renormalized energy scale of the biased system  $T_b \approx \sqrt{\Delta_r^2 + \epsilon^2}/k_B$  which makes the bath virtually memory-less while  $K \ll 1$  lends credibility to the Born approximation. The results for a static asymmetry we discussed above fall into this regime. Indeed, for the case of  $T_1 \gg T > T_b$ , where  $T_1$  is the lowest of the new transition temperatures (its form can be found in Weiss [33, Equation (22.66)]), one obtains the rates derived in Part 5. This dependence implies that for rising temperatures the one-phonon approximation implied in Born-Markov treatments starts to fail as multi-phonon processes become more important [33].

## 6.2 Formulation for a linearly driven bath

In this section, we are going to derive the effective force for a linearly driven bath using path integrals. We will see how the effective force integrates the memory of the bath by considering a driven bath before it couples to the system as seen in the previous chapter. After rederiving the effective force, we numerically solve the dynamic equation of motion (6.36) for a time-dependent asymmetry and discuss the resulting dynamics. Appendix E contains additional details about the calculation of the path integrals below.

### 6.2.1 The influence functional for a linearly driven bath

The dynamics of the spin-boson model is determined by the influence functional (6.9) which encodes the effect of the bath on the behavior of the coupled TSS. For a driven

bath the influence functional needs to be rederived. We start by assuming the bath to be in thermal equilibrium at time  $t_0$  where the combined density matrix  $W(t)$  factorizes into a system and bath part as seen in Equation (5.6). By doing so, we can follow the steps for the derivation of the path integral and find the propagators for the density matrix as (cf. Equation (2.71))

$$K(\sigma_f, \mathbf{x}_f, t; \sigma_i, \mathbf{x}_i, t_0) = \int_{\sigma_i}^{\sigma_f} \mathcal{D}\sigma \int_{\mathbf{x}_i}^{\mathbf{x}_f} \mathcal{D}\mathbf{x} A[\sigma] e^{\frac{i}{\hbar}(S_B^{\text{Dr}}[\mathbf{x}] + S_{\text{SB}}[\sigma, \mathbf{x}])}. \quad (6.45)$$

Here, we have rewritten the propagators in terms of the effective spin paths as in Equation (6.3). The integration over  $\mathbf{x}$  is to be understood as path integrations over the positions  $x_\alpha$  of every oscillator in the bath. Final states are labeled by the letter  $f$  and initial states by the letter  $i$ . The impact of bath driving is captured in the driven bath action  $S_B^{\text{Dr}}[\mathbf{x}]$  which uses the definition of Equation (4.12) based on position operators. As in the previous chapter, we do not take direct driving terms into account in order to find the influence from the driven bath only. A single oscillator  $\alpha$  then has the action

$$S_{\alpha, \text{B}}^{\text{Dr}}[x_\alpha] = \int_{t_0}^t ds \left[ \frac{m_\alpha}{2} \dot{x}_\alpha^2(s) - \frac{m_\alpha}{2} \omega_\alpha^2 x_\alpha^2(s) + \frac{d_\alpha}{2} F(s) x_\alpha(s) \right]. \quad (6.46)$$

By introducing integrations over auxiliary variables, the reduced density matrix of the system is given by

$$\begin{aligned} \rho_{\sigma_f, \sigma'_f}(t) &= \int d\mathbf{x}_f \int d\mathbf{x}_i \int d\mathbf{x}'_i \sum_{\sigma_i, \sigma'_i} K(\sigma_f, \mathbf{x}_f, t; \sigma_i, \mathbf{x}_i, t_0) \\ &* K^*(\sigma'_f, \mathbf{x}_f, t; \sigma'_i, \mathbf{x}'_i, t_0) \rho_{\sigma_i, \sigma'_i}(t_0) \rho_{\text{B}}(\mathbf{x}_i, \mathbf{x}'_i, t_0), \end{aligned} \quad (6.47)$$

with the bath density matrix element  $\rho_{\text{B}}(\mathbf{x}_i, \mathbf{x}'_i, t_0)$  for the (collective) positions  $\mathbf{x}_i$  and  $\mathbf{x}'_i$  evaluated at coupling time  $t_0$ . The influence functional follows from

$$\begin{aligned} F_{\text{FV}}^{\text{Dr}}[\sigma, \sigma'] &= \int d\mathbf{x}_f \int d\mathbf{x}_i \int d\mathbf{x}'_i \int_{\mathbf{x}_i}^{\mathbf{x}_f} \mathcal{D}\mathbf{x} \int_{\mathbf{x}'_i}^{\mathbf{x}_f} \mathcal{D}\mathbf{x}' \\ &* e^{\frac{i}{\hbar}(S_{\text{SB}}[\sigma, \mathbf{x}] - S_{\text{SB}}[\sigma', \mathbf{x}'])} e^{\frac{i}{\hbar}(S_B^{\text{Dr}}[\mathbf{x}] - S_B^{\text{Dr}}[\mathbf{x}'])} \rho_{\text{B}}(\mathbf{x}_i, \mathbf{x}'_i, t_0). \end{aligned} \quad (6.48)$$

We are now faced with the task of recalculating functional integrals of the form

$$I_\alpha^{\text{Dr}}[\sigma] = \int_{x_{\alpha, i}}^{x_{\alpha, f}} \mathcal{D}x_\alpha e^{\frac{i}{\hbar}(S_{\alpha, \text{SB}}[\sigma, x_\alpha] + S_{\alpha, \text{B}}^{\text{Dr}}[x_\alpha])}. \quad (6.49)$$

The total action in Equation (6.49) can be written as

$$\begin{aligned} &S_{\alpha, \text{SB}}[\sigma, x_\alpha] + S_{\alpha, \text{B}}^{\text{Dr}}[x_\alpha] \\ &= \int_{t_0}^t ds \left[ \frac{m_\alpha}{2} \dot{x}_\alpha^2(s) - \frac{m_\alpha}{2} \omega_\alpha^2 x_\alpha^2(s) + \left( \frac{d_\alpha}{2} F(s) + \frac{c_\alpha}{2} q_0 \sigma(s) \right) x_\alpha(s) \right] \\ &= \int_{t_0}^t ds \left[ \frac{m_\alpha}{2} \dot{x}_\alpha^2(s) - \frac{m_\alpha}{2} \omega_\alpha^2 x_\alpha^2(s) + \frac{c_\alpha}{2} q_0 \sigma_{\text{eff}}(s) x_\alpha(s) \right]. \end{aligned} \quad (6.50)$$

Here, we have combined the driving force  $F(t)$  and the state of the system  $\sigma(t)$  into an effective perturbation

$$\sigma_{\text{eff}}(t) = \sigma(t) + \frac{d_\alpha}{q_0 c_\alpha} F(t). \quad (6.51)$$

Equation (6.50) shows that the action remains that of forced harmonic oscillators. Therefore, the usual methods still apply (cf. Appendix E) and we can rewrite the path as the classical solution  $\bar{x}_\alpha(t)$  plus a term describing quantum fluctuations  $\zeta_\alpha(t)$ . We find the classical equation of motion as

$$m_\alpha \frac{d^2 \bar{x}_\alpha(s)}{ds^2} + m_\alpha \omega_\alpha^2 \bar{x}_\alpha(s) = \frac{c_\alpha}{2} q_0 \sigma_{\text{eff}}(s). \quad (6.52)$$

Meanwhile, the action of the fluctuations is unchanged and leads to the usual prefactor [210]. The path integral (6.49) becomes

$$I_\alpha^{\text{Dr}}[\sigma_{\text{eff}}] = \sqrt{\frac{m_\alpha \omega_\alpha}{2\pi i \hbar \sin[\omega_\alpha(t-t_0)]}} e^{i\hbar \Phi[x_{\alpha,i}, x_{\alpha,f}, \sigma_{\text{eff}}]}, \quad (6.53)$$

with the phase

$$\begin{aligned} \Phi[x_{\alpha,i}, x_{\alpha,f}, \sigma_{\text{eff}}] = & \\ & \frac{m_\alpha \omega_\alpha}{2\chi_\alpha(t-t_0)} \{ [x_{\alpha,f}^2 + x_{\alpha,i}^2] \chi'_\alpha(t-t_0) - 2x_{\alpha,f} x_{\alpha,i} \} \\ & + \frac{c_\alpha q_0}{2} \int_{t_0}^t ds \left[ \frac{\chi_\alpha(s-t_0)}{\chi_\alpha(t-t_0)} x_{\alpha,f} + \frac{\chi_\alpha(t-s)}{\chi_\alpha(t-t_0)} x_{\alpha,i} \right] \sigma_{\text{eff}}(s) \\ & - \frac{c_\alpha^2 q_0^2}{4} \int_{t_0}^t ds \int_{t_0}^s du \frac{\chi_\alpha(u-t_0) \chi_\alpha(t-s)}{m_\alpha \omega_\alpha \chi_\alpha(t-t_0)} \sigma_{\text{eff}}(s) \sigma_{\text{eff}}(u). \end{aligned} \quad (6.54)$$

Here,  $\bar{x}_\alpha(t_0) = x_{\alpha,i}$  and  $\bar{x}_\alpha(t) = x_{\alpha,f}$  are boundary values and  $\chi_\alpha(t) = \sin(\omega_\alpha t)$  and  $\chi'_\alpha(t) = \cos(\omega_\alpha t)$  are fundamental solutions of the harmonic oscillator. As discussed, we assume the bath to be in thermal equilibrium at coupling time, allowing us to replace  $\rho_B(x_{\alpha,i}, x'_{\alpha,i}, t_0) = \rho_B^{\text{eq}}(x_{\alpha,i}, x'_{\alpha,i})$  as given in Equation (E.8). Similarly, insertion of the result (6.53) into Equation (6.48) leads to Gaussian integrations over the boundary values. After some tedious manipulations, we obtain the influence functional for a linearly driven bath as

$$\begin{aligned} F_{\text{FV}}^{\text{Dr}}[\sigma, \sigma'] = & \exp \left[ - \int_{t_0}^t dt' \int_{t_0}^{t'} dt'' \xi_{\text{eff}}(t') L'(t' - t'') \xi_{\text{eff}}(t'') \right] \\ & * \exp \left[ -i \int_{t_0}^t dt' \int_{t_0}^{t'} dt'' \xi_{\text{eff}}(t') L''(t' - t'') \eta_{\text{eff}}(t'') \right]. \end{aligned} \quad (6.55)$$

For brevity we have absorbed  $\sigma_{\text{eff}}$  and  $\sigma'_{\text{eff}}$  into effective blips and sojourns as in Equation (6.8). We note that the bath autocorrelation function  $L(t)$  is unchanged from the equilibrium case. Effects of bath driving only appear as a time-dependent shift of the system coordinates  $\sigma$  and  $\sigma'$  via Equation (6.51). As  $F(t)$  is real, insertion shows that the blips are unchanged because  $\xi_{\text{eff}}(t) = \xi(t)$  while the sojourns give  $\eta_{\text{eff}}(t) = \eta(t) + (d_\alpha/q_0 c_\alpha)F(t)$ . This allows us to rewrite Equation (6.55) as

$$F_{\text{FV}}^{\text{Dr}}[\sigma, \sigma'] = F_{\text{FV}}[\sigma, \sigma'] * \exp \left[ -i \int_{t_0}^t dt' \int_{t_0}^{t'} dt'' \xi(t'') \bar{L}''(t' - t'') F(t'') \right], \quad (6.56)$$

where we have absorbed the factor  $d_\alpha/q_0 c_\alpha$  into  $L(t)$  for a new  $\bar{L}(t)$  while  $F_{\text{FV}}[\sigma, \sigma']$  is the bare influence functional found in Equation (6.4). Direct comparison with the results for the system amplitudes in Equation (6.25) shows that the additional term represents an effective time-dependent asymmetry. We read off

$$\epsilon(t)/\hbar = F_{\text{eff}}(t) = \frac{1}{\pi} \int_0^\infty d\omega \bar{J}(\omega) \int_{t_0}^t dt' F(t') \sin[\omega(t' - t)], \quad (6.57)$$

which directly gives the effective force  $F_{\text{eff}}(t)$  found in Equations (4.19) and (5.17). We note that the factor  $q_0$  vanishes naturally from the rescaling.

We have shown again that a linearly driven bath merely produces a force which appears as a time-dependent asymmetry. In the next subsection, we derive the density matrix of the driven bath itself and show that it leads to the non-Markovian force.

### 6.2.2 Initial correlations and emergence of the non-Markovian force

We utilize the same driving protocol as shown in Figure 5.1. This means, we consider a pulsed bath driving scheme where the time  $t_a$  labels the moment when the bath driving pulse  $F(t)$  becomes non-zero while system and bath are (instantaneously) coupled at  $t_0$  with  $t_0 \geq t_a$ . The effect of the bath driving pulse prior to  $t_0$  is then encoded in the bath density matrix element  $\rho_{\text{B}}(x_{\alpha,i}, x'_{\alpha,i}, t_0)$  that appears in Equation (6.48). In order to find an explicit expression, we assume that the bath is in equilibrium at time  $t_a$ . We can formulate its time evolution using path integrals as

$$\rho_{\text{B}}(\mathbf{x}_i, \mathbf{x}'_i, t_0) = \int d\mathbf{x}_p \int d\mathbf{x}'_p K_{\text{B}}(\mathbf{x}_i, t_0; \mathbf{x}_p, t_a) K_{\text{B}}^*(\mathbf{x}'_i, t_0; \mathbf{x}'_p, t_a) \rho_{\text{B}}^{\text{eq}}(\mathbf{x}_p, \mathbf{x}'_p), \quad (6.58)$$

where  $\mathbf{x}_p$  are new boundary value integrations for the prehistory of the bath. The driven bath propagators  $K_{\text{B}}(\dots)$  are given as

$$K_{\alpha,\text{B}}(x_{\alpha,i}, t_0; x_{\alpha,p}, t_a) = \int_{x_{\alpha,p}}^{x_{\alpha,i}} \mathcal{D}x_\alpha e^{\frac{i}{\hbar} S_{\alpha,\text{B}}^{\text{Dr}}[x_\alpha]}, \quad (6.59)$$

with the driven bath action of Equation (6.46) and written for a single bath oscillator  $\alpha$ , for brevity. Since the action describes forced oscillators the propagators can be evaluated as usual. We obtain

$$K_{\alpha,B}(x_{\alpha,i}, t_0; x_{\alpha,p}, t_a) = \sqrt{\frac{m_\alpha \omega_\alpha}{2\pi i \hbar \sin[\omega_\alpha(t_0 - t_a)]}} e^{\frac{i}{\hbar} \Phi_B[x_{\alpha,p}, x_{\alpha,i}, F(s)]}, \quad (6.60)$$

with the phase

$$\begin{aligned} \Phi_B[x_{\alpha,p}, x_{\alpha,i}, F] = & \\ & \frac{m_\alpha \omega_\alpha}{2\chi_\alpha(t_0 - t_a)} \{ [x_{\alpha,i}^2 + x_{\alpha,p}^2] \chi'_\alpha(t_0 - t_a) - 2x_{\alpha,i} x_{\alpha,p} \} \\ & + \frac{d_\alpha}{2} \int_{t_a}^{t_0} ds \left[ \frac{\chi_\alpha(s - t_a)}{\chi_\alpha(t_0 - t_a)} x_{\alpha,i} + \frac{\chi_\alpha(t_0 - s)}{\chi_\alpha(t_0 - t_a)} x_{\alpha,p} \right] F(s) \\ & - \frac{d_\alpha^2}{4} \int_{t_a}^{t_0} ds \int_{t_a}^s du \frac{\chi_\alpha(u - t_a) \chi_\alpha(t_0 - s)}{m_\alpha \omega_\alpha \chi_\alpha(t_0 - t_a)} F(s) F(u). \end{aligned} \quad (6.61)$$

Insertion into Equation (6.58) eventually yields

$$\rho_B(x_{\alpha,i}, x'_{\alpha,i}, t_0) = \frac{1}{Z_\alpha} \sqrt{\frac{m_\alpha \omega_\alpha}{2\pi \hbar \sinh(\omega_\alpha \hbar \beta)}} e^{-\frac{1}{\hbar} \Phi_{\text{eff}}^{\text{eq}}[x_{\alpha,i}, x'_{\alpha,i}, F]}. \quad (6.62)$$

Here, we have defined the effective equilibrium phase

$$\begin{aligned} \Phi_{\text{eff}}^{\text{eq}}[x_{\alpha,i}, x'_{\alpha,i}, F] = & \\ \Phi^{\text{eq}}[\bar{x}_{\alpha,i}, \bar{x}'_{\alpha,i}] - i \frac{d_\alpha}{2} (x_{\alpha,i} - x'_{\alpha,i}) \int_{t_a}^{t_0} du \cos[\omega_\alpha(u - t_0)] F(u). \end{aligned} \quad (6.63)$$

Equation (6.63) also includes the equilibrium result of Equation (E.9) but for shifted variables, defined by

$$\bar{x}_{\alpha,i} = x_{\alpha,i} - \frac{d_\alpha}{2m_\alpha \omega_\alpha} \int_{t_a}^{t_0} du \sin[\omega_\alpha(t_0 - u)] F(u). \quad (6.64)$$

The equivalent Equation for  $\bar{x}'_{\alpha,i}$  follows by replacing  $x_{\alpha,i}$  by  $x'_{\alpha,i}$ . We note that the variables in Equation (6.64) exhibit a similar time evolution as the Heisenberg dynamics in Equation (5.12).

It is now a straightforward matter to insert the result of Equation (6.62) into Equation (6.48) in order to find the dynamics of the system following  $t_0$ . In order to perform the required integrations over the boundary values we substitute the shifted variables of

Equation (6.64) to find after some calculations (cf. Appendix E)

$$F_{\text{FV}}^{\text{Dr}}[\sigma, \sigma'] = \exp \left[ - \int_{t_a}^t dt' \int_{t_a}^{t'} dt'' \xi_{\text{eff}}(t') L'(t' - t'') \xi_{\text{eff}}(t'') \right] \quad (6.65)$$

$$* \exp \left[ -i \int_{t_a}^t dt' \int_{t_a}^{t'} dt'' \xi_{\text{eff}}(t') L''(t' - t'') \eta_{\text{eff}}(t'') \right].$$

In order to acquire the form (6.65) we have absorbed the implicit time dependence of the coupling constants  $c_\alpha$  into the  $\sigma(t)$ , such that  $\sigma(t < t_0) = 0$ . Explicitly making use of this time dependence eliminates  $t_a$  in all but one term. We find the corrected influence functional as

$$F_{\text{FV}}^{\text{Dr}}[\sigma, \sigma'] = F_{\text{FV}}[\sigma, \sigma'] * \exp \left[ -i \int_{t_0}^t dt' \int_{t_a}^{t'} dt'' \xi(t') \bar{L}''(t' - t'') F(t'') \right], \quad (6.66)$$

where  $F_{\text{FV}}[\sigma, \sigma']$  only depends on the coupling time  $t_0$ . The onset of the perturbation at time  $t_a$  appears solely in the lower bound of the integral of the time-dependent asymmetry. Therefore, the effect of initial bath driving is absorbed completely in the additional force contribution. We have recovered the non-Markovian force of Equation (5.17) once again.

### 6.2.3 NIBA dynamics for a linearly driven bath

As outlined in Section 6.1.3, the NIBA allows us to obtain the dynamics for a wide range of parameters. In the same section, we presented analytical results for the specific case of  $K = 1/2$  in Equations (6.41) and (6.43), as well as a high-temperature solution (6.42) for arbitrary  $K$ . We also noted an analytic zero-temperature result for the symmetric case, based on the Mittag-Leffler function, whose exact form is given in Weiss [33, Equation (22.5)]. In the following, we evaluate the NIBA result (6.36) numerically and include the effective force found in Equation (6.57) via the bias phase (6.39). Comparison with the analytic results then allows us to make statements about the effect of a driven bath with respect to the coupling strength and higher temperatures.

We look at the dynamics for Ohmic and Lorentzian spectral densities again. In this part of the thesis we use the forms

$$J^{(1)}(\omega) = 2\pi\omega K e^{-\omega/\omega_c} \quad \text{and} \quad (6.67)$$

$$J^{(2)}(\omega) = 2\pi\omega K' \frac{\Omega^4}{(\omega^2 - \Omega^2)^2 + (\Gamma\omega)^2}. \quad (6.68)$$

The additional factor of  $\pi$  makes the prefactor equivalent to the definition in Weiss [33] and Caldeira [31], as discussed in Section 2.2.3. This allows us to directly compare the

numerical results to the analytic expressions presented in Section 6.1.3. However, these expressions were derived for an Ohmic spectral density in the scaling limit such that we cannot expect agreement for the Lorentzian spectral density. Nevertheless, we have included a prefactor  $K' = \kappa\Gamma/2\Omega^2$  in  $J^{(2)}(\omega)$  as an equivalent to  $K$ . For perspective, the corresponding coupling constants  $K$  and  $K'$  with the values from Part 5 are of the order of  $10^{-3}$  and  $10^{-4}$ , respectively.

In the following, we continue to disregard direct driving contributions and only look at the population  $\langle\sigma_z(t)\rangle$  for the initial condition  $\langle\sigma_z(t_0)\rangle = 1$ . A generalization to other initial conditions is, in principle, possible by following the derivation in Weiss [33] and Grifoni and Hänggi [32].

### *Driving terms*

We use approximate expressions for the effective force in order to minimize the numerical effort. In case of an Ohmic spectral density, a Gaussian pulse recreated a Gaussian albeit slightly shifted, negative, and with smaller peak height (see Figure 5.2). For the Ohmic spectral density in Equation (6.67) we therefore use

$$F_{\text{eff}}^{(1)}(t) \approx -A \Theta(t - t_0) e^{-\frac{(t-s)^2}{2\sigma^2}}. \quad (6.69)$$

Here, we have defined  $s$  as a generic shift which includes the position of the Gaussian  $t_g$  as well as a slight deviation to model the retardation of the pulse. The prefactor  $A$  has a dimension of frequency and determines the peak height of the force while the variable  $\sigma$  gives the width of the Gaussian. The Heaviside function is included to make sure that the effective force will only be nonzero following  $t_0$ . Equation (6.69) leads to an effective bias phase given by

$$\begin{aligned} \vartheta^{(1)}(t, t') = & \Theta(t - t')\Theta(t - t_0)\Theta(t' - t_0) \\ & * A \left[ \sigma\sqrt{\pi/2} \right] \left[ \text{erf} \left( \frac{t' - s}{\sqrt{2}\sigma} \right) - \text{erf} \left( \frac{t - s}{\sqrt{2}\sigma} \right) \right]. \end{aligned} \quad (6.70)$$

Here,  $\text{erf}(x)$  designates the error function such that the difference above gives the impact of the lower and upper bound of the integral, respectively.

For the Lorentzian bath, we consider the fit in Equation (5.29) which was seen to be valid for both the  $\delta$ -pulse and the Gaussian at long times. The fit describes damped oscillations given by

$$F_{\text{eff}}^{(2)}(t) \approx -B \Theta(t - t_a) \sin[\Omega(t - t_a)] e^{-\frac{\Gamma}{2}(t - t_a)}. \quad (6.71)$$

Here,  $t_a$  is the time of the onset of the perturbation with  $t_a > t_0$ . The variables  $\Omega$  and  $\Gamma$  are the position and the width of the Lorentzian peak given in Equation (6.68). The



generic prefactor  $B$  determines the peak height for very small values of  $\Gamma$ . Equation (6.71) leads to the phase

$$\begin{aligned} \vartheta^{(2)}(t, t') &= \left[ \frac{B}{(\Gamma/2)^2 + \Omega^2} \right] \Theta(t - t') \Theta(t - t_a) \Theta(t' - t_a) \\ &* \left\{ \frac{\Gamma}{2} \left( \sin[\Omega(t - t_a)] e^{-\frac{\Gamma}{2}(t-t_a)} - \sin[\Omega(t' - t_a)] e^{-\frac{\Gamma}{2}(t'-t_a)} \right) \right. \\ &\quad \left. + \Omega \left( \cos[\Omega(t - t_a)] e^{-\frac{\Gamma}{2}(t-t_a)} - \cos[\Omega(t' - t_a)] e^{-\frac{\Gamma}{2}(t'-t_a)} \right) \right\}. \end{aligned} \quad (6.72)$$

Before progressing, we discuss the resulting equilibrium values of  $\langle \sigma_z(t) \rangle$ . Since we assume transient forces with  $\epsilon(t \rightarrow \infty) = 0$ , they will correspond to the results for a symmetric system. However, some care must be taken as the equilibrium results in the NIBA are known to be incorrect at low temperatures. For vanishing  $\epsilon$ , we find [33] (cf. the exact values in Equations (2.51) and (2.52))

$$\langle \sigma_z(t \rightarrow \infty) \rangle = - \tanh \left( \frac{\epsilon}{2k_B T} \right) \stackrel{\epsilon \rightarrow 0}{=} 0, \quad (6.73)$$

$$\langle \sigma_x(t \rightarrow \infty) \rangle = - \frac{\Delta}{\epsilon} \tanh \left( \frac{\epsilon}{2k_B T} \right) \stackrel{\epsilon \rightarrow 0}{=} - \frac{\Delta}{2k_B T}. \quad (6.74)$$

Equation (6.74) makes this failure obvious because it diverges for zero temperature instead of yielding  $-1$  as seen in Part 5. While we will not present the dynamics of  $\langle \sigma_x(t) \rangle$  in the following, it should be noted that our numerical implementation of Equation (6.36) indeed yields results consistent with Equation (6.74).

### ***Strength of the effective force***

In order to determine the strength of the bath driving contribution, we note that the magnitude of  $F_{\text{eff}}$  is determined chiefly by the prefactor of the effective spectral density  $\bar{J}(\omega)$ ,  $\bar{\eta}$ , and the field strength of the associated driving field  $E_0$ . Using Equation (2.56), we find the prefactor corresponding to  $K$  as  $\hat{K} = q_0 \bar{\eta} / 2\pi \hbar$ . Since the field strength also enters into the effective force, the actual dimensionless quantity of interest is given by  $\bar{K} = \hat{K} E_0$ . We used a similar definition in Part 5 where we parametrized the driving strength by combined prefactors. A general relationship between  $K$  and  $\bar{K}$  can be derived on the basis of the Onsager sphere model in Section 4.2.3 as

$$\bar{K} = LK = \left[ \frac{2\pi \epsilon_0 a^3}{q_0 e} E_0 \right] K = \frac{(q_0 e) E_0}{2\pi \hbar} \bar{\chi}'', \quad (6.75)$$

where we have used Equation (4.25) for the second equality sign, whereas the first defines the proportionality constant  $L$ . The relationship (6.75) is based on the simplest solvation

model, that is, for a dipole with one elementary charge  $e$  located inside a spherical cavity of radius  $a$ . Since we have used a TSS, the quantized position  $q_0$  associated with the states  $\sigma_z = \pm 1$  also enters. The third equality is given for completeness. It has used Equation (3.52) to express  $K$  in model parameters. Therein,  $\bar{\chi}_o'' = \text{Im}[\chi_o(\omega_{\max})]/\omega_{\max}$  is a normalization factor with the dimension of a frequency and depends on the Onsager susceptibility found in Equation (3.48). This factor ensures that  $K$  has the right order of magnitude. The factor  $\bar{K}$  then determines the effective force according to

$$F_{\text{eff}}(t, t_a) = 2\bar{K} \int_0^\infty d\omega \left( \frac{\bar{J}^{(1,2)}(\omega)}{2\hat{K}\pi} \right) \int_{t_a}^t dt' \left( \frac{F(t')}{E_0} \right) \sin[\omega(t' - t)]. \quad (6.76)$$

The superscripts of  $\bar{J}(\omega)$  indicate that we consider similar forms as in Equations (6.67) and (6.68). The integrals can be collected in a single factor  $I(t, t_a)$ . If we assume that the time integral over the force is of the order of  $\omega_0^{-1}$ , the result is determined by the frequency scale of the bath. Specifically, if we insert the Ohmic spectral density of Equation (6.67) we may approximate

$$F_{\text{eff}}(t, t_a) = 2\bar{K}I(t, t_a) \sim 2\bar{K}\omega_c(\omega_c/\omega_0), \quad (6.77)$$

where  $\omega_c$  is the cutoff frequency. Insertion of the proportionality between  $K$  and  $\bar{K}$  then yields for the asymmetry

$$\epsilon(t) = \hbar F_{\text{eff}}(t, t_a) \sim 2LK(\hbar\omega_c)(\omega_c/\omega_0), \quad (6.78)$$

Using Equation (6.75),  $L$  can be gauged as  $L \approx 3 \times 10^{-5}$  where we use a moderate field strength of  $E_0 = 10$  kV/cm,  $a = 2\text{\AA}$  as approximated in Part 4, and a dipole of length  $q_0 = 1\text{\AA}$ . For a generic cutoff frequency of  $\omega_c = 10\omega_0$  with  $K = 1$  this yields  $\epsilon(t) \sim 10^{-3}\hbar\omega_0$  which is a fairly small result, overall. The same holds true for the Lorentzian density of Equation (6.66): by using the values from Part 5, the cutoff frequency can be approximated from a numerical evaluation of the frequency integral as  $\sim 7\hbar\omega_0$ . While this result depends on  $\Omega$  and  $\Gamma$  in a nontrivial way, we aim to use the same values as in the previous chapter such that the resulting asymmetry would be too small for moderate fields.

However, we note that the molecular dynamics studies by Mishra, Vendrell and Santra [38, 39] which investigated the effect of strong THz pulses on water used field strengths up to  $10^5$  kV/cm, such that values of  $\epsilon(t) \sim 10$  may be realistic. Thus, we employ a larger  $L$  defined by the constraint  $\epsilon(t) \sim \mathcal{O}(1)$ . A look at Equation (6.75) for fixed  $K$  shows that this can be achieved with field strengths of about  $E_0 = 10^4$  kV/cm but also by using larger cavities (that is, larger molecules) with smaller induced dipole moments. It is also possible to choose larger cutoffs, but their role is questionable as they have to be physically motivated or are completely immaterial and are meant to drop out. In fact, Equation (5.28) implies that the approximation is only valid near the

very peak of a pulse where  $\omega_c(t - t_g) \approx 1$ , such that its application for large cutoffs is dubious. In short, we set the constants  $A$  and  $B$  of Equations (6.69) and (6.71) to

$$A = K\omega_0 \quad \text{and} \quad B = K'\omega_0. \quad (6.79)$$

In order to compare  $A$  and  $B$  above to their values in the previous chapter, we note that  $\bar{\eta}/\eta \approx \bar{\kappa}/\kappa \approx 10^2$ . Hence, by use of Equation (6.79) we probe the dynamics for much smaller driving strengths.

Before evaluating the NIBA, we stress the importance of the relationships (6.75) and (6.78): By way of the Onsager model, they directly relate the coupling constant of the spectral density to the effective force and include the impact of the electric field strength. While this result merely reformulates the conclusions drawn at various stages of this thesis, generalizations of these identities should enable easy comparisons in future research. For the present case, the proportionality in Equation (6.79) is especially important as we investigate a range of different values for  $K$  and  $K'$ .

### *Population dynamics for the Ohmic spectral density $J^{(1)}(\omega)$*

First, we investigate the population  $\langle \sigma_z(t) \rangle$  for the Ohmic spectral density in Equation (6.67) and the Gaussian effective force used in Equation (6.69). The parameters of the Gaussian are determined using the results in Figure 5.2 (b). Specifically, we can see that the width is nearly unchanged by the mediation by the bath, such that we use  $\sigma = \omega_0^{-1}$ . The Gaussian is also slightly displaced implying that the force is retarded with respect to the direct driving pulse. We therefore set  $s = 5.25 \omega_0^{-1}$ . Using these values, together with the parameter  $A = K\omega_0$  from the previous subsection, we obtain the results shown in Figure 6.2 for four different combinations of  $K$  and temperature. For comparison, we used  $K \approx 10^{-3}$  in Part 5.

We start by stating agreement of our numerical solutions obtained from Equation (6.36) and the analytical results discussed in Section 6.1.3. As expected, the dynamics transition to incoherent behavior at  $K \geq 0.5$  or for large enough temperatures while the high temperature solution of Equation (6.42) agrees for large enough temperatures. Furthermore, we obtain full agreement with the exact solution in Equation (6.41) at  $K = 0.5$ . However, the impact of driving is comparably small in all cases, even more so when the dynamics is incoherent or the temperature becomes too large. The only conceivable effect can be seen for small coupling when a coherent dynamics is still present or for the zero temperature solution at  $K = 0.5$ .

Thus, temperature has a strong effect on the relative efficacy of the effective force. When the dynamics becomes incoherent with  $k_B T \gg \epsilon(t)$ , its effect is rapidly washed out even though  $\epsilon(t)$  becomes closer to  $\Delta$  for increasing coupling strength. Interestingly, using a comparably strong coupling with small temperatures also makes any driving contributions matter less. In this regime, the decay becomes so sluggish that any

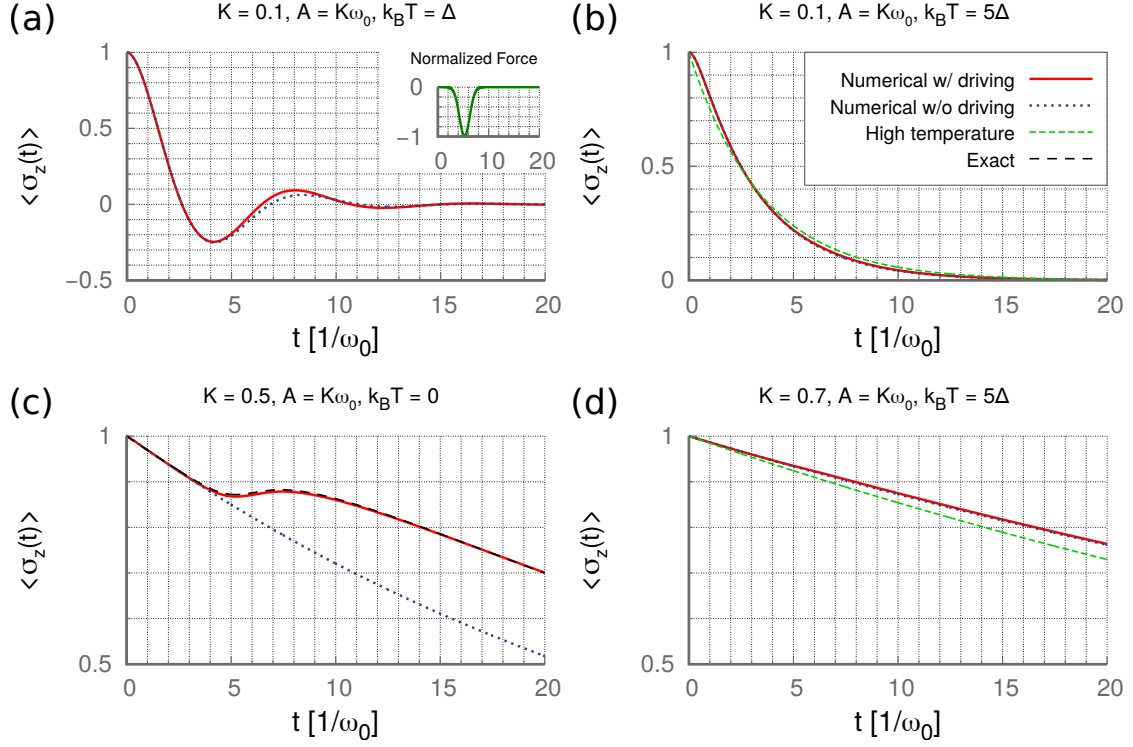


**Figure 6.2:** Resulting numerical solutions of Equation (6.36) for the population  $\langle \sigma_z(t) \rangle$  (solid red lines) using the Ohmic spectral density (6.67) and the effective force (6.69) for four different combinations of  $K$  and temperature. Each panel also shows the results without driving effects (blue dotted lines). The parameters are  $A = K\omega_0$ ,  $\sigma = \omega_0^{-1}$ ,  $s = 5.25 \omega_0^{-1}$  and  $\omega_c = 50 \omega_0$ . The legend for all four panels is found in the upper right corner of panel (b) while the normalized effective force is shown as an inset in panel (a). (a) Result for  $K = 0.1$  at low temperature ( $k_B T = \Delta$ ). (b) Result for  $K = 0.1$  at higher temperature ( $k_B T = 5\Delta$ ). This panel also shows the high temperature solution given by Equation (6.42) (green dashed line). (c) Result for  $K = 0.5$  at zero temperature. This panel also shows the result of the exact solution given in Equation (6.43) (black dashed line). (d) Result for stronger coupling  $K = 0.7$  at high temperature ( $k_B T = 5\Delta$ ). This panel shows the high temperature solution as well.

effect cannot change the state much, because the result is always close to one within a reasonable time frame ( $\omega_0^2 t / \omega_c \sim 1$ ). Further increase of the coupling strength does not lead to significant changes for the same reason.

The former arguments depend on the actual strength of the bath driving contribution that we have already chosen large but still smaller than in Part 5. It is therefore useful to compare results for larger driving strength. For this reason, Figure 6.3 shows the weak coupling results at  $K = 0.1$  for  $A = \omega_0$  (thus,  $\bar{K}/K \approx 10$ ). The impact of the effective force is now clearly visible, even in the incoherent regime. However, the net

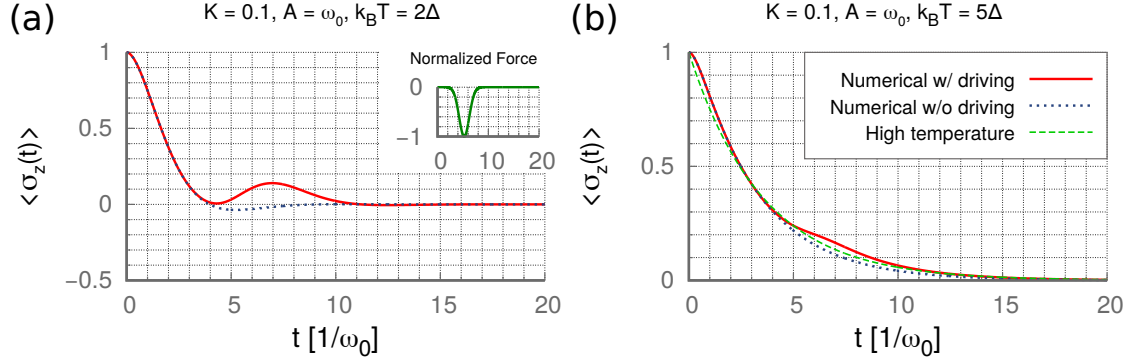


**Figure 6.3:** Resulting numerical solutions of Equation (6.36) for the population  $\langle \sigma_z(t) \rangle$  (solid red lines) using the Ohmic spectral density (6.67) and the effective force (6.69) at  $K = 0.1$  with stronger driving of  $A = \omega_0$  at two different temperatures. Both panels also show the results without driving effects (blue dotted lines). The parameters are  $\sigma = 1 \omega_0^{-1}$ ,  $s = 5.25 \omega_0^{-1}$  and  $\omega_c = 50 \omega_0$ . (a) Result at low temperature ( $k_B T = 2\Delta$ ). (b) Result at a higher temperature ( $k_B T = 5\Delta$ ). This panel also shows the high temperature solution of Equation (6.42) (green dashed line). The normalized effective force for both panels is shown in an inset in panel (a).

effect is still smaller for larger temperatures suggesting that our conclusion about its influence is valid. Both effects also vanish rapidly as soon as the pulse concludes. A comparison with the results from Part 5 suggests that this is due to increased damping from the larger system-bath coupling and temperature we employed here. It should be noted that the low-temperature result uses a slightly higher temperature than in Figure 6.2. This is because the NIBA becomes unreliable for non-zero asymmetry at temperatures below  $k_B T_b = \sqrt{\Delta_{\text{eff}}^2(K) + \epsilon(t)^2}$  which is at most  $\sim 1.2\Delta$  for the choice of parameters here.

#### **Population dynamics for the Lorentzian spectral density $J^{(2)}(\omega)$**

We next consider the Lorentzian spectral density of Equation (6.68) with the bias phase (6.72). In this case, the results from Section 6.1.3 cannot be compared directly as they were derived for an Ohmic spectral density. Still, by using  $K'$  we are able to make a qualitative comparison. In order to parametrize the Lorentzian, we use the same values as in Part 5, that is, a fairly small peak width of  $\Gamma = 0.1 \omega_0$  and a position at  $\Omega = 1.5 \omega_0$ . The results for four different combinations of  $K'$  and temperature are shown in Figure 6.4. For the sake of comparison, Part 5 employed  $K' \approx 10^{-4}$ .

The most evident result of Figure 6.4 is a complete absence of driving effects for the chosen strength of  $B = K'$  in all cases. The reason for this is two-fold: First, the Lorentzian spectral density shows incoherent behavior at much weaker coupling strength. This is why we have chosen a comparably weak coupling in order to illustrate the dynamics, but also entails an extremely weak driving strength. Second, the oscillat-

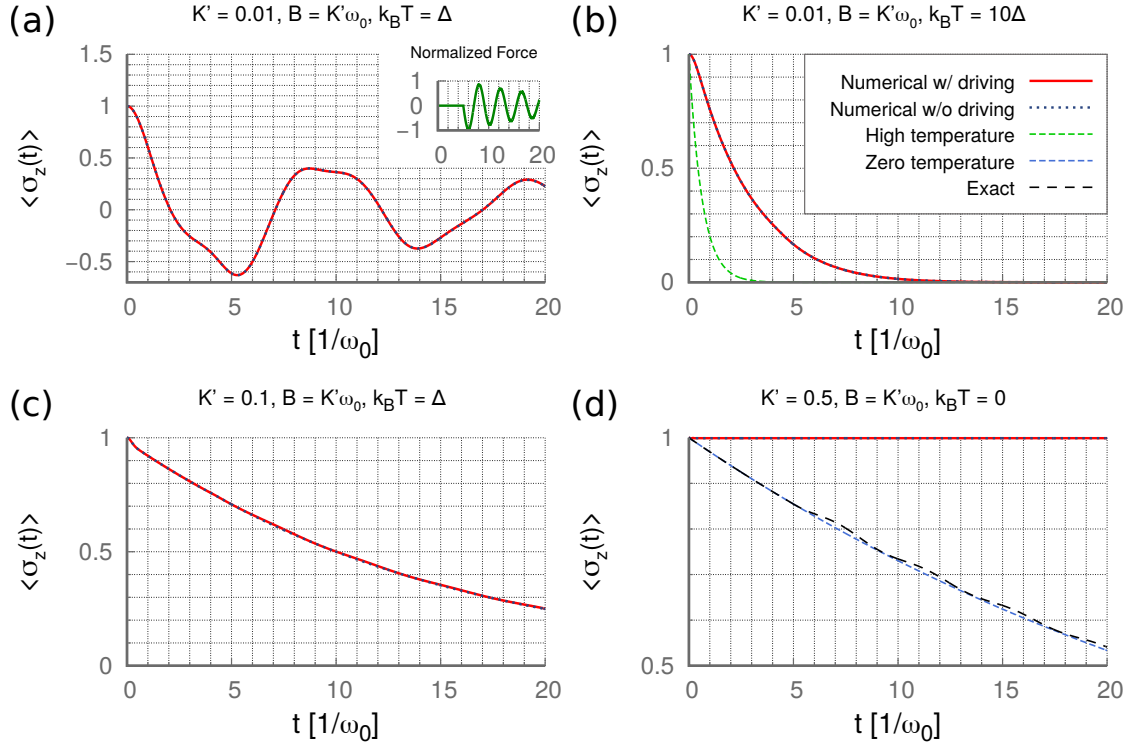


**Figure 6.4:** Resulting numerical solutions of Equation (6.36) for the population  $\langle \sigma_z(t) \rangle$  (solid red lines) using the Lorentzian spectral density (6.68) and the effective force (6.71) for four different combinations of  $K'$  and temperature. Each panel also shows the results without driving effects (blue dotted lines). The parameters are  $B = K'\omega_0$ ,  $\Gamma = 0.1\omega_0$  and  $\Omega = 1.5\omega_0$ . The legend for all four panels is found in the upper right corner of panel (b) while the normalized effective force is shown as an inset in panel (a). (a) Result for  $K' = 0.01$  at low temperatures ( $k_B T = 1\Delta$ ). (b) Result for  $K' = 0.01$  at higher temperature ( $k_B T = 10\Delta$ ). This panel also shows the high temperature solution (6.42) (green dashed line). (c) Result for stronger coupling  $K' = 0.1$  at low temperature ( $k_B T = 1\Delta$ ). (d) Result for  $K' = 0.5$  at zero temperature. This panel also shows the result of the exact solution (6.43) (black dashed line) as well as a solution for a symmetric system at zero temperature based on the Mittag-Leffler function [33, Equation (22.5)] as a comparison (light-blue dashed line). Note, that all analytical results shown here are derived for the Ohmic spectral density (6.67) such that agreement with the numerical results is not expected.

ing driving force also seems to influence the dynamics less. This can be gleaned from the exact solution for the Ohmic spectral density at  $K = 0.5$  which exhibits a much weaker change than for the Gaussian in Figure 6.2. In fact, this result only imperceptibly differs from the exact zero temperature solution. The Lorentzian solutions, in turn, show incoherent decay for  $K' = 0.1$  already at low temperatures and are (almost) completely constant at 1 for zero temperature at  $K = 0.5$ . For very weak coupling, distorted oscillations are visible at low temperature. The reason for their peculiar shape

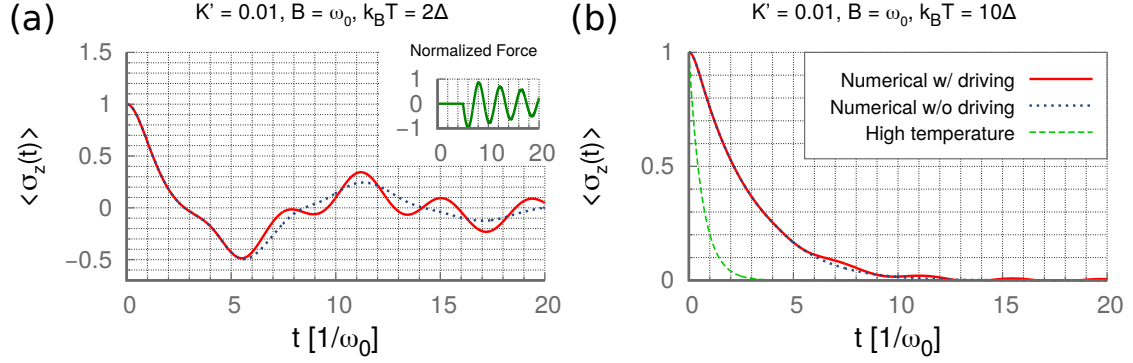


**Figure 6.5:** Resulting numerical solutions of Equation (6.36) for the population  $\langle \sigma_z(t) \rangle$  (solid red lines) using the Lorentzian spectral density (6.68) and the effective force (6.71) at  $K' = 0.01$  with stronger driving of  $B = \omega_0$  at two different temperatures. Both panels also show the results without driving effects (blue dotted lines). The parameters are  $\Gamma = 0.1\omega_0$  and  $\Omega = 1.5\omega_0$ . (a) Result at low temperature ( $k_B T = 2\Delta$ ). (b) Result at a higher temperature ( $k_B T = 10\Delta$ ). This panel also shows the high temperature solution of Equation (6.42) (green dashed line). The normalized effective force for both panels is shown in an inset in panel (a).

can be found in the Fourier spectrum (not shown) which now includes frequencies around  $\Omega$ , as we could suspect from the analyses in Sections 2.2.2 and 5.3.4. For a temperature of  $k_B T = 10\Delta$  the result becomes incoherent. Interestingly, this happens much earlier than for the Ohmic case where  $k_B T^* \approx 32\Delta$  for  $K = 0.01$ . The result at a higher temperature also does not agree with the solution in Equation (6.42).

Again, we consider the dynamics at even larger driving strength of  $B = \omega_0$  for the weak coupling cases given here with  $K' = 0.01$  (thus  $\bar{K}'/K' \approx 10^2$ ). The results are shown in Figure 6.5. The impact of the long-lasting oscillations is clearly visible, albeit extremely suppressed in the case of high temperatures. There, the strongest deviation is on the order of 0.02, or about a third of the remaining population at this point. In contrast, the low temperature results show large oscillations where the largest peak is increased by about 0.2 in comparison to the undriven result. The oscillations follow the force with a frequency close to  $\Omega$ . The reason for this can be found in the frequency spectrum as the force adds to the contribution at the oscillator frequency. The competition between the oscillations at the renormalized TSS frequency and at  $\Omega$  is then shifted more towards the latter such that the contributions from the mode are more pronounced.

### Summary

Before proceeding, we sum up the results of the previous analysis. We have seen that the simple proportionality of Equation (6.79) is not sufficient to see any significant impact of the driven bath. In fact, at least an order of magnitude more is needed in

the driving strength to observe any relevant effects in the dynamics. Even then our considerations suggest that bath driving contributions are most relevant in the coherent regime, i.e., for small to intermediate system-bath coupling at low temperatures. Higher temperatures seem to wash out effects of the effective force very efficiently and strong coupling implies only very slow decay of the population where any observable effect is also small. The latter stands in contrast to the larger driving strength implied by the proportionality to the coupling constant.

#### 6.2.4 Parametrically driven baths

We close this section with a brief outlook on a potential improvement to our treatment which was limited to driving terms linear in the position of the oscillators up until now. The next more complicated case is a quadratic coupling which could correspond, for instance, to interaction with an electric field via a quadrupole moment. This gives rise to a time-dependent frequency in the associated equation of motion, turning the harmonic oscillators into parametrically driven ones. The driven bath Hamiltonian is now given by

$$H_B^{\text{Dr}} = \sum_{\alpha=1}^N \frac{1}{2} \left[ \frac{p_{\alpha}^2(t)}{m_{\alpha}} + m_{\alpha} \omega_{\alpha}^2(t) x_{\alpha}^2 \right]. \quad (6.80)$$

For this case, Hu and Matacz [40] and Shao and Makri [41] have already derived the influence functional. In the following, we outline some of their results.

Parametric oscillators show intricate dynamics and closed analytic solutions are, in general, not available [211]. Nevertheless, the influence functional can be found by using the unknown fundamental solutions of the equation of motion and constructing the associated Green's function for the relevant boundary conditions (cf. Equation (E.7)). Specifically, we define the functions  $R_{a,b}^{(\alpha)}(t)$  to fulfill [41]

$$\ddot{R}_{a,b}^{(\alpha)}(t) + \omega_{\alpha}(t) R_{a,b}^{(\alpha)}(t) = 0. \quad (6.81)$$

Here, the superscript  $(\alpha)$  labels the solutions for the different modes, while  $a$  and  $b$  describe their boundary conditions, given by

$$R_a^{(\alpha)}(t_0) = 1, \dot{R}_a^{(\alpha)}(t_0) = 0, \quad (6.82)$$

$$R_b^{(\alpha)}(t_0) = 0, \dot{R}_b^{(\alpha)}(t_0) = 1. \quad (6.83)$$

The influence functional is then found to take the same form as in thermal equilibrium (cf. Equation (2.78)) [41],

$$F_{\text{FV}}^{\text{Dr}}[q, q'] = \exp \left[ -\frac{1}{\hbar} \int_{t_0}^t dt' \int_{t_0}^{t'} dt'' [q(t') - q'(t')] \right. \\ \left. * [M(t', t'') q(t'') - M^*(t', t'') q'(t'')] \right], \quad (6.84)$$



with the kernel  $M(t, t')$  defined by

$$\begin{aligned} \text{Re}[M(t', t'')] &= \sum_{\alpha=1}^N \frac{c_{\alpha}^2}{2m_{\alpha}\omega_{\alpha}(t_0)} \coth\left(\frac{\hbar\omega_{\alpha}(t_0)\beta}{2}\right) \\ &\quad * \left( \omega_{\alpha}^2(t_0)R_b^{(\alpha)}(t')R_b^{(\alpha)}(t'') + R_a^{(\alpha)}(t')R_a^{(\alpha)}(t'') \right), \end{aligned} \quad (6.85)$$

$$\text{Im}[M(t', t'')] = \sum_{\alpha=1}^N \frac{c_{\alpha}^2}{2m_{\alpha}} \left( R_a^{(\alpha)}(t')R_b^{(\alpha)}(t'') - R_b^{(\alpha)}(t')R_a^{(\alpha)}(t'') \right), \quad (6.86)$$

where we used the same notation as Shao and Makri [41] for system coordinates  $q$ , assumed the  $R(t)$  as real and the bath to be in thermal equilibrium at coupling time  $t_0$ . Two consequences are immediately obvious: First, parametric driving does not necessarily change the temperature, as the temperature-dependent prefactor in Equation (6.85) only depends on the initial frequency and is therefore identical to the equilibrium result. Any additional time dependence is encoded within the fundamental solutions  $R_a$  and  $R_b$ . Second, the kernels are now non-stationary and depend on the two time-points  $t'$  and  $t''$ , explicitly. However, the kernel itself still follows from the correlator of the underlying fluctuating force (cf. Equation (2.25)) [40, 41]. It is also possible to include the spectral density in Equations (6.85) and (6.86) [40]. In this case, a continuous frequency replaces  $\omega_{\alpha}(t_0)$  such that the spectral density is given by its value at  $t_0$ . Finally, the kernel properly reduces to the usual result of Equation (2.28) for time-independent frequencies where  $R_a^{(\alpha)}(t) = \cos(\omega_{\alpha}t)$  and  $R_b^{(\alpha)}(t) = \omega_{\alpha}^{-1} \sin(\omega_{\alpha}t)$ .

In order to obtain the dynamics of a coupled system, we need to find the  $R_{a,b}(t)$  as defined in Equation (6.81) as well as a way to treat the more complicated time dependence of the kernels in the influence functional. In principle, the former can be done numerically. The latter, however, is more problematic as it forces us to consider the center-of-mass time  $t' + t''$  in addition to their difference. Even so, Hu and Matacz [40] successfully derive a master and a Fokker-Planck equation for a parametrically driven oscillator as the system. It may also be possible to derive results similar to the NIBA, as the influence functional still depends on the blip-blip/blip-sojourn structure we encountered before. Finally, we also note that the driven bath Hamiltonian (6.80) can be extended with a dipolar bath driving term and additional damping from a superbath. Their interplay will have a profound impact on the underlying dynamics, as well [211].

### 6.3 Conclusion of Part 6

In this part of the thesis, we have successfully reformulated the problem of driven quantum baths in terms of path integrals. First, we have derived a general formulation of the spin-boson model in the path integral language and proceeded to present the

non-interacting blip approximation, valid for strong system-bath coupling and high-temperatures. The dynamics determined by the NIBA shows a rich behavior with a smooth transition between coherent and incoherent regimes but also allows for results in the case of very weak coupling. Linear bath driving was shown to yield an effective force which emerges from the influence functional as an additive contribution to the dynamics. By using approximate results for the effective force, we have determined numerical results within the NIBA and have compared them to its analytic solutions. Our analyses found that high temperatures reduce the impact of the effective force while results in the strong coupling regime decay too slowly for the force to have any significant effect. The effective force is most relevant in the coherent regime, that is, with small to intermediate system-bath coupling for low enough temperatures. Nevertheless, a comparison with results from the Onsager model has shown that large driving strengths are required to see a significant impact of the bath driving contribution. We have closed this chapter with an outlook to parametrically driven baths, where we have seen that an influence functional can also be derived for this case.

This concludes our discussion of driven baths on the basis of system-bath models in this thesis. However, many avenues have yet to be analyzed further, starting from the actual size of the bath-driving contributions in specific applications to the impact of higher-order driving terms. We provide a brief overview in our closing remarks in Part 8.

## THz Kerr effect dynamics in liquid water

After discussing some implications of driven baths in the last chapters, we now treat a different situation: the dynamics underlying the Kerr effect in the terahertz frequency regime. While the topic does not have a direct connection to system-bath models, it serves as an illuminating example on how a polarized environment quantitatively shapes the response characteristics of a medium. This part of the thesis is based on a theoretical description developed by Kalmykov and detailed further in a book by Coffey and Kalmykov [13, 131]. In contrast to before, we will not detail the exact derivation and largely refer to aforementioned sources. Instead, we focus on a qualitative discussion and a comparison to experimental results which we analyzed in a recent joint publication [3]. In the first section, we give a brief overview of the underlying theoretical treatment and identify the relevant dynamical quantities that determine the dynamics of a Kerr effect signal. We proceed with a matrix method for the dynamic Kerr effect which eventually leads to a simple description of the time-dependent signal via two vector-differential Equations. In Section 7.2, we apply the model to the case of liquid water subject to terahertz radiation and compare our results to experimental findings. Finally, we close this chapter with a short summary and an outlook on possible extensions to the theoretical approach to better fit the experimental data.

### 7.1 Kerr effect dynamics

The Kerr effect is a nonlinear optical effect. It describes a change to the refractive index in the direction of an electric field. We have already discussed the basics in Section 3.1.5 and have explained how the polarization axis of an incoming beam can be changed by way of the Kerr effect (cf. Figure 3.3). In this section, we provide an approximate description utilizing the molecular formulation of Section 3.1.6. Specifically, we determine the nonlinear polarization of the sample by looking at the rotational dynamics of the molecules involved. This will eventually lead to a description of the Kerr effect dynamics by way of two vector-differential equations. We begin with a short presentation of the static result found in Boettcher and Bordewijk [113] to identify the relevant physical parameters.

### 7.1.1 Microscopic description

From a classical perspective, a dielectric medium reacts to an external field by becoming polarized; an effect which we have reduced to molecular parameters in Section 3.1.6. The polarization was determined on a molecular level by using the molecular dipole moment  $p_{\text{mol}}$  which was averaged over all molecules to yield the net macroscopic polarization. We have also seen in Equation (3.30) that the molecular dipole moment can be written as a series in powers of the electric field strength. The constant contribution in Equation (3.30) describes the permanent dipole moment of a molecule  $\mu$ , whereas the first order is determined by the polarizability tensor  $\alpha$ . Higher orders are known as hyperpolarizabilities of which we label the first two with  $\beta$  and  $\gamma$ . This means, terms of first and higher order give the contribution of an induced dipole moment. It is worth mentioning that we already used this description in Section 4.3 to calculate the induced dipole moment of a polarizable molecule in a driven bath. In this section, we merely note that we can relate the change of the refractive index in the Kerr effect to a change in the molecular polarizability  $\Delta\alpha_{\text{mol}}$  by way of the Lorentz-Lorenz equation (3.28). For small differences of the refractive index  $\Delta n$ , we can approximate the expression to obtain [113, 117, 212, 213]

$$\Delta n(t) \approx \frac{2\pi\rho_0}{n} \Delta\alpha(t). \quad (7.1)$$

If molecules in a solution are probed,  $n$  is the mean refractive index of the solvent and  $\rho_0$  the number density of the molecules in solution. In Equation (7.1),  $\Delta\alpha(t)$  is given as a polarizability volume

$$\Delta\alpha(t) = \frac{\Delta\alpha_{\text{mol}}(t)}{4\pi\epsilon_0}, \quad (7.2)$$

where  $\alpha_{\text{mol}}$  is defined as in Part 3. The definition (7.2) is useful because it gives values of the order of one in units of  $\text{\AA}^3$  (see e.g. [214]). In this part of the thesis, we will exclusively use  $\Delta\alpha$  to quantify the birefringence. Equation (7.1) allows us to express the Kerr effect as a difference between molecular polarizabilities parallel and perpendicular to the field as per Equation (3.26).  $\Delta\alpha$  contains the corrections implied in Equation (3.30) so that the overall difference of the refractive indices is now directly linked to molecular parameters. Hence,  $\Delta\alpha(t)$  must be an averaged quantity. It can be determined by considering the averaged rotation of molecules with respect to the direction of the electric field. For dilute gases and in the static case one finds for the Kerr constant [113, §83]

$$K \propto \sum_{k,l=1}^3 \left[ \frac{3}{k_{\text{B}}T} (\alpha_{kl}\epsilon_{lk} - \frac{1}{3}\alpha_{kk}\epsilon_{ll}) + \frac{3}{(k_{\text{B}}T)^2} (\alpha_{kl}\mu_k\mu_l - \frac{1}{3}\alpha_{kk}\mu_l^2) + \frac{4}{k_{\text{B}}T} \beta_{kl}\mu_k + 2\gamma_{lkkl} \right]. \quad (7.3)$$

Here, we have omitted all frequency dependencies but used  $\alpha$  for the polarizability at the optical probing frequency and  $\epsilon$  as the corresponding value at the driving frequency (which is zero here). The indices describe spatial components in the molecular coordinate system. According to Equation (7.3), the static Kerr effect is determined by a competition between temperature, permanent dipole moments and polarizabilities which give rise to induced dipole moments. As we have seen in Part 3, a dielectric reacts to an external field by becoming polarized which originates from reorientation of molecular dipoles into the direction of an external field (cf. Figure 3.1). The description of the Kerr effect in Equation (7.3) then describes the competition between the orientation of molecules due to their permanent dipole moments (*orientation*) and due to their induced dipole moments (*alignment*) [166, 215, 216]. This explanation also implies a strong frequency dependence: For optical pump frequencies, molecules will not be able to rotate quickly enough to follow the rapidly changing electric field and the contribution from the permanent dipole moment vanishes. Instead, the Kerr effect is dominated by the rapidly changing electron cloud, i.e., the induced dipole moment [13, 113]. In the following, we present a matrix method derived by explicitly considering the dynamics of molecular rotations, detailed in Kalmykov [131] and the book by Coffey and Kalmykov [13]. It should be noted, that this description is still largely reductionist and one can generally find a complicated and rich behavior in optical Kerr effect spectra for simple liquids where a variety of physical contributions can come into play [128, 130].

### 7.1.2 Euler-Langevin description

As we have seen, we can formulate the Kerr effect in terms of the interaction of the external field with induced and permanent dipoles. These lead to a rotation of molecules such that their net orientation and alignment determines the overall size of the effect on the macroscopic scale. This is counteracted by thermal fluctuations. This behavior may be described by way of a three-dimensional Langevin equation of motion for the rotation of a molecule where the molecule is described as a rigid rotator. Specifically, [13, 131, 217]

$$\frac{d}{dt}\hat{I}\boldsymbol{\omega}(t) + \boldsymbol{\omega} \times \hat{I}\boldsymbol{\omega} + \hat{\zeta}\boldsymbol{\omega} = -\nabla V(\varphi(t), \theta(t), \psi(t), t) + \boldsymbol{\lambda}(t). \quad (7.4)$$

Here,  $\hat{I}$  is the tensor of inertia of the molecule,  $\hat{\zeta}$  is the damping tensor,  $\boldsymbol{\lambda}(t)$  describes noise and  $V(\dots)$  is a potential. Equation (7.4) describes the rotation in a body-fixed coordinate system related to the laboratory coordinate system by the Euler angles  $\varphi(t)$ ,  $\theta(t)$  and  $\psi(t)$ . Their definition and our convention for the axes is shown exemplary for a water molecule in Figure 7.1. In this way, the potential  $V$  describes the dynamic torque applied to a molecule because of its relative orientation to an external field with  $\nabla V(\dots)$  being the gradient in orientation space. The noise term  $\boldsymbol{\lambda}(t)$  is assumed to be Gaussian

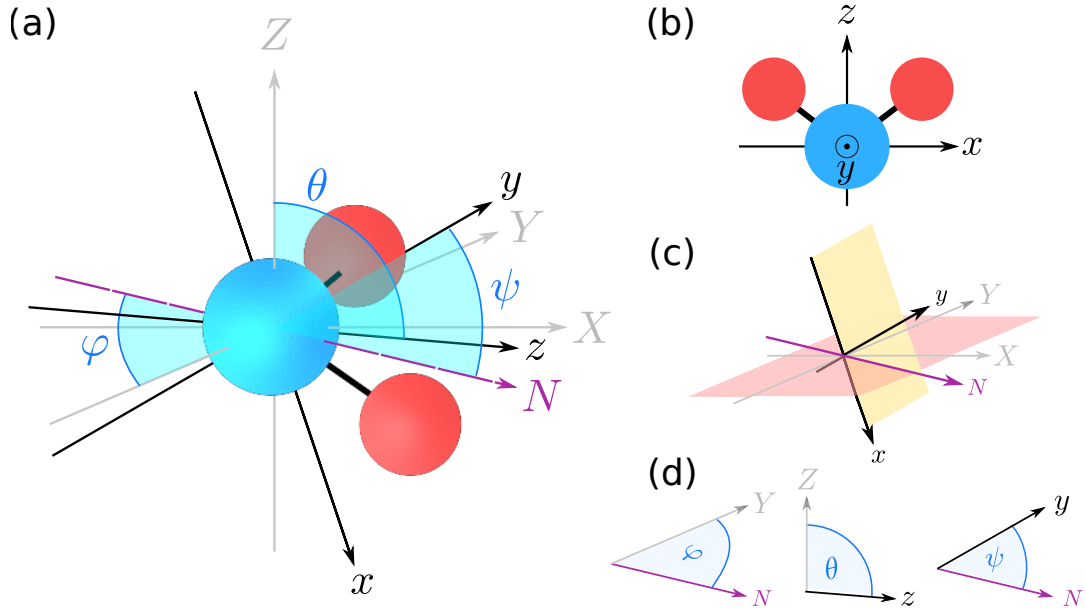


**Figure 7.1:** Euler angles for a water molecule. (a) The Euler angles  $\varphi$ ,  $\theta$  and  $\psi$  are defined between a body-fixed  $(x, y, z)$  and an external coordinate system  $(X, Y, Z)$  [13, 63] shown here for a water molecule. An arbitrary rotation is given by a sequence of rotations around the Euler angles. First, around the  $Z$ -axis by  $\varphi$  (which transforms the  $Y$ -axis into the line of nodes  $N$ ) then around  $N$  by  $\theta$ , and finally around the new  $z$ -axis by the angle  $\psi$ . (b) Our convention for the body-fixed axes of a water molecule. Note that the  $z$ -axis corresponds to the direction of the permanent dipole moment. (c) Definition of the line of nodes  $N$  which is given by the intersecting line between the two planes  $X, Y$  (pink) and  $x, y$  (yellow).  $N$  can also be obtained by rotation of the axis  $Y$  by the angle  $\varphi$ . (d) Pictorial definition of the Euler angles we use throughout the thesis [13].

white noise which creates an additional torque due to thermal fluctuations. This means that the description of Equation (7.4) neglects memory effects. It also does not include interparticle interactions, conduction and quantum effects. Therefore, Equation (7.4) amounts to a description of molecular dynamics purely as diffusive reorientational motion of single particles [13, 218, 219].

A particularly convenient approximation of Equation (7.4) neglects the inertial term and focuses on overdamped dynamics. This case is usually referred to as the *Debye approximation* and a subsequent calculation of the linear response yields the typical Debye form (3.20) of the dielectric function [13, Chapter 8.3.1]. This approximation is justified if the frequency of the electric field is low enough or, more generally, valid for small angular velocities  $\omega(t)$ . In this regime, we obtain

$$\omega(t) \approx \frac{1}{k_B T} \hat{D} \{ \lambda(t) - \nabla V[\varphi(t), \theta(t), \psi(t), t] \}. \quad (7.5)$$

Here,  $\hat{D} = (k_B T) \hat{\zeta}^{-1}$  is the rotational diffusion tensor. We assume here that  $\hat{D}$  does not necessarily have the same principal axes as  $\hat{I}$  which, in general, applies to asymmetric top molecules [13]. Solutions of Equation (7.5) are obtained by an expansion in Wigner's D-functions [13, 113, 220]. We give a short account of them in the following.

### 7.1.3 Wigner's D-functions

Wigner's D-functions  $D_{mm'}^J$  are defined as matrix elements of rotations along the Euler angles  $R(\varphi, \theta, \psi)$  in the space of the total angular momentum  $J$  and the quantum number of its  $z$ -component  $m$ , i.e. [220]

$$\langle Jm | R(\varphi, \theta, \psi) | J'm' \rangle = \delta_{J,J'} e^{-im\varphi} d_{mm'}^J(\theta) e^{-im'\psi} = \delta_{J,J'} D_{mm'}^J(\varphi, \theta, \psi). \quad (7.6)$$

They represent wave functions of a rigid symmetric top molecule [13, 217] and are eigenfunctions of the angular momentum operators  $\mathbf{J}^2$ ,  $J_z$  and  $J_{z'}$ , where the prime in  $z'$  denotes the axis in the body-fixed coordinate system. The first equation introduced a convenient formulation using a purely  $\theta$ -dependent function  $d_{mm'}^J(\theta)$  [220]. For the specific case where  $m = m' = 0$ , the D-functions are related to Legendre polynomials  $P_J(x)$  by

$$P_J(\cos(\theta)) = D_{00}^J(\varphi, \theta, \psi). \quad (7.7)$$

The  $D_{mm'}^J(\dots)$  form a basis and can be used to expand any function  $f(\varphi, \theta, \psi)$  defined in the volume of the three-dimensional rotation group as [220, Chapter 4.10]

$$f(\varphi, \theta, \psi) = \sum_{J=0}^{\infty} \sum_{m=-J}^J \sum_{m'=-J}^J b_{mm'}^J D_{mm'}^J(\varphi, \theta, \psi). \quad (7.8)$$

Here,  $J$  runs over either integer or half-integer values and the angles are defined in the domain  $0 \leq \varphi < 2\pi$ ,  $0 \leq \theta \leq \pi$  and  $0 \leq \psi < 2\pi$ . The  $b_{mm'}^J$  are expansion coefficients in this basis (see [220]).

It turns out, that many observables correspond to combinations of only very few  $D_{mm'}^J(\dots)$ . For instance, the polarization along a laboratory  $Z$ -axis for a solution of unpolarizable molecules with number density  $\rho_0$  can be obtained as (cf. Equation (3.2)) [13, 113, 220]

$$P_Z(t) = \rho_0 \langle \mu_Z \rangle(t) = \rho_0 \mu \langle \cos(\vartheta) \rangle(t) = \rho_0 \sum_{k=-1}^{+1} (-1)^k \mu^{(-k)} \langle D_{0k}^1 \rangle(t). \quad (7.9)$$

In this Equation,  $\mu^{(0)} = \mu_z$ ,  $\mu^{(\pm 1)} = \mp(1/\sqrt{2})(\mu_x \pm i\mu_y)$  are the spherical components of the permanent dipole vector where the  $\mu_i$  are its elements in the molecular coordinate

system defined by the axes  $xyz$  (cf. Figure 7.1). The unlabeled  $\mu$  is the magnitude of the permanent dipole moment such that  $\mu \cos(\vartheta)$  with polar angle  $\vartheta$  gives the appropriate projection along  $Z$ . This illustrates that Equation (7.9) merely describes a dynamic coordinate transformation between the laboratory and the molecular system where the time-dependent Euler angles are encoded in the D-functions. As discussed in Part 3, the polarization represents an averaged quantity such that the  $D_{mm'}^J(\dots)$  have to be averaged over all possible values of the Euler angles. Similarly, the difference in the molecular polarizability of Equation (7.1) can be written as [13, 213, 221]

$$\begin{aligned} \Delta\alpha(t) &= \langle \alpha_{ZZ} - \alpha_{XX} \rangle(t) \\ &= \sum_{k=-2}^{+2} \alpha^{(k)} \left[ \langle D_{0k}^{2*} \rangle(t) - \frac{1}{\sqrt{6}} (\langle D_{2k}^{2*} \rangle(t) + \langle D_{-2k}^{2*} \rangle(t)) \right]. \end{aligned} \quad (7.10)$$

Here, the  $*$  denotes the complex conjugate and we have considered the difference between the laboratory  $Z$  and  $X$ -axes. For an axially symmetric potential and a diagonal polarizability tensor with  $\alpha_{xx} \approx \alpha_{yy}$ ,  $\Delta\alpha(t)$  is determined by the second Legendre polynomial which often appears in dynamical equations [117, 212, 222, 223]. The  $\alpha^{(m)}$  describe spherical components of the molecular polarizability tensor constructed from differences in the molecular reference frame. For later purposes, we give them in the form of a vector  $\mathbf{a}$  where the  $\alpha^{(m)}$  are given by its elements [13]. We have that

$$\mathbf{a} = \begin{pmatrix} \alpha^{(2)} \\ -\alpha^{(1)} \\ \alpha^{(0)} \\ -\alpha^{(-1)} \\ \alpha^{(-2)} \end{pmatrix} = \sqrt{\frac{3}{8}} \begin{pmatrix} \alpha_{xx} - \alpha_{yy} + 2i\alpha_{xy} \\ 2(\alpha_{xz} + i\alpha_{yz}) \\ \sqrt{6}[\alpha_{zz} - \text{Tr}[\hat{\alpha}]/3] \\ 2(-\alpha_{xz} + i\alpha_{yz}) \\ \alpha_{xx} - \alpha_{yy} - 2i\alpha_{xy} \end{pmatrix}. \quad (7.11)$$

Note that the polarizability tensor elements of Equation (7.11) refer to their values at the probing frequency.

According to Equations (7.1) and (7.10), the Kerr effect is then given by corrections to the differences  $\alpha^{(m)}$  introduced by the dynamics of the D-functions. While the representation of the polarization and the change in polarizability using the D-functions seems heavy-handed, it turns out that the Euler-Langevin equation (7.5) yields a set of differential recurrence relations for the averages  $\langle D_{mm'}^J \rangle(t)$ . If the potential  $V(\Omega, t)$  with Euler angles  $\Omega$  is specified and the series truncated at some point, results for the  $\langle D_{mm'}^J \rangle(t)$  can be determined [13, 131].

In order to find expressions for the Kerr effect in particular, we consider the potential  $V(t)$  of a particle subject to a driving field  $\mathbf{E}(t)$ . We assume that the molecules couple to the field via permanent and induced dipole moments only, so that we can formulate



the potential in the laboratory system as (cf. Equation (3.53)) [112, §44]

$$\begin{aligned}
V(t) &= -\boldsymbol{\mu} \cdot \mathbf{E}(t) - \boldsymbol{\mu}_{\text{ind}}[\mathbf{E}(t)] \cdot \mathbf{E}(t) \\
&= -\sum_{i=X,Y,Z} \mu_i E_i(t) - \frac{1}{2} \sum_{i,j=X,Y,Z} \varepsilon_{ij} E_i(t) E_j(t) + \dots \quad (7.12)
\end{aligned}$$

Here, we have labeled components of vectors and tensors by  $i$  and  $j$  and have neglected the time dependence of the quantities except for the electric field. This means that the polarizabilities (and, by extension, the induced dipole moment) react instantaneously to the driving field. The second-order values  $\varepsilon_{ij}$  are then constant and belong to the response at the driving frequency. The dots contain the effect from hyperpolarizabilities which we will not take into account further. We restrict the electric field  $\mathbf{E}(t)$  to the  $Z$ -axis such that the potential (7.12) becomes axially symmetric. With Equations (7.9) and (7.10), the potential can then be expressed by D-functions as [13]

$$\begin{aligned}
V(\Omega, t) &= -E(t) \sum_{k=-1}^{+1} (-1)^k \mu^{(-k)} D_{0k}^1(\Omega) \\
&+ \frac{E^2(t)}{6} \left[ \text{Tr} \hat{\varepsilon} - 2 \sum_{k=-2}^{+2} (-1)^k \varepsilon^{(-k)} D_{0k}^2(\Omega) \right]. \quad (7.13)
\end{aligned}$$

Here,  $\hat{\varepsilon}$  signifies the polarizability tensor with the elements  $\varepsilon_{ij}$ . As before, the  $\mu^{(k)}$  and  $\varepsilon^{(k)}$  give spherical elements as defined below Equation (7.9) and in Equation (7.11). With Equation (7.13) it is now possible to specify the recurrence relations of the  $\langle D_{mm'}^J \rangle(t)$ . Their exact forms and more details on the derivation can be found in Coffey and Kalmykov [13]. At this point we merely note that the dependence on both the permanent as well as the polarizability tensor in Equation (7.3) arises naturally from the choice of the potential energy.

#### 7.1.4 Matrix formulation of the dynamic Kerr effect

An expansion of the Euler-Langevin Equation (7.5) in terms of Wigner's D-functions creates an infinite hierarchy of coupled differential recurrence relations which have to be truncated to yield solutions. The hierarchy can be ordered in powers of the electric field  $E(t)$ . If the field strength is sufficiently weak in comparison to the thermal energy but still strong enough to induce the Kerr effect, one may truncate the hierarchy at the order  $E^2(t)$ . Furthermore, the choice of potential in Equation (7.13) as axially symmetric implies that the potential is independent of the Euler angle  $\varphi$ , such that only D-functions with  $m = 0$  are relevant (cf. Equation (7.6)). Both points leave just eight D-functions. Their dynamics can be cast in the form of two vector-differential

equations given by [13, 131]

$$\frac{d}{dt}\mathbf{c}_1(t) = \hat{A}_1\mathbf{c}_1(t) + E(t)\mathbf{B}_1, \quad (7.14)$$

$$\frac{d}{dt}\mathbf{c}_2(t) = E(t)\hat{Q}\mathbf{c}_1(t) + \hat{A}_2\mathbf{c}_2(t) + E^2(t)\mathbf{B}_2. \quad (7.15)$$

The vectors  $\mathbf{c}_1(t)$  and  $\mathbf{c}_2(t)$  contain averages of first and second-order D-functions as

$$\mathbf{c}_1(t) = \begin{pmatrix} \langle D_{0-1}^1 \rangle(t) \\ \langle D_{00}^1 \rangle(t) \\ \langle D_{01}^1 \rangle(t) \end{pmatrix}, \quad \mathbf{c}_2(t) = \begin{pmatrix} \langle D_{0-2}^2 \rangle(t) \\ \langle D_{0-1}^2 \rangle(t) \\ \langle D_{00}^2 \rangle(t) \\ \langle D_{01}^2 \rangle(t) \\ \langle D_{02}^2 \rangle(t) \end{pmatrix}. \quad (7.16)$$

Their time evolution is determined by elements of the rotational diffusion tensor  $\hat{D}_{ij}$  (cf. Equation (7.5)) and the response to the perturbing electric field  $E(t)$  as formulated in the potential in Equation (7.13). Here, we set the molecular reference frame  $xyz$  in such a way that the rotational diffusion tensor is diagonal and encoded in the quantities

$$\Delta = (\hat{D}_{zz})(\hat{D}_{xx} + \hat{D}_{yy})^{-1} - \frac{1}{2}, \quad (7.17)$$

$$\tau_D = (\hat{D}_{xx} + \hat{D}_{yy})^{-1}, \quad (7.18)$$

$$\text{and } \Xi = (\hat{D}_{xx} - \hat{D}_{yy})(\hat{D}_{xx} + \hat{D}_{yy})^{-1}. \quad (7.19)$$

As implied by the designation  $\tau_D$ , the inverse elements of the rotational diffusion tensor determine the time scales of dielectric relaxation. In fact, for the case of non-polarizable molecules and to first order in  $E$ , one can recover Debye relaxation for the polarization of the sample. Up to three relaxation times emerge in this case depending on the orientation of the dipole moment in the molecular reference frame. If the molecular  $z$ -axis is chosen to coincide with the dipole moment,  $\tau_D$  represents the only time scale [13, Chapter 8.3.1]. The matrices  $\hat{A}_1$  and  $\hat{A}_2$  are related to relaxation towards the equilibrium distribution and read

$$\hat{A}_1 = -\tau_D^{-1} \begin{pmatrix} 1+\Delta & 0 & \Xi/2 \\ 0 & 1 & 0 \\ \Xi/2 & 0 & 1+\Delta \end{pmatrix}, \quad (7.20)$$

$$\hat{A}_2 = -\tau_D^{-1} \begin{pmatrix} 3+4\Delta & 0 & \Xi\sqrt{3/2} & 0 & 0 \\ 0 & 3+\Delta & 0 & 3\Xi/2 & 0 \\ \Xi\sqrt{3/2} & 0 & 3 & 0 & \Xi\sqrt{3/2} \\ 0 & 3\Xi/2 & 0 & 3+\Delta & 0 \\ 0 & 0 & \Xi\sqrt{3/2} & 0 & 3+4\Delta \end{pmatrix}. \quad (7.21)$$

If  $\Xi$  and  $\Delta$  can be neglected, the diagonal entries give rise to relaxation times of the order of  $\tau_D$  and  $\tau_D/3$ , respectively. The vector  $\mathbf{B}_1$  and the matrix  $\hat{Q}$  relate to the impact of the permanent dipole moment

$$\hat{Q} = \frac{\sqrt{3}}{10\tau_D k_B T} \begin{pmatrix} \mu^-(3+4\Delta) - \mu^+\Xi & \sqrt{2}\mu_z\Xi & 0 \\ 3\mu_z & [\mu^-(3+2\Delta) - 2\mu^+\Xi]/\sqrt{2} & \mu_z\Xi \\ \sqrt{3/2}(\mu^-\Xi - \mu^+) & 2\sqrt{3}\mu_z & \sqrt{3/2}(\mu^- - \mu^+\Xi) \\ \mu_z\Xi & [2\mu^-\Xi - \mu^+(3+2\Delta)]/\sqrt{2} & 3\mu_z \\ 0 & \sqrt{2}\mu_z\Xi & \mu^-\Xi - \mu^+(3+4\Delta) \end{pmatrix}, \quad (7.22)$$

$$\mathbf{B}_1 = \frac{1}{3\sqrt{2}\tau_D k_B T} \begin{pmatrix} \mu^-(1+\Delta) - \mu^+\Xi/2 \\ \sqrt{2}\mu_z \\ -\mu^+(1+\Delta) + \mu^-\Xi/2 \end{pmatrix}, \quad (7.23)$$

where  $\mu^\pm = \mu_x \pm i\mu_y$ . Finally, the vector  $\mathbf{B}_2$  involves the polarizability at the driving frequency and reads

$$\mathbf{B}_2 = \frac{1}{10\sqrt{6}\tau_D k_B T} \begin{pmatrix} (\varepsilon_{xx} - 2i\varepsilon_{xy} - \varepsilon_{yy})(3+4\Delta) - (\varepsilon_{xx} + \varepsilon_{yy} - 2\varepsilon_{zz})\Xi \\ 2(\varepsilon_{xz} - i\varepsilon_{yz})(3+\Delta) - 3(\varepsilon_{xz} + i\varepsilon_{yz})\Xi \\ \sqrt{6}[2\varepsilon_{zz} - \varepsilon_{xx} - \varepsilon_{yy} + \Xi(\varepsilon_{xx} - \varepsilon_{yy})] \\ -2(\varepsilon_{xz} + i\varepsilon_{yz})(3+\Delta) + 3(\varepsilon_{xz} - i\varepsilon_{yz})\Xi \\ (\varepsilon_{xx} + 2i\varepsilon_{xy} - \varepsilon_{yy})(3+4\Delta) - (\varepsilon_{xx} + \varepsilon_{yy} - 2\varepsilon_{zz})\Xi \end{pmatrix}. \quad (7.24)$$

For the Kerr measurement, we use the definition implied in Equation (7.13), that is, the perturbing electric field is polarized along the  $Z$ -axis in the laboratory system spanned by the axes  $XYZ$ . The birefringence is then measured between the axes  $X$  and  $Z$  such that Equation (7.10) can be used. By making use of the vector in Equation (7.11),  $\Delta\alpha(t)$  can be written as a dot product and the birefringence of Equation (7.1) is obtained as [13]

$$\Delta n(t) = \frac{2\pi\rho_0}{n} (\mathbf{a} \cdot \mathbf{c}_2(t)). \quad (7.25)$$

### 7.1.5 Exact solution for isotropic diffusion

In order to gain more insight about the actual solutions to Equations (7.14) and (7.15), we note that it is possible to derive an exact solution for the case of isotropic rotational diffusion. In this case,  $D_{xx} = D_{yy} = D_{zz} = D$  such that  $\Xi = \Delta = 0$  and only the diagonal elements of the matrices (7.20) and (7.21) remain. We assume isotropic initial conditions where  $\mathbf{c}_1(0) = 0$  and  $\mathbf{c}_2(0) = 0$  and choose the molecular  $z$ -axis to coincide with the permanent dipole moment. We obtain

$$\begin{aligned} \Delta\alpha(t) &= \frac{1}{5\tau_D} \left[ \frac{3}{4} \frac{\Delta\alpha_0^\perp \Delta\varepsilon_0^\perp}{k_B T} + \frac{\Delta\alpha_0^\parallel \Delta\varepsilon_0^\parallel}{k_B T} \right] \int_0^t du E^2(u) e^{-3\frac{(t-u)}{\tau_D}} \\ &+ \frac{\Delta\alpha_0^\parallel \mu_z^2}{5(k_B T)^2 \tau_D^2} \int_0^t du \int_0^u ds \left[ E(u) e^{-3\frac{(t-u)}{\tau_D}} \right] \left[ E(s) e^{-\frac{(u-s)}{\tau_D}} \right]. \end{aligned} \quad (7.26)$$

In Equation (7.26) we have defined  $\Delta\alpha_0^\perp = \alpha_{xx} - \alpha_{yy}$  and  $\Delta\alpha_0^\parallel = \alpha_{zz} - (1/2)(\alpha_{xx} + \alpha_{yy})$  as the polarizability differences between the components parallel and perpendicular to the dipole moment.  $\Delta\varepsilon_0^\parallel$  and  $\Delta\varepsilon_0^\perp$  are defined correspondingly. Equation (7.26) implies two distinct behaviors: the first term describes a unipolar signal which depends on the anisotropies of the polarizability at the driving frequency, whereas the second term can create a bipolar contribution that depends on the permanent dipole moment  $\mu_z$ . For molecules with no permanent dipole moment, Equation (7.26) implies a unipolar signal determined by the polarizability and defined by the time scale  $\tau_D/3$ . For molecules with a non-zero permanent dipole moment, the second term contributes as well and we expect an interplay between both contributions. Finally, we remark that the temperature dependence of both terms is consistent with Equation (7.3).

## 7.2 Implementation for liquid water

In this section, we apply Equations (7.14) and (7.15) to the case of liquid water under THz-radiation and compare the result to an experimental measurement [3]. As noted in Section 4.3, the THz-regime has recently become more accessible to experimental methods [163, 164]. The terahertz Kerr effect (TKE) in particular uses single-cycle driving pulses in the THz regime to induce birefringence in a sample. This makes it possible to better resolve the polarizability dynamics on time scales on the order of time constants of molecular relaxations [123, 126] and gives access to the contribution of the permanent dipole moment in the Kerr effect dynamics [3, 224]. However, the creation of pulses with an intensity high enough to produce strong nonlinear effects has proved challenging [123, 126]. This issue is compounded with high absorption and heating of the sample in the case of liquid water and small polar molecules while the signal itself is also particularly small in the case of water [126, 167, 225] [3, cf. Supplementary Figure 6]. Despite these difficulties, several recent studies successfully measured the TKE for water and small alcohols [166, 224–227]. In a collaborative paper on the TKE [3], we compared experimental results for liquid water obtained by Peter Zalden, Liwei Song and others to the predictions of Equations (7.14) and (7.15). We detail this comparison in the following.

### 7.2.1 The case of liquid water

For a detailed comparison, realistic parameters for liquid water are required. The most important question concerns the time scales involved in the dynamics of the birefringence. According to Equation (7.26), we expect them to be determined by the time-dependent electric field and the exponential decays related to dielectric relaxation. However, the exact nature and the number of decays in this frequency range is debated and the fits to the experimental data vary [118, 167, 168]. Usually, one finds Debye-type

relaxations in the picosecond range with relaxation times of  $\tau_1 \approx 8.3$  ps (for 25°C, the so-called *Debye peak* which dominates relaxation),  $\tau_2 \approx 1$  ps (which has been reported as low as 0.2 ps) and sometimes also of  $\tau_3 \approx 0.2$  ps (cf. Figure 4.2) [118, 120, 167, 168, 228]. Their purported origin is illuminating: while the largest decay time is usually associated with the dynamics of the full hydrogen bond network [118, 167, 228] and the sub-picosecond scales with rapid breaking and reforming of bonds [167, 168, 229], the time scale  $\tau_2$  is often attributed to rotational dynamics of free or almost free water molecules [120, 167, 168]. The latter can be made manifest by considering the Debye-Stokes-Einstein relation for a spherical molecule in a viscous medium and using an argument made by Elton [118]: It was noted empirically that using the rotational friction for half radius in the Debye-Stokes-Einstein relation yields relaxation times which agree for many liquids [118, 230]. In the case of water, we find

$$\tau = \frac{4\pi\eta(a/2)^3}{k_B T} \approx 1 \text{ ps} \approx \tau_2 \approx \tau_1/8, \quad (7.27)$$

where we have used  $a = 1.44$  Å for the radius of a water molecule [231],  $\eta = 0.89$  mPas for its viscosity [232] and have assumed 25°C. Note that using the full radius in Equation (7.27) leads to the Debye peak but this can be argued to be coincidental, given its supposed origin in the collective dynamics [118]. Nevertheless, as this calculation rests on the assumption of uncorrelated single-particle dynamics of a Brownian particle, its success is curious and the Debye-Stokes-Einstein relation has been the subject of extensive research in this context [118, 233–235]. Indeed, a measurement of the Kerr effect via Raman spectroscopy performed in 2000 by Winkler et al. [236] found its dynamics dominated by two decays with time constants  $\tau_a \approx 3$  ps and  $\tau_b \approx \tau_a/3 \approx 1$  ps where  $\tau_a$  was likewise attributed to single-particle dynamics. We can therefore argue that the single-particle theory behind Equations (7.14) and (7.15) may prove suitable for the analysis of the Kerr effect in liquid water.

In our model, the decay times are given by inverse elements of the rotational diffusion tensor. In principle, its elements can be estimated from angular-velocity autocorrelation functions or by relating time scales found in NMR measurements [13, 237]. In our case, we utilize tensor elements obtained from molecular dynamics simulations. Specifically we use a tensor obtained by Chevrot et al. [238] which reads

$$\hat{D}^{(1)} = \begin{pmatrix} 0.211 & 0 & 0 \\ 0 & 0.114 & 0 \\ 0 & 0 & 0.272 \end{pmatrix} 1/\text{ps}. \quad (7.28)$$

Here, we assume that the principal axes coincide with the principal axes of inertia such that the  $z$ -direction points in the direction of the permanent dipole-moment,  $x$  spans the H-H-direction and  $y$  points out of the molecular plane as shown in Figure 7.1 (b). By using Equation (7.28), we naturally arrive at  $\tau_D \approx 3$  ps where  $\tau_D/3 \approx 1$

ps as predicted for a Kerr measurement [236]. However,  $\tau_D$  is related to the decay of the polarization and one would expect that  $\tau_D$  (as the name suggests) relates to the Debye peak at  $\tau_1 \approx 8.3$  ps. We note that the averaged rotational diffusion constant is given in our model by  $D_r = \text{Tr}[\hat{D}]/3$ , such that  $D_r^{-1} = 2\tau_D$  for isotropic rotational diffusion, suggesting a factor of two for a proper comparison. Indeed,  $2\tau_D \approx 6$  ps is much closer to  $\tau_1$  and this relationship has also been exploited in Chevrot et al. [238]. Nevertheless, the time scale of the polarization is determined by  $\tau_D$  and we note that other simulations found similar results between 3 and 5 ps for the dynamics of the first Legendre polynomial [239]. Still, we stress that more choices of the decay times are possible and different conventions compound the issue of choosing a proper  $\hat{D}$  further [239–242]. In the end, we simply note that the choice in Equation (7.28) represents a good fit to the experimental observations while other values do not fundamentally lead to a different dynamics.

Next, values for the polarizability tensor of water in the terahertz and in the optical regime are required. However, the anisotropy of the tensor in the optical regime proves to be very small and rather difficult to measure. In particular the quantities

$$\Delta\alpha_0^{\parallel} = \alpha_{zz} - \frac{1}{2}(\alpha_{xx} + \alpha_{yy}) \quad \text{and} \quad \Delta\alpha_0^{\perp} = \alpha_{xx} - \alpha_{yy}, \quad (7.29)$$

introduced in Equation (7.26), are of the order of  $0.1 \text{ \AA}^3$  (cf. Equations (7.30) and (7.31) below). For comparison, the equivalent for carbon disulfide is of the order of almost  $10 \text{ \AA}^3$  [243]. The signs of the  $\Delta\alpha_0^{\perp, \parallel}$  are unclear as well [3]. To enable a comparison, we use two sets of values corresponding to positive and negative sign. Specifically, we utilize values for water vapor in the form [244]

$$\hat{\alpha}_0^{(1)} = \begin{pmatrix} 1.626 & 0 & 0 \\ 0 & 1.286 & 0 \\ 0 & 0 & 1.495 \end{pmatrix} \text{ \AA}^3, \quad (7.30)$$

which has a  $\Delta\alpha_0^{\parallel, (1)} \approx 0.04 \text{ \AA}^3 > 0$  and a  $\Delta\alpha_0^{\perp, (1)} \approx 0.3 \text{ \AA}^3 > 0$ . The second set is derived by way of coupled cluster theory calculations and reads [245]

$$\hat{\alpha}_0^{(2)} = \begin{pmatrix} 1.375 & 0 & 0 \\ 0 & 1.442 & 0 \\ 0 & 0 & 1.321 \end{pmatrix} \text{ \AA}^3, \quad (7.31)$$

which features a  $\Delta\alpha_0^{\parallel, (2)} \approx -0.09 \text{ \AA}^3 < 0$  and a  $\Delta\alpha_0^{\perp, (2)} \approx -0.07 \text{ \AA}^3 < 0$ . Note that we assume the polarizability tensors to be diagonal in the molecular frame chosen. Moreover, the difference between values in the optical regime and the static case has been found to be fairly small [246]. We may therefore assume that the polarizability in the THz regime does not differ from the values in Equations (7.30) and (7.31), such that we set  $\varepsilon_{ij} \approx \alpha_{ij}$ .

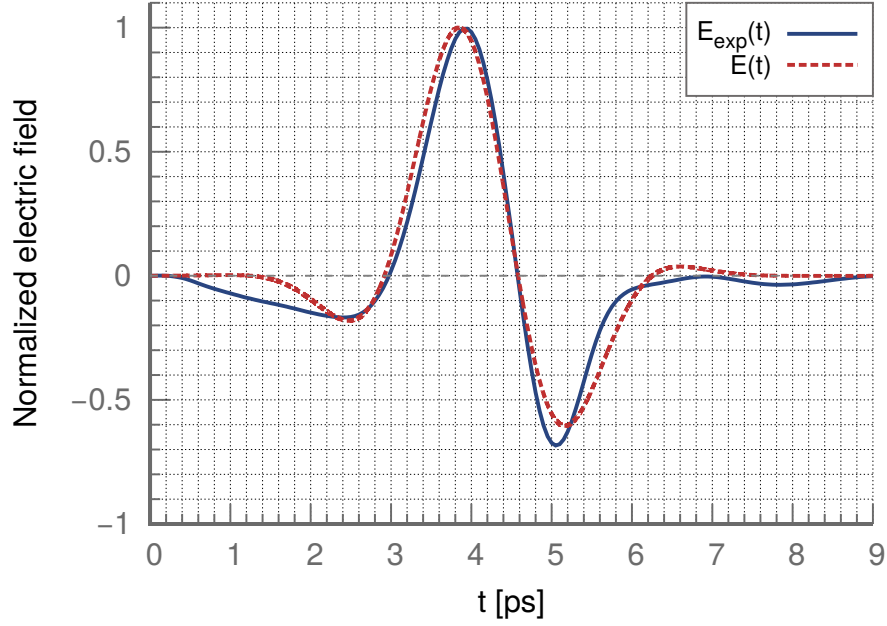


**Figure 7.2:** Comparison of the measured electric field profile (blue solid line) [3] and the approximate fit of Equation (7.32) (red dashed line) we use in this part of the thesis. Both curves are shown normalized.

Finally, the permanent dipole moment of a water molecule is given by  $\boldsymbol{\mu} = \mu \mathbf{e}_z$  in our molecular system with  $\mu = 2.95$  D [247] which is an appropriate value in the liquid phase. It should be noted that this dipole moment differs from the result in the gas phase where  $\mu \approx 1.85$  D. This is believed to originate from polarization induced by nearby molecules in the liquid, or, more generally, from interaction effects [247, 248].

With these values at hand, we may gauge the impact of the two components in the isotropic solution of Equation (7.26). A comparison of prefactors between the two terms directly yields  $(4\pi\epsilon_0\Delta\alpha_0/k_B T)/(\mu^2/(k_B T)^2) \approx 10^{-4}$  at room temperature. This implies that the effect from induced dipole moments is small in contrast to the dynamics related to the orientation of permanent dipole moments. For a suitable field, the resulting signal may therefore be bipolar in nature.

### 7.2.2 Resulting dynamics

Before we can determine the dynamics, the electric field  $E(t)$  has to be specified. We use a parametrization which coincides with the experimentally measured field strength, i.e.

$$E(t) = AE_0 \cos(\omega_c t + \phi) e^{-(t_p - t)^2 / (2\sigma^2)}, \quad (7.32)$$

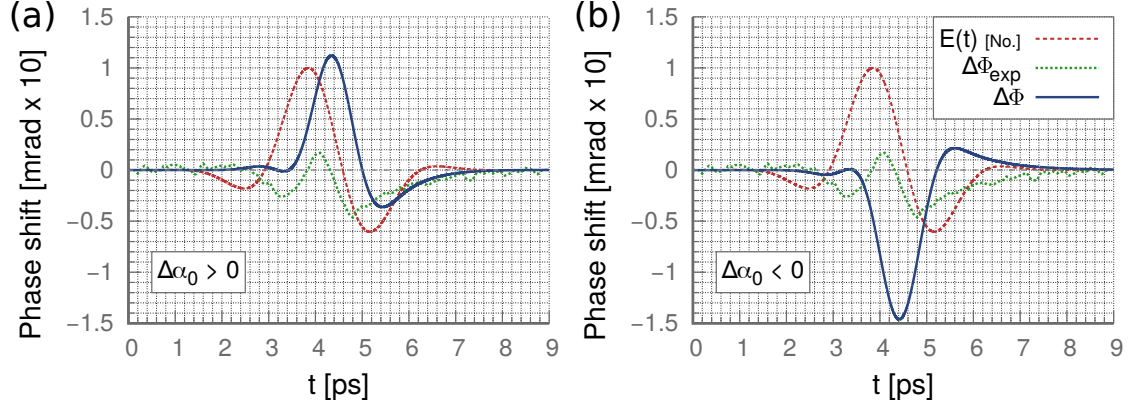


**Figure 7.3:** Phase shift for liquid water (blue solid lines) obtained via Equation (7.33) from the theory, versus the experimental data obtained by Zalden, Song et al. [3] (green dotted lines). (a) The resulting phase shift for the polarizability of Equation (7.30) for which  $\Delta\alpha_0^{\perp,||} > 0$ . (b) The phase shift for the polarizability in Equation (7.31) for which  $\Delta\alpha_0^{\perp,||} < 0$ . Both pictures show the normalized electric field from Equation (7.32) (red dashed lines).

where we have used  $\omega_c = 2\pi \times 0.3$  THz for the carrier frequency with phase  $\phi = -\pi/4$ . The pulse is centered at  $t_p = 4.2$  ps and its width is set to  $\sigma = 1$  ps. The prefactor  $A \approx 1.1$  normalizes the pulse such that its maximum gives  $E_0$ . Figure 7.2 shows the normalized pulse profile (7.32) in contrast to the measured pulse profile [3].

The experiment itself employs a center frequency of 0.25 THz with a field strength of 510 kV/cm [3]. However, due to the strong absorption of water and dispersion, we can expect a frequency shift as well as a lower effective field strength inside the liquid. Thus, we use  $E_0 \approx 150$  kV/cm in this thesis which is a more reasonable value for the average field strength inside the cuvette [3]. We obtain  $\mu E_0/k_B T \approx 0.04$  at room temperature which is appropriate for the low field strength approximation.

In general, we also assume room temperature with  $k_B T = 25$  meV and the number density of liquid water as  $\rho_0 = (1/30) \text{ \AA}^{-3}$ . As initial conditions we have isotropy, i.e.,  $\mathbf{c}_1(0) = 0$  and  $\mathbf{c}_2(0) = 0$ .

### Phase shift

The experimental measurement determines the relative phase shift between the electric field in  $x$  and  $z$ -direction. The time-dependent phase is obtained by multiplying the time-dependent change in wave number with the distance traveled by the probe beam within the sample, i.e.

$$\Delta\Phi(t) \approx \Delta k(t)L = 2\pi L \Delta n(t)/\lambda. \quad (7.33)$$



Here,  $\lambda = 800$  nm is the optical probing wavelength and  $L = 0.2$  mm is the thickness of the liquid sheet in the cuvette. It should be noted that we neglect any kind of spatial dependence in Equation (7.33).

Figure 7.3 shows the result for the polarizabilities in Equations (7.30) and (7.31) in comparison to the experimental results with  $E(t)$  given in Equation (7.32). As suspected, the bipolar pulse indeed creates a bipolar signal dominated by the contribution from the permanent dipole moment. This is visible from the comparably large contribution given by  $c_1$ . However, both curves only agree very roughly with the experimental data. While the results show some qualitative agreement with similar relaxation behavior and similar structure, they differ in both the height as well as the exact position of the minima and maxima. This becomes worse for the polarizability with negative  $\Delta\alpha_0$  shown in Figure 7.3 (b) where the overall shape suggests even less agreement with the experimental data. Taken together, the results imply a positive  $\Delta\alpha_0$  as well as an evident failure of the theoretical description in the case of liquid water.

### ***Orientation and alignment***

As noted in Equation (7.7), the central elements of the vectors  $c_1$  and  $c_2$  can be exchanged with Legendre polynomials. Specifically, they give direct measures for orientation and alignment of the molecules as

$$\langle D_{00}^1 \rangle(t) = \langle \cos(\theta) \rangle(t), \quad (7.34)$$

$$\langle D_{00}^2 \rangle(t) = \frac{1}{2} [\langle 3 \cos^2(\theta) \rangle(t) - 1]. \quad (7.35)$$

Here,  $\theta$  is the Euler angle between the laboratory  $Z$ -axis and the molecular  $z$ -axis. Since we have chosen the  $z$ -axis to coincide with the permanent dipole moment, the first identity is directly responsible for the polarization of the sample because of Equation (7.9). The second yields the birefringence via Equation (7.10) when  $\alpha_{xx} = \alpha_{yy}$ . In general, Equation (7.34) describes the orientation of the molecules while Equation (7.35) refers to the alignment along the axes of largest polarizability [215, 216].

The results are shown in Figure 7.4. As suspected, the theory predicts far more orientation of the molecules than alignment. Orientation follows the electric field profile with a slight delay – a result we expect from the considerations in Section 3.1.3. Furthermore, the orientation only yields a very small negative contribution despite the strong negative field profile at this time. This likely originates from the fact that the field cannot rotate the molecules fast enough to make up for the rapidly vanishing electric field. In contrast, the alignment exhibits a similar behavior as the phase shift, suggesting that Equation (7.35) gives a large contribution to  $\Delta\alpha(t)$ .

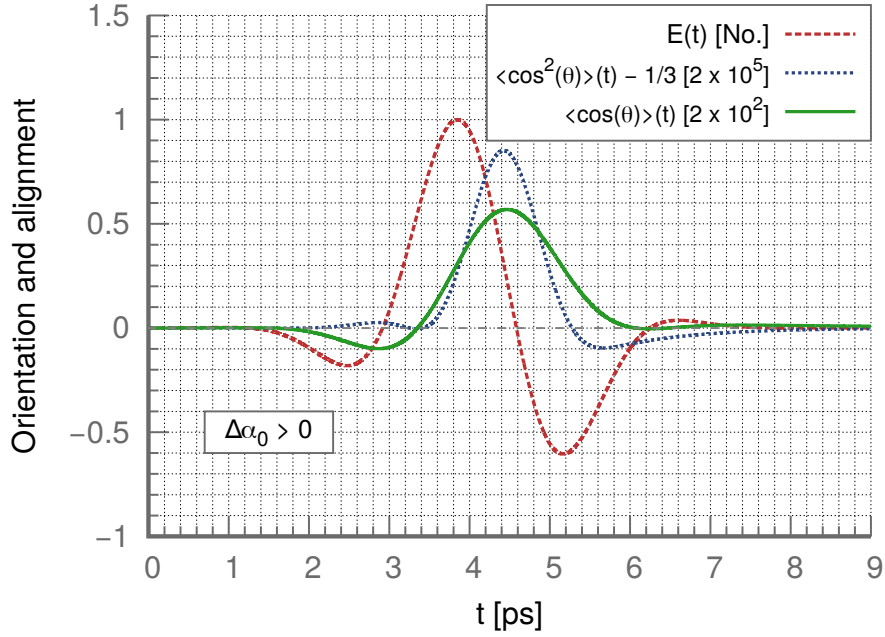


**Figure 7.4:** Measures for orientation and alignment in the case of liquid water. Orientation (green solid line) gives a measure of the polarization of the sample, while the measure of alignment (blue dotted line) describes orientation along the axes of highest polarizability. The values were evaluated for the polarizability in Equation (7.30) for which  $\Delta\alpha_0^{\perp,\parallel} > 0$ . The normalized effective field (7.32) is also shown (red dashed line).

### Discussion

As we have seen, the results for the phase shift in Figure 7.3 only agree partially with the observed dynamics, leading us to conclude that a more involved treatment is needed to describe the measurement. In particular, the Debye approximation assumes overdamped dynamics where excitation energies are not higher than the low GHz range [13]. This may be insufficient for small molecules such as water for which damping might be too small or for the larger driving frequency used. Another particularly strong limitation is given by the assumption of a dilute liquid and, thus, non-interacting molecules. It is well known that water molecules interact via the formation of hydrogen bonds which strongly impacts the rotational dynamics of water [118, 229, 249]. While we may suppose that interaction effects are also partially taken into account by the elements of the rotational diffusion tensor which we obtained from MD simulations, explicit many-particle interactions should be included in the potential of Equation (7.4). The theory also neglects hyperpolarizabilities. Indeed, hyperpolarizabilities can usually be assumed to be small [166] and an instantaneous response, commonly associated with hyperpolarizabilities [128, 130], was not observed [3]. We can gauge the impact

of the second hyperpolarizability by relating scales according to Equation (7.3). Using results from simulations [250], we find  $\gamma_{||}(0; 0, 0, 0)/(4\pi\epsilon_0\Delta\alpha_0\mu^2/(k_B T)^2) \sim 10^{-2}$  for the mean second hyperpolarizability at zero frequency. While small, a proper frequency dependence or taking into account the correct elements of the tensor may invalidate this comparison. Other potential sources of errors include quantum, memory and conduction effects which are neglected a priori in the present theory. In terms of the electric field, we also stress that any position dependence was neglected such that absorption and diffraction was only taken into account by using a comparably low field strength.

Despite the shortcomings, the overall shape of  $\Delta\Phi(t)$  coincides with the experimental results for positive  $\Delta\alpha_0$ . This suggests that the functional dependence is at least partially correct. In fact, the orientation and alignment dynamics presented in Figure 7.4 agree with results obtained from MD simulations performed by Welsh, Mishra and Santra as discussed in the joint paper [3, Figure 2]. While the simulations also do not take hyperpolarizabilities into account, both methods predict that the sample becomes polarized by orientation of molecular dipoles and exhibits a comparably strong contribution due to the permanent dipole moment. The latter conclusion has also been drawn in other works [166, 225].

Nevertheless, if the experimental measurement results are convoluted with a Gaussian as a proxy for a longer pulse [3, Figure 1 c], a broadly negative signal is obtained which is better reproduced by the result for negative  $\Delta\alpha_0$  in Figure 7.3 (b). A fit to the experimental data based on the isotropic solution (7.26) also predicts a negative  $\Delta\alpha_0$  [3, Table 1]. This stands in contrast to usual results obtained for water vapor which predict a positive sign [166, 251], but a negative signal is also found in other recent THz measurements albeit at different frequencies [165, 227]. As a way to resolve the issue, Kampfrath et al. [165] put forward the idea that instead of the rotational dynamics of single water molecules, the TKE dynamics in the liquid phase correspond to motions of aggregated water molecules such as water dimers. These clusters are then assumed to have a negative  $\Delta\alpha_0$  – in contrast to results obtained at THz frequencies in the gas phase [166].

In short, while some agreement exists, we must state that the single-particle theory employed here does not describe the experimental dynamics sufficiently well. However, the overall shape shows some promising similarities such that inclusion of additional contributions may be able to alleviate some of the underlying issues.

### 7.2.3 Possible corrections

Next, we discuss a few possible extensions to the underlying theory. While we are not going to derive any new results, this section aims to provide avenues for further research and may lead to better agreement with experimental results.

### ***Dipole-dipole interactions***

In two recent papers, Dejardin, Kalmykov and others [138, 252] expanded on the theory by taking into account dipole-dipole interactions. This was done on the basis of mean-field theory while assuming a comparably small interaction strength. For spherical molecules and a simple AC driving field of the form  $E(t) = E_0 \cos(\omega t)$ , they derive corrections to the (non-) linear susceptibilities (cf. Equation (3.23)). By using an expansion of the angular probability distribution function in Legendre polynomials, they derive the relevant expansion coefficients  $f_n$  to third order in the field strength. The coefficient of the second Legendre polynomial in second order of the field strength,  $f_2^{(2)}(t)$ , is what determines the dynamic Kerr effect for a symmetric top molecule (cf. Equation (7.35) and the remark below (7.10)). They find [138, Equation (35)]

$$f_2^{(2)}(t) = -\frac{3\Lambda}{5\tau_D} \int_{-\infty}^t dt' [f_1^{(1)}(t')]^2 e^{-3\frac{(t-t')}{\tau_D}} + \dots, \quad (7.36)$$

where the dots give corrections we had already included. The coefficient  $f_1^{(1)}$  is linear in the field strength and determines the linear electric susceptibility and the linear polarization (see Equation (3.18)). The prefactor  $\Lambda = (4\pi\rho_0\mu^2)/(3k_B T)$  characterizes the coupling strength and depends on the number density  $\rho_0$ . The interaction term in the potential is proportional to the orientation  $\langle \cos(\theta) \rangle(t)$ . Thus, the mean-field approach amounts to a correction to the effective field experienced by a dipole from polarization (cf. Equations (7.9) and (3.1)).

The functional shape seems a promising way to correct the theory with respect to the experimental results. This is because the fitting procedure employed in the experimental paper [3] uses the second term in Equation (7.26) and finds that one of the two decay times is much smaller than the other. This effectively recreates the shape of the first term with a dependence on  $E^2(t)$  and a decay time of  $\tau_D/3$ . A similar functional dependence can be ascribed to the interaction term in Equation (7.36) while the negative sign gives the desired decrease of the theoretical signal for positive  $\Delta\alpha_0$ . To gauge its impact, we have considered a naive implementation of Equation (7.36) in Appendix F. While the resulting effect is small, it nevertheless corrects the result in promising ways. A proper derivation for asymmetric top molecules and an implementation for arbitrary pulse shapes may be able to find a better agreement with the measurement.

### ***Bath driving effects***

It is also possible to include bath driving effects into the description of the Kerr effect in a simple phenomenological way by making use of the results derived in the previous chapters. We saw that dipolar bath driving merely creates an additional force component onto an immersed quantum system. Naively, one may include this effect by replacing

$E(t)$  in our theory by  $E_{\text{eff}}(t)$ . We start with the Onsager result of Equation (4.24), given here by

$$E_{\text{eff}}(t) = \int_{t_0}^t ds \chi_c(t-s)E(s) = E(t) + \int_{t_0}^t ds \chi_o(t-s)E(s). \quad (7.37)$$

Here,  $\chi_c(t)$  is the susceptibility of the cavity field and  $\chi_o(t)$  the Onsager susceptibility as defined in Equation (3.48). Since the Onsager model treats the surrounding molecules as a dielectric, one may see the correction as a sort of mean-field theory and Equation (7.37) as a direct consequence of polarization. The parallels to the correction from dipole-dipole interactions discussed above are obvious.

Alternatively, one may use a form of the effective force derived without recourse to the Onsager model, given by Equations (4.9) and (4.10) as

$$F_{\text{eff}}(t) = d_0 E(t) + \frac{2}{\pi} \int_0^{\infty} d\omega \bar{J}(\omega) \int_{t_0}^t ds E(s) \sin[\omega(t-s)]. \quad (7.38)$$

Here, we have replaced the arbitrary function  $F(t)$  by the electric field  $E(t)$ . The coupling constants  $d_0$  and  $d_\alpha$  are then measures for the charge of molecular dipoles. In Equation (7.38) the quantity of interest is the effective spectral density defined in Equation (4.11). In principle, it is possible to model this quantity by inserting appropriate functional forms independent of the Onsager model where we just found that  $\bar{J}(\omega) \propto J(\omega)$ . However, this sort of modeling is as of yet physically unmotivated. This is further complicated by the fact that the theory presented in Section 7.1 assumes no resonances and only treats overdamped dynamics. Yet, we have seen in Part 5 that a structureless Ohmic spectral density leads to almost no effect for large  $\omega_c$ , or rather, no changes to the overall shape of the effective driving field. Thus we just expect a mere increase or decrease of the external field strength in this case.

Nevertheless, we considered the naive approach in Equation (7.37) in Appendix F in order to gauge its impact. The effect is fairly small but shifts the maxima and minima as required for a fit to the experimental measurement.

Still, much remains unclear. For instance, Equations (7.37) and (7.38) were derived for one-dimensional models such that the actual spatial direction of the resulting field contributions is not known. The Onsager model assumes that the dipole is oriented in the direction of the electric field. Implementation of Equations (7.37) and (7.38) would also assume that no bath driving occurs by way of the optical probing pulse. Thus, a proper derivation on the basis of the Euler-Langevin equation is required and a comparison with the dipole-dipole correction (7.36) should also be performed in future research.

### ***Hyperpolarizabilities***

Hyperpolarizabilities can be readily included in the theory on the level of the potential (7.12) [13]. They describe higher-order corrections to the polarizability, that is to the induced dipole moment, such that Equation (7.12) can be extended according to [112, 113, 117]

$$\begin{aligned}
 V(t) &= -\boldsymbol{\mu} \cdot \mathbf{E}(t) - \boldsymbol{\mu}_{\text{ind}}[\mathbf{E}(t)] \cdot \mathbf{E}(t) \\
 &= - \sum_{i=X,Y,Z} \mu_i E_i(t) - \sum_{i,j=X,Y,Z} \varepsilon_{ij} E_i(t) E_j(t) - \sum_{i,j,k=X,Y,Z} \beta_{ijk} E_i(t) E_j(t) E_k(t) \\
 &\quad - \sum_{i,j,k,l=X,Y,Z} \gamma_{ijkl} E_i(t) E_j(t) E_k(t) E_l(t) + \dots .
 \end{aligned} \tag{7.39}$$

Here, we omitted all numerical factors for brevity. Similar to Equation (7.13), Equation (7.39) must be expressed in terms of Wigner's D-functions. This allows us to include the potential into the differential recurrence relations presented by Coffey and Kalmykov [13]. As the  $\langle D_{mm'}^j \rangle(t) \propto (E_0)^j$  for  $E_0 \rightarrow 0$  [13], we expect that in the low field strength approximation only contributions which couple to  $\langle D_{mm'}^2 \rangle(t)$  will become relevant for the dynamics. We can therefore suppose that the matrix theory of Equations (7.14) and (7.15) will be extended by new terms but additional degrees of freedom will not be introduced. This matches with the result in Equation (7.3) where hyperpolarizabilities were explicitly included for the DC case while low field strength was also assumed [113]. Note that Equation (7.39) omits any kind of time dependence in the hyperpolarizabilities which need to be properly accounted for during the derivation.

### ***Beyond the Debye approximation***

Here we merely note that it is also possible to extend the dynamics beyond the overdamped case by including inertia into the description. This is performed in some detail in the book by Coffey and Kalmykov [13, Chapter 10 and 11] which may pave a way for further extension of the theory.

## **7.3 Conclusion of Part 7**

In this part of the thesis, we have presented a matrix theory for the analysis of the dynamic Kerr effect, based on the rotational motion of free molecules described by a classical Langevin Equation in the non-inertial approximation [13, 131]. We have seen that the dynamical motion of a molecule is determined by the (hyper-) polarizabilities and the permanent dipole moment. The relaxation times emerge from this formulation by way of the inverse elements of the rotational diffusion tensor. In the following, we have applied the theory to the case of liquid water driven by an electric field in the THz

regime and have compared our result to an experimental measurement [3]. While the resulting dynamics has proven to be qualitatively similar, quantitative agreement with the experimental results could not be achieved. Despite this major shortcoming, we could conclude that the signal is dominated by orientation and the permanent dipole moments as the effect from polarizabilities was found to be small. This is an important result for the THz Kerr response, as optical frequencies do not lead to any contribution from permanent dipole moments [113, 224].

In order to improve upon the theory, we have discussed a few possible corrections as well. In particular, we have noted dipole-dipole interactions and the effects from linear bath driving. Both describe the effect of polarization of the environment and may lead to desired changes in the effective field responsible for the Kerr effect. We have also noted corrections from hyperpolarizabilities and inertial effects which should also be investigated in future research.

## Summary and outlook

Throughout this thesis, we have seen how bath driving can impact an open quantum system. Our method of choice has been the use of system-bath models and a simple linear coupling of the bath modes to a classical external field. We have seen in Part 4 that the quantum Langevin equation produces a new term which we could interpret as an additional force contribution. This contribution includes the history of the driven bath and represents the effect of the nonequilibrium distribution created by the external force. It depends on the system-bath couplings, as well as the coupling to the external force by way of an additional effective spectral density. By utilizing a simple continuum solvation model, we have managed to show a proportionality of this quantity to the ordinary spectral density of the bath. The resulting effective force has then been evaluated in Part 5 for two typical spectral densities and driving pulse shapes. Only minor deviations to the original pulse have been found in case of an Ohmic environment while long-lasting oscillations could be seen for a Lorentzian spectral density. Especially the latter implies that bath driving effects can be expected to be stronger when environmental resonances have to be taken into account. However, the overall strength of the additional contribution was gauged to be rather small and no significant impact could be observed even for larger system-bath coupling strengths, as we have discussed in Part 6. In fact, the influence of the additional force has been most visible for strong electric fields in the coherent regime at comparably low temperatures and small to intermediate coupling strength. Nevertheless, the response spectra discussed in Parts 4 and 5 have shown a visible impact from bath driving contributions, including qualitative changes and negative absorbance. This implies, that bath driving may very well lead to interesting effects in specific applications.

One such application may be *surface enhanced Raman spectroscopy* (SERS). This method achieves higher Raman intensities by adsorbing molecules on metallic surfaces or colloidal metal nanoparticles. In fact, the impact of the metallic surfaces is so strong that the signal is boosted by multiple orders of magnitude. In what has been called the *electromagnetic mechanism*, this is explained with local field hot spots emerging from interactions of the external field with plasmon modes inside the metal [148, 253]. Their location, size and the resulting enhancement factor depend on the particular geometry of the setup [148]. Exemplarily, we can consider the Onsager susceptibility of equation



(3.48) for a metallic sphere. For gold, the real part of the dielectric function becomes negative in the optical regime (cf. equation (4.42)). The real part of the denominator in equation (3.48) can therefore cancel at specific frequencies, leaving just the imaginary part. For materials with low absorbance this can lead to very large values of induced dipole fields [148]. This connection illustrates that our bath driving approach may be suitable for an analysis of SERS with the added advantage that the strong fields involved can make bath driving effects more relevant. Moreover, we already laid the foundations for a simple model of a colloidal dimer in Part 4 which could be generalized to a model for SERS. Tomasi [134] already proposed an analysis of SERS using continuum solvation models in 2004, such that a careful review of recent literature on the subject is required.

Next, we have also shown that bath driving is able to excite a system of interest. This begs the question if bath driving effects can be exploited in *chemical reaction dynamics*. Chemical reactions have been investigated previously using system-bath models and an abundance of literature exists on the subject [5, 6]. By driving the system off-resonance but close to a bath mode, we may expect the impact of bath driving to be relatively strong and an investigation using an appropriate reaction should give insights about enhancing yields. In this sense, it may also be useful to extend the analysis of transition probabilities, performed in Appendix D. Since chemical reactions are often associated with thermally activated barrier crossing [6], a particularly pertinent question is if bath driving can also be used to achieve higher temperatures in the bath. As we have seen, this is not the case for linear driving and may not necessarily be the case for parametric driving either. Still, it may be possible to define an effective temperature in the latter case by carefully absorbing the emerging time dependence. Properly outlining the requirements of a temperature change in the bath from a driving process is therefore mandated.

Finally, we address the *terahertz Kerr effect* as discussed in Part 7. Extensions to the theory which may help to explain the experimental signal of water have already been discussed and may provide an interesting outlook for future research. To fully use it as an example of a driven bath, however, requires one to establish a clearer connection to system-bath models. In addition to defining an appropriate system, the problem has to be generalized to three spatial dimensions and appropriate nonlinear interaction terms have to be introduced. A possible connection to experimental quantities might be achievable by looking at nonlinear generalizations of continuum solvation models.

In closing, bath driving represents a natural extension to usual system-bath approaches, with possible applications in a variety of different fields. We hope that the research presented in this thesis provides another step in the understanding of driven environments and informs the development of new models and applications.

## Appendix A

### Mathematical identities and definitions

In this appendix, we give some general mathematical definitions used throughout the thesis. Most are given for completeness and are not referenced explicitly.

#### *Fourier transforms*

We define the Fourier transform in accordance with Nitzan [5] as

$$g(\omega) = \int_{-\infty}^{\infty} dt g(t) e^{i\omega t} \quad \text{and} \quad g(t) = \frac{1}{2\pi} \int_{-\infty}^{\infty} d\omega g(\omega) e^{-i\omega t}, \quad (\text{A.1})$$

such that the  $\delta$ -function is defined by

$$\delta(x - a) = \frac{1}{2\pi} \int_{-\infty}^{\infty} dk e^{ik(x-a)}. \quad (\text{A.2})$$

This gives rise to the definition of the Sokhotski–Plemelj identity as

$$\lim_{\epsilon \rightarrow 0} \frac{1}{\omega - \omega_0 + i\epsilon} = \mathcal{P} \frac{1}{\omega - \omega_0} - i\pi\delta(\omega - \omega_0), \quad (\text{A.3})$$

where  $\mathcal{P}$  denotes the principal part of an integral. The Heaviside function can be written as

$$\Theta(t) = \lim_{\epsilon \rightarrow 0^+} \frac{1}{2\pi i} \int_{-\infty}^{\infty} d\omega \frac{e^{i\omega t}}{\omega - i\epsilon} = \lim_{\epsilon \rightarrow 0^+} \left( -\frac{1}{2\pi i} \right) \int_{-\infty}^{\infty} d\omega \frac{e^{-i\omega t}}{\omega + i\epsilon}. \quad (\text{A.4})$$

#### *Creation and annihilation operators*

Creation ( $a^\dagger$ ) and annihilation operators ( $a$ ) are related to position and momentum operators according to [5]

$$x = \frac{1}{2} \sqrt{\frac{2\hbar}{m\omega}} (a + a^\dagger) \quad \text{and} \quad p = \frac{im\omega}{2} \sqrt{\frac{2\hbar}{m\omega}} (a^\dagger - a). \quad (\text{A.5})$$

They fulfill the bosonic commutation relation  $[a, a^\dagger] = 1$ , and are related to the eigenstates of the harmonic oscillator  $|n\rangle$  by

$$a|n\rangle = \sqrt{n}|n-1\rangle \quad \text{and} \quad a^\dagger|n\rangle = \sqrt{n+1}|n+1\rangle. \quad (\text{A.6})$$

Hence, their thermal averages vanish. This is most important for the position operator

$$\langle x \rangle^{\text{eq}} = \text{Tr}[x\rho^{\text{eq}}] = \frac{1}{2} \sqrt{\frac{2\hbar}{m\omega}} \sum_n \langle n|(a+a^\dagger)|n\rangle \frac{e^{-\beta E_n}}{\mathcal{Z}} = 0, \quad (\text{A.7})$$

because the  $|n\rangle$  are orthogonal.

### ***Time evolution of the density matrix***

The time evolution from  $t_0$  to  $t$  of a time-independent system with Hamiltonian  $H$ , can be written in terms of the time evolution operator [5]

$$U(t, t_0) = e^{-\frac{i}{\hbar}H(t-t_0)}. \quad (\text{A.8})$$

In the following, we set  $t_0 = 0$  and abbreviate  $U(t, 0) = U(t)$ . In the Schrödinger picture (subscript  $S$ ), we have time-dependent states according to

$$|\Psi(t)\rangle_S = U(t)|\Psi(0)\rangle_S = e^{-\frac{i}{\hbar}Ht}|\Psi(0)\rangle_S. \quad (\text{A.9})$$

Since the density matrix can be written as a sum of projectors times a probability, it shares the same time evolution as the states. This means

$$\rho_S(t) = U(t)\rho(0)U^\dagger(t). \quad (\text{A.10})$$

In the Heisenberg picture (subscript  $H$ ) operators absorb the time evolution such that the states become time-independent. The density matrix is then constant, as

$$\rho_H(t) = U^\dagger(t)\rho_S(t)U(t) = \rho(0). \quad (\text{A.11})$$

In the interaction picture (subscript  $I$ ) the Hamiltonian is assumed to be perturbed according to  $H = H_0 + V$ . States evolve according to the perturbation  $V$  while operators follow the unperturbed time evolution of  $H_0$  given by the operator  $U_0(t)$ . We have

$$|\Psi(t)\rangle_I = U_0^\dagger(t)|\Psi(t)\rangle_S = e^{\frac{i}{\hbar}H_0t}|\Psi(t)\rangle_S. \quad (\text{A.12})$$

The density matrix is still time-dependent in this case, as

$$\rho_I(t) = U_0^\dagger(t)\rho_S(t)U_0(t). \quad (\text{A.13})$$

Equation (A.10) gives rise to the Liouville-von Neumann equation [5]

$$\frac{d}{dt}\rho_S(t) = -\frac{i}{\hbar}[H, \rho_S(t)]. \quad (\text{A.14})$$

In the interaction picture, the Hamiltonian is replaced by the perturbation such that

$$\frac{d}{dt}\rho_I(t) = -\frac{i}{\hbar}[V_I(t), \rho_I(t)]. \quad (\text{A.15})$$

For explicitly time-dependent density matrices an additional partial derivative enters on the right-hand side. For the case of a time-dependent Hamiltonian, (A.14) and (A.15) retain their form. Note that Equation (A.8) is then replaced by a time-ordered exponential over the integral of  $H(t)$  (see e.g. [61, 254]).

## Appendix B

### Cavity and reaction field for a layered sphere and an ellipsoid

Here, we present results for the cavity and the reaction field of two different geometries of the Onsager solvation model discussed in Section 3.2. First, we focus on a layered sphere as depicted in Figure B.1 (a). We outline the derivation of the cavity and the reaction field, based on the presentation in Gilmore and McKenzie [26]. The former has not been given in the cited paper but has been calculated by Scholte [255] previously. We apply this more complicated geometry to a polarizable molecule in water, as discussed in Section 4.3 and briefly discuss the results. Finally, we give expressions for an ellipsoidal geometry taken from Scholte [255] and Boettcher [112]. The geometry of the latter is depicted in Figure B.1 (b).

#### *Derivation of the layered model*

For the layered sphere, we can directly adapt the discussion from Sections 3.3 and 4.2. We now find a total of six boundary conditions for the potential in the cavity ( $\Phi_c$ ), inside the dielectric layer ( $\Phi_d$ ) and in the surrounding dielectric region ( $\Phi_s$ ). The interfaces yield

$$\Phi_d(r = a) = \Phi_c(r = a), \quad (\text{B.1})$$

$$\Phi_d(r = b) = \Phi_s(r = b), \quad (\text{B.2})$$

$$\varepsilon_d \frac{\partial \Phi_d}{\partial r} \Big|_{r=a} = \varepsilon_c \frac{\partial \Phi_c}{\partial r} \Big|_{r=a}, \quad (\text{B.3})$$

$$\varepsilon_d \frac{\partial \Phi_d}{\partial r} \Big|_{r=b} = \varepsilon_s \frac{\partial \Phi_s}{\partial r} \Big|_{r=b}, \quad (\text{B.4})$$

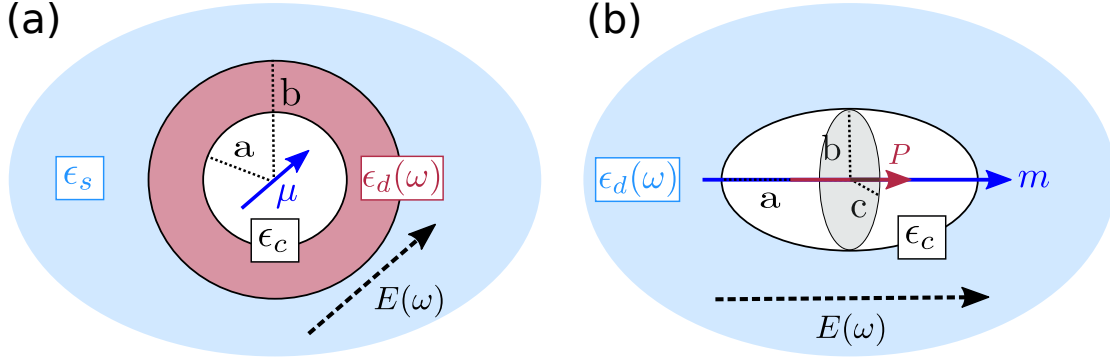


**Figure B.1:** *Extended Onsager models. (a) Layered sphere geometry, where the dielectric with frequency-dependent dielectric function  $\epsilon_d(\omega)$  constitutes a layer (light red) around the cavity with thickness  $b - a$ . The setup is embedded in another dielectric region with dielectric constant  $\epsilon_s$  (light blue). (b) Ellipsoidal geometry of the cavity with half-axes  $a, b$  and  $c$ . The ellipsoid has a homogeneous polarization  $P$  (red arrow) which gives rise to a total dipole moment  $m$  (blue arrow) of the ellipsoid. The polarization and the dipole moment is oriented along  $a$  for simplicity. An external electric field  $E(\omega)$  (black arrows) acts on both setups in the direction of  $\mu$  and  $m$ , respectively.*

where we have dropped the frequency dependence in most quantities for brevity. The last two conditions are given by the external field and the source term of the dipole

$$\Phi_s(r \rightarrow \infty) = -E(\omega) r \cos(\theta) \quad (\text{B.5})$$

$$\Phi_c(r \rightarrow 0) = \frac{\mu(\omega)}{4\pi\epsilon_0 r^2} \cos(\theta). \quad (\text{B.6})$$

Conditions (B.5) and (B.6) yield

$$A_1^s = -E(\omega), \quad B_1^c = \mu(\omega)/4\pi\epsilon_0, \quad A_{l \neq 1}^s = 0, \quad B_{l \neq 1}^c = 0. \quad (\text{B.7})$$

The  $l \neq 1$ -terms do not contribute because of the symmetry, while the  $l = 1$  coefficients must fulfill

$$A_1^d b + \frac{B_1^d}{b^2} = -E(\omega) b + \frac{B_1^s}{b^2}, \quad (\text{B.8})$$

$$A_1^d a + \frac{B_1^d}{a^2} = A_1^c a + \frac{\mu(\omega)}{4\pi\epsilon_0 a^2}, \quad (\text{B.9})$$

$$\epsilon_d A_1^d - 2\epsilon_d \frac{B_1^d}{a^3} = \epsilon_c A_1^c - 2\epsilon_c \frac{\mu(\omega)}{4\pi\epsilon_0 a^3}, \quad (\text{B.10})$$

$$\epsilon_d A_1^d - 2\epsilon_d \frac{B_1^d}{b^3} = -\epsilon_s E(\omega) - 2\epsilon_s \frac{B_1^s}{b^3}. \quad (\text{B.11})$$

As before, the coefficient  $A_1^c$  gives the reaction and the cavity field as

$$\begin{aligned} A_1^c &= -\frac{\mu(\omega)}{4\pi\epsilon_0 a^3} \left[ 1 + \frac{3\epsilon_c}{\epsilon_d - \epsilon_c} \right] + \frac{B_1^d}{a^3} \left[ \frac{2\epsilon_d + \epsilon_c}{\epsilon_d - \epsilon_c} + 1 \right] \\ &= -\frac{\mu(\omega)}{4\pi\epsilon_0 a^3} \chi_r(\omega) - E(\omega) \chi_c(\omega). \end{aligned} \quad (\text{B.12})$$

The reaction field is characterized by

$$\begin{aligned} \chi_r(\omega) &= \frac{2a^3(\epsilon_s - \epsilon_d)(2\epsilon_c + \epsilon_d) + 2b^3(2\epsilon_s + \epsilon_d)(\epsilon_d - \epsilon_c)}{2a^3(\epsilon_s - \epsilon_d)(\epsilon_d - \epsilon_c) + b^3(2\epsilon_s + \epsilon_d)(2\epsilon_d + \epsilon_c)} \\ &= \frac{2}{1 + 2\frac{a^3}{b^3}\chi_{sd}\chi_{dc}} \left[ \chi_{dc} + \left(\frac{a}{b}\right)^3 \chi_{sd} \left(\frac{2\epsilon_c + \epsilon_d}{2\epsilon_d + \epsilon_c}\right) \right], \end{aligned} \quad (\text{B.13})$$

which coincides with the expression (56) of Gilmore and McKenzie [26]. The cavity field is characterized by

$$\chi_c(\omega) = \frac{(3\epsilon_d)(3\epsilon_s)b^3}{2a^3(\epsilon_s - \epsilon_d)(\epsilon_d - \epsilon_c) + b^3(2\epsilon_s + \epsilon_d)(2\epsilon_d + \epsilon_c)} = \frac{[1 + \chi_{dc}][1 + \chi_{sd}]}{1 + 2\frac{a^3}{b^3}\chi_{sd}\chi_{dc}}, \quad (\text{B.14})$$

which coincides with Equation (28) of Scholte [255]. In both equations, we have defined  $\chi_{ab} = (\epsilon_a - \epsilon_b)/(2\epsilon_a + \epsilon_b)$  as the Onsager susceptibilities at the interfaces. Both expressions reduce to the results given in Sections 3.2 and 4.1 when the layer is absent, i.e.,  $\chi_{sd} = 0$ . For small ratios  $a/b$ , (B.14) can be expanded into a Taylor series as

$$\chi_c(\omega) \approx [1 + \chi_{dc}\chi_{sd} + \chi_{dc} + \chi_{sd}] \left[ 1 - 2 \left(\frac{a^3}{b^3}\right) \chi_{dc}\chi_{sd} \right] = 1 + \bar{\chi}_c(\omega), \quad (\text{B.15})$$

with

$$\bar{\chi}_c(\omega) = [\chi_{dc}\chi_{sd} + \chi_{dc} + \chi_{sd}] \left[ 1 - 2 \left(\frac{a^3}{b^3}\right) \chi_{dc}\chi_{sd} \right] - 2 \left(\frac{a^3}{b^3}\right) \chi_{dc}\chi_{sd}. \quad (\text{B.16})$$

Approximation (B.15) restores a separable direct driving contribution.

### ***Polarizable molecule in water with the layered sphere model***

We now apply the results for the cavity and the reaction field, given in Equations (B.13) and (B.14), to the case of the polarizable molecule in water, as discussed in Section 4.3. In practice, we assume that the molecule interacts dynamically only with its hydration

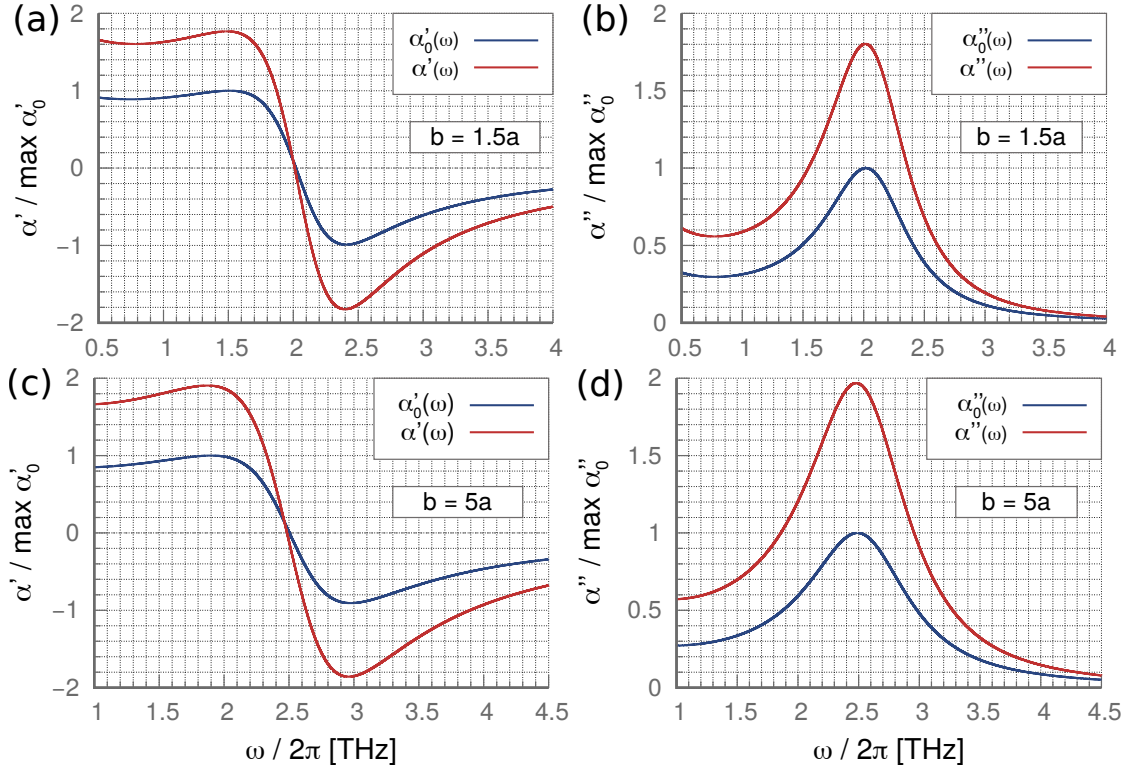


**Figure B.2:** Response of a molecule in water derived from Equation (4.32) using the layered sphere geometry depicted in Figure B.1 (a). The associated reaction and cavity fields are given in Equations (B.13) and (B.14). A single prime denotes the real and two denote the imaginary part. (a),(b) Results for a thin layer with  $b = 1.5a$ . (c),(d) Results for a thicker layer with  $b = 5a$ .

shell. The surrounding dielectric represents bulk water far away from the molecule. We therefore have

$$\varepsilon_d = \varepsilon(\omega) , \quad \varepsilon_c = 1 \quad \text{and} \quad \varepsilon_s = \varepsilon(0), \quad (\text{B.17})$$

where we substituted  $\varepsilon(\omega)$  as the dielectric function of water from Equation (4.26) and its zero frequency contribution  $\varepsilon(0) \approx 79$  therein. The results are shown in Figure B.2 for two values of  $a/b$ . The results are given in relation to results for  $\chi_c = 1$ , although the susceptibility in Equation (B.14) always introduces a dressed field. However, the effect of the latter is small and we aim for a comparison to the undressed field. The results exhibit the same structure as in Figures 4.3 and 4.4: the response peaks are enhanced and a small negative undershoot occurs for the imaginary parts (not shown). Most importantly, the effect of the dielectric is stronger with a more pronounced shift of the resonance and a larger enhancement by a factor of almost 2 in both cases. A thinner layer leads to a more pronounced shift of the frequency but reduces the enhancement.



Since the relevant terms scale with  $(a/b)^3$ , the results for the thicker layer do not deviate much from results for even larger  $b$ .

### **Results for the ellipsoid**

It is also possible to derive the cavity and the reaction field for an ellipsoidal geometry. However, the solution for an ideal dipole inside such a cavity is very intricate and can be found in Boettcher [112, §20]. The reason for this is that in the spherical case the series (3.37) exactly truncates at  $l = 1$ , because the Onsager sphere itself reduces to a large dipole [112]. This is not the case for an ellipsoid where an infinite number of terms contribute to the potential. In this part, we therefore give shorter expressions derived for a homogeneous polarization inside the ellipsoid, which gives rise to a dipole moment  $m$ . The results are taken from Scholte [255] and Boettcher [112, §20], while we assume that  $m$  plays a role equivalent to the point dipole we have used up until now. The model is depicted in Figure B.1 (b) with the ellipsoidal half-axes  $a$ ,  $b$  and  $c$ . For simplicity, we assume that both the external field as well as the polarization are oriented along the long axis  $a$  and we consider the result for a cavity with  $\varepsilon_c = 1$ . One finds

$$\chi_r(\omega) = \frac{3A(1-A)(\varepsilon_d(\omega) - 1)}{\varepsilon_d(\omega) + (1 - \varepsilon_d(\omega))A}, \quad (\text{B.18})$$

Here, the susceptibility  $\chi_r(\omega)$  couples to a prefactor  $m(\omega)/(4\pi\varepsilon_0 abc)$  which is equivalent to the definition in Equation (B.12). The cavity field is then characterized by

$$\chi_c(\omega) = \left[ \frac{\varepsilon_d(\omega)}{\varepsilon_d(\omega) + (1 - \varepsilon_d(\omega))A} \right]. \quad (\text{B.19})$$

The factor  $A$  depends on the orientation of  $m$  and the external field. For our choice above, we have [255]

$$\begin{aligned} A &= \frac{abc}{2} \int_0^\infty ds \frac{1}{(s+a^2)^{\frac{3}{2}}(s+b^2)^{\frac{1}{2}}(s+c^2)^{\frac{1}{2}}} \\ &\stackrel{a < b = c}{=} \frac{1}{(1 - (a/b)^2)} - \frac{(a/b)}{(1 - (a/b)^2)^{\frac{3}{2}}} \arccos(a/b). \end{aligned} \quad (\text{B.20})$$

The second equation is a solution for an oblate spheroid, which could, for instance, stand in for a molecule such as benzene. In general, the cavity field can also be written as a superposition if the field does not occur along one of the axes of the ellipsoid [112, 255].

## Appendix C

### Evaluation of correlators in the Liouville space formalism

In this appendix, we give more insight into the correlators (5.38) that appear within the Liouville space quantum master equation of Part 5. Specifically, we outline the emergence of bath response and symmetric bath autocorrelation functions from the second-order correlator given in Liouville space as

$$\Phi^{(2)}(t_2, t_1) = \langle \mathcal{L}_{\text{SB}}(t_2) \mathcal{U}_0(t_2, t_1) \mathcal{L}_{\text{SB}}(t_1) \mathcal{U}_0(t_1, t_0) \rangle_{\text{B}}. \quad (\text{C.1})$$

For simplicity, we work in thermal equilibrium and drop the explicit time dependence of the  $\mathcal{L}_{\text{SB}}$ . The latter can be restored easily by respecting the time ordering in the correlators. In order to evaluate Equation (C.1), it needs to be split into system and bath parts. To do so, we note that  $\mathcal{L}_{\text{SB}} = (-i/\hbar)[H_{\text{SB}}, \cdot]$  which produces commutators of composite operators. For general composite operators  $O_i = A_i B_i$ , where  $A_i$  acts on the system subspace and  $B_i$  on the subspace of the bath such that  $[A_i, B_i] = 0$ , we have [198]

$$[A_1 B_1, A_2 B_2] = \frac{1}{2} [A_1, A_2] \{B_1, B_2\} + \frac{1}{2} \{A_1, A_2\} [B_1, B_2], \quad (\text{C.2})$$

where  $\{\cdot, \cdot\}$  denotes the anticommutator. Equation (C.2) shows that the resulting correlators involve both commutators and anticommutators. This gives rise to a natural definition of two superoperators as

$$\hat{A} = [A, \cdot] \quad \text{and} \quad \check{A} = \frac{1}{2} \{A, \cdot\}, \quad (\text{C.3})$$

which fulfill  $\widehat{AB} = \hat{A}\check{B} + \check{B}\hat{A}$  as a generalization of Equation (C.2). We now assume  $\mathcal{L}_{\text{SB}} = \widehat{AB}$  and split the bare time evolution superoperator into system and bath parts according to  $\mathcal{U}_0(t_2, t_1) = \mathcal{U}_{\text{S}}(t_2, t_1) \mathcal{U}_{\text{B}}(t_2, t_1)$ . Insertion into Equation (C.1) and use of

Equation (C.2) yields

$$\begin{aligned}
\Phi^{(2)}(t_2, t_1) &= \text{Tr}_B[\widehat{A}\widehat{B}\mathcal{U}_S(t_2, t_1)\mathcal{U}_B(t_2, t_1)\widehat{A}\widehat{B}\mathcal{U}_S(t_1, t_0)\mathcal{U}_B(t_1, t_0)\rho_B^{\text{eq}}] \\
&= (\widehat{A}\mathcal{U}_S(t_2, t_1)\widehat{A}\mathcal{U}_S(t_1, t_0))\text{Tr}_B[\check{B}\mathcal{U}_B(t_2, t_1)\check{B}\mathcal{U}_B(t_1, t_0)\rho_B^{\text{eq}}] \\
&\quad + (\check{A}\mathcal{U}_S(t_2, t_1)\check{A}\mathcal{U}_S(t_1, t_0))\text{Tr}_B[\hat{B}\mathcal{U}_B(t_2, t_1)\hat{B}\mathcal{U}_B(t_1, t_0)\rho_B^{\text{eq}}] \\
&\quad + (\widehat{A}\mathcal{U}_S(t_2, t_1)\check{A}\mathcal{U}_S(t_1, t_0))\text{Tr}_B[\check{B}\mathcal{U}_B(t_2, t_1)\hat{B}\mathcal{U}_B(t_1, t_0)\rho_B^{\text{eq}}] \\
&\quad + (\check{A}\mathcal{U}_S(t_2, t_1)\widehat{A}\mathcal{U}_S(t_1, t_0))\text{Tr}_B[\hat{B}\mathcal{U}_B(t_2, t_1)\check{B}\mathcal{U}_B(t_1, t_0)\rho_B^{\text{eq}}].
\end{aligned} \tag{C.4}$$

Equation (C.1) is now split between system and bath parts: The bath parts are contained in the traces and the superoperators act on the bath density matrix  $\rho_B^{\text{eq}}$ . The system parts are given in the brackets and act on the system density matrix that appears on the right in the quantum master equation (5.36).

We now focus on the bath parts. Because of cyclical invariance of the trace, terms where a commutator (the superoperator  $\hat{B}$ ) is on the left vanish. In the same way, having an anticommutator on the left allows us to replace  $\check{B}$  by the bare operator  $B$ . This gives rise to

$$\begin{aligned}
\text{Tr}_B[\check{B}\mathcal{U}_B(t_2, t_1)\check{B}\mathcal{U}_B(t_1, t_0)\rho_B^{\text{eq}}] &= \frac{1}{2}\text{Tr}_B[B\mathcal{U}_B(t_2, t_1)(B\rho_B^{\text{eq}} + \rho_B^{\text{eq}}B)U_B^\dagger(t_2, t_1)] \\
&= \frac{1}{2}\text{Tr}_B[(\check{B}(t_2 - t_1)B + B\check{B}(t_2 - t_1))\rho_B^{\text{eq}}] = \hbar^2 B_C(t_2, t_1),
\end{aligned} \tag{C.5}$$

and

$$\begin{aligned}
\text{Tr}_B[\hat{B}\mathcal{U}_B(t_2, t_1)\hat{B}\mathcal{U}_B(t_1, t_0)\rho_B^{\text{eq}}] &= \text{Tr}_B[B\mathcal{U}_B(t_2, t_1)(B\rho_B^{\text{eq}} - \rho_B^{\text{eq}}B)U_B^\dagger(t_2, t_1)] \\
&= \text{Tr}_B[(\hat{B}(t_2 - t_1)B - B\hat{B}(t_2 - t_1))\rho_B^{\text{eq}}] = -2i\hbar^2 B_R(t_2, t_1).
\end{aligned} \tag{C.6}$$

The last equation used  $B = \sum_\alpha^N \hbar\lambda_\alpha x_\alpha$ , to recover the symmetric bath auto-correlation function  $B_C$  and the bath response function  $B_R$  as defined in Equations (5.23) and (5.24) (cf. Equations (5.64) and (5.65)). Tildes signify Heisenberg operators. To obtain Equations (C.5) and (C.6) we have applied Equation (5.35) for the time evolution superoperators and have exploited  $\mathcal{U}_B(t)\rho_B^{\text{eq}} = \rho_B^{\text{eq}}$  which holds for the unperturbed time evolution and thermal equilibrium. If the latter does not hold, the additional times  $t_1$  and  $t_0$  will enter, but can also be absorbed into Heisenberg operators. This is the case in the bath driving scheme of Part 5, where terms as in Equation (5.40) follow naturally.

We briefly consider the fourth order result, which reads

$$\begin{aligned}
\Phi^{(4)}(t_4, t_3, t_2, t_1) = & \\
& \langle \mathcal{L}_{\text{SB}}(t_4) \mathcal{U}_0(t_4, t_3) \mathcal{L}_{\text{SB}}(t_3) \mathcal{U}_0(t_3, t_2) \mathcal{L}_{\text{SB}}(t_2) \mathcal{U}_0(t_2, t_1) \mathcal{L}_{\text{SB}}(t_1) \mathcal{U}_0(t_1, t_0) \rangle_{\text{B}} \\
& = (\hat{A} \mathcal{U}_{\text{S}}(t_4, t_3) \hat{A} \mathcal{U}_{\text{S}}(t_3, t_2) \hat{A} \mathcal{U}_{\text{S}}(t_2, t_1) \hat{A} \mathcal{U}_{\text{S}}(t_1, t_0)) \\
& \quad * \text{Tr}_{\text{B}}[\check{B} \mathcal{U}_{\text{B}}(t_4, t_3) \check{B} \mathcal{U}_{\text{B}}(t_2, t_1) \check{B} \mathcal{U}_{\text{B}}(t_2, t_1) \check{B} \mathcal{U}_{\text{B}}(t_1, t_0) \rho_{\text{B}}^{\text{eq}}] \\
& \quad + (\hat{A} \mathcal{U}_{\text{S}}(t_4, t_3) \hat{A} \mathcal{U}_{\text{S}}(t_3, t_2) \hat{A} \mathcal{U}_{\text{S}}(t_2, t_1) \check{A} \mathcal{U}_{\text{S}}(t_1, t_0)) \\
& \quad * \text{Tr}_{\text{B}}[\check{B} \mathcal{U}_{\text{B}}(t_4, t_3) \check{B} \mathcal{U}_{\text{B}}(t_3, t_2) \check{B} \mathcal{U}_{\text{B}}(t_2, t_1) \hat{B} \mathcal{U}_{\text{B}}(t_1, t_0) \rho_{\text{B}}^{\text{eq}}] \\
& + \dots,
\end{aligned} \tag{C.7}$$

where we have omitted the six other non-zero terms that enter at this order. The bath parts of Equation (C.7) give rise to higher-order bath correlation functions. By looking at their structure, we can already see that expressions such as Equation (5.42) emerge naturally from this procedure, as well.

## Appendix D

### Transition probabilities from the nonequilibrium Bloch equations

This appendix contains an analysis of the emerging transition probabilities in our treatment of Part 5. Since we have considered dynamics for a system starting in the ground state of  $\sigma_x$ , we can construct a proxy for the transition probability  $P_T(t_s)$  by considering the population in the excited state. Specifically,

$$P_T(t_s) \sim \rho_{22}(t_s) = \frac{1}{2} [1 - r_x(t_s)]. \quad (\text{D.1})$$

The time  $t_s$  has to be chosen after the pulse has terminated and the momentary eigenbasis coincides with the bare (diabatic) basis once again. However, due to relaxation the transition probability will depend on the exact time when it is sampled. In addition, the Lorentzian cases show long-lasting oscillations, which require us to choose a time point even further away (see Figure 5.3). As such, our considerations can only go so far as to discuss the general shape of the transition probabilities and not their absolute size.

Nevertheless, Figure D.1 shows the population in dependence of the driving strength, parametrized by the parameters  $\bar{\eta}$  and  $\bar{\kappa}$  as defined in Equation (5.25). For the sampling times, we have chosen  $t_s = 50 \omega_0^{-1}$  in the case of the Ohmic spectral density and  $t_s = 500 \omega_0^{-1}$  for the Lorentzian spectral density. We also point out that we have neglected any carrier frequency and have only used an envelope to describe the driving process in Part 5. The external driving frequency is then formally zero and the detuning is equal to the TSS splitting frequency  $\omega_0$ . Comparison with Equations (3.73) and (3.74) suggests that the RWA is not needed in this case.

From our considerations in Section 3.3.3, we expect regular oscillations which are indeed visible in all cases. However, a simple squared-sine-like dependence can only be observed in the Ohmic plus Gaussian case. For the Dirac pulse, the transition probability exhibits minima but no zeroes and the Lorentzian cases behave similarly, in addition to a more complicated frequency dependence. This behavior likely originates from the more complicated pulse shapes involved. Specifically, the effective force was given by the narrow shape of Equation (5.28) for an Ohmic bath driven by a  $\delta$ -pulse, while the influence of the Lorentzian bath led to damped oscillations as seen in Equation

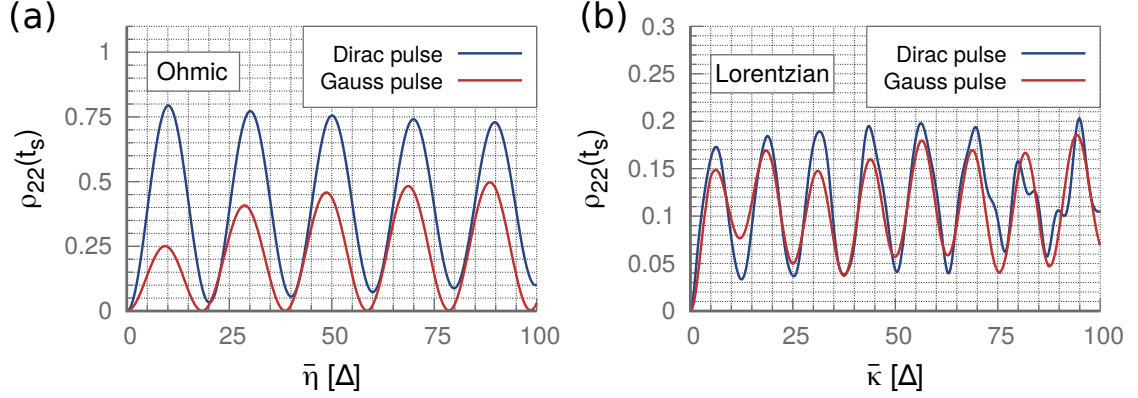


**Figure D.1:** Populations  $\rho_{22}(t_s)$  versus driving strength for the dynamics calculated in Part 5 as a proxy for the transition probabilities  $P_T(t_s)$ . The populations are obtained via Equation (D.1) from the non-equilibrium Bloch equations (5.71) with the parameters listed below Figures 5.6 and 5.7. (a) Results for a Dirac pulse (blue solid lines) and a Gaussian pulse (red solid lines) for the Ohmic spectral density sampled at  $t_s = 50\omega_0^{-1}$ . (b) Results for both pulse shapes for a Lorentzian spectral density sampled at  $t_s = 500\omega_0^{-1}$ .

(5.29). Indeed, for time asymmetric pulses with non-zero detuning, it is known that the transition probability does not vanish in many cases, even while periodic Rabi oscillations do exist [158, 256]. For the Lorentzian spectral density, the oscillations of Equation (5.29) can be seen as a single asymmetric pulse with a carrier frequency  $\Omega$ . While a complete analysis has not been performed yet, it is interesting to note, that the Dirac pulse creates a more involved interference pattern after  $\bar{\kappa}/\Delta \sim 75$ , while the Gaussian pulse produces a fairly regular modulation of the Rabi oscillations. A look at the Fourier spectrum (not shown) reveals that more frequencies are indeed involved in the former. In contrast, the effective force for an Ohmic spectral density and a Gaussian pulse is also Gaussian shaped. Thus, we recover a slowly rising amplitude and regular oscillations as discussed in Section 3.3.3.

To conclude, the results from Part 5 show an interesting non-trivial dynamics in the light of the emerging pulse shapes and we find some general features in agreement with known results. A more detailed analysis of the Rabi oscillations presented could be used to optimize the excitation probability when bath driving is involved.

## Appendix E

### Evaluation of the path integrals

To evaluate the path integrals shown in Part 6, a variety of calculations have been omitted. We aim to fill some of these gaps here. Specifically, we outline the split into classical and fluctuation parts following Equation (6.52), the emergence of the phases in Equations (6.54) and (6.61) and give some hints on the integration over the boundary values performed for Equations (6.55) and (6.65).

#### *Fluctuation integral*

We start with the path integral given in Equation (6.49) and the action (6.50). The paths are now split into a classical part  $\bar{x}_\alpha(t)$  and fluctuations  $\zeta_\alpha(t)$  according to  $x_\alpha(t) = \bar{x}_\alpha(t) + \zeta_\alpha(t)$ . The classical part fulfills the Euler-Lagrange equation (6.52). Insertion into the action (6.50) yields

$$\begin{aligned}
S_{\alpha, \text{SB+B}}^{\text{Dr}}[x_\alpha, \sigma] &= \int_{t_0}^t ds \left[ \frac{m_\alpha}{2} \dot{x}_\alpha^2(s) - \frac{m_\alpha}{2} \omega_\alpha^2 x_\alpha^2(s) + \frac{c_\alpha}{2} q_0 \sigma_{\text{eff}}(s) x_\alpha(s) \right] \\
&= \int_{t_0}^t ds [-\zeta_\alpha(s)] \left[ m_\alpha \ddot{\bar{x}}_\alpha(s) + \omega_\alpha^2 \bar{x}_\alpha(s) - \frac{c_\alpha}{2} q_0 \sigma_{\text{eff}}(s) \right] \\
&\quad + \int_{t_0}^t ds \left\{ \frac{m_\alpha}{2} [\dot{\zeta}_\alpha^2(s) - \omega_\alpha^2 \zeta_\alpha^2(s)] \right\} \\
&\quad + \int_{t_0}^t ds \left[ \frac{m_\alpha}{2} \dot{\bar{x}}_\alpha^2(s) - \frac{m_\alpha}{2} \omega_\alpha^2 \bar{x}_\alpha^2(s) + \frac{c_\alpha}{2} q_0 \sigma_{\text{eff}}(s) \bar{x}_\alpha(s) \right] \\
&= + \int_{t_0}^t ds \left\{ \frac{m_\alpha}{2} [\dot{\zeta}_\alpha^2(s) - \omega_\alpha^2 \zeta_\alpha^2(s)] + \frac{\bar{x}_\alpha(s)}{2} \left[ \frac{c_\alpha}{2} q_0 \sigma_{\text{eff}}(s) \right] \right\} \\
&\quad + \frac{m_\alpha}{2} (\dot{\bar{x}}_\alpha(t) \bar{x}_\alpha(t) - \dot{\bar{x}}_\alpha(t_0) \bar{x}_\alpha(t_0)).
\end{aligned} \tag{E.1}$$

The bracket multiplying  $\zeta_\alpha(t)$  yields zero because of Equation (6.52) so the first equality directly leads to

$$I_\alpha^{\text{Dr}}[\sigma] = e^{\frac{i}{\hbar} S_{\alpha, \text{SB+B}}^{\text{Dr}}[\bar{x}_\alpha, \sigma]} \int_{\zeta_\alpha, i=0}^{\zeta_\alpha, f=0} \mathcal{D}\zeta_\alpha e^{\frac{i}{\hbar} \int_{t_0}^t ds \frac{m_\alpha}{2} [\dot{\zeta}_\alpha^2(s) - \omega_\alpha^2 \zeta_\alpha^2(s)]}, \quad (\text{E.2})$$

with the action (E.1) now given for the classical path  $\bar{x}_\alpha(t)$ , only. The second equality in Equation (E.1) leads to a convenient form which we make use of below. Since the classical path does not vary, the path integral is now reduced to a path integration over the fluctuations  $\zeta_\alpha(t)$ . Note that its boundary values are zero as the full path  $x_\alpha(t)$  does not vary at its endpoints. In order to evaluate the integral, we follow the arguments presented by Grabert et al. [94, Appendix 86,2A]. First, the fluctuations are written as a Fourier series according to 86,2

$$\zeta_\alpha(s) = \sum_{n=1}^{\infty} \zeta_\alpha^{(n)} \sin[\nu_n(s - t_0)], \quad (\text{E.3})$$

which fulfills the boundary conditions with the frequencies  $\nu_n = \pi n / \Delta t$  and  $\Delta t = t - t_0$ . Insertion into the action and use of the orthogonality of the sine and cosine functions for different  $n$  yields

$$S_\alpha^{\text{Fl}}[\zeta_\alpha] = \int_{t_0}^t ds \frac{m_\alpha}{2} [\dot{\zeta}_\alpha^2(s) - \omega_\alpha^2 \zeta_\alpha^2(s)] = \frac{m_\alpha}{4} \Delta t \sum_{n=1}^{\infty} (\zeta_\alpha^{(n)})^2 [\nu_n^2 - \omega_\alpha^2]. \quad (\text{E.4})$$

The action (E.4) leads to a product of  $n$  Gaussians while the measure can be substituted by  $n$  integrals over the  $\zeta_\alpha^{(n)}$ . Thus, the whole path integral is reduced to a product of Gaussian integrations and we can write

$$\int_{\zeta_\alpha, i=0}^{\zeta_\alpha, f=0} \mathcal{D}\zeta_\alpha e^{\frac{i}{\hbar} S_\alpha^{\text{Fl}}[\zeta_\alpha]} = C \prod_{n=1}^{\infty} \left[ 1 - \frac{\omega_\alpha^2 \Delta t^2}{n^2 \pi^2} \right]^{-\frac{1}{2}} = C \sqrt{\frac{\omega_\alpha \Delta t}{\sin(\omega_\alpha \Delta t)}}. \quad (\text{E.5})$$

Here, the last equation used  $\prod_n [1 - (\omega_\alpha^2 / \nu_n^2)] = \sin(\omega_\alpha \Delta t) / (\omega_\alpha \Delta t)$ . The constant  $C$  absorbed all emerging factors such as the Jacobian from the substitution (E.3). In this way,  $C$  coincides with the result for a free particle and can be found easily by comparison (see e.g. [61, Chapter 8.3]). We finally obtain

$$I_\alpha^{\text{Dr}}[\sigma] = \sqrt{\frac{m_\alpha \omega_\alpha}{2\pi i \hbar \sin[\omega_\alpha(t - t_0)]}} e^{\frac{i}{\hbar} S_{\alpha, \text{SB+B}}^{\text{Dr}}[\bar{x}_\alpha, \sigma]}. \quad (\text{E.6})$$

A similar derivation can also be found in Altland and Simons [17, Chapter 3.3] where the solution is constructed from the determinant of the operator inside the action (the Klein-Gordon operator). We close by noting, that a split into a classical part and fluctuations can also be performed for more general potentials [61, Chapter 8.6].



### Resulting phases

Equation (E.6) shows that the phases of Equations (6.54) and (6.61) are determined by the action for the classical path  $\bar{x}_\alpha(t)$ . For a forced harmonic oscillator the Euler-Lagrange equation can be solved by standard Green's function methods. With  $\chi_\alpha(s) = \sin(\omega_\alpha s)$  one obtains [94, Appendix A]

$$\begin{aligned}\bar{x}_\alpha(s) &= \frac{\chi_\alpha(s-t_0)}{\chi_\alpha(t-t_0)}x_{\alpha,f} + \frac{\chi_\alpha(t-s)}{\chi_\alpha(t-t_0)}x_{\alpha,i} \\ &+ \frac{q_0 c_\alpha}{2m_\alpha \omega_\alpha} \int_{t_0}^s du \chi_\alpha(s-u) \sigma_{\text{eff}}(u) \\ &- \frac{q_0 c_\alpha}{2m_\alpha \omega_\alpha} \frac{\chi_\alpha(s-t_0)}{\chi_\alpha(t-t_0)} \int_{t_0}^t du \chi_\alpha(t-u) \sigma_{\text{eff}}(u).\end{aligned}\quad (\text{E.7})$$

We can already see how the different terms of the phase (6.54) arise by comparison with the second equality in Equation (E.1). Here, the last term gives rise to the free solution while the term proportional to  $\bar{x}_\alpha(s)$  produces the terms that depend on  $c_\alpha$ . Thus, insertion and rearrangement leads directly to Equations (6.54) and (6.61). Finally, we give expressions for the equilibrium density matrix which reads [94]

$$\rho_{\text{B}}^{\text{eq}}(x_\alpha, x'_\alpha) = \frac{1}{\mathcal{Z}_\alpha} \sqrt{\frac{m_\alpha \omega_\alpha}{2\pi \hbar \sinh(\hbar\beta\omega_\alpha)}} e^{-\frac{1}{\hbar} \Phi^{\text{eq}}[x_\alpha, x'_\alpha]}, \quad (\text{E.8})$$

with the phase

$$\Phi^{\text{eq}}[x_\alpha, x'_\alpha] = \frac{m_\alpha \omega_\alpha}{2 \sinh(\hbar\beta\omega_\alpha)} \{ [(x_\alpha)^2 + (x'_\alpha)^2] \cosh(\hbar\beta\omega_\alpha) - 2x_\alpha x'_\alpha \}. \quad (\text{E.9})$$

The partition function  $\mathcal{Z}_\alpha$  is given by the usual expression for free harmonic oscillators [94], i.e.,

$$\mathcal{Z}_\alpha = [2 \sinh(\hbar\beta\omega_\alpha/2)]^{-1}. \quad (\text{E.10})$$

Evidently, the equilibrium density matrix gives the imaginary time analogue to the considerations in the previous subsection.

### Boundary value integrations

These calculations are simple Gaussian integrations and can be performed without difficulty. Due to the number of terms involved, ordering the intermediate results can still be quite daunting. We therefore give some convenient parametrizations. First, it is useful to define

$$A = \coth(\hbar\beta\omega_\alpha) + i \cot[\omega_\alpha(t-t_0)] \quad \text{and} \quad M = \frac{m_\alpha \omega_\alpha}{2\hbar}. \quad (\text{E.11})$$

Both can be used to define the factors of the resulting Gaussian integrations with the form  $\exp(-a_i x^2 + b_i x + c_i)$ . For the integrations required to arrive at Equation (6.65), the  $a_i$  can be chosen according to

$$a_1 = MA, \quad (\text{E.12})$$

for an integration over  $\bar{x}'_{\alpha,i}$  first, then

$$a_2 = MA^* - \frac{M}{A} \left[ \frac{1}{\sinh^2(\hbar\beta\omega_\alpha)} \right] = \frac{M}{A} \left[ 1 + \cot^2[\omega_\alpha(t - t_0)] \right] \quad (\text{E.13})$$

for a subsequent integration over  $\bar{x}_{\alpha,i}$  and

$$\begin{aligned} a_3 &= MA \left[ 1 - \frac{1}{A \sinh(\hbar\beta\omega_\alpha)} \right] + \frac{M}{A} \left[ \frac{1}{\sinh^2(\hbar\beta\omega_\alpha)} + \frac{1}{\sin^2[\omega_\alpha(t - t_0)]} \right] \\ &= 2M \tanh(\hbar\omega_\alpha\beta/2), \end{aligned} \quad (\text{E.14})$$

for the final integration over the remaining  $x_{\alpha,f}$ . All  $a_i$  then feature a positive real part such that the Gaussian integrations can be performed. The  $b_i$  and  $c_i$  are lengthier expressions that we will not give in detail. However,  $b_1$  can be simplified by using

$$\begin{aligned} B &= \frac{d_\alpha}{2} \int_{t_a}^{t_0} du \sin[\omega_\alpha(t_0 - u)] \cos[\omega_\alpha(t - t_0)] F(u) \\ &\quad + \frac{d_\alpha}{2} \int_{t_a}^{t_0} du \cos[\omega_\alpha(t_0 - u)] \sin[\omega_\alpha(t - t_0)] F(u) \\ &\quad + \frac{q_0 c_\alpha}{2} \int_{t_0}^t du \sin[\omega_\alpha(t - u)] \sigma_{\text{eff}}(u) \\ &= \frac{q_0 c_\alpha}{2} \int_{t_a}^t du \sin[\omega_\alpha(t - u)] \sigma_{\text{eff}}(u). \end{aligned} \quad (\text{E.15})$$

Here, the first term originates from the shift (6.64), the second from the additional term in Equation (6.63) and the third comes from the phase (6.54). In the last equality, the implicit time dependence of the system-bath coupling has been used such that Equation (E.15) serves as an example how the non-Markovian force emerges from the integrations. A similar definition can be used for the primed variables. The rest of the calculation concerns the proper rewriting of double integrals which can be done by carefully interchanging the order of the integrations.

## Appendix F

### Corrections to the THz Kerr effect in water due to interactions and bath driving

In this appendix we consider two simple extensions of the Kerr effect theory of Part 7, as outlined in Section 7.2.3.

#### *Dipole-dipole interactions*

We start with dipole-dipole interactions, as given in Equation (7.36), and follow the work by Déjardin and Ladieu [138]. They derive a correction to the dynamic Kerr effect on the basis of spherical molecules and an AC driving field. We may assume that the correction applies only to the dynamics of the second Legendre polynomial and depends on the anisotropy  $\Delta\alpha_0^{\parallel}$  due to the considerations below Equation (7.10). Specifically, we use the correction

$$\Delta\alpha_{\text{int}}(t) = -\frac{3\Delta\alpha_0^{\parallel}}{5\tau_D} \frac{\mu^2}{(k_B T)^2} \frac{\Lambda}{(3 + \Lambda)^2} \int_0^t du e^{-3\frac{(t-u)}{\tau_D}} E^2(u), \quad (\text{F.1})$$

where  $\Lambda = (\rho_0\mu^2)/(3\varepsilon_0k_B T)$  defines the strength of the interaction and depends on the number density  $\rho_0$  and the absolute value of the permanent dipole moment  $\mu$ . The prefactor has been set to agree with that obtained for the (steady-state) polarizabilities at zero frequency [138, Equation (31)]. Using the values of Part 7, we obtain  $\Lambda \approx 30$  such that the prefactor is about a fourth of the size of the permanent dipole contribution in Equation (7.26). We stress that Equation (F.1) does not involve a detailed rederivation and should only be seen as an approximate estimate of the effect of these interaction contributions. The results are shown in Figure F.1 (a) for the polarizability in Equation (7.30). The interaction term shifts the result downwards, as expected, and brings it closer to the experimental results. However, the overall change is still too small to yield significant agreement and the difference in the peak positions still persists.

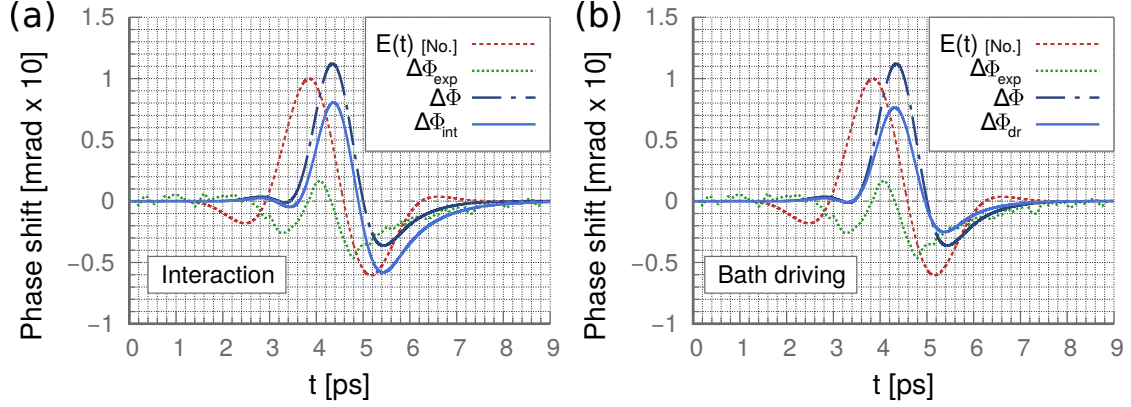


**Figure F.1:** Results for the phase shift (7.33) with additional corrections (light blue solid lines). (a) Results for additional dipole-dipole interactions ( $\Delta\Phi_{\text{int}}$ ) according to Equation (F.1). (b) Results for additional bath driving corrections ( $\Delta\Phi_{\text{bd}}$ ) according to Equation (F.2). Both panels show the experimental results by Zalden et al. [3],  $\Delta\Phi_{\text{exp}}$  (green dotted lines), as well as the uncorrected results of Part 7,  $\Delta\Phi$  (dark blue dash-dotted lines). The (normalized) electric field of Equation (7.32) is also shown (red dashed lines).

### Bath driving contribution

We proceed to bath driving effects which we implement as a correction to the electric field experienced by the water molecules. Specifically, we apply Equation (7.38) and use the results from the Onsager sphere model to correct the field in the Kerr effect theory of Part 7. Naturally, this assumes that the correction occurs parallel to the external driving field. By combining Equations (3.52), (4.24) and (4.25), we can write the corrected electric field as

$$E_{\text{eff}}(t) = E(t) - \frac{2}{\pi} \int_0^\infty d\omega \text{Im}[\chi_o(\omega)] \int_{t_0}^t ds E(s) \sin[\omega(t-s)]. \quad (\text{F.2})$$

The Onsager susceptibility is given by Equation (3.48) and we use the dielectric function of water as given in Equation (4.26) [119]. As before, this approach should only be seen as an estimate of the size of relevant bath driving effects. Finally, we have included a minus sign in Equation (F.2) because we aim for a reduction of the field due to bath driving effects and no enhancement. The results are shown in Figure F.1 (b) for the polarizability of Equation (7.30). In contrast to the effect from the interactions, the contribution from bath driving leads to modulations on the basis of the field strength and its impact is most relevant at the positive and negative peaks. We see both a reduction of the peak height as well as a shift of the peaks to earlier times. Both changes lead to a slightly better agreement with the experimental results. However, the overall effect is still too small to lead to any significant improvement.

## Bibliography

- [1] H. Grabert, P. Nalbach, J. Reichert, and M. Thorwart, “Nonequilibrium Response of Nanosystems Coupled to Driven Quantum Baths”, *The Journal of Physical Chemistry Letters* **7**, 2015–2019 (2016).
- [2] J. Reichert, P. Nalbach, and M. Thorwart, “Dynamics of a quantum two-state system in a linearly driven quantum bath”, *Physical Review A* **94**, 032127 (2016).
- [3] P. Zalden, L. Song, X. Wu, H. Huang, F. Ahr, O. D. Mücke, J. Reichert, M. Thorwart, P. K. Mishra, R. Welsch, R. Santra, F. X. Kärtner, and C. Bressler, “Molecular polarizability anisotropy of liquid water revealed by terahertz-induced transient orientation”, *Nature Communications* **9**, 2142 (2018).
- [4] W. Nolting, *Grundkurs Theoretische Physik 6: Statistische Physik*, 7th edition (Springer, Berlin, Heidelberg, 2014).
- [5] A. Nitzan, *Chemical Dynamics in Condensed Phases* (Oxford University Press, Oxford, 2012).
- [6] P. Hänggi, P. Talkner, and M. Borkovec, “Reaction-rate theory: fifty years after Kramers”, *Reviews of Modern Physics* **62**, 251 (1990).
- [7] N. Pottier, *Nonequilibrium Statistical Physics: Linear Irreversible Processes* (Oxford University Press, Oxford, 2009).
- [8] N. H. Lindner, G. Refael, and V. Galitski, “Floquet topological insulator in semiconductor quantum wells”, *Nature Physics* **7**, 490–495 (2011).
- [9] T. Iadecola, D. Campbell, C. Chamon, C.-Y. Hou, R. Jackiw, S.-Y. Pi, and S. V. Kusminskiy, “Materials Design from Nonequilibrium Steady States: Driven Graphene as a Tunable Semiconductor with Topological Properties”, *Physical Review Letters* **110**, 176603 (2013).
- [10] M. Mitrano, A. Cantaluppi, D. Nicoletti, S. Kaiser, A. Perucchi, S. Lupi, P. Di Pietro, D. Pontiroli, M. Riccò, S. R. Clark, et al., “Possible light-induced superconductivity in K3C60 at high temperature”, *Nature* **530**, 461–464 (2016).
- [11] A. Cavalleri, “Photo-induced superconductivity”, *Contemporary Physics* **59**, 31–46 (2018).

- [12] J.-B. Bru and W. de Siqueira Pedra, “Microscopic foundations of Ohm and Joule’s laws – The relevance of thermodynamics”, in *Mathematical Results in Quantum Mechanics*, edited by P. Exner, W. König, and H. Neidhardt (2014), pp. 151–163.
- [13] W. T. Coffey and Y. P. Kalmykov, *The Langevin Equation*, 3rd edition (World Scientific, Singapore, 2012).
- [14] H. Schoeller, “A perturbative nonequilibrium renormalization group method for dissipative quantum mechanics”, *The European Physical Journal Special Topics* **168**, 179–266 (2009).
- [15] M. J. Hartmann, J. Prior, S. R. Clark, and M. B. Plenio, “Density matrix renormalization group in the Heisenberg picture”, *Physical Review Letters* **102**, 057202 (2009).
- [16] R. Bulla, T. A. Costi, and T. Pruschke, “Numerical renormalization group method for quantum impurity systems”, *Reviews of Modern Physics* **80**, 395 (2008).
- [17] A. Altland and B. Simons, *Condensed Matter Field Theory*, 2nd edition (Cambridge University Press, Cambridge, 2010).
- [18] A. Kamenev, *Field Theory of Non-Equilibrium Systems* (Cambridge University Press, Cambridge, 2011).
- [19] H. Matsubara, G. Kikugawa, T. Bessho, S. Yamashita, and T. Ohara, “Non-equilibrium molecular dynamics simulation as a method of calculating thermodynamic coefficients”, *Fluid Phase Equilibria* **421**, 1–8 (2016).
- [20] B. Meng and W. Weinberg, “Monte Carlo simulations of temperature programmed desorption spectra”, *The Journal of Chemical Physics* **100**, 5280–5289 (1994).
- [21] Y. Makhlin, G. Schön, and A. Shnirman, “Quantum-state engineering with Josephson-junction devices”, *Reviews of Modern Physics* **73**, 357 (2001).
- [22] R. Hanson, L. P. Kouwenhoven, J. R. Petta, S. Tarucha, and L. M. Vandersypen, “Spins in few-electron quantum dots”, *Reviews of Modern Physics* **79**, 1217 (2007).
- [23] M. T. Allen, J. Martin, and A. Yacoby, “Gate-defined quantum confinement in suspended bilayer graphene”, *Nature Communications* **3**, 934 (2012).
- [24] H. van Amerongen, L. Valkunas, and R. van Grondelle, *Photosynthetic Excitons* (World Scientific, Singapore, 2000).
- [25] P. Nalbach and M. Thorwart, “Multiphonon transitions in the biomolecular energy transfer dynamics”, *The Journal of Chemical Physics* **132**, 194111 (2010).
- [26] J. Gilmore and R. H. McKenzie, “Quantum Dynamics of Electronic Excitations in Biomolecular Chromophores: Role of the Protein Environment and Solvent”, *The Journal of Physical Chemistry A* **112**, 2162–2176 (2008).

- [27] W. A. Phillips, “Two-level states in glasses”, *Reports on Progress in Physics* **50**, 1657 (1987).
- [28] P. Strehlow, C. Enss, and S. Hunklinger, “Evidence for a Phase Transition in Glasses at Very Low Temperature: A Macroscopic Quantum State of Tunneling Systems?”, *Physical Review Letters* **80**, 5361 (1998).
- [29] P. Nalbach, D. Osheroff, and S. Ludwig, “Non-equilibrium Dynamics of Interacting Tunneling States in Glasses”, *Journal of Low Temperature Physics* **137**, 395–452 (2004).
- [30] A. J. Leggett and D. C. Vural, “‘Tunneling two-level systems’ model of the low-temperature properties of glasses: Are ‘smoking-gun’ tests possible?”, *The Journal of Physical Chemistry B* **117**, 12966–12971 (2013).
- [31] A. O. Caldeira, *Macroscopic Quantum Phenomena and Quantum Dissipation* (Cambridge University Press, Cambridge, 2014).
- [32] M. Grifoni and P. Hänggi, “Driven quantum tunneling”, *Physics Reports* **304**, 229–354 (1998).
- [33] U. Weiss, *Quantum Dissipative Systems*, 4th edition (World Scientific, Singapore, 2012).
- [34] H. Grabert, “Dynamical Coulomb blockade of tunnel junctions driven by alternating voltages”, *Physical Review B* **92**, 245433 (2015).
- [35] M. Frey and H. Grabert, “Effect of the electromagnetic environment on current fluctuations in driven tunnel junctions”, *Physical Review B* **94**, 045429 (2016).
- [36] M. Frey and H. Grabert, “Current noise in tunnel junctions”, *Fortschritte der Physik* **65** (2017).
- [37] P. K. Mishra, O. Vendrell Romagosa, and R. Santra, “Ultrafast Energy Transfer to Liquid Water by Sub-Picosecond High-Intensity Terahertz Pulses: An Ab Initio Molecular Dynamics Study”, *Angewandte Chemie / International edition* **52**, 13685–13687 (2013).
- [38] P. K. Mishra, O. Vendrell, and R. Santra, “Ultrafast Energy Transfer from Solvent to Solute Induced by Subpicosecond Highly Intense THz Pulses”, *The Journal of Physical Chemistry B* **119**, 8080–8086 (2015).
- [39] P. K. Mishra, O. Vendrell, and R. Santra, “Subpicosecond energy transfer from a highly intense THz pulse to water: A computational study based on the TIP4P/2005 rigid-water-molecule model”, *Physical Review E* **93**, 032124 (2016).
- [40] B. L. Hu and A. Matacz, “Quantum Brownian motion in a bath of parametric oscillators: A model for system-field interactions”, *Physical Review D* **49**, 6612–6635 (1994).

- [41] J. Shao and N. Makri, “Influence functional from a bath of coupled time-dependent harmonic oscillators”, *Physical Review E* **59**, 269–274 (1999).
- [42] R. M. Stratt, “The Instantaneous Normal Modes of Liquids”, *Accounts of Chemical Research* **28**, 201–207 (1995).
- [43] H. Grabert and M. Thorwart, “Quantum mechanical response to a driven Caldeira-Leggett bath”, *Physical Review E* **98**, 012122 (2018).
- [44] H. D. Zeh, “On the interpretation of measurement in quantum theory”, *Foundations of Physics* **1**, 69–76 (1970).
- [45] W. T. Strunz, “Decoherence in Quantum Physics”, in *Coherent Evolution in Noisy Environments*, edited by A. Buchleitner and K. Hornberger (Springer, Berlin, Heidelberg, 2002), pp. 199–233.
- [46] G.-L. Ingold, “Path Integrals and Their Application to Dissipative Quantum Systems”, in *Coherent Evolution in Noisy Environments*, edited by A. Buchleitner and K. Hornberger (Springer, Berlin, Heidelberg, 2002), pp. 1–53.
- [47] P. Hänggi and G.-L. Ingold, “Fundamental aspects of quantum Brownian motion”, *Chaos: An Interdisciplinary Journal of Nonlinear Science* **15**, 026105 (2005).
- [48] R. Zimmermann and J. Wauer, “Non-Markovian relaxation in semiconductors: an exactly soluble model”, *Journal of Luminescence* **58**, 271–274 (1994).
- [49] P. Meystre and M. Sargent, *Elements Of Quantum Optics*, 4th edition (Springer, Berlin, Heidelberg, 2007).
- [50] M. A. Schlosshauer, *Decoherence and the Quantum-to-Classical Transition* (Springer, Berlin, Heidelberg, 2007).
- [51] O. Svelto, *Principles of Lasers*, 5th edition (Springer, Berlin, Heidelberg, 2010).
- [52] J. Gilmore and R. H. McKenzie, “Spin boson models for quantum decoherence of electronic excitations of biomolecules and quantum dots in a solvent”, *Journal of Physics: Condensed Matter* **17**, 1735 (2005).
- [53] C. H. Bennett and D. P. DiVincenzo, “Quantum information and computation”, *Nature* **404**, 247–255 (2000).
- [54] G. S. Engel, T. R. Calhoun, E. L. Read, T.-K. Ahn, T. Mančal, Y.-C. Cheng, R. E. Blankenship, and G. R. Fleming, “Evidence for wavelike energy transfer through quantum coherence in photosynthetic systems”, *Nature* **446**, 782–786 (2007).
- [55] P. Nalbach, D. Braun, and M. Thorwart, “Exciton transfer dynamics and quantumness of energy transfer in the Fenna-Matthews-Olson complex”, *Physical Review E* **84**, 041926 (2011).



- [56] D. M. Wilkins and N. S. Dattani, “Why Quantum Coherence Is Not Important in the Fenna–Matthews–Olsen Complex”, *Journal of Chemical Theory and Computation* **11**, 3411–3419 (2015).
- [57] H.-G. Duan, V. I. Prokhorenko, R. J. Cogdell, K. Ashraf, A. L. Stevens, M. Thorwart, and R. D. Miller, “Nature does not rely on long-lived electronic quantum coherence for photosynthetic energy transfer”, *Proceedings of the National Academy of Sciences* **114**, 8493–8498 (2017).
- [58] G. Rempe, H. Walther, and N. Klein, “Observation of quantum collapse and revival in a one-atom maser”, *Physical Review Letters* **58**, 353 (1987).
- [59] B. W. Shore and P. L. Knight, “The Jaynes–Cummings Model”, *Journal of Modern Optics* **40**, 1195–1238 (1993).
- [60] V. May and O. Kühn, *Charge and Energy Transfer Dynamics in Molecular Systems*, 2nd edition (Wiley-VCH, Weinheim, 2004).
- [61] R. Shankar, *Principles of Quantum Mechanics*, 2nd edition (Springer, Berlin, Heidelberg, 1994).
- [62] J. W. Negele and H. Orland, *Quantum Many Particle Physics* (Perseus, Reading (Mass.), 1998).
- [63] W. Nolting, *Grundkurs Theoretische Physik 1: Klassische Mechanik*, 8th edition (Springer, Berlin, Heidelberg, 2006).
- [64] C. Cohen-Tannoudji, J. Dupont-Roc, and G. Grynberg, *Atom-Photon Interactions: Basic Processes and Applications* (Wiley-VCH, Weinheim, 2004).
- [65] M. Thorwart, “Tunneling and vibrational relaxation in driven multilevel systems”, PhD thesis (Universitaet Augsburg, 2000).
- [66] T. Renger and R. A. Marcus, “On the relation of protein dynamics and exciton relaxation in pigment–protein complexes: an estimation of the spectral density and a theory for the calculation of optical spectra”, *The Journal of Chemical Physics* **116**, 9997–10019 (2002).
- [67] T. Renger, A. Klinger, F. Steinecker, M. Schmidt am Busch, J. Numata, and F. Müh, “Normal Mode Analysis of the Spectral Density of the Fenna–Matthews–Olson Light-Harvesting Protein: How the Protein Dissipates the Excess Energy of Excitons”, *The Journal of Physical Chemistry B* **116**, 14565–14580 (2012).
- [68] T. Yang, P. Vöhringer, D. C. Arnett, and N. F. Scherer, “The solvent spectral density and vibrational multimode approach to optical dephasing: Two-pulse photon echo response”, *The Journal of Chemical Physics* **103**, 8346–8359 (1995).
- [69] F. Gottwald, S. D. Ivanov, and O. Kühn, “On computing spectral densities from classical, semiclassical, and quantum simulations”, *The Journal of Chemical Physics* **150**, 084109 (2019).

- [70] F. Wilhelm, S. Kleff, and J. Von Delft, “The spin-boson model with a structured environment: A comparison of approaches”, *Chemical Physics* **296**, 345–353 (2004).
- [71] P. Lambropoulos, G. M. Nikolopoulos, T. R. Nielsen, and S. Bay, “Fundamental quantum optics in structured reservoirs”, *Reports on Progress in Physics* **63**, 455 (2000).
- [72] M. Thorwart, E. Paladino, and M. Grifoni, “Dynamics of the spin-boson model with a structured environment”, *Chemical Physics* **296**, 333–344 (2004).
- [73] C. Gan, P. Huang, and H. Zheng, “Non-Markovian dynamics of a biased qubit coupled to a structured bath”, *Journal of Physics: Condensed Matter* **22**, 115301 (2010).
- [74] A. Garg, J. N. Onuchic, and V. Ambegaokar, “Effect of friction on electron transfer in biomolecules”, *The Journal of Chemical Physics* **83**, 4491–4503 (1985).
- [75] T. Palm and P. Nalbach, “Nonperturbative environmental influence on dephasing”, *Physical Review A* **96**, 032105 (2017).
- [76] T. Palm and P. Nalbach, “Quasi-adiabatic path integral approach for quantum systems under the influence of multiple non-commuting fluctuations”, *The Journal of Chemical Physics* **149**, 214103 (2018).
- [77] S. Javanbakht, P. Nalbach, and M. Thorwart, “Dissipative Landau-Zener quantum dynamics with transversal and longitudinal noise”, *Physical Review A* **91**, 052103 (2015).
- [78] A. J. Leggett, S. Chakravarty, A. T. Dorsey, M. P. A. Fisher, A. Garg, and W. Zwerger, “Dynamics of the dissipative two-state system”, *Reviews of Modern Physics* **59**, 1–85 (1987).
- [79] A. A. Louis and J. P. Sethna, “Atomic Tunneling from a Scanning-Tunneling or Atomic-Force Microscope Tip: Dissipative Quantum Effects from Phonons”, *Physical Review Letters* **74**, 1363 (1995).
- [80] M. Zwolak, “Numerical ansatz for solving integro-differential equations with increasingly smooth memory kernels: spin-boson model and beyond”, *Computational Science & Discovery* **1**, 015002 (2008).
- [81] D. V. Shalashilin, “Quantum mechanics with the basis set guided by Ehrenfest trajectories: Theory and application to spin-boson model”, *The Journal of Chemical Physics* **130**, 244101 (2009).
- [82] G. D. Mahan, *Many-Particle Physics*, 3rd edition (Kluwer Academic/Plenum Publishers, New York, 2000).
- [83] P. Nalbach, “Adiabatic-Markovian bath dynamics at avoided crossings”, *Physical Review A* **90**, 042112 (2014).

- [84] A. G. Redfield, “On the Theory of Relaxation Processes”, *IBM Journal of Research and Development* **1**, 19–31 (1957).
- [85] H.-P. Breuer and F. Petruccione, *The Theory of Open Quantum Systems* (Oxford University Press, Oxford, 2002).
- [86] P. Nalbach, A. Ishizaki, G. R. Fleming, and M. Thorwart, “Iterative path-integral algorithm versus cumulant time-nonlocal master equation approach for dissipative biomolecular exciton transport”, *New Journal of Physics* **13**, 063040 (2011).
- [87] Y. Dakhnovskii, “Nonadiabatic chemical reactions in a strong time-dependent electric field: An electron transfer reaction in a polar solvent”, *The Journal of Chemical Physics* **100**, 6492–6499 (1994).
- [88] S. Boixo, V. N. Smelyanskiy, A. Shabani, S. V. Isakov, M. Dykman, V. S. Denchev, M. H. Amin, A. Y. Smirnov, M. Mohseni, and H. Neven, “Computational multi-qubit tunnelling in programmable quantum annealers”, *Nature Communications* **7**, 10327 (2016).
- [89] G. Wagner, D. X. Nguyen, D. L. Kovrizhin, and S. H. Simon, “Driven quantum dot coupled to a fractional quantum Hall edge”, arXiv:1908.05658v2 [cond-mat.str-el] (preprint), 2019.
- [90] N. Makri, “Improved Feynman propagators on a grid and non-adiabatic corrections within the path integral framework”, *Chemical Physics Letters* **193**, 435–445 (1992).
- [91] N. Makri and D. E. Makarov, “Tensor propagator for iterative quantum time evolution of reduced density matrices. I. Theory”, *The Journal of Chemical Physics* **102**, 4600–4610 (1995).
- [92] N. Makri and D. E. Makarov, “Tensor propagator for iterative quantum time evolution of reduced density matrices. II. Numerical methodology”, *The Journal of Chemical Physics* **102**, 4611–4618 (1995).
- [93] R. P. Feynman and F. L. Vernon Jr., “The Theory of a General Quantum System Interacting with a Linear Dissipative System”, *Annals of Physics* **24**, 118–173 (1963).
- [94] H. Grabert, P. Schramm, and G.-L. Ingold, “Quantum Brownian motion: The functional integral approach”, *Physics Reports* **168**, 115–207 (1988).
- [95] A. Ishizaki and Y. Tanimura, “Quantum Dynamics of System Strongly Coupled to Low-Temperature Colored Noise Bath: Reduced Hierarchy Equations Approach”, *Journal of the Physical Society of Japan* **74**, 3131–3134 (2005).

- [96] Y. Tanimura and R. Kubo, “Time Evolution of a Quantum System in Contact with a Nearly Gaussian-Markoffian Noise Bath”, *Journal of the Physical Society of Japan* **58**, 101–114 (1989).
- [97] Y. Tanimura, “Nonperturbative expansion method for a quantum system coupled to a harmonic-oscillator bath”, *Physical Review A* **41**, 6676 (1990).
- [98] M. E. Fisher, “Renormalization group theory: Its basis and formulation in statistical physics”, *Reviews of Modern Physics* **70**, 653 (1998).
- [99] B. Delamotte, “A hint of renormalization”, *American Journal of Physics* **72**, 170–184 (2004).
- [100] P. Kopietz, L. Bartosch, and F. Schütz, *Lectures on the Renormalization Group* (Springer, Berlin, Heidelberg, 2010).
- [101] S. G. Jakobs, V. Meden, and H. Schoeller, “Nonequilibrium Functional Renormalization Group for Interacting Quantum Systems”, *Physical Review Letters* **99**, 150603 (2007).
- [102] U. Schollwöck, “The density-matrix renormalization group”, *Reviews of Modern Physics* **77**, 259 (2005).
- [103] J. M. Schurer, A. Negretti, and P. Schmelcher, “Unraveling the Structure of Ultracold Mesoscopic Collinear Molecular Ions”, *Physical Review Letters* **119**, 063001 (2017).
- [104] H. Wang, “Basis set approach to the quantum dissipative dynamics: Application of the multiconfiguration time-dependent Hartree method to the spin-boson problem”, *The Journal of Chemical Physics* **113**, 9948–9956 (2000).
- [105] H.-D. Meyer, F. Gatti, and G. A. Worth, *Multidimensional Quantum Dynamics: MCTDH Theory and Applications* (John Wiley & Sons, Hoboken (New Jersey), 2009).
- [106] M. H. Beck, A. Jäckle, G. A. Worth, and H.-D. Meyer, “The multiconfiguration time-dependent Hartree (MCTDH) method: a highly efficient algorithm for propagating wavepackets”, *Physics Reports* **324**, 1–105 (2000).
- [107] G. Worth, H. Meyer, L. Cederbaum, W. Domcke, D. Yarkony, and H. Köppel, “Multidimensional dynamics involving a conical intersection: Wavepacket calculations using the MCTDH method”, in *Conical intersections: Electronic structure, Dynamics and Spectroscopy*, edited by D. Wolfgang, K. Horst, et al. (World Scientific, Singapore, 2004) Chap. 15, pp. 583–617.
- [108] L. Diósi and W. T. Strunz, “The non-Markovian stochastic Schrödinger equation for open systems”, *Physics Letters A* **235**, 569–573 (1997).
- [109] W. T. Strunz, “The Brownian motion stochastic Schrödinger equation”, *Chemical Physics* **268**, 237–248 (2001).

- [110] D. Suess, A. Eisfeld, and W. Strunz, “Hierarchy of Stochastic Pure States for Open Quantum System Dynamics”, *Physical Review Letters* **113**, 150403 (2014).
- [111] J. D. Jackson, *Klassische Elektrodynamik*, 4th edition (Walter de Gruyter, Berlin, 2006).
- [112] C. Boettcher, *Theory Of Electric Polarization Volume I - Dielectrics in static fields* (Elsevier, Amsterdam, 1973).
- [113] C. Boettcher and P. Bordewijk, *Theory Of Electric Polarization Volume II - Dielectrics in time-dependent fields* (Elsevier, Amsterdam, 1978).
- [114] T. Fließbach, *Elektrodynamik*, 6th edition (Springer, Berlin, Heidelberg, 2012).
- [115] W. Nolting, *Grundkurs Theoretische Physik 3: Elektrodynamik*, 10th edition (Springer, Berlin, Heidelberg, 2013).
- [116] G. New, *Introduction to Nonlinear Optics* (Cambridge University Press, Cambridge, 2011).
- [117] R. W. Boyd, *Nonlinear Optics*, 3rd edition (Academic Press, Burlington, 2008).
- [118] D. C. Elton, “The origin of the Debye relaxation in liquid water and fitting the high frequency excess response”, *Physical Chemistry Chemical Physics* **19**, 18739–18749 (2017).
- [119] H. Yada, M. Nagai, and K. Tanaka, “The intermolecular stretching vibration mode in water isotopes investigated with broadband terahertz time-domain spectroscopy”, *Chemical Physics Letters* **473**, 279–283 (2009).
- [120] H. Yada, M. Nagai, and K. Tanaka, “Origin of the fast relaxation component of water and heavy water revealed by terahertz time-domain attenuated total reflection spectroscopy”, *Chemical Physics Letters* **464**, 166–170 (2008).
- [121] E. Garmire, “Nonlinear optics in daily life”, *Optics Express* **21**, 30532–30544 (2013).
- [122] J. Elkins, “Harold’s Edgerton’s Rapatronic photographs of atomic tests”, *History of Photography* **28**, 74–81 (2004).
- [123] E. Freysz and J. Degert, “Terahertz Kerr effect”, *Nature Photonics* **4**, 131–132 (2010).
- [124] H. A. Haus, “Mode-locking of lasers”, *IEEE Journal of Selected Topics in Quantum Electronics* **6**, 1173–1185 (2000).
- [125] A. Hasegawa, “Theory of information transfer in optical fibers: A tutorial review”, *Optical Fiber Technology* **10**, 150–170 (2004).
- [126] M. C. Hoffmann, N. C. Brandt, H. Y. Hwang, K.-L. Yeh, and K. A. Nelson, “Terahertz Kerr effect”, *Applied Physics Letters* **95**, 231105 (2009).

- [127] M. Melnichuk and L. T. Wood, “Direct Kerr electro-optic effect in noncentrosymmetric materials”, *Physical Review A* **82**, 013821 (2010).
- [128] Q. Zhong and J. T. Fourkas, “Optical Kerr Effect Spectroscopy of Simple Liquids”, *The Journal of Physical Chemistry B* **112**, 15529–15539 (2008).
- [129] R. Righini, “Ultrafast Optical Kerr Effect in Liquids and Solids”, *Science* **262**, 1386–1390 (1993).
- [130] D. McMorow, W. T. Lotshaw, and G. A. Kenney-Wallace, “Femtosecond optical Kerr studies on the origin of the nonlinear responses in simple liquids”, *IEEE Journal of Quantum Electronics* **24**, 443–454 (1988).
- [131] Y. P. Kalmykov, “Matrix method calculation of the Kerr effect transient and ac stationary responses of arbitrary shaped macromolecules”, *The Journal of Chemical Physics* **131**, 074107 (2009).
- [132] D. Meschede, *Gerthsen Physik*, 22nd edition (Springer, Berlin, Heidelberg, 2004).
- [133] J. Tomasi, B. Mennucci, and R. Cammi, “Quantum Mechanical Continuum Solvation Models”, *Chemical Reviews* **105**, 2999–3094 (2005).
- [134] J. Tomasi, “Thirty years of continuum solvation chemistry: a review, and prospects for the near future”, *Theoretical Chemistry Accounts* **112**, 184–203 (2004).
- [135] J. Tomasi and M. Persico, “Molecular Interactions in Solution: An Overview of Methods Based on Continuous Distributions of the Solvent”, *Chemical Reviews* **94**, 2027–2094 (1994).
- [136] B. Mennucci and R. Cammi, *Continuum Solvation Models in Chemical Physics: From Theory to Applications* (John Wiley & Sons, Hoboken (New Jersey), 2007).
- [137] B. Bagchi, D. W. Oxtoby, and G. R. Fleming, “Theory of the time development of the Stokes shift in polar media”, *Chemical Physics* **86**, 257–267 (1984).
- [138] P. M. Déjardin and F. Ladieu, “Nonlinear susceptibilities of interacting polar molecules in the self-consistent field approximation”, *The Journal of Chemical Physics* **140**, 034506 (2014).
- [139] M. Born, “Volumen und Hydratationswärme der Ionen”, *Zeitschrift für Physik A* **1**, 45–48 (1920).
- [140] J. G. Kirkwood, “Theory of Solutions of Molecules Containing Widely Separated Charges with Special Application to Zwitterions”, *The Journal of Chemical Physics* **2**, 351–361 (1934).
- [141] L. Onsager, “Electric Moments of Molecules in Liquids”, *Journal of the American Chemical Society* **58**, 1486–1493 (1936).

- [142] Y. Luo, H. Ågren, and K. V. Mikkelsen, “Unique determination of the cavity radius in Onsager reaction field theory”, *Chemical Physics Letters* **275**, 145–150 (1997).
- [143] D. E. Leahy, “Intrinsic Molecular Volume as a Measure of the Cavity Term in Linear Solvation Energy Relationships: Octanol-Water Partition Coefficients and Aqueous Solubilities”, *Journal of Pharmaceutical Sciences* **75**, 629–636 (1986).
- [144] B. Mennucci, “Continuum Solvation Models: What Else Can We Learn from Them?”, *The Journal of Physical Chemistry Letters* **1**, 1666–1674 (2010).
- [145] P. Macak, P. Norman, Y. Luo, and H. Ågren, “Modeling of dynamic molecular solvent properties using local and cavity field approaches”, *The Journal of Chemical Physics* **112**, 1868–1875 (2000).
- [146] D. V. Matyushov, “On the theory of dielectric spectroscopy of protein solutions”, *Journal of Physics: Condensed Matter* **24**, 325105 (2012).
- [147] B. Mennucci, G. Scalmani, and D. Jacquemin, “Excited-State Vibrations of Solvated Molecules: Going Beyond the Linear-Response Polarizable Continuum Model”, *Journal of Chemical Theory and Computation* **11**, 847–850 (2015).
- [148] P. G. Etchegoin and E. C. Le Ru, “Basic Electromagnetic Theory of SERS”, in *Surface Enhanced Raman Spectroscopy*, edited by S. Schlücker (John Wiley & Sons, Hoboken (New Jersey), 2011) Chap. 1, pp. 1–37.
- [149] P. Nalbach, A. Achner, M. Frey, M. Grosser, C. Bressler, and M. Thorwart, “Hydration shell effects in the relaxation dynamics of photoexcited Fe-II complexes in water”, *The Journal of Chemical Physics* **141**, 044304 (2014).
- [150] H. Kirchberg, P. Nalbach, and M. Thorwart, “Nonequilibrium quantum solvation with a time-dependent Onsager cavity”, *The Journal of Chemical Physics* **148**, 164301 (2018).
- [151] P. Nalbach and M. Thorwart, “Landau-Zener Transitions in a Dissipative Environment: Numerically Exact Results”, *Physical Review Letters* **103**, 220401 (2009).
- [152] L. Landau, “Zur Theorie der Energieübertragung I”, *Phys. Z. Sowjetunion* **1**, 88–95 (1932).
- [153] C. Zener, “Non-adiabatic crossing of energy levels”, *Proceedings of the Royal Society of London. Series A, Containing Papers of a Mathematical and Physical Character* **137**, 696–702 (1932).
- [154] E. Stueckelberg, “Two-level strong binding approximation”, *Helvetica Physica Acta* **5**, 370–395 (1932).
- [155] P. M. V. B. Barone and A. O. Caldeira, “Quantum mechanics of radiation damping”, *Physical Review A* **43**, 57 (1991).

- [156] C. W. S. Conover, “Effects of pulse shape on strongly driven two-level systems”, *Physical Review A* **84**, 063416 (2011).
- [157] I. I. Boradjiev and N. V. Vitanov, “Control of qubits by shaped pulses of finite duration”, *Physical Review A* **88**, 013402 (2013).
- [158] B. T. Torosov and N. V. Vitanov, “Exactly soluble two-state quantum models with linear couplings”, *Journal of Physics A: Mathematical and Theoretical* **41**, 155309 (2008).
- [159] P. R. Berman, L. Yan, K.-H. Chiam, and R. Sung, “Nonadiabatic transitions in a two-level quantum system: Pulse-shape dependence of the transition probability for a two-level atom driven by a pulsed radiation field”, *Physical Review A* **57**, 79 (1998).
- [160] N. Rosen and C. Zener, “Double Stern-Gerlach Experiment and Related Collision Phenomena”, *Physical Review* **40**, 502 (1932).
- [161] G. S. Vasilev and N. V. Vitanov, “Coherent excitation of a two-state system by a Gaussian field”, *Physical Review A* **70**, 053407 (2004).
- [162] R. W. Munn, Y. Luo, P. Macák, and H. Ågren, “Role of the cavity field in nonlinear optical response in the condensed phase”, *The Journal of Chemical Physics* **114**, 3105–3108 (2001).
- [163] A. I. McIntosh, B. Yang, S. M. Goldup, M. Watkinson, and R. S. Donnan, “Terahertz spectroscopy: a powerful new tool for the chemical sciences?”, *Chemical Society Reviews* **41**, 2072–2082 (2012).
- [164] P. Jepsen, D. Cooke, and M. Koch, “Terahertz spectroscopy and imaging – Modern techniques and applications”, *Laser & Photonics Reviews* **5**, 124–166 (2011).
- [165] T. Kampfrath, M. Wolf, and M. Sajadi, “Anharmonic Coupling between Intermolecular Motions of Water Revealed by Terahertz Kerr Effect”, arXiv:1707.07622v1 [cond-mat.soft] (preprint), 2017.
- [166] T. Kampfrath, M. Wolf, and M. Sajadi, “The sign of the polarizability anisotropy of polar molecules is obtained from the terahertz Kerr effect”, *Chemical Physics Letters* **692**, 319–323 (2018).
- [167] N. Q. Vinh, M. S. Sherwin, S. J. Allen, D. K. George, A. J. Rahmani, and K. W. Plaxco, “High-precision gigahertz-to-terahertz spectroscopy of aqueous salt solutions as a probe of the femtosecond-to-picosecond dynamics of liquid water”, *The Journal of Chemical Physics* **142**, 164502 (2015).
- [168] A. Beneduci, “Which is the effective time scale of the fast Debye relaxation process in water?”, *Journal of Molecular Liquids* **138**, 55–60 (2008).
- [169] T. Shimanouchi, *Tables of Molecular Vibrational Frequencies. Consolidated Volume I* (National Bureau of Standards, 1972).



- [170] T. Shimanouchi, "Tables of molecular vibrational frequencies. Consolidated volume II", *Journal of Physical and Chemical Reference Data* **6**, 993–1102 (1977).
- [171] F. R. Dollish, W. G. Fateley, and F. F. Bentley, *Characteristic Raman Frequencies of Organic Compounds* (Wiley, 1974).
- [172] I. Kleiner, M. Godefroid, M. Herman, and A. McKellar, "The fundamental torsion band in acetaldehyde", *Journal of Molecular Spectroscopy* **142**, 238–253 (1990).
- [173] M. Tasumi, T. Urano, and M. Nakata, "Some thoughts on the vibrational modes of toluene as a typical monosubstituted benzene", *Journal of Molecular Structure* **146**, 383–396 (1986).
- [174] M. A. Spackman, "Accurate prediction of static dipole polarizabilities with moderately sized basis sets", *The Journal of Physical Chemistry* **93**, 7594–7603 (1989).
- [175] E. F. Archibong and A. J. Thakkar, "Polarizabilities of aromatic six-membered rings: azines and 'inorganic benzenes'", *Molecular Physics* **81**, 557–567 (1994).
- [176] M. Borenstein and W. E. Lamb Jr., "Classical laser", *Physical Review A* **5**, 1298 (1972).
- [177] U. Fano, "Effects of configuration interaction on intensities and phase shifts", *Physical Review* **124**, 1866 (1961).
- [178] M. F. Limonov, M. V. Rybin, A. N. Poddubny, and Y. S. Kivshar, "Fano resonances in photonics", *Nature Photonics* **11**, 543–554 (2017).
- [179] M. Kroner, A. O. Govorov, S. Remi, B. Biedermann, S. Seidl, A. Badolato, P. M. Petroff, W. Zhang, R. Barbour, B. D. Gerardot, et al., "The nonlinear Fano effect", *Nature* **451**, 311–314 (2008).
- [180] A. P. Alivisatos, "Semiconductor Clusters, Nanocrystals, and Quantum Dots", *Science* **271**, 933–937 (1996).
- [181] C. J. Murphy, "Peer Reviewed: Optical Sensing with Quantum Dots", *Analytical Chemistry* **74**, 520 A–526 A (2002).
- [182] K.-S. Cho, E. K. Lee, W.-J. Joo, E. Jang, T.-H. Kim, S. J. Lee, S.-J. Kwon, J. Y. Han, B.-K. Kim, B. L. Choi, et al., "High-performance crosslinked colloidal quantum-dot light-emitting diodes", *Nature Photonics* **3**, 341–345 (2009).
- [183] E. H. Sargent, "Colloidal quantum dot solar cells", *Nature Photonics* **6**, 133–135 (2012).
- [184] P. V. Kamat, J. A. Christians, and J. G. Radich, "Quantum Dot Solar Cells: Hole Transfer as a Limiting Factor in Boosting the Photoconversion Efficiency", *Langmuir* **30**, 5716–5725 (2014).

- [185] M. S. Tame, K. McEnery, Ş. K. Özdemir, J. Lee, S. Maier, and M. Kim, “Quantum plasmonics”, *Nature Physics* **9**, 329–340 (2013).
- [186] A. V. Akimov, A. Mukherjee, C. L. Yu, D. E. Chang, A. S. Zibrov, P. R. Hemmer, H. Park, and M. D. Lukin, “Generation of single optical plasmons in metallic nanowires coupled to quantum dots”, *Nature* **450**, 402–406 (2007).
- [187] D. E. Chang, A. S. Sørensen, P. R. Hemmer, and M. D. Lukin, “Quantum Optics with Surface Plasmons”, *Physical Review Letters* **97**, 053002 (2006).
- [188] G.-Y. Chen, N. Lambert, Y.-A. Shih, M.-H. Liu, Y.-N. Chen, and F. Nori, “Plasmonic bio-sensing for the Fenna-Matthews-Olson complex”, *Scientific Reports* **7**, Article, 39720 (2017).
- [189] K. Okamoto, I. Niki, Y. Shvartser Alexanderand Narukawa, T. Mukai, and A. Scherer, “Surface-plasmon-enhanced light emitters based on InGaN quantum wells”, *Nature Materials* **3**, 601–605 (2004).
- [190] K. Catchpole and A. Polman, “Plasmonic solar cells”, *Optics Express* **16**, 21793–21800 (2008).
- [191] W. Zhang, A. O. Govorov, and G. W. Bryant, “Semiconductor-Metal Nanoparticle Molecules: Hybrid Excitons and the Nonlinear Fano Effect”, *Physical Review Letters* **97**, 146804 (2006).
- [192] J.-Y. Yan, W. Zhang, S. Duan, X.-G. Zhao, and A. O. Govorov, “Optical properties of coupled metal-semiconductor and metal-molecule nanocrystal complexes: Role of multipole effects”, *Physical Review B* **77**, 165301 (2008).
- [193] A. O. Govorov, Z. Fan, P. Hernandez, J. M. Slocik, and R. R. Naik, “Theory of Circular Dichroism of Nanomaterials Comprising Chiral Molecules and Nanocrystals: Plasmon Enhancement, Dipole Interactions, and Dielectric Effects”, *Nano Letters* **10**, 1374–1382 (2010).
- [194] R. L. Olmon, B. Slovick, T. W. Johnson, D. Shelton, S.-H. Oh, G. D. Boreman, and M. B. Raschke, “Optical dielectric function of gold”, *Physical Review B* **86**, 235147 (2012).
- [195] A. L. Routzahn, S. L. White, L.-K. Fong, and P. K. Jain, “Plasmonics with Doped Quantum Dots”, *Israel Journal of Chemistry* **52**, 983–991 (2012).
- [196] D. J. Norris and M. G. Bawendi, “Measurement and assignment of the size-dependent optical spectrum in CdSe quantum dots”, *Physical Review B* **53**, 16338 (1996).
- [197] P. Nalbach, J. Knörzer, and S. Ludwig, “Nonequilibrium Landau-Zener-Stueckelberg spectroscopy in a double quantum dot”, *Physical Review B* **87**, 165425 (2013).
- [198] A. Würger, “Perturbation theory for the spin-phonon model”, *Journal of Physics: Condensed Matter* **9**, 5543 (1997).

- [199] H. Horner, “Low frequency, low temperature properties of the spin-boson problem”, *The European Physical Journal B* **18**, 453–458 (2000).
- [200] P. Nalbach, “Weakly coupled tunneling systems in mixed crystals”, *Physical Review B* **66**, 134107 (2002).
- [201] P. Nalbach and M. Thorwart, “Competition between relaxation and external driving in the dissipative Landau–Zener problem”, *Chemical Physics* **375**, 234–242 (2010).
- [202] P. Nalbach, “Dynamik von Tunneldefekten - Der [111]-Defekt”, PhD thesis (Ruprecht-Karls Universität Heidelberg, Fakultät für Physik und Astronomie, 1999).
- [203] E. Merzbacher, *Quantum Mechanics*, 3rd edition (John Wiley & Sons, Hoboken (New Jersey), 1998).
- [204] M. Grifoni, M. Sasseti, and U. Weiss, “Exact master equations for driven dissipative tight-binding models”, *Physical Review E* **53**, R2033 (1996).
- [205] H. Dekker, “Noninteracting-blip approximation for a two-level system coupled to a heat bath”, *Physical Review A* **35**, 1436–1437 (1987).
- [206] T. Tsuzuki, “Quantum Langevin Dynamics of a Two-State System Coupled to a Bosonic Bath”, *Progress of Theoretical Physics* **81**, 770–782 (1989).
- [207] B. Misra and E. C. G. Sudarshan, “The Zeno’s paradox in quantum theory”, *Journal of Mathematical Physics* **18**, 756–763 (1977).
- [208] A. Z. Chaudhry, “A general framework for the Quantum Zeno and anti-Zeno effects”, *Scientific Reports* **6**, 29497 (2016).
- [209] U. Weiss, H. Grabert, and S. Linkwitz, “Influence of friction and temperature on coherent quantum tunneling”, *Journal of Low Temperature Physics* **68**, 213–244 (1987).
- [210] R. P. Feynman, *Quantum Mechanics and Path Integrals* (McGraw-Hill, New York, 1965).
- [211] C. Zerbe and P. Hänggi, “Brownian parametric quantum oscillator with dissipation”, *Physical Review E* **52**, 1533–1543 (1995).
- [212] H. Watanabe and A. Morita, “Kerr effect relaxation in high electric fields”, *Advances in Chemical Physics* **56**, 255 (1984).
- [213] W. A. Wegener, F. R. M. Dowben, and V. J. Koester, “Time-dependent birefringence, linear dichroism, and optical rotation resulting from rigid-body rotational diffusion”, *The Journal of Chemical Physics* **70**, 622–632 (1979).

- [214] M. Gussoni, M. Rui, and G. Zerbi, “Electronic and relaxation contribution to linear molecular polarizability. An analysis of the experimental values”, *Journal of Molecular Structure* **447**, 163–215 (1998).
- [215] B. Friedrich, D. P. Pullman, and D. R. Herschbach, “Alignment and orientation of rotationally cool molecules”, *The Journal of Physical Chemistry* **95**, 8118–8129 (1991).
- [216] S. Fleischer, Y. Zhou, R. W. Field, and K. A. Nelson, “Molecular Orientation and Alignment by Intense Single-Cycle THz Pulses”, *Physical Review Letters* **107**, 163603 (2011).
- [217] J. L. McHale, *Molecular Spectroscopy*, 2nd edition (CRC Press, Boca Raton (Florida), 2017).
- [218] B. J. Berne, “A self-consistent theory of rotational diffusion”, *The Journal of Chemical Physics* **62**, 1154–1160 (1975).
- [219] L. D. Favro, “Theory of the Rotational Brownian Motion of a Free Rigid Body”, *Physical Review* **119**, 53 (1960).
- [220] D. A. Varshalovich, A. N. Moskalev, and V. K. Khersonskii, *Quantum Theory of Angular Momentum* (World Scientific, Singapore, 1988).
- [221] W. A. Wegener, “Transient electric birefringence of dilute rigid-body suspensions at low field strengths”, *The Journal of Chemical Physics* **84**, 5989–6004 (1986).
- [222] J.-L. Déjardin, *Dynamic Kerr Effect: The Use and Limits of the Smoluchowski Equation and Nonlinear Inertial Responses* (World Scientific, Singapore, 1995).
- [223] J. Déjardin, P. Déjardin, and Y. P. Kalmykov, “Analytical solutions for the dynamic Kerr effect: Linear response of polar and polarizable molecules to a weak ac electric field superimposed on a strong dc bias field”, *The Journal of Chemical Physics* **107**, 508–523 (1997).
- [224] M. Sajadi, M. Wolf, and T. Kampfrath, “Transient birefringence of liquids induced by terahertz electric-field torque on permanent molecular dipoles”, *Nature Communications* **8**, 14963 (2017).
- [225] S. Bodrov, Y. Sergeev, A. Murzanev, and A. Stepanov, “Terahertz induced optical birefringence in polar and nonpolar liquids”, *The Journal of Chemical Physics* **147**, 084507 (2017).
- [226] T. Kampfrath, R. K. Campen, M. Wolf, and M. Sajadi, “The Nature of the Dielectric Response of Methanol Revealed by the Terahertz Kerr Effect”, *The Journal of Physical Chemistry Letters* **9**, 1279–1283 (2018).

- [227] F. Novelli, L. R. Pestana, K. C. Bennett, N. Dessmann, F. Sebastiani, E. M. Adams, K. S. Ilkhchy, N. Stavrias, V. Eless, T. Ockelmann, A. Colchero, C. Hoberg, G. Schwaab, L. A. F. G. Van Der Meer, T. Head-Gordon, and M. Havenith, “Strong Anisotropy in Liquid Water upon Librational Excitation using Terahertz Laser Fields”, arXiv:1809.04261v2 [physics.chem-ph] (preprint), 2019.
- [228] R. Buchner, J. Barthel, and J. Stauber, “The dielectric relaxation of water between 0 C and 35 C”, *Chemical Physics Letters* **306**, 57–63 (1999).
- [229] A. Luzar and D. Chandler, “Hydrogen-bond kinetics in liquid water”, *Nature* **379**, 55–57 (1996).
- [230] J. S. Hansen, A. Kisiuk, A. P. Sokolov, and C. Gainaru, “Identification of structural relaxation in the dielectric response of water”, *Physical Review Letters* **116**, 237601 (2016).
- [231] N. Agmon, “Tetrahedral Displacement: The Molecular Mechanism behind the Debye Relaxation in Water”, *The Journal of Physical Chemistry* **100**, 1072–1080 (1996).
- [232] L. Korson, W. Drost-Hansen, and F. J. Millero, “Viscosity of water at various temperatures”, *The Journal of Physical Chemistry* **73**, 34–39 (1969).
- [233] S. R. Becker, P. H. Poole, and F. W. Starr, “Fractional Stokes-Einstein and Debye-Stokes-Einstein Relations in a Network-Forming Liquid”, *Physical Review Letters* **97**, 055901 (2006).
- [234] M. G. Mazza, N. Giovambattista, H. E. Stanley, and F. W. Starr, “Connection of translational and rotational dynamical heterogeneities with the breakdown of the Stokes-Einstein and Stokes-Einstein-Debye relations in water”, *Physical Review E* **76**, 031203 (2007).
- [235] D. A. Turton and K. Wynne, “Stokes–Einstein–Debye Failure in Molecular Orientational Diffusion: Exception or Rule?”, *The Journal of Physical Chemistry B* **118**, 4600–4604 (2014).
- [236] K. Winkler, J. Lindner, H. Bürsing, and P. Vöhringer, “Ultrafast Raman-induced Kerr-effect of water: Single molecule versus collective motions”, *The Journal of Chemical Physics* **113**, 4674–4682 (2000).
- [237] W. T. Huntress Jr., “Effects of Anisotropic Molecular Rotational Diffusion on Nuclear Magnetic Relaxation in Liquids”, *The Journal of Chemical Physics* **48**, 3524–3533 (1968).
- [238] G. Chevrot, K. Hinsén, and G. R. Kneller, “Model-free simulation approach to molecular diffusion tensors”, *The Journal of Chemical Physics* **139**, 154110 (2013).

- [239] N. Meyer, V. Piquet, J.-F. Wax, H. Xu, and C. Millot, “Rotational and translational dynamics of the SPC/E water model”, *Journal of Molecular Liquids* **275**, 895–908 (2019).
- [240] D. Rozmanov and P. G. Kusalik, “Transport coefficients of the TIP4P-2005 water model”, *The Journal of Chemical Physics* **136**, 044507 (2012).
- [241] I. Svishchev and P. Kusalik, “Dynamics in liquid water, water-d<sub>2</sub>, and water-t<sub>2</sub>: a comparative simulation study”, *The Journal of Physical Chemistry* **98**, 728–733 (1994).
- [242] D. E. O’Reilly, “Self-diffusion coefficients and rotational correlation times in polar liquids. VI. Water”, *The Journal of Chemical Physics* **60**, 1607–1618 (1974).
- [243] G. Maroulis, “Electric moments, polarizabilities and hyperpolarizabilities for carbon disulfide (S=C=S) from accurate SCF calculations”, *Chemical Physics Letters* **199**, 250–256 (1992).
- [244] R. Chelli, M. Pagliai, P. Procacci, G. Cardini, and V. Schettino, “Polarization response of water and methanol investigated by a polarizable force field and density functional theory calculations: Implications for charge transfer”, *The Journal of Chemical Physics* **122**, 074504 (2005).
- [245] H. Ito, J.-Y. Jo, and Y. Tanimura, “Notes on simulating two-dimensional Raman and terahertz-Raman signals with a full molecular dynamics simulation approach”, *Structural Dynamics* **2**, 054102 (2015).
- [246] G. Avila, “Ab initio dipole polarizability surfaces of water molecule: Static and dynamic at 514.5 nm”, *The Journal of Chemical Physics* **122**, 144310 (2005).
- [247] A. V. Gubskaya and P. G. Kusalik, “The total molecular dipole moment for liquid water”, *The Journal of Chemical Physics* **117**, 5290–5302 (2002).
- [248] J. K. Gregory, D. C. Clary, K. Liu, M. G. Brown, and R. J. Saykally, “The Water Dipole Moment in Water Clusters”, *Science* **275**, 814–817 (1997).
- [249] D. Laage and J. T. Hynes, “A Molecular Jump Mechanism of Water Reorientation”, *Science* **311**, 832–835 (2006).
- [250] J. Kongsted, A. Osted, K. V. Mikkelsen, and O. Christiansen, “Second harmonic generation second hyperpolarizability of water calculated using the combined coupled cluster dielectric continuum or different molecular mechanics methods”, *The Journal of Chemical Physics* **120**, 3787–3798 (2004).
- [251] W. F. Murphy, “The Rayleigh depolarization ratio and rotational Raman spectrum of water vapor and the polarizability components for the water molecule”, *The Journal of Chemical Physics* **67**, 5877–5882 (1977).

- [252] S. D. Deshmukh, P.-M. Déjardin, and Y. P. Kalmykov, “Dynamic Kerr effect in a strong uniform AC electric field for interacting polar and polarizable molecules in the mean field approximation”, *The Journal of Chemical Physics* **147**, 094501 (2017).
- [253] G. C. Schatz, M. A. Young, and R. P. Van Duyne, “Electromagnetic Mechanism of SERS”, in *Surface-Enhanced Raman Scattering: Physics and Applications*, edited by K. Kneipp, M. Moskovits, and H. Kneipp (Springer, Berlin, Heidelberg, 2006), pp. 19–45.
- [254] M. E. Peskin and D. V. Schroeder, *An Introduction to Quantum Field Theory* (Westview Press, Boulder (Colorado), 1995).
- [255] T. Scholte, “A contribution to the theory of the dielectric constant of polar liquids”, *Physica* **15**, 437–449 (1949).
- [256] N. V. Vitanov, “Asymmetrized Rosen-Zener model”, *Journal of Physics B: Atomic, Molecular and Optical Physics* **27**, 1351 (1994).